Membrane Modulating DNA Nanostructures for Diagnostics and Immunotherapeutics

by

Leeza Abraham

A Dissertation Presented in Partial Fulfillment
of the Requirement for the Degree
Doctor of Philosophy

Approved May 2023 by the
Graduate Supervisory Committee:

Hao Yan, Chair
Yan Liu
Nicholas Stephanopoulos

ARIZONA STATE UNIVERSITY

August 2023

ABSTRACT

The biological lipid bilayer on cells or the cell membrane is a surface teeming with activity. Several membrane proteins decorate the lipid bilayer to carry out various functionalities that help a cell interact with the environment, gather resources and communicate with other cells. This provides a repertoire of biological structures and processes that can be mimicked and manipulated. Since its inception in the late 20^{th} century deoxyribonucleic acid (DNA) nanotechnology has been used to create nanoscale objects that can be used for such purposes. Using DNA as the building material provides the user with a programmable and functionalizable tool box to design and demonstrate these ideas. In this dissertation, I describe various DNA nanostructures that can insert or interact with lipid bilayers for cargo transport, diagnostics and therapeutics.

First, I describe a reversibly gated DNA nanopore of 20.4nm x 20.4nm cross sectional width. Controlled transport of cargoes of various sizes across a lipid bilayer through a channel formed by the DNA nanopore was demonstrated. This demonstration paves the way for a class of nanopores that can be activated by different stimuli. The membrane insertion capability of the DNA nanopore is further utilized to design a nanopore sensor that can detect oligonucleotides of a specific sequence inside a lipid vesicle. The ease with which the sensor can be modified to identify different diagnostic markers for disease detection was shown by designing a sensor that can identify the non small cell lung cancer marker micro ribonucleic acid -21 (miRNA21). Finally, I demonstrate the therapeutic capabilities of DNA devices with a DNA tetrabody that can recruit natural killer cells (NK cells) to target cancer cells. The DNA tetrabody functionalized with cholesterol molecules and Her2 affibody inserts into NK cell membrane leading it to Her2 positive cancer cells. This shows that in the presence of DNA tetrabody, the NK cell activation gets accelerated.

ACKNOWLEDGEMENTS

The past five years have been the biggest learning experience in my life and this opportunity has enabled me to grow into the person I am today. I would like to express my deepest gratitude to all those who have supported and contributed to the completion of this dissertation. Their assistance and encouragement have played a significant role in shaping the outcome of this research endeavor.

First and foremost, I am immensely grateful to my advisor, Prof. Hao Yan, for his guidance, expertise, and unwavering support throughout this entire process. His invaluable insights and constructive feedback have been instrumental in refining my research objectives and methodology. I am grateful for his commitment to my academic growth and for believing in my abilities.

I extend my sincere appreciation to the members of my dissertation committee, Prof. Yan Liu and Prof. Nicholas Stephanopoulos, for their insightful comments, suggestions, and the time they dedicated to reviewing my work. Their expertise and feedback have greatly enriched this study, and I am grateful for their valuable contributions.

I put forward my sincere gratitude to Dr. Yang Xu for her unlimited bank of ideas and her cheerful disposition that has helped me several times through out my PhD journey. I am indebted to all the present and past Yan lab members, who have provided me with a stimulating academic environment and resources necessary for conducting this research. I especially thank Raghu Pradeep for helping me start my journey here and Swarup Dey for his timely intervention into it. I also thank Fei Zhang, Xiadong Qi, Shouxing Jiang, Guangbao Yao, Xu Zhou, Hao Liu, Yue Tang, Lan Liu, Lu Yu, Liangxiao Chen, Deeksha, Abhay Kuriyal, Xinyi Tu, Rong Zheng and Lanshen Zhao for their commitment to fostering an atmosphere of learning and research excellence which been instrumental in shaping my academic journey.

I thank my roommates Pritha and Sanchari for all the fun and food and love. I would like to express my heartfelt thanks to my friends Soma, Arshia, Nikila, Srivatsan, Sreeganesh, Mayukh, Julio, Alamin, Beth, Skanda, Hiamlini, Merlin, Nikitha, Tincy, Sanu, Karthik, Ashwin, Namitha, Madhuri, Maria and Mathew who have offered their support and encouragement throughout this challenging process. Their presence, discussions, and shared experiences have been a constant source of motivation and inspiration. I am grateful for the camaraderie and intellectual exchange we have enjoyed together.

I would like to express my deepest gratitude to my family, Appa, Amma, Chinma chechi, Moby chettan, Susa, Mathew, Lulu and Marissa. Their unwavering love, understanding, and support have been my pillar of strength throughout this journey. Their encouragement and belief in me have been the driving force behind my pursuit of knowledge and academic excellence. I am deeply grateful to my Karteek for being the best companion one could ask for. I thank him for his love and care and all the plans that we continue to make.

To all those mentioned above, and to those whom I may have inadvertently omitted, please accept my sincere gratitude for your contributions and support. This dissertation would not have been possible without your assistance, and I am truly grateful for your presence in my academic life.

Finally, I thank God for leading me in the right path and helping me back up when I stumble.

TABLE OF CONTENTS

CHAPTER Page

CHAPTER Page

CHAPTER Page

LIST OF TABLES

Table Page

LIST OF FIGURES

Figure Page

Figure Page

Figure Page

Chapter 1

INTRODUCTION

Part of this chapter has been published in R. Narayanan, & **L. Abraham**, Structural DNA Nanotechnology: Immobile Holliday Junctions to Artificial Robots. *Current Topics in Medicinal Chemistry*, 22, (**2022**).

1.1 Biomimetics

Through the process of evolution and natural selection, nature has established well defined systems and processes, that dictate life. Theses systems work with utmost efficiency from the molecular level to macroscale. They are able to produce energy, communicate, mend, move, and create new life with the resources available around them. But despite being a product of this illustrious entity, human beings built machines that gets the work done, without giving significance to efficiency of energy consumption or about the pollution caused by waste products. But due to increased awareness we are now borrowing designs and ideas from nature to build tools that work with efficiency and simplicity. Leonardo Da Vinci designed flying machines by observing birds in flight and shark skin that has micro scales [3] has inspired swim suits that gives minimum resistance in water. Even the Japanese bullet trains were re-engineered to mimic the kingfisher's beak in order to eliminate the loud sounds it produced in tunnels (**Figure 1.1**).

The umbrella term used to define design and engineering approaches that borrow ideas from the nature is 'biomimcry' a word coined by Otto Schmitt in 1960's. This definition includes the study of formation, structure, or function of biologically produced substances and materials (eg. enzymes or silk) and biological mechanisms and

processes (as protein synthesis or photosynthesis) especially for the purpose of synthesizing similar products by artificial mechanisms that mimic natural ones". Since the 20^{th} century this concept has gained momentum as researchers turn to green and environment friendly alternatives.

With recent advancements in science and engineering biomimicry has also been expanded to the microscale functioning of living system. The microscopic arrangement of nanostructured scales on the wings Morpho butterflies, credited for its brilliant blue colour [13], inspired the creation of silica based flexible colour reflectors with valuable photonic properties [4]. Spiders weave silk from soluble protein to insoluble fibers [19] which now has a big influence in the field of smart wearables that can replace unsustainable synthetic fibres [2]. These two examples demonstrate the potential of how microscopic manipulations can change the macroscopic world. Such adaptations are classified into the sub-field of molecular biomimetics where nanotechnology interplays with molecular biology.

Biomaterials provide a gold standard in materials that are highly organized in the nano to macroscales. Using the genetic blueprint, myriad of functional and structural nano-architectures are synthesized in mild physiological conditions in an aqueous environment. These structures are mostly made of proteins with substantial quantities of other biomolecules like carbohydrates and lipids. Material science seeks to discover and harness unique properties of these biomolecules at nanoscale dimensions that could lead to novel engineering systems. But despite great strides in the advancement of technology, ordered assemblies and nano scale control in two dimensional and three dimensions like in nature remain elusive. An emerging field established by Nadrian Seeman, DNA nanotechnology offers promising developments in creating bottom-up assemblies that are reminiscent of biomolecular self assembly.

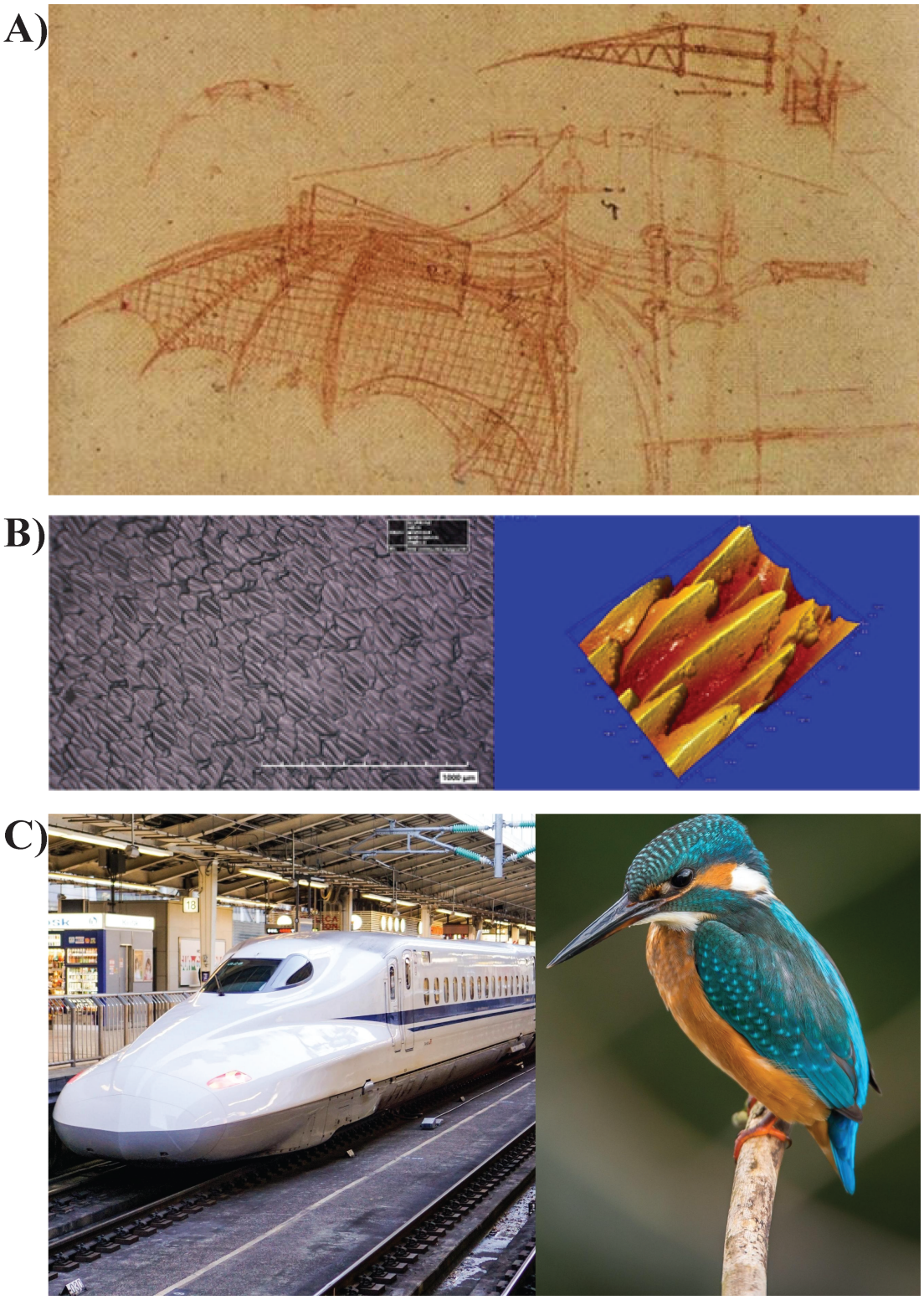

Figure 1.1: Nature is the greatest inspiration for creating efficient machines (A) Leonardo Da Vinci's plans for a flying machine [5]. (B) Micro-structure of shark skin [3]. (C) Japanese bullet train inspired by the beak of a kingfisher bird [12].

1.2 DNA Nanotechnology

The structure elucidation of double-stranded DNA in the year 1953 [32] created a paradigm shift in genetic research, but it was not until crystallographer Ned Seeman came along that the thought of using this material to build programmable lattice structures [22] was ruminated, thereby giving birth to the field of DNA nanotechnology. Forming tunable lattice structures to elucidate the structural details of encapsulated proteins/other biomolecules was the main motivation that drove him and his team to develop this field. Although the field has grown exponentially during the past 40 years, this is still an unmet challenge in the field.

The most common and structurally utilized version of this molecule for constructing higher ordered nanostructures is the B form of DNA (note a few exceptions using the other forms of DNA [16], which is composed of two anti-parallel single strands running from 5' to 3' end with a right-handed twist brought together by the predictable programmable Watson and Crick base pairing as shown in (**Figure 1.2 A and B**). However, the biomolecule could also form other structurally variant forms like the triplex DNA (**Figure 1.2 D**), G-quadruplex (**Figure 1.2** E) and kissing loop based structures (**Figure 1.2 F**). Although the available literature on constructing DNA nanostructures is largely biased towards using just the Watson and Crick base pairing and $(\pi - \pi)$ stacking interactions (**Figure 1.2 C**), off late a number of other nanostructures using other interactions (triplex/ G-quadruplex/ kissing loop interactions) are also being constructed.

The first idea to construct programmable lattice structures was to build them in a bottom-up way. Thus, the thought was to construct a building block that could self-assemble itself to build a higher ordered structure and the first motif thought to achieve this was the Holliday Junction (HJ) (**Figure 1.3 A**).

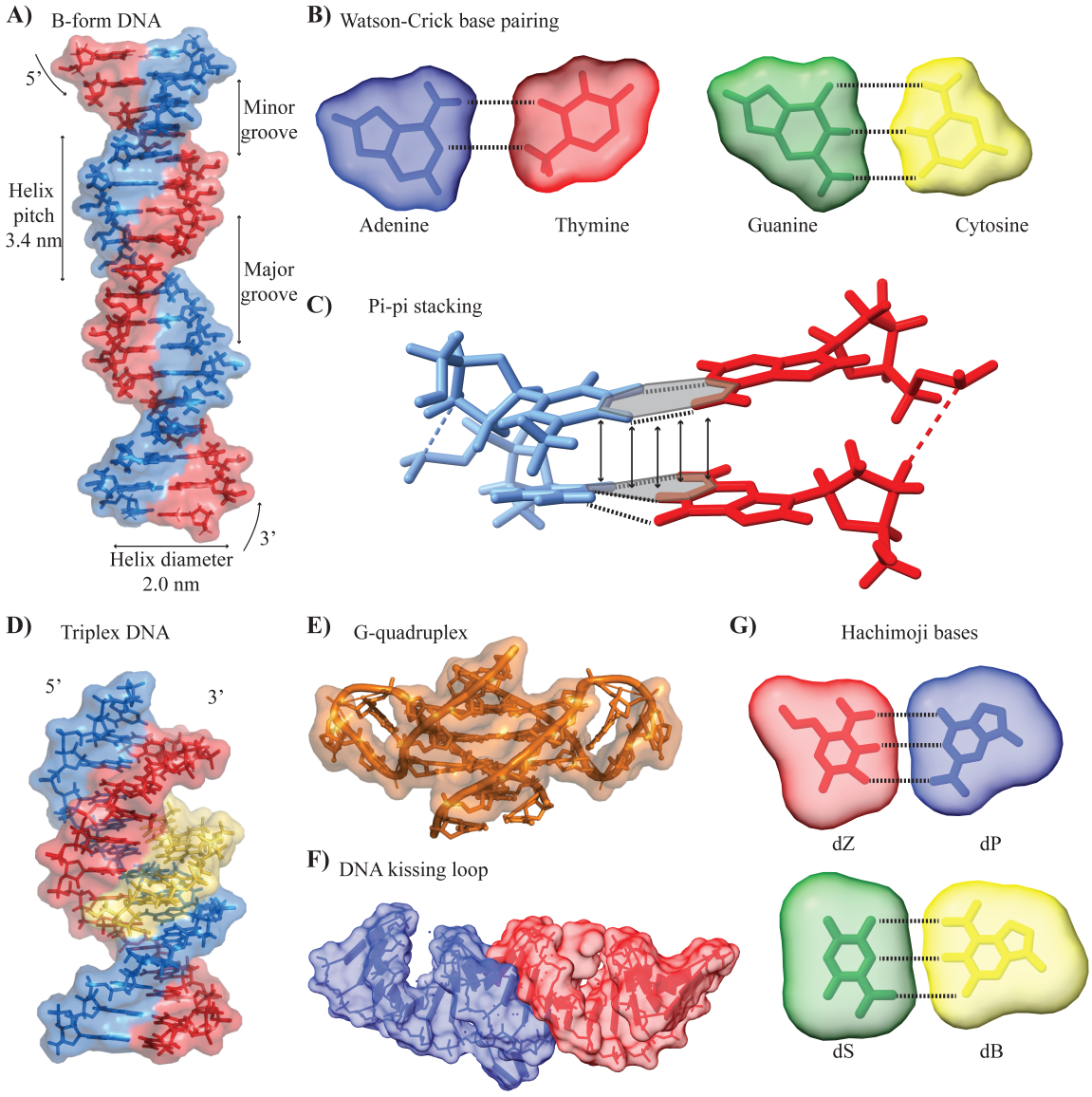

Figure 1.2: (A) B form of duplex DNA showing the helical diameter and width pitch of 2nm and 3.4nm, respectively, having alternating major and minor grooves having with a right-handed twist consisting of two antiparallel strands running from 5' to 3' end. (B) Watson and Crick base pairing between adenine (blue) and thymine (red) and guanine (green) and cytosine (yellow), the dotted black lines denote the respective number of H-Bonds in between them. (C) Zoomed in image showing pi-pi stacking spacing in between each base. The dotted line, blue and red represent the phosphate backbone, black represents the H bonding. (D) Triplex form of DNA based on Hoogstein base pairing. (E) Schematic representation of a G-quadruplex structure that forms when 4 guanines come together. (F) Kissing loop interaction formed when two duplex DNA structures interact with each other using single stranded loops. (G) Hachi-Moji interactions are an example of artificial interactions inspired from the Watson and Crick base pairing.

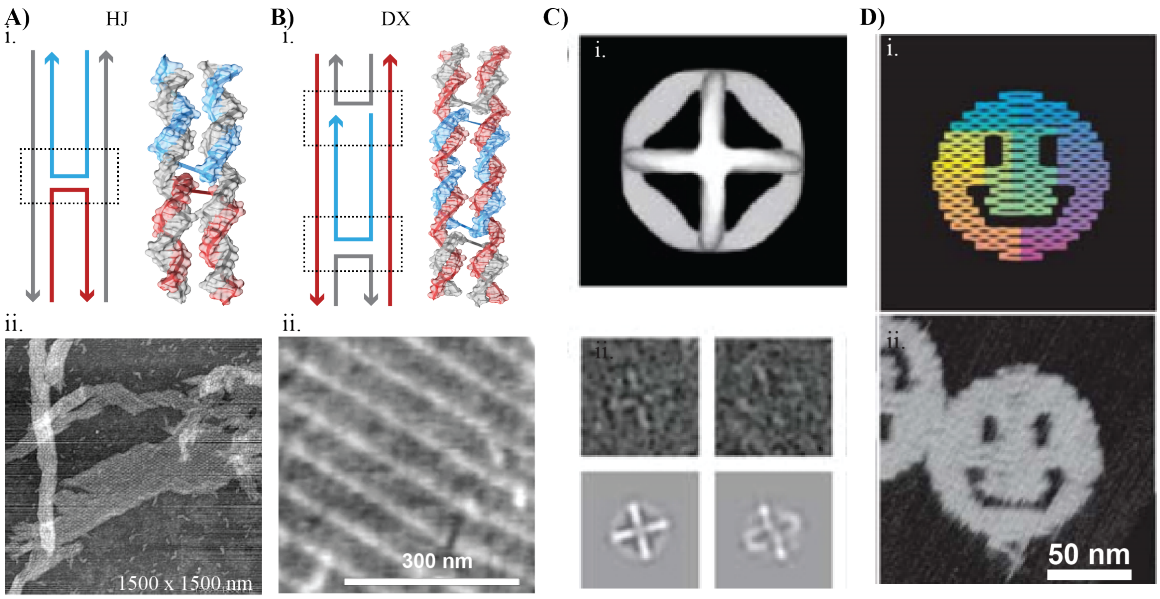

Figure 1.3: A) (i.) Schematic of Holliday Junction (HJ) and (ii) AFM image of 2D array formed from it. Reprinted (adapted) with permission from [18]. Copyright (1999) American Chemical Society. (B) (i) Schematic of double crossover (DX) tile and (ii) AFM image of 2D array formed from it. Reprinted (adapted) with permission from [33]. Copyright (1998) Springer Nature. (C) (i) Schematic and (ii) raw cryo-EM images of individual particles and the corresponding projections of DNA octahedron made of a single strand DNA. Reprinted (adapted) with permission from [24]. Copyright (2004) Springer Nature (D) (i) Schematic and (ii) AFM of a smiley face made by DNA origami technique. Reprinted (adapted) with permission from [20]. Copyright (2006) Springer Nature

Holliday junctions that occur in nature are traditionally mobile, however, the utilization of unique sequences at the junctions makes it possible to immobilize it. Using this construction, DNA nanostructure lattices both in 1 and 2 dimensions have been experimentally demonstrated as shown in (**Figure 1.3 A**) [18]. Although the experimental demonstrations using HJ based higher ordered assemblies were shown later in literature [18], a large amount of work prior to this was to understand the basic design rules on how to bring together different single strands of DNA. These studies were about the positioning of crossovers (how a strand would go into another and the position of transfer to another duplex is known as a crossover)[8].

Until 2004, the thought of constructing higher ordered nanostructures was mostly

limited to the bottom-up approach wherein programmed lattices/higher ordered structures could be formed by building block(s) that could self-assemble with itself or others. The demonstration by William Shih to fold a 1.7 kilobase single strand onto itself to form a DNA octahedron [24] changed the way the community thought of DNA self-assembly (**Figure 4A**). This demonstration led up (or was thought of in parallel) to the technology of DNA origami by Paul Rothemund [20], wherein a single-stranded long DNA strand (also popularly known as the scaffold strand) could be folded together with the help of hundreds of short oligonucleotides into complex 2D shapes (**Figure 1.4 B**) [6]. Following this demonstration, a great amount of interest was felt in the community to utilize this technology to build 3D objects as well. Several other techniques like DNA bricks and design parameters for introducing curvature into the the structure, gridiron and wireframe structures were added to the design handbook of DNA nanotechnology. This has enabled the use of DNA nanotechnology in building nanostructures for in a wide range of applications.

1.2.1 Biomimetic DNA Nanotechnology

With the advances in the design end of DNA nanotechnology, the field emerges as a promising choice to build machinery and robotics at the micro and nanoscales. In addition, the chemical flexibility and biochemical addressability of DNA nanostructures add value to this versatile platform to build designer machines that could be employed towards a variety of applications ranging from molecular sensing to drug delivery. Several dynamic systems made of DNA have already been demonstrated in the past few years.

DNA tweezers are one of the prime examples of a tile based dynamic DNA device [17] (**Figure 1.4 A**). The device actuates the activity of a dehydrogenase enzyme by controlling its distance from the cofactor. The open and close conformation of the

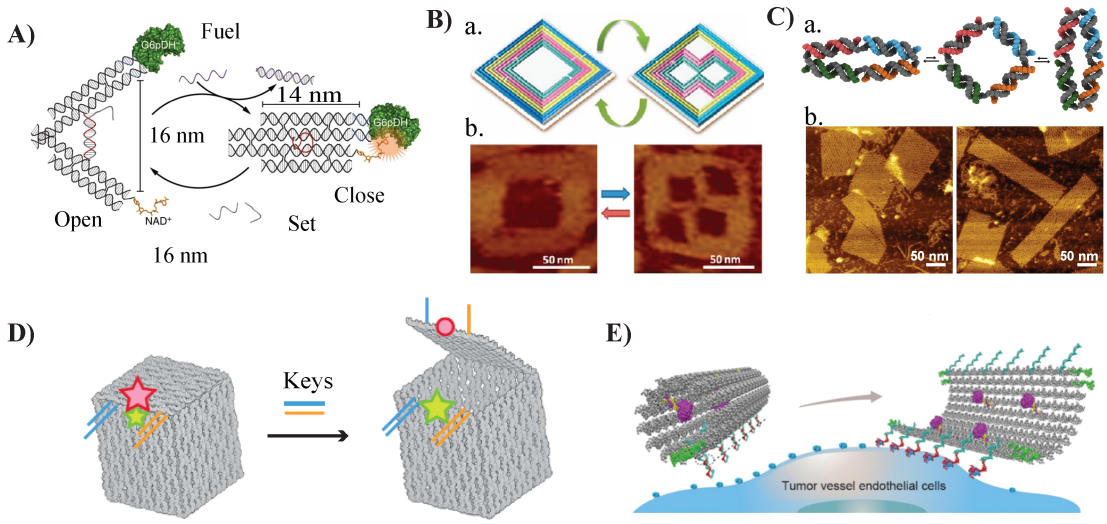

Figure 1.4: (A) Schematic of a tile-based DNA tweezer actuating enzyme activity. Reprinted (adapted) with permission from [17]. Copyright (2013) Springer Nature. (B) AFM image of reconfigurable quasifractal architectures in a DNA origami rectangle. Reprinted (adapted) with permission from [38]. Copyright (2012) American Chemical Society (C) (a) Schematic and (b) AFM image of reconfigurable DNA nanoarrays by information relay. Reprinted (adapted) with permission from [27]. Copyright (2017) AAAS (D) Schematic of strand displacement-based opening and closing of DNA box. Reprinted (adapted) with permission from [1]. Copyright (2009) Springer Nature. (E) Schematic of a cancer therapeutic DNA nanorobot. Reprinted (adapted) with permission from [15]. Copyright (2018) Springer Nature.

tweezer is controlled by specific oligonucleotides that can form a wedge separating the two arms of the tweezer.DNA walker is another example of a biomimetic tile-based dynamic DNA system that has been developed by Shin et al. [26]. Using a repeated strand displacement reaction, the DNA tile is able to move along. Such a system provides a platform for the movement of DNA structures in a controlled manner.

Reconfiguration of nanostructures post-assembly to create changes at the microscopic scale in response to environmental cues is a desirable quality for structures used for applications such as sensing and targeted drug delivery. This has been demonstrated in various capacities using DNA nanostructures. Zhang et al. have designed and synthesized DNA origami structures that can generate complex quasifractal patterns based on the addition of external oligonucleotides [38], as shown in Figure 1.4

B. The authors describe a fold-release-fold method where multiple strand release and hybridization steps enable a simple DNA structure to demonstrate complex patterns reversibly. The work shows that simultaneous strand displacement reactions can occur efficiently to produce complex changes in DNA structure. This study established the possibility of composite transformation in DNA nanoarchitectures. The method can be extrapolated into forming reconfigurable arrangements of other nanoparticles for nanophotonic applications.

Later, Song et al. showed that reconfiguration through long-range information relay is also possible in DNA nanostructures (**Figure 1.4 C**) [27]. They demonstrated long-range transformation of a DNA nanoarray by a trigger strand which when hybridized to one edge of the array went on to change the shape of the array. The effect is propagated along the larger array by the reconfiguration of base units, called the dynamic anti-junction unit. The unit shifts between two configurations through an unstable open configuration as depicted in (**Figure 1.4 C**). A change in the configuration of one anti-junction can activate a change in the configuration of a neighboring anti-junction, which creates a domino effect that is carried through the structure, thus changing transforming it. They also showed further that the binding location of the trigger strand also determined the type of transformation.

Gathering from the examples stated above, oligonucleotide based dynamic systems (**Figure 1.4 D**) [1],[37], [35] are the most commonly used ones in the field. Nevertheless, other external stimuli have also been used to demonstrate dynamics in DNA nanostructures. A photoresponsive DNA nanostructure was designed and built by Kuzyk and coworkers based on azobenzene mediated hybridization of DNA strands [14]. The DNA structure consisted of two 14 helix bundles that are connected to form an object with a tunable angle. The two azobenzene modified DNA strands, complementary to each other, were added to the two parts, which made the struc-

ture sensitive to light. In the presence of visible light, the azobenzene strands were hybridized and the structure stayed in the locked state. On exposure to UV light the azobenzene strands were unhybridized, shifting the structure to the relaxed state. The reconfiguration of the structure was monitored by the relative position of the plasmonic gold nanoparticles attached to the two bundles. This work validated the use of such structures in sensing applications.

One of the most promising and exciting applications of DNA nanotechnology is targeted drug delivery. The common practice in the field has been to create a drug-loaded DNA container that opens up only when the target location is reached. This is possible because DNA can be easily modified and decorated with target specific molecules like aptamers and proteins. An example of such a system is a DNA origami platform loaded with thrombin (**Figure 1.4 E**) [15].

1.2.2 DNA Structures for Lipid Bilayer Interaction

Membrane proteins are involved in diverse functions involving signal transduction, interaction with environment, energy conversion,substrate transport and inter-cellular communication. Due to their amphiphillic nature they possess a unique ability to be embedded into lipid bilayers of cell membranes while still being able to interact with the aqueous environment of the cytoplasm and the extracellular matrix. But due to this, these proteins are difficult to study in their native environment. Building models that are mimic these structures is an alternative way to unravel and understand the functioning of these protein structures. Also, these special characteristics can also be adopted to artificial nanostructures which can be used for sensing and therapeutic applications.

Several strategies have been put forward to funtionalize DNA structures so that it can interact with the cell membrane as shown in Figure 1.5 A [21]. Hydrophobic

tags like cholesterol and synthetic fatty acids can be used to target any cell membrane without any modifications on the cell itself [36]. But hydrophobic tagged DNA are not distributed homogeneously on a membrane, with cholesterol tagged DNA preferring to insert into lipid- ordered phase [28]. Another option that is used involves chemical cross-linking where in the DNA is linked to the proteins or glycans present on the cell membrane. Natively present amino acids like cysteines or lysines are modified by thiolated oligonucleotides through crosslinkers like 3-(2-pyridyldithio) propionate [10]. Alternatively, the DNA can be chemically attached to the glycocalyx by altering the metabolic pathway of the cell by introducing azide bearing unnatural sugars. This method uses click chemistry to irreversibly and orthogonally attach a phosphine or dibenzocyclooctyne modified oligonucleotide to the cell surface (Figure 1.5 C) [23].

DNA structures developed using these strategies have been reportedto mimic lipid bilayer interacting proteins. These structures were designed to interact with a cell membrane in varying degrees of association. DNA origami nanorods were used to programmably arrange cell clusters to induce controllable cell to cell communication [10]. The targeted cells were modified with single strand DNA (ssDNA) overhangs through crosslinking molecules. DNA nanotechnology has also been used to attain deeper understanding of the cell membrane itself. **Figure 1.5 B** shows a DNA probe that inserts into the membrane through fatty acid modification was able to monitor rapid events on cell membrane through fluorescence signalling [36].

Glycocalyx is a mesh like coating on eukaryotic cells made of polysaccahrides. They play an important role in cell adhesion and cell to cell communication. A DNA armor that coats the glycocalyx of a cell was recently reported. The work utilized azide incorporated glycocalyx to create a mesh of DNA nanorods on the cell surface. This armor was shown to increase the cells resistance to external pressure [31]. Attachment of DNA nanostructures to the glycocalyx was even reported to show

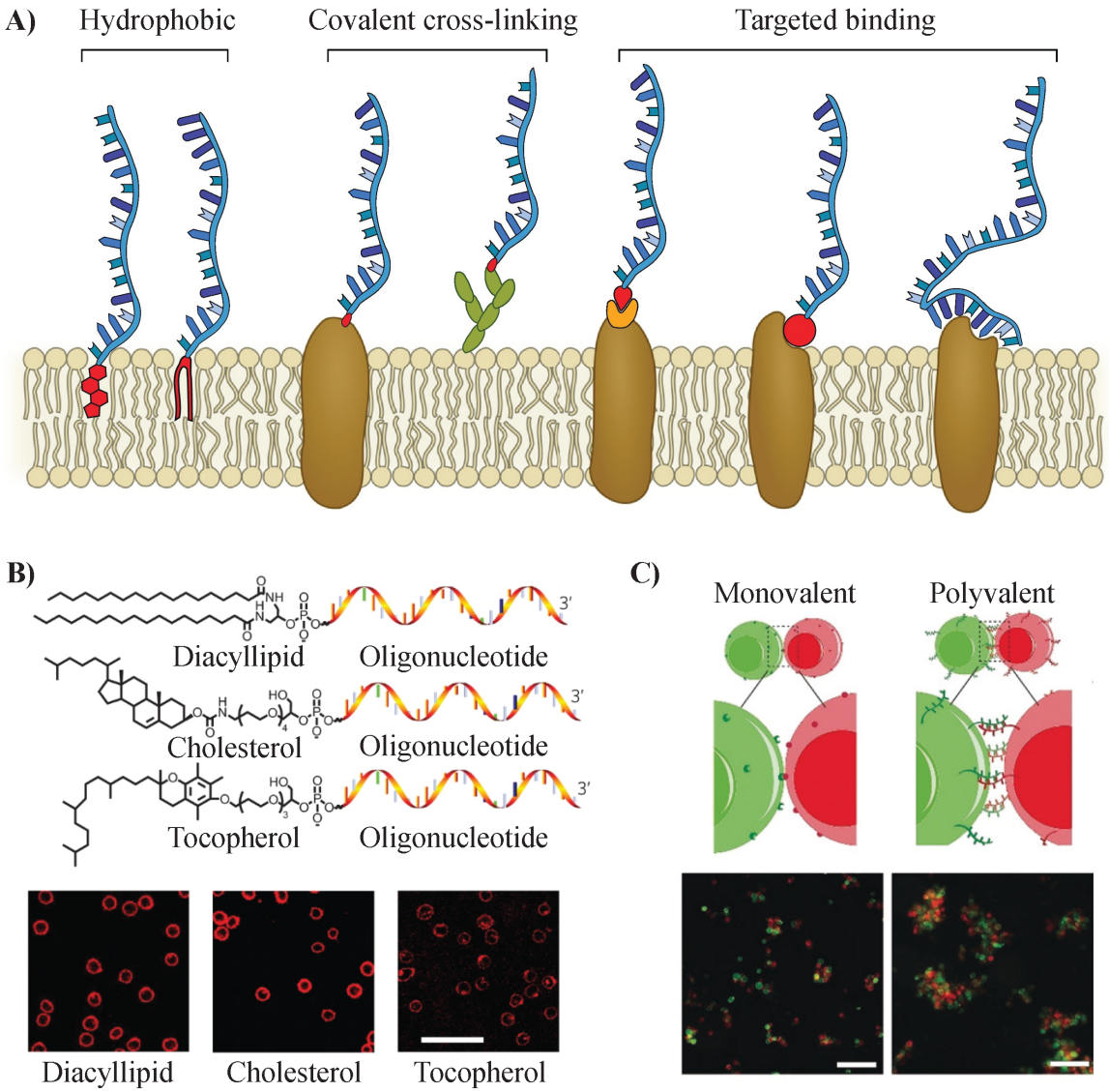

Figure 1.5: (A) Different kind of interactions that can be used to modify a lipid bilayer with DNA. Reprinted (adapted) with permission from [21] Copyright (2021) Elsevier. (B) Using different kind of hydrophobic moieties for modifying live cell membrane. Scale bar- $50\mu m$ Reprinted (adapted) with permission from [36] Copyright (2017) Springer Nature. (C) Cells brought together modification of the glycocalyx through click chemistry. Scale bar - $100\mu m$. Reprinted (adapted) with permission from [23] Copyright (2018) John Wiley and sons.

increased intake of such structures [30].

The most prominent lipid interacting DNA structures are DNA nanopores. Such pores made of DNA can span the width of the bilayer, forming a pore in it. One of the first DNA nanopores reported was a 2 nm wide pore made of vertically routed scaffold of DNA that was modified with 26 cholesterol molecules. Using electrophysical measurements it was proved that the structure can insert into a lipid bilayer a transport ions through the channel. Several iterations of DNA nanopores of varying pore diameters, reversible gating, and cargo specificity has been reported since. Nanopores that can be reconfigured to different sizes even after insertion into a lipid bilayer has been designed and executed recently as well [34].

1.2.3 Immune Modulation Through Membrane Interacting DNA Nanostructures

To maintain a well organized defense system against pathogens and even self cells that becomes cancerous, the body's immune system has evolved complex mechanisms that requires communication between the different entities of the system. The guards and the effectors need to be able to pass on information about the intruders in order to mount a attack on them and this is carried out by chemical messengers like chemokines and cytokines that are detected by membrane bound receptors [9]. The binding of the messengers or ligands sets forth a signal transduction pathway that allows the cells to act as necessitated. As a result, the cell membrane offers a rich repertoire of processes for the external manipulation of immune system to augment its functionality. Due to the ease of programmability and site specific functionalization, DNA nanostructres can be designed to study these complex interactions as well as be immunomodulators [29].

In one study precisely placed T Cell receptor (TCR) ligands on DNA origami was employed to study the importance of clustering of T cell receptors in the activation of

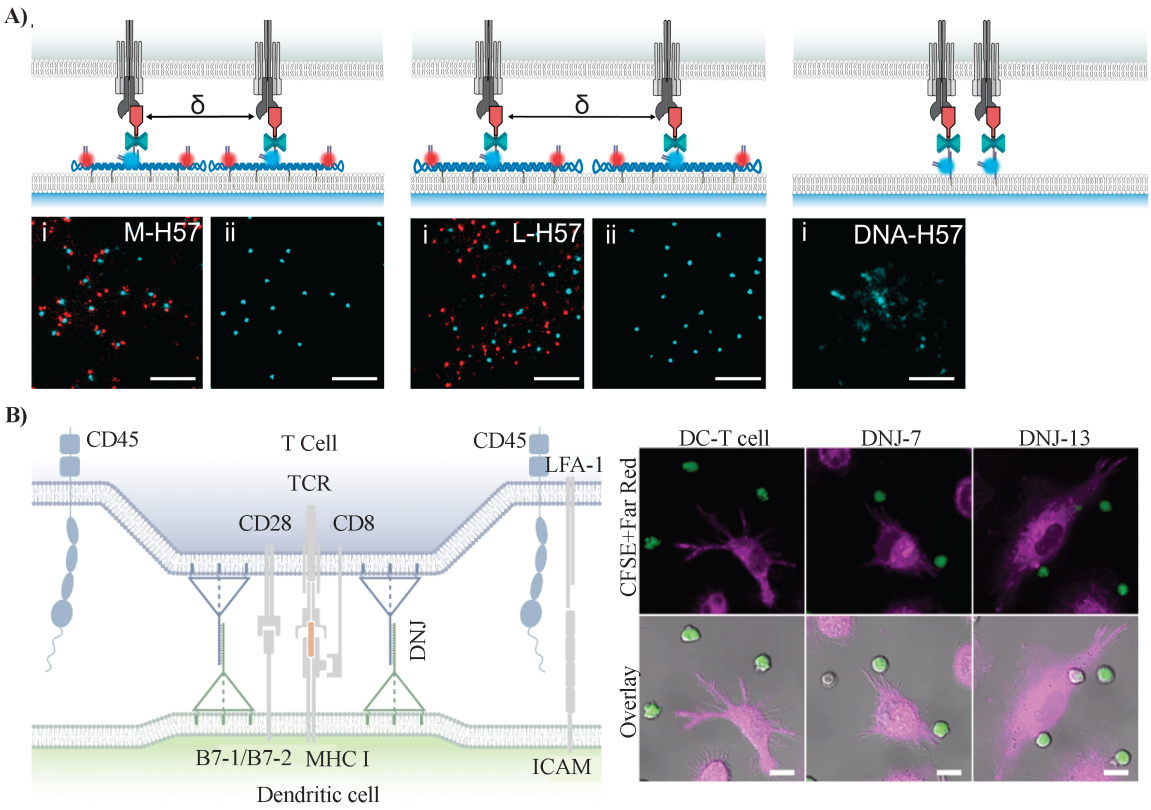

Figure 1.6: (A) DNA nanostructure providing a platform for the organization of ligands (top) and cell clusters formed through interaction of the ligands with T cells (bottom). Scale bar- 200nm. (B) Schematic of membrane anchored DNA tetrahedrons (DNJ) bringing together T cells and Dendritic cells(left). Confocal fluorescence microscopy images of T cells being anchored on Dendritic cell surfaces through DNJ formation (right). Scale bar - 10μm. Reprinted (adapted) with permission from [7] Copyright (2023) Springer Nature.

the T cell [11]. This DNA origami biointerface enabled the study of spatial reorganization of the T cell receptors in the process of activation, as shown in **Figure 1.6 A**. The intermembrane distance between the antigen presenting cell and effector T cells is critical in the activation of T cell presumably due to variability of the mechanical force in the reorganization of the cell receptors. Using different sized DNA tetrahedrons that interact with ssDNA overhangs from the cell membranes, researchers were able to observe this phenomenon (**Figure 1.6 B**) [7].

1.3 Outstanding Challenges

Molecular biomimetics have come a long way since the time the term was coined. DNA nanotechnology offers a versatile toolbox that can be programmed precisely to function as needed. This enabled scientists to create bio-mimetic devices that can augment life or study the intricate mechanisms and pathways in nano-scale. DNA nanostructures that are capable of modifying and modulating lipid bilayer has been build and characterized. In nature the membrane spanning pores are reversibly gated and are specific to the substrate passing through them. They also react to certain stimuli to open or to close. As mentioned previously, several iterations of the DNA nanopore has been reported but a reversibly gated pore that can be opened or closed to an external stimuli is yet to be designed. Creating a system mimicking this property of a protein pore will enable to study how a cell responds to the environment around it. It also opens up the possibility of engineering devices that can release drugs in response to specific stimuli like oligonucleotides or light. In another direction, devices that can insert into the lipid bilayer has another important property. They have the ability to interact with the inner compartment of the membrane and relay the information to the outside. This can circumvent the need of breaking open a membrane bound system and allows its study in its native state. To accomplish this, the device inserted into the membrane or a part of it will have to reconfigure to transmit the information, which is yet to be accomplished.

Membrane modification is also widely used in immune modulation. But most of them deals with T cells of the immune system. But artificial activation of T cells are tainted with myriad problems. Due to excessive reaction, T cells are known to cause unwanted reaction even leading death. NK cells, on the other hand, are effector cells of the innate system, and are known to have a subtler activation reaction. NK cells

are harnessed to target cancer cells that evade immune surveillance using different mechanisms. But the systems employed currently are time consuming to manufacture and cannot be easily modified.

1.4 Dissertation Overview

In this dissertation, I present three projects I have undertaken to address the challenges discussed in section 1.2. We have used DNA nanotechnology as our platform to build systems that bridges the gaps in current technology. In chapter 2, I discuss a large reversibly gated DNA nanopore that are mimetic of protein pores that open and close in response to external stimuli. The nanopore is a 416 nm^2 wide channel that is gated by a nanomechanical lid that can be opened or closed in response to specific DNA strand via toe hold mediated strand displacement. The pore is able to transport a variety of cargo like small dyes to larger proteins through a membrane in a controlled manner. The ability of the nanopore to insert into a membrane without its destruction is then harnessed to build a sensor that can detect oligonucleotides in membrane bound vesicle. Chapter 3 describes how this DNA based sensor was optimized to create an efficient device that can detect cancer markers like miRNA-21. This prototype sensor can be easily redesigned to detect a variety of oligonucleotide based disease markers.

In chapter 4, we take a slight deviation and move on to a different type of DNA nanodevice. NK cells form an important role in immune surveillance of tumor in the body [25]. This ability of the NK cells can be augmented with help of entities that can bring the immune cells in close proximity to the cancer cells. Using DNA nanotechnology, we have designed a DNA tetrabody that can insert into the cell membrane of NK cells and recruit it to tumor microenvironment. We demonstrate that the device accelerates NK cell mediated detection and elimination of cancer cells

in vitro. We envision that the addition of the DNA tetrabody augments the NK cell immune surveillance in order to detect and eliminate tumor inside the body.

REFERENCES

[1] Andersen, E. S., M. Dong, M. M. Nielsen, K. Jahn, R. Subramani, W. Mamdouh, M. M. Golas, B. Sander, H. Stark, C. L. P. Oliveira, J. S. Pedersen, V. Birkedal, F. Besenbacher, K. V. Gothelf and J. Kjems, "Self-assembly of a nanoscale DNA box with a controllable lid", Nature **459**, 7243, 73–76, URL http://www.nature.com/articles/nature07971 (2009).

[2] Blamires, S. J., P. T. Spicer and P. J. Flanagan, "Spider Silk Biomimetics Programs to Inform the Development of New Wearable Technologies", (2020).

[3] Chen, D., Y. Liu, H. Chen and D. Zhang, "Bio[U+2010]inspired drag reduction surface from sharkskin", Biosurface and Biotribology **4**, 2, 39–45, URL https://onlinelibrary.wiley.com/doi/10.1049/bsbt.2018.0006 (2018).

[4] Chung, K., S. Yu, C. J. Heo, J. W. Shim, S. M. Yang, M. G. Han, H. S. Lee, Y. Jin, S. Y. Lee, N. Park and J. H. Shin, "Flexible, angle-independent, structural color reflectors inspired by morpho butterfly wings", Advanced Materials **24**, 18 (2012).

[5] Da vinci, "Da vinci's flying machine", (????).

[6] Dey, S., C. Fan, K. V. Gothelf, J. Li, C. Lin, L. Liu, N. Liu, M. A. D. Nijenhuis, B. Saccà, F. C. Simmel, H. Yan and P. Zhan, "DNA origami", Nature Reviews Methods Primers **1**, 1, 13, URL https://doi.org/10.1038/s43586-020-00009-8 (2021).

[7] Du, Y., Y. Lyu, J. Lin, C. Ma, Q. Zhang, Y. Zhang, L. Qiu and W. Tan, "Membrane-anchored DNA nanojunctions enable closer antigen-presenting cell–T-cell contact in elevated T-cell receptor triggering", Nature Nanotechnology URL https://doi.org/10.1038/s41565-023-01333-2 (2023).

[8] Fu, T. J. and N. C. Seeman, "DNA double-crossover molecules", Biochemistry **32**, 13, 3211–3220, URL https://doi.org/10.1021/bi00064a003 (1993).

[9] Gajewski, T. F., H. Schreiber and Y. X. Fu, "Innate and adaptive immune cells in the tumor microenvironment", (2013).

[10] Ge, Z., J. Liu, L. Guo, G. Yao, Q. Li, L. Wang, J. Li and C. Fan, "Programming Cell-Cell Communications with Engineered Cell Origami Clusters", Journal of the American Chemical Society **142**, 19 (2020).

[11] Hellmeier, J., R. Platzer, A. S. Eklund, T. Schlichthaerle, A. Karner, V. Motsch, M. C. Schneider, E. Kurz, V. Bamieh, M. Brameshuber, J. Preiner, R. Jungmann, H. Stockinger, G. J. Schütz, J. B. Huppa and E. Sevcsik, "DNA origami demonstrate the unique stimulatory power of single pMHCs as T cell antigens", Proceedings of the National Academy of Sciences **118**, 4, URL https://pnas.org/doi/full/10.1073/pnas.2016857118 (2021).

[12] Japanese, "Japanese bullet train", (????).

[13] Kinoshita, S., S. Yoshioka and J. Miyazaki, "Physics of structural colors", Reports on Progress in Physics **71**, 7 (2008).

[14] Kuzyk, A., R. Schreiber, H. Zhang, A. O. Govorov, T. Liedl and N. Liu, "Reconfigurable 3D plasmonic metamolecules", Nature Materials **13**, 9 (2014).

[15] Li, S., Q. Jiang, S. Liu, Y. Zhang, Y. Tian, C. Song, J. Wang, Y. Zou, G. J. Anderson, J.-Y. Han, Y. Chang, Y. Liu, C. Zhang, L. Chen, G. Zhou, G. Nie, H. Yan, B. Ding and Y. Zhao, "A DNA nanorobot functions as a cancer therapeutic in response to a molecular trigger in vivo", Nature Biotechnology **36**, 3, 258–264, URL http://www.nature.com/articles/nbt.4071 (2018).

[16] Lin, C., Y. Ke, Z. Li, J. H. Wang, Y. Liu and H. Yan, "Mirror image DNA nanostructures for chiral supramolecular assemblies", Nano Letters **9**, 1 (2009).

[17] Liu, M., J. Fu, C. Hejesen, Y. Yang, N. W. Woodbury, K. Gothelf, Y. Liu and H. Yan, "A DNA tweezer-actuated enzyme nanoreactor", Nature Communications **4**, 1, 2127, URL https://www.nature.com/articles/ncomms3127 (2013).

[18] Mao, C., W. Sun and N. C. Seeman, "Designed Two-Dimensional DNA Holliday Junction Arrays Visualized by Atomic Force Microscopy", Journal of the American Chemical Society **121**, 23, 5437–5443, URL https://pubs.acs.org/doi/10.1021/ja9900398 (1999).

[19] Römer, L. and T. Scheibel, "The elaborate structure of spider silk", Prion **2**, 4 (2008).

[20] Rothemund, P. W. K., "Folding DNA to create nanoscale shapes and patterns", Nature **440**, 7082, 297–302, URL http://www.nature.com/articles/nature04586 (2006).

[21] Schoenit, A., E. A. Cavalcanti-Adam and K. Göpfrich, "Functionalization of Cellular Membranes with DNA Nanotechnology", Trends in Biotechnology **39**, 11, 1208–1220, URL https://linkinghub.elsevier.com/retrieve/pii/S0167779921000342 (2021).

[22] Seeman, N. C., "Nucleic acid junctions and lattices", Journal of Theoretical Biology **99**, 2 (1982).

[23] Shi, P., N. Zhao, J. Lai, J. Coyne, E. R. Gaddes and Y. Wang, "Polyvalent Display of Biomolecules on Live Cells", Angewandte Chemie **130**, 23, 6916–6920, URL https://onlinelibrary.wiley.com/doi/10.1002/ange.201712596 (2018).

[24] Shih, W. M., J. D. Quispe and G. F. Joyce, "A 1.7-kilobase single-stranded DNA that folds into a nanoscale octahedron", Nature **427**, 6975, 618–621, URL https://doi.org/10.1038/nature02307 (2004).

[25] Shimasaki, N., A. Jain and D. Campana, "NK cells for cancer immunotherapy", (2020).

[26] Shin, J. S. and N. A. Pierce, "A synthetic DNA walker for molecular transport", Journal of the American Chemical Society **126**, 35 (2004).

[27] Song, J., Z. Li, P. Wang, T. Meyer, C. Mao and Y. Ke, "Reconfiguration of DNA molecular arrays driven by information relay", Science **357**, 6349, URL https://www.science.org/doi/10.1126/science.aan3377 (2017).

[28] Sun, L., Y. Su, J. G. Wang, F. Xia, Y. Xu and D. Li, "DNA nanotweezers for stabilizing and dynamically lighting up a lipid raft on living cell membranes and the activation of T cells", Chemical Science **11**, 6 (2020).

[29] Tseng, C. Y., W. X. Wang, T. R. Douglas and L. Y. Chou, "Engineering DNA Nanostructures to Manipulate Immune Receptor Signaling and Immune Cell Fates", (2022).

[30] Wang, W., B. Chopra, V. Walawalkar, Z. Liang, R. Adams, M. Deserno, X. Ren and R. E. Taylor, "Membrane and glycocalyx tethering of DNA nanostructures for enhanced uptake", bioRxiv URL https://www.biorxiv.org/content/early/2023/03/10/2023.03.09.529286 (2023).

[31] Wang, W., P. Hayes, X. Ren and R. Taylor, "Synthetic cell armor made of DNA origami", URL https://doi.org/10.1101/2023.02.20.529284 (2023).

[32] Watson, J. D. and F. H. Crick, "Molecular structure of nucleic acids: A structure for deoxyribose nucleic acid", Nature **171**, 4356 (1953).

[33] Winfree, E., F. Liu, L. A. Wenzler and N. C. Seeman, "Design and self-assembly of two-dimensional DNA crystals", Nature **394**, 6693, 539–544, URL http://www.nature.com/articles/28998 (1998).

[34] Xing, Y., A. Dorey and S. Howorka, "Multi-Stimuli Responsive and Mechano-Actuated Biomimetic Membrane Nanopores Self-Assembled from DNA", Advanced Materials **n/a**, n/a, 2300589, URL https://doi.org/10.1002/adma.202300589 (2023).

[35] Yin, P., H. M. Choi, C. R. Calvert and N. A. Pierce, "Programming biomolecular self-assembly pathways", Nature **451**, 7176 (2008).

[36] You, M., Y. Lyu, D. Han, L. Qiu, Q. Liu, T. Chen, C. Sam Wu, L. Peng, L. Zhang, G. Bao and W. Tan, "DNA probes for monitoring dynamic and transient molecular encounters on live cell membranes", Nature Nanotechnology **12**, 5, 453–459, URL http://www.nature.com/articles/nnano.2017.23 (2017).

[37] Yurke, B., A. J. Turberfield, A. P. Mills, F. C. Simmel and J. L. Neumann, "A DNA-fuelled molecular machine made of DNA", Nature **406**, 6796 (2000).

[38] Zhang, F., J. Nangreave, Y. Liu and H. Yan, "Reconfigurable DNA Origami to Generate Quasifractal Patterns", Nano Letters **12**, 6, 3290–3295, URL https://pubs.acs.org/doi/10.1021/nl301399z (2012).

Chapter 2

A REVERSIBLY GATED PROTEIN-TRANSPORTING MEMBRANE CHANNEL MADE OF DNA

This chapter was published in S.Dey, A. Dorey, **L. Abraham**, Y. Xing, I. Zhang,F. Zhang, S. Howorka* & H. Yan*, **Reversibly Gated Protein Conductive Large Diameter DNA Nanopore**, *Nature communications* 13 (**2022**)

2.1 Abstract

Controlled transport of biomolecules across lipid bilayer membranes is of profound significance in biological processes. In cells, cargo exchange is mediated by dedicated channels that respond to triggers, undergo a nanomechanical change to reversibly open, and thus regulate cargo flux. Replicating these processes with simple yet programmable chemical means is of fundamental scientific interest. Artificial systems that go beyond nature's remit in transport control and cargo are also of considerable interest for biotechnological applications but challenging to build. Here, we describe a synthetic channel that allows precisely timed, stimulus-controlled transport of folded and functional proteins across bilayer membranes. The channel is made via DNA nanotechnology design principles and features a 416 nm^2 opening cross-section and a nanomechanical lid which can be controllably closed and re-opened via a lock-and-key mechanism. We envision that the functional DNA device may be used in highly sensitive biosensing, drug delivery of proteins, and the creation of artificial cell networks.

2.2 Introduction

Controlled molecular transport across membranes is biologically vital as illustrated by myriads of ligand-gated channels with sophisticated architecture and defined func-

tion. The channels perform a wide range of roles such as in signal transduction and amplification and import of nutrients. While varied, most channels regulate the transport of ions and small molecules by binding a ligand, which causes a nanomechanical change to alter the channels' transport properties, until the ligand dissociates. Harnessing this valve-like function is of considerable technological interest in signal-amplified point-of-care diagnostics, delivery of therapeutics [66, 61], cell biological research [4], [34], and biomimetic cell signaling [41, 67]. Yet, using natural channels beyond their biogenic remit can be difficult due to not only their often-fragile protein architectures and narrow size-range for cargo, but also a limited choice of triggers, and reduced control when a channel switches back to its original state.

Building programmable synthetic channels for defined transport of large bio relevant cargo would hence be a step-change. So far, de novo design has been achieved with barrel-like and constitutively open protein pores of a few nm width [37, 62]. The membrane pores are key in portable DNA sequencing [10, 25, 5, 56]) and label-free sensing [60, 61, 8, 42, 46, 16] by registering molecules that pass the pore lumen [39, 22, 49]. Leveraging the success of nanopores for constructing proteinaceous ligand-gated channels is, however, hindered by the current challenges in integrating molecular recognition, nanomechanical change, and transport function.

Compared to other construction routes, de novo design with DNA nanotechnology [48**?** , 11, 26] offers unprecedented structural precision and tunability [13], dynamic-nanomechanical control [68, 32, 28], [58, 1], a wide range of chemical modifications [63, 45, 17, 44] and stability in harsh conditions [47, 24, 15, 3, 35, 30, 55, 12, 27, 19, 18, 6, 31, 29, 23, 7]. Rational design with DNA has previously led to various types of membrane-spanning DNA nanopores. Mimicking the reversible gating behavior similar to that of natural ion channels has been a long-standing desire of the field due to the potential to expand the application of DNA nanopores to transport bioactive

cargo into cells, or to construct cell–cell communication for artificial gap junctions and to enable integration of artificial tissues with living cells for tissue engineering. However, on-demand reversible gating has remained elusive, as previously demonstrated DNA nanopores are one-way and partial—once the lid is opened it cannot be closed or vice-versa. Moreover, systematically increasing the internal pore diameter has been a constant driver in the field. Wider pore lumens would advance the application of DNA nanopores in the field of protein sensing, to bridge the gap between narrow-biological pores that cannot accommodate fully folded proteins and solid-state nanopores that lack the tunability and precision of biological pores. DNA nanopores have previously demonstrated large molecule transport, but not in the context of a reversibly gated pore. This is due to the inherent design challenges associated with parallel lattice alignment64 in all previous designs that limits available scaffold to simultaneously accommodate a wide pore, a controllable lid, and a plate wide enough to place a large number of cholesterol moieties to balance the energetics of a wide pore insertion (more detailed discussion in the results section and **Supplementary Figure 1a**).

Here, we use a "horizontal routing" based DNA origami design strategy for building a reversibly key-and-lock gated square-channel with $20.4\,\mathrm{nm} \times 20.4\,\mathrm{nm}$ cross-sectional opening to allow precisely timed transport of folded proteins across membranes (Figure 2.1 A-C), which is all beyond nature's functional remit. The creation of our synthetic channel explores the wider scope of DNA nanotechnology to integrate binding of artificial ligands, triggered nanomechanical changes for opening and closing, and transport of nanoscale large cargo across membranes.

2.3 Results

2.3.1 Design of a Large and Gated DNA Channel

Before designing our large and gated channel (LGC) (**Figure 2.1 A-C**) we examined whether previous nanoarchitecture principles could be applied. In the previous DNA nanopores, duplex helices are aligned parallel in lattice fashion, as dictated by the widely used caDNAno design software. In those cases, the duplexes were routed "vertically", i.e. at 90 degrees relative to the membrane plane (**Supplementary Figure 1a**). This arrangement places the majority of DNA into an extramembrane cap region with multi-duplex layer-thick channel walls while restricting the amount of DNA available for forming a wide membrane-embedded pore (**Supplementary Figure 1a**). The small lateral footprint of the pore also limits the number of attachment points for lipid anchors required for efficient pore insertion into bilayer membranes. To overcome these restrictions, we opted to route the component helices 'horizontally' to the membrane by using the free-form software Tiamat (**Supplementary Figure 1b, c**).

Using the horizontal routing, we rationally designed the channel featuring a square-channel lumen with 20.4 nm × 20.4 nm opening cross-section into a single-duplex layer DNA origami plate of 70 nm × 70 nm external dimensions (**Figure 2.1 A-C**). The four-duplex deep channel spans the bilayer membrane while the large base plate sits on top of the bilayer (**Figure 2A**). By drastically expanding the footprint of the extramembrane cap, total 160 hydrophobic cholesterol anchors can be accommodated for efficient membrane insertion, out of which, 64 cholesterol anchors were used in the current study (**Figure 2 A and Supplementary Figure 2**). As a further advantage of the design, the channel with 416 nm^2 opening cross-section can be reversibly closed and opened with a square lid composed of horizontally routed DNA duplexes to yield

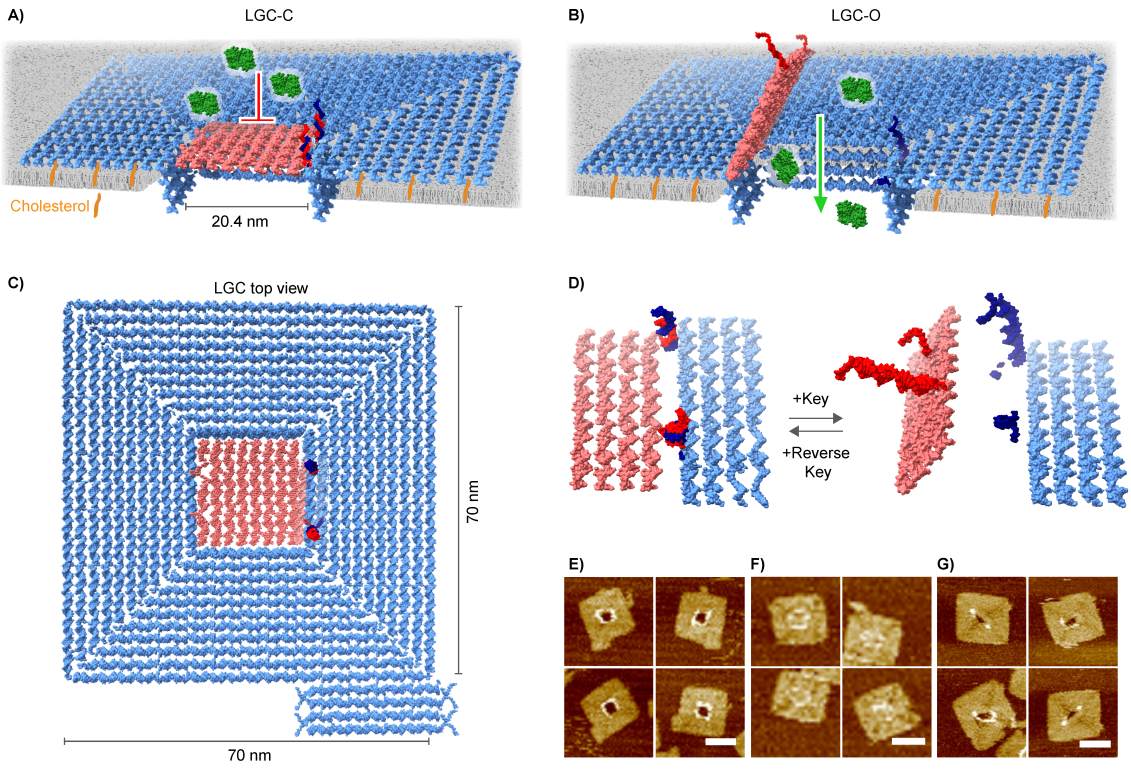

Figure 2.1: (A-C) Structural model of the large and gated channel (LGC) containing a channel lumen with 20.4 nm x 20.4 nm opening cross-section into a 70 nm x 70 nm single-duplex layer square plate (blue). A total of 64 hydrophobic cholesterol anchors (orange), placed around the pore on the bottom surface of the plate helps the nanopore to insert through the bilayer. A lid (pink) can be reversibly closed (A) and opened (B), by a key and reverse key mechanism to control the transmembrane flux of cargoes. (C) Top view of LGC. (D) Opening and closing mechanism with key and reverse key. Two locks formed by the hybridization of two sets of complementary strands, one set (red) placed on the lid (pink) and the other set (dark blue) on the plate (blue) initially keep the lid closed. The addition of key displaces the locks and thereby opens the lid. The addition of the reverse key displaces the key as a key-reverse key complex, leading to reclosing of the lock back to the initial state. e–g AFM images of cholesterol-free LGC without lid (E), with closed lid (F), and with opened lid (G). Scale bars, 50 nm.

the closed channel LGC-C (**Figure 2.1 A**) and the open version LGC-O (**Figure 2.1 B**). To achieve this dynamic change, the lid is attached at one side to the channel plate by flexible hinges (**Supplementary Figure 3**). The other lid side carries two single-stranded half locks which can hybridize with the complementary half locks at the base plate to form complete duplex locks (**Figure 2.1 D**). To open the lock and lid of the closed channel (LGC-C), a pair of single-stranded DNA keys dissociate the locks to form the open channel (LGC-O) (**Figure 1d and Supplementary Figure 4**). The opened lid can be switched back to close by a single-stranded reverse key pair (**Figure 2.1 D**). This externally controlled mechanism is expected to reversibly switch the lid-gated channel between an open and closed state to regulate the flow of large molecular cargo.

We first assembled non-lid version LGC-N and the nanostructures LGC-C and LGC-O carrying the lid in two states, by annealing the scaffold DNA with staple oligonucleotides (Supplementary Data 1). The structures did not yet contain the cholesterol anchors. OxDNA simulations66 showed the desirable formation of LGC-N, LGC-C, and LGC-O in solution (**Supplementary Figure 6 and Supplementary Video 1**) and gel electrophoresis confirmed that single assembly products had formed (**Supplementary Figure 5**). Atomic force microscopy (AFM) (**Figure 2.1 E-G and Supplementary Figure 6**) and transmission electron microscopy (TEM) (**Supplementary Figure 7**) established the expected dimensions. For example, the AFM-derived external average side-lengths of LGC-N was 78.0 ± 2.9 nm for the square plate and 22.7 ± 5.1 nm ($n = 65$) (**Figure 2.1 E and Supplementary Figure 6**) for the square opening, close to the expected values of 70 and 20.4 nm, respectively. The elevations at the nanostructure center stem from the four-duplex-high channel walls extending from LGC bound top-down to the mica substrate. By comparison, the closed-lid LGC-C featured no central opening, and the side-lengths were 77.4 ± 2.6 nm

for the plate and 22.7 ± 1.9 nm for the channel wall (n = 11) (**Figure 2.1 F and Supplementary Figure 6**). Similarly, open-lid LGC-O appeared partly closed as the lid can obstruct the channel opening and the dimensions were 78.4 ± 3.5 nm and 21.8 ± 2.5 nm (n = 13) (**Figure 2.1 G and Supplementary Figure 6**). The slightly larger-than-nominal dimensions of all LGC variants are likely due to the flattening of the negatively charged DNA plate on mica surface in presence of Mg^{2+}, compression by the AFM tip, or both factors ([36]). The channels were lipid-tagged by incubating with cholesterol-modified DNA oligonucleotides that bound to designed sites at the bottom side of the large membrane cap (**Figure 2.1 A and Supplementary Figure 2**).

2.3.2 Nanopore Interaction and Insertion Into Lipid Bilayers

Following successful formation, we tested whether the cholesterol-modified channel can bind to and insert into lipid bilayers. To probe for membrane binding, channel variant LGC-N was added to small unilamellar vesicles (SUVs) and analyzed by agarose gel electrophoresis (AGE). The AGE tests were performed under conditions with and without Mg^{2+}, and we found that an Mg^{2+} free buffer condition is essential to prevent non-specific adsorption to chelating lipid head-groups while still ensuring the stability of the LGC variants (**Supplementary Note 1 and Supplementary Figure 8**). The stability of LGC in Mg^{2+} free buffer was ascertained by AFM imaging (**Supplementary Figure 9**). Increasing SUV concentrations led to concomitant gel electrophoretic upshift **Figure 2.2 A**), suggesting that pores can bind efficiently to lipid membranes of slowly migrating vesicles [30]. No gel-upshift was observed when LGC lacked cholesterol, underscoring its role for membrane binding. Cholesterol-mediated binding was also confirmed with direct visualization by TEM imaging (**Figure 2.2 B, blue arrows and Supplementary Figure 10**).

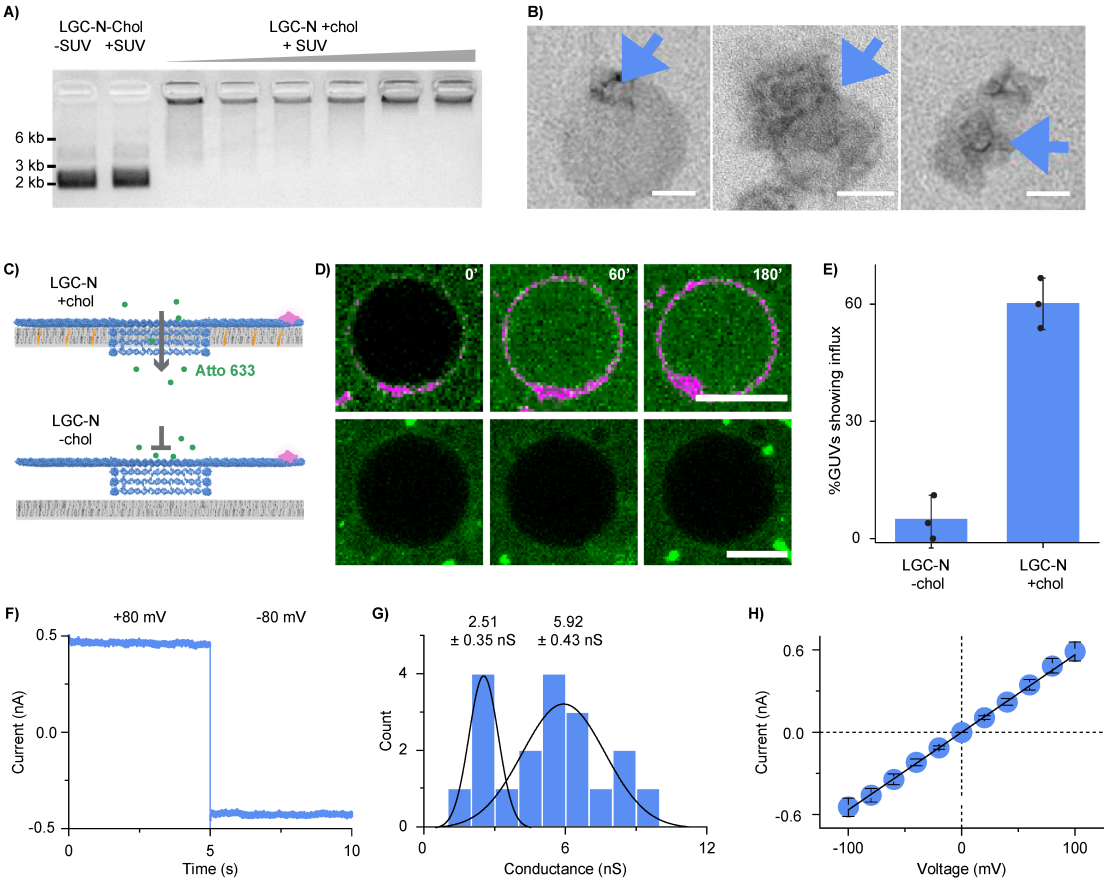

Figure 2.2: A) 1.5% agarose gel analysis of the DNA pore and its binding activity to lipid membrane vesicles. Lanes from left to right: no lid LGC without cholesterol modifications (LGC-N-Chol) without SUVs, incubated with SUVs (DOPC/DOPE = 7:3, 0.5 mM total lipid), no lid LGC with 64 cholesterol modifications (LGC-N+Chol) incubated with SUVs (total lipid concentration 0, 0.01, 0.025, 0.05, 0.25, and 0.5 mM, respectively). Data are representative of more than three repeats. (B) Representative TEM images of LGC-N+Chol pores bound to lipid vesicles. Blue arrowheads pinpoint the pores. Scale bars: 50 nm. The data are representative of n = 2 independent experiments. (C) Scheme of the GUV-dye-influx assay and (D) a time series of corresponding confocal GUV images with Cy3-labeled LGC (magenta) and Atto633 dye (green). Top: LGC-N+Chol readily interacts with bilayer (magenta circle around GUVs). Their insertion leads to an influx of the Atto633 dye inside the GUV interior. Bottom: LGC-N-Chol does not interact with bilayer (no magenta circle around GUV) or insert into GUV, showing no dye influx over the course of 3 h. The data are representative of n = 3 independent experiments (E) Bar plot showing the percentage of GUVs with a filled interior after 3 h. The data summarize the average percentage of influx and error bars show the standard deviation of mean percentage influx counted from three independent experiments across n = 49 GUVs in case of LGC-N+Chol and n = 59 for LGC-N-Chol. Scale bars: 10 µm. (F) Current trace showing a single LGC-N+Chol channel inserted into a planar DPhPC membrane. The trace was recorded at an applied voltage of +80 mV for the first 5 s after which voltage potential was switched to −80 mV. (G) Conductance histogram

Figure 2.2: of 19 individual LGC-N+Chol channels recorded at −20 mV. (H) Current-voltage (IV) plot showing the average current of 19 individual insertions ±SEM at membrane potentials ranging from −100 mV to +100 mV in 20 mV steps. All electrophysiological experiments were conducted in buffers composed of 1 M KCl, 10 mM HEPES pH 7.6.

The extent of membrane binding was probed by incubating Cy3-labeled LGC-N with giant unilamellar vesicles (GUVs) and examination with fluorescence microscopy. Co-localization of the cholesterol labeled pore with the vesicle perimeter indicated successful membrane binding (**Figure 2.2 C, D and Supplementary Figure 11**).

To explore whether LGC-N punctures lipid bilayers, we tested the influx of membrane-impermeable Atto633 dye into the interior of GUVs [55, 27, 19]. GUVs were placed in a solution of Atto633, and fluorescence microscopy tracked any changes in the fluorescence content of GUVs after adding LGC-N. The channel successfully inserted into, and punctured membranes as indicated by Atto633 signals that increased within GUVs over the full incubation time (**Figure 2.2 D, top**). A total of 59% of GUVs showed dye influx in case of LGC-N with cholesterol (LGC-N + Chol) (**Figure 2.2 E and Supplementary Videos 2, 3**), which compares to solely 3.5% of GUVs incubated with LGC-N lacking cholesterol (LGC-N-Chol) (**Figure 2.2 E, bottom**); membrane insertion via cholesterol is key for puncturing the bilayer for cargo transport (see Methods for details on how data were analyzed to identify influx). We further validated the membrane-spanning of our large and gated channel with a fluorescence resonance energy transfer (FRET) assay (**Supplementary Figure 12**), which detects the interaction of a donor dye at the inserted channel with acceptor dyes in the GUV lumen.

The observed 59% influx via the LGC pores is significantly higher than the 8–11% increase detected in previous reports [24, 12] Moreover, the LGC mediated influx was completed within 1 h after channel addition, which is considerably faster than the

5–8 h completion time required in the case of previous DNA nanopores [24, 12]. The differences in influx rates may be a result of several interdependent phenomena that lead to DNA nanopore-mediated transport: (i) nanopore binding to the membrane, (ii) reorientation of the stem and puncturing of the lipid bilayer to form a channel, and (iii) the diffusion of the dye through the pore. The nanopore binding to the membrane is strongly governed by the number of cholesterol molecules, ionic concentration, and temperature. The reorientation is the rate-determining step and depends on the flexibility of cholesterol-bearing segments of the nanopore. The final step of dye diffusion is a function of the size of the dye molecules, medium viscosity, temperature, concentration gradient, and pore dimensions [24, 55]. We attribute the faster flux in the case of LGC-N compared to previous pores due to the placement of a large number of cholesterol anchors to accelerate membrane binding (step i). The flexibility of the cholesterol-bearing one-layer origami plate allows for rapid reorientation of the pores. Faster insertion kinetics were observed with LGC-N compared to previous origami pores that always placed the cholesterol molecules in a rigid framework, thereby slowing this reorientation step. Interestingly, the dye diffusion rate in LGC-N was approximately five times slower compared to the theoretically calculated time required for diffusion (**Supplementary Figure 13 and Supplementary Note 2**). This is likely due to the large pore diameter slowing the rate-limiting reorientation step.

The membrane-spanning nature of LGC-N was confirmed by single-channel current recordings (**Figure 2.2 F-H**). Individual channels were inserted into a planar DPhPC lipid bilayer that separates two chambers filled with electrolyte (1 M KCl, 10 mM HEPES pH 7.6). To induce ion flow across an inserted channel, a transmembrane potential was applied. An ensuing steady current of 461 pA (**Figure 2.2 F, +80 mV**) indicated membrane insertion. LGC-N's average conductance values distribute into multiple conductance states (**Figure 2.2 G and Supplementary**

Figure 16), in line with previous measurements of large diameter DNA nanopores [12, 19]. Two peaks are seen in the conductance histogram, a smaller peak with an average of 2.51 ± 0.35 nS (n = 6, ±error of Gaussian fit) and a larger peak with an average of 5.92 ± 0.43 nS (n = 16, ±error of Gaussian fit) (**Figure 2.2 G**). The linear relationship between current magnitude and voltage is expected for a channel lumen with vertical symmetry (**Figure 2.2 H**). Control experiments using fluorescence microscopy (**Supplementary Figure 14**) and electrical current readout (**Supplementary Figure 15**) of a flat origami plate without the stem established that the translocation of dye is indeed through the central pore and not through the toroidal pores known to form between the sides of DNA nanopores and the lipid membrane.

2.3.3 Reversibly Ligand-gated Lid-controlled Transport of Small-molecule Cargo

Unlike constitutively open pores, biological ion channels usually open solely upon specific stimuli and then close by passive ligand dissociation. Attempts have not been able to functionally replicate and transcend biology by actively controlling pore opening and closing via external triggers. Our large gated channel was designed to achieve defined transport control via a toehold-mediated strand displacement reaction [65, 21] between lock and key (**Figure 2.1 D and Supplementary Figure 4**). We tested the reversible opening and closing of the lid using FRET. A Cy3 donor and Cy5 acceptor dye were placed in the lid and plate, respectively (**Figure 2.3 A, D and A**). Due to spatial proximity between the dyes, FRET occurred in the closed state (Closed or LGC-C) as reflected by the low donor fluorescence at $\lambda Cy3_{max} = 564nm$ and high acceptor fluorescence at $\lambda Cy5_{max} = 670nm$ (Figure 2.3 B, solid pink line). Opening the lid by adding a key (Dyn. Open) increased the distance between the reporter dyes and resulted in a low FRET, a higher donor emission, and a drop in the acceptor

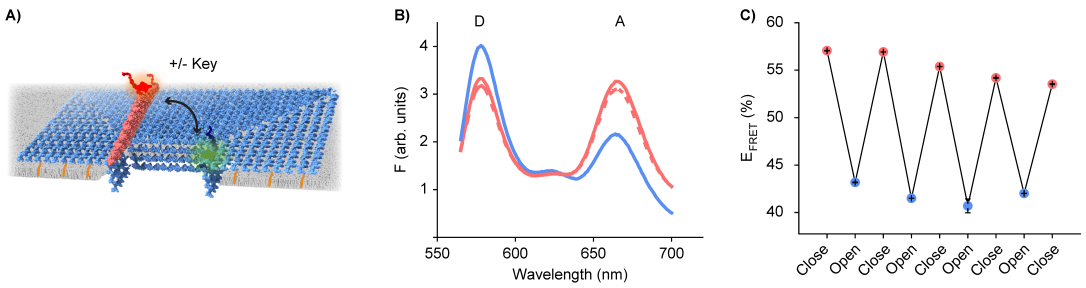

Figure 2.3: (A) Scheme showing LGC, containing donor dye on the plate (green) and acceptor dye on the lid (red). The addition of key and reverse key leads to respectively, opening and closing of the lid—resulting in closing or increasing the distance between the two dyes. (B) Representative fluorescence spectra for one full cycle of lid opening-closing (D and A on the graph represent fluorescence maxima for donor and acceptor respectively) and (C) FRET efficiency corresponding to reversible gating of LGC lid over four full cycles; data points and error bars respectively represent average relative FRET efficiency and standard deviation of the mean from n = 3 technical repeats. Initially, when the lid is closed, the spatial proximity of the donor and acceptor enables FRET, resulting in lower donor fluorescence, higher acceptor fluorescence (b, solid pink), and high FRET efficiency (c, close, pink dots). Opening the lid using a key (dynamic-open) moves the donor and acceptors far from each other. Thus, FRET ceases, resulting in higher donor fluorescence, lower acceptor fluorescence (b, solid blue) and lower FRET efficiency (c, open, blue dots). Closing the lid back from its open state using a reverse key (dynamic-closed) restores FRET, again resulting in lower donor fluorescence, higher acceptor fluorescence (b, dashed pink), and high FRET efficiency (c, closed, pink dots).

emission (Figure 2.3 B, blue line). Closing the lid back from its open state using a reverse key (Dyn. Closed) restored FRET, lowered donor fluorescence, and increased acceptor fluorescence (Figure 2.3 B, dashed pink line). The key-controlled switch was sequence-specific as confirmed by a mismatch key (**Supplementary Figure 17**). Analysis of the kinetic FRET signal revealed that lid opening followed second-order kinetics [33] at a rate constant of $1940 \pm 50\,\mathrm{M}{-}1\,\mathrm{s}{-}1$ until transport completion after 2 h (**Supplementary Figure 18 and Supplementary Note 3**). Cyclic opening (**Figure 2.3 C, blue dots**) and closing (**Figure 2.3 C, pink dots**) of the lid was also demonstrated by comparing the FRET efficiency at each stage.

After establishing reversible gating, we utilized the GUV-dye influx assay to

demonstrate controlled transport through the channel. GUVs were immersed in a solution of Atto633, and influx was probed via fluorescence microscopy. In control analysis, cholesterol-modified LGC-C bound to the vesicle membranes whereas the non-cholesterol version did not show binding, as indicated by the presence or absence of fluorescent rings around the GUV perimeter (**Supplementary Figure 19**). Probing of the fluorescence intensity within GUVs established that membrane-bound LGC-C did not lead to dye flux into the vesicles (**Figure 2.4 A,B, top; Supplementary Video 4**). This implies that the lid completely blocked transport through the LGC channel. Upon addition of keys, however, dye fluxed inside GUVs demonstrating that the opened-lid channel is transport active (**Figure 2.4 A,B middle and Supplementary Video 5**). To confirm that the channel can be shut back to cease transport function, a "dynamically closed pore" was obtained by first, dynamically opening the closed LGC by addition of key, followed by addition of the reverse key. After dynamically closing the membrane-inserted LGC in the absence of Atto633, the dye was added to the GUVs. No dye influx was seen in this case (**Figure 2.4 A,B, bottom and Supplementary Video 6**), which confirms that the dynamically closed LGC blocks transport. Negative control experiments with LGC-C without cholesterol modification (**Supplementary Video 7**) and the mismatch keys (**Supplementary Figure 20**) did not show similar Atto633 dye influx. Moreover, a two-color confocal microscopy experiment was performed (**Supplementary Figure 21**). Firstly, red dye (Atto633) was allowed to influx into the vesicle through the open lid pore LGC-O. Closure of the lid did not allow a second green dye (Atto 488) to the influx, demonstrating successful closure of the opened lid. These data clearly confirm that the lid can be reversibly opened and closed with external triggers. Although previously one-way or partial opening and closing has been shown in separate reports, dynamic and reversible gating has not been shown in a synthetic nanopore

before.

Single-channel current recordings probed the characteristics of cholesterol-modified closed lid (LGC-C) and open-lid (LGO-O) LGCs (**Figure 2.4 C–H**), and the dynamic transitions between the two. As would be expected from the steric blockade by the closed lid, LGC-C featured a far smaller current and corresponding conductance at 0.64 ± 0.10 nS (n = 12, ±error of Gaussian fit) (**Figure 2.4 C, E**) than had been obtained with no lid LGC at 5.92 ± 0.43 nS (n = 15, ±error of Gaussian fit) (**Fig. 2.2 F,G**). The presence of the lid did not affect linear voltage-current dependence (**Figure 2.4 D**). The small residual current of LGC-C might stem from ion leakage either through the periphery of the pore (at the DNA duplex/lipid interface) [18, 19, 6] or through the DNA duplexes of the lid, or a combination of both. By comparison, the conductance of LGO-O at 2.31 ± 0.18 nS (n = 17, ±error of Gaussian fit) (**Figure 2.4 F,H**) is almost four times the value of LGC-C (**Figure 2.4 E**), reflecting that the open lid allows more ion transport. However, it is still more than half the value of no-lid LGC in agreement with a residual blockade by an open lid (Figure 2.2 F,G). Control experiments were performed using a DNA plate construct without a pore-forming cap region (**Supplementary Fig. 15**). These constructs did not produce pore-forming currents, highlighting the importance of the cap region for lipid bilayer penetration.

The single-channel analysis provided further insight into the dynamic nature of the LGC lid. Current traces of the single LGC-O channels had more high-frequency fluctuations (**Fig. 2.4 F and Supplementary Figures 22b, 23**) than the less noisy trace of LGC-C (**Figure 2.4 C and Supplementary Figures 22a, 2**3) at all voltages from −100 to +100 mV (**Supplementary Figure 22**). The current fluctuations likely reflect the dynamic movements of the lid to and from the channel base in LGC-O compared to the static lid in LGC-C. Indeed, electrophoret-

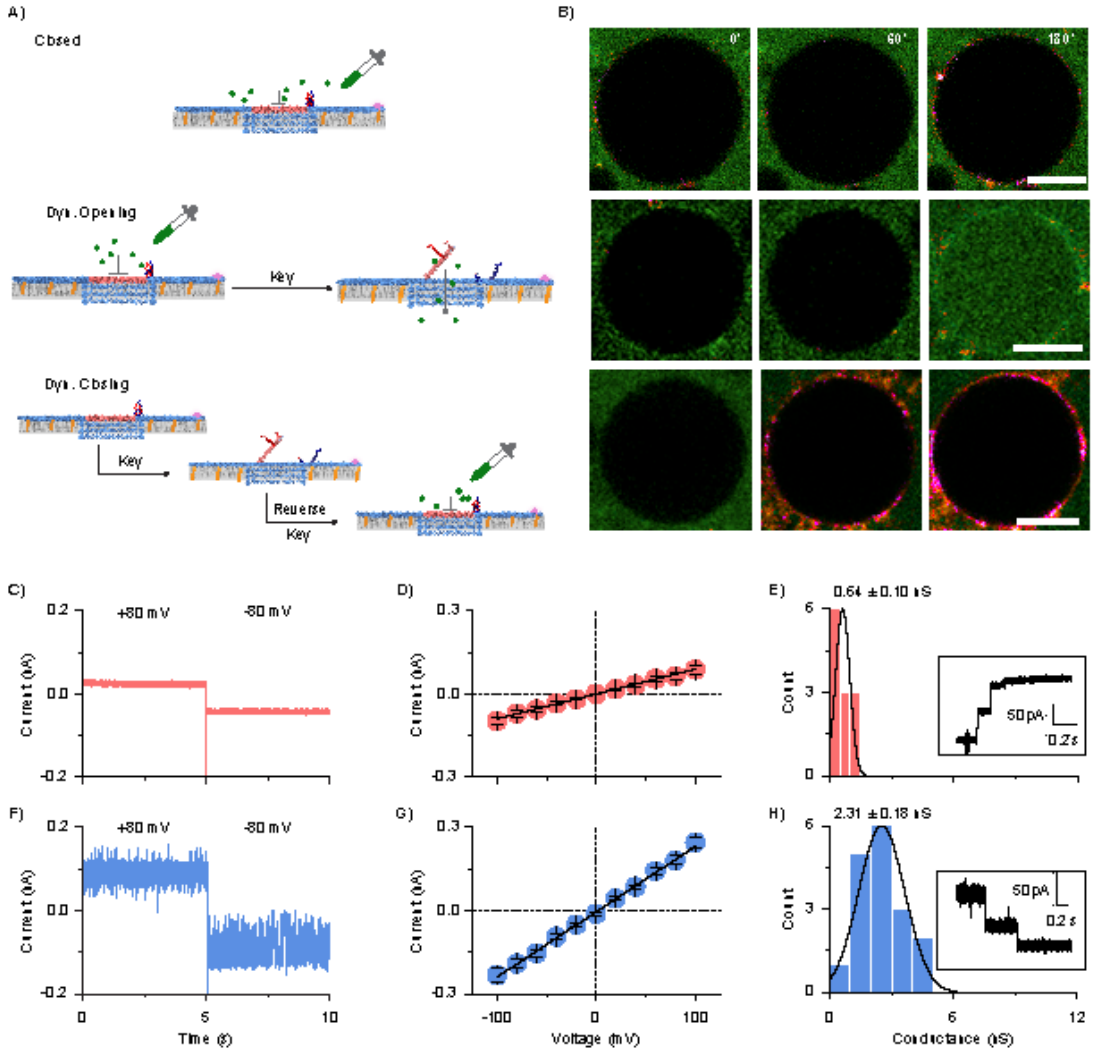

Figure 2.4: (A) GUV-dye-influx assay scheme. (B) A time series of corresponding confocal images of GUVs incubated with cholesterol and Cy3-labeled LGC (magenta) and Atto633 dye (green), dropper represents the time point at which Atto633 dye was added. Top—closed lid LGC does not allow Atto633 dye influx into GUV interior. Middle—dynamically opening the LGC lid with key results in the influx of Atto633 dye into GUV. Bottom—separate experiment in which adding Atto633 to dynamically closed LGC does not lead to any dye influx into GUVs, showing dynamic closing is effective. Scale bars: 10 μm. The data were representative of n = 3 independent experiments. (C) Current trace of a single LGC-C channel inserted into a planar DPhPC membrane. The trace was recorded at a voltage of +80 mV for the first 5 s, after which the potential was is switched to −80 mV. (D) Current-voltage (IV) plot showing average current of 12 individual insertions ± standard error of the mean of LGC-C at membrane potentials ranging from −100 to +100 mV in 20 mV steps. (E) Conductance histogram of 12 individual insertions of LGC-C obtained at −20 mV. Inset shows an example trace on the transition from closed-lid pore to open-lid after addition of 15 nM key. f Current trace of a single LGC-N + Chol channel inserted into a planar DPhPC membrane. The trace was recorded at a voltage of +80 mV

Figure 2.4: for the first 5 s, after which the voltage potential was switched to −80 mV. (G) Current-voltage (IV) trace showing average current of 17 individual insertions ± standard error of mean of LGC-O at membrane potentials ranging from −100 to +100 mV in 20 mV steps. (H) Conductance histogram of 19 individual LGC-N + Chol channels recorded at −20 mV. Inset shows an example trace on the transition from open-lid pore to closed-lid after addition of 15 nM reverse key. All electrophysiological experiments were conducted in buffers composed of 1 M KCl, 10 mM HEPES pH 7.6.

ically driving the lid of LGC-O to its base plate via a negative potential led to an additional current level at -37.8 ± 15.6 pA (−60 mV, ±STD) next to the main conductance peak at -96.7 ± 7.8 pA (−60 mV, ±STD) (**Supplementary Figure 22**), an increase in noise at negative potentials shown by power spectrum noise analysis (**Supplementary Figure 24**), and an increase in event frequency at negative potentials (**Supplementary Figure 25**). By contrast, moving the lid away from the plate via positive potentials only led to a single, main peak at 78.5 ± 5.8 pA (60 mV, ±STD) (**Supplementary Figure 22**) and resulted in less noise (**Supplementary Figure 24**) and fewer blocking events (**Supplementary Figure 25**). The voltage-dependent noise strikingly reveals nanomechanical-dynamic changes of a DNA structure at the single-molecule level.

Single-channel analysis revealed insight into the closing and opening mechanism. LGC-O could be closed by adding a reverse key, as demonstrated by the transition from an open state current at 97.4 ± 5.2 pA (10 mV, ±STD) to the lower-amplitude closed state at 17.7 ± 2.9 pA (10 mV, ±STD) (**Figure 2.4 H, inset and Supplementary Figure 26**). This transition occurred in a stepwise fashion, likely because the two lid locks are closed one after the other leading to an intermediate state of one closed and one open lock (**Figure 2.1 D**). Similarly, LGC-C was opened by adding key as indicated by a switch from the closed state at an amplitude of 8.7 ± 2.7 pA (−10mV, ±STD) to the open-state at amplitude 146.9 ± 2.8 pA (−10 mV, ±STD)

(**Figure 2.4 E, inset and Supplementary Figure 26**). This transition occurred also in a stepwise fashion. Our data reveal the opening and closing mechanism of the LGC channel in unprecedented detail and indicates ways to fine-tune the opening by varying the lock number.

2.3.4 Transport of Folded Proteins Across the Nanopore

We finally exemplified the power of large and gated channels by regulating the flux of folded proteins across membranes via defined lid opening and closing. GUVs were immersed in a solution of green fluorescent protein (GFP, hydrodynamic diameter = 5.6 nm [53]). Cholesterol-modified channels bound to GUV membranes whereas unmodified versions did not bind (**Supplementary Figure 27, 28 and Supplementary Videos 8, 12**). When influx was monitored by determining fluorescence intensity in GUVs, control channel LGC-N with cholesterol without lid led to transport across membranes (**Supplementary Figure 27 and Supplementary Video 8**). By contrast, cholesterol-modified closed-lid LGC-C blocked protein flux (**Figure 2.5 A-C, top and Supplementary Video 9**). However, adding the key opened up the transport function (**Figure 2.5 A-C, middle and Supplementary Video 10**). Again, in the dynamically closed pore, no protein influx was observed (**Figure 2.5 A-C, bottom and Supplementary Video 11**). Negative control experiments with 500 kDa FITC-dextran featuring a hydrodynamic diameter of 31.8 nm [2] established that channel transport did not occur due to size-exclusion (**Supplementary Figure 29**); FITC-dextran also ruled out membrane rupturing. Another control experiment using pre-encapsulated cargo in GUVs demonstrated that LGC can release nucleic acid cargo such as dye-labeled DNA (**Supplementary Figure 30**) which can prove to be valuable for vaccine delivery. The successful data on the precisely timed transport of folded proteins and small organic dyes with equal ease (**Figure**

2.4 A,B and Supplementary Figure 31) is beyond the scope of biological and any previously engineered membrane channels.

The transport of folded protein across the membrane-nanopore lumen was examined with single-channel current recordings (**Figure 2.5 D-G**). As a model protein, trypsin (hydrodynamic diameter of 4.0 nm [20]) and net positive charge (pI 10.1, pH 7.6) was used. No translocation events occurred upon the addition of 6.6 μM trypsin to the cis chamber of membrane inserted LGC-C (**Supplementary Figure 32**) as shown by relatively steady current flow (**Supplementary Figure 32a, b**). By contrast, with LGC-N channels increasing concentrations of trypsin led to blockades (**Figure 2.5 D-G and Supplementary Figure 33**), which clustered into two event types (**Figure 2.5 D-G**). When analyzed by their relative percentage blocking amplitude, A/IO (amplitude of block/ open current amplitude), and dwell time, off, (**Figure 2.5 F,G**), events clustered at $1.88 \pm 1.5\%$ (Type I) and at $10.8 \pm 4.8\%$ A (Type II). We suggest that Type I events occur due to the brief interaction of the protein with the nanopore at the lumen opening (**Figure 2.5 D**), while in Type II events proteins fully translocate through the nanopore (**Figure 2.5 E**). In order for translocation events to be detected, intermittent interactions of the positively charged trypsin to the negatively charged pore wall must occur [27, 40]. Voltage-dependent analysis (**Supplementary Figure 34**) revealed that Type II blocking events have longer dwell times at lower voltages (1.65 ± 0.10 ms at -20 mV) than higher voltages (0.28 ± 0.04 ms at -50 mV) in line with the expected faster translocation of trypsin through the pore at higher voltages.

The transport of folded GFP through LGC-N was also studied. GFP is larger than trypsin (hydrodynamic diameter of 5.6 nm) and has a lower isoelectric point (pI 5.8) and will therefore have a net negative charge in standard electrophysiological buffers of pH 7.6. Little interaction of GFP with the nanopore is expected at neu-

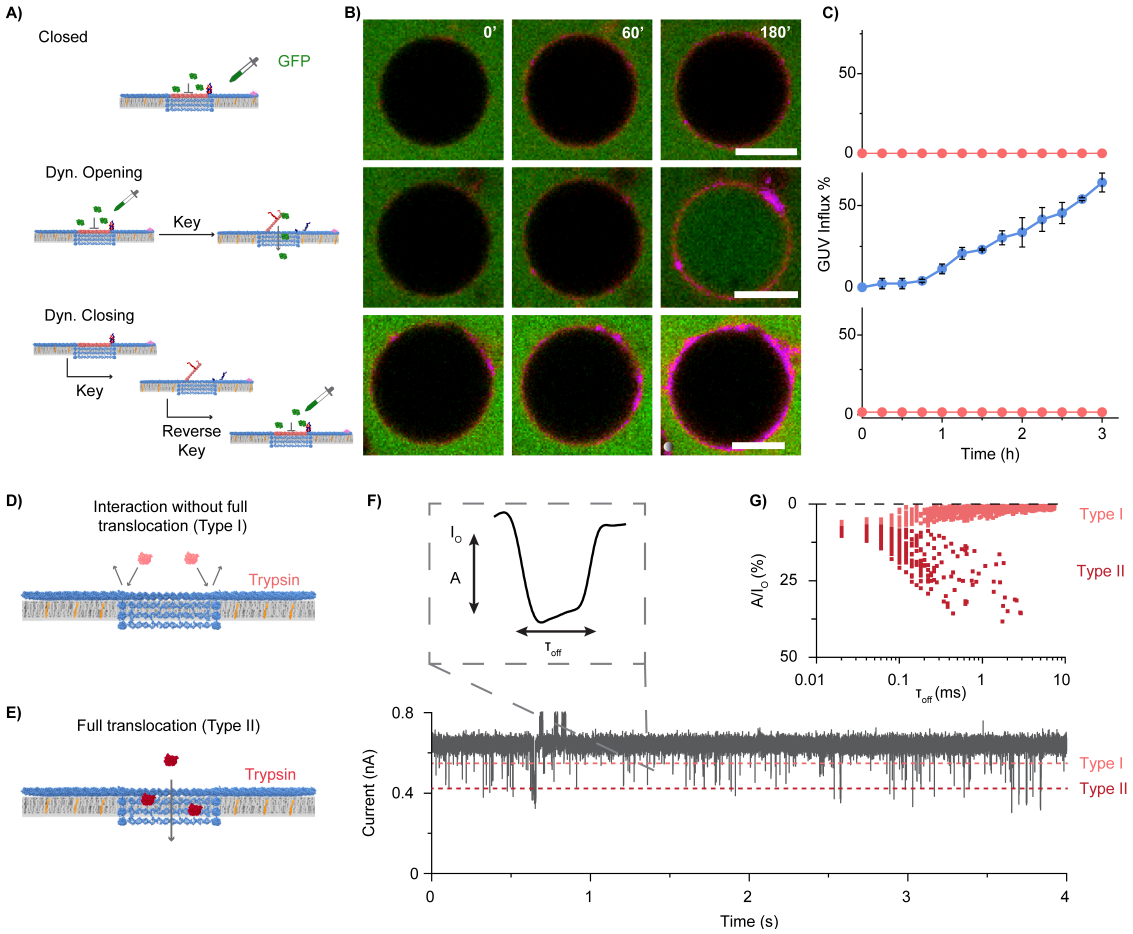

Figure 2.5: (A) Scheme of GFP-influx assay using GUVs. (B) Respective time series of confocal images at the given time points showing Cy5-labeled LGC (magenta) and GFP (green). Scale bars: 10 μm. (C) Percentage of GUVs showing influx over time for Closed, Dyn. Open, and Dyn. Closed versions of LGC. The plots show the average percentage of influx and standard deviation from n = 125, 255, and 125 GUVs, respectively, from three independent experiments. See Methods section on how data were analyzed to identify influx. (D), (E) Scheme depicting the electrophysiological characterization of trypsin transport through an LGC showing Type I (D) and Type II (E) events. (F) Representative single-channel current trace of LGC-N at +80 mV after the addition of 6.6 µM trypsin to the cis chamber obtained at 50 kHz sampling rate. Inset shows an isolated translocation event characterized by dwell time (off) and blocking amplitude (A/IO). (G) A scatter plot of individual trypsin translocation events based on off and A/IO. Electrophysiological experiments were conducted in buffers composed of 1 M KCl, 10 mM HEPES pH 7.6.

tral pH as intermittent electrostatic binding of a positively charged protein with the negatively charged DNA pore wall is thought to be necessary to resolve translocation events. Indeed, when 310 nM GFP was added at neutral pH to LGC-N no obvious translocation events could be seen (**Supplementary Figure 35 a–c**). However, when the pH of the electrophysiological buffer was dropped below the pI of GFP to pH 4.5 clear blockade events could be detected (**Supplementary Figure 35d–f**) suggesting electrostatic interaction between GFP and the pore wall. GFP blockade events clustered into two types of events when each event was plotted in relation to its blocking amplitude and dwell time (**Supplementary Figure 36**), similar to the blockades caused by trypsin. Type I GFP events clustered at $3.8 \pm 3.7\%$ and Type II events clustered at $26.1 \pm 7.3\%$. The latter events are interpreted to fully translocate through the nanopore. The bigger blocking amplitude of GFP is expected for the protein's larger size (hydrodynamic diameter = 5.6 nm) compared to trypsin (hydrodynamic diameter = 4.0 nm), in line with the previous reports [27].

2.3.5 Advantages and Limitations of Pore Design

In this work, we set out to construct a reversibly gated DNA nanopore with a luminal diameter large enough to accommodate proteins for transport assays. Whilst achieving these goals, characterization of the pore has highlighted some key advantages of the DNA nanopore design over existing artificial nanopore designs, as well as revealing some limitations of the design. Discussing the advantages and limitations here could help future researchers improve the design and sensing abilities of DNA nanopores, accelerating the advancement of research in the field of DNA nanostructures.

One advantage of the pore design in this study lies in the nanomechanical control of pore activity, which enables controlled transmembrane transport of an array of

cargoes ranging from small-molecule dyes to large folded protein. Fluorophore flux studies have shown high fidelity of dye transport through open lid nanopores, with no such transport seen in closed lid nanopores (Figure 2.4 A,B). However, single-channel current recordings revealed some inherent ionic leak through the closed lid nanopore (**Figure 2.4 C-F**), with an average conductance of 0.64 ± 0.10 nS, highlighting the high sensitivity of these single-molecule experiments. Such leaks have been shown previously with a closed lid DNA nanopore [6]. Leak currents likely stem from toroidal pore formation of lipid bilayer spanning DNA duplexes [18, 19], as well as ionic flow through the nanopore lid76 (**Supplementary Figure 37**). Dye transport studies (**Fig. 2.4 A,B**) show that the closed lid nanopore is not permeable to the larger dyes (Atto633 diameter = 1.3 nm), suggesting the leak of ions only (chloride ion Stoke's radius = 0.1 nm). Major groove binders [43] or hydrophobic coating [9] have been proposed as potential strategies to reduce leak currents of DNA nanostructures.

In this study, open lid nanopores have been successfully designed to controllably accommodate the folded proteins trypsin and GFP for fluorophore release flux studies (**Figure 2.5 A-C**) and single-molecule electrophysiological transport studies (**Figure 2.5 D-G**) which is a major advantage over current small-diameter protein-based nanopores. However, single-channel current recordings have revealed smaller experimental conductances of no lid nanopores when compared to designed pore diameters. No lid nanopores have an average conductance of 5.92 ± 0.43 nS, with protein transport studies of both trypsin and GFP attributing average current blocks of 11 and 26% respectively. Taking into consideration these measurements, it is therefore likely that the pore does not have the designed pore size of 20 nm, but is closer to 5–8 nm when measured in a planar lipid bilayer (based on estimated protein volumes). Whilst there is an apparent reduction in pore diameter, this is still of a size large enough to accommodate folded protein. Previous research has shown buckling and voltage-

dependent conformational changes of DNA origami structures [54, 52] and compression of lipid spanning helices of the lumen [27] that may account for low experimental conductances. Electro-osmotic effects due to the charged DNA backbone as well as increased access resistance in nanopores with low thickness-to-diameter ratios and charged surfaces [59] may also have integral roles in reducing experimental conductance. Future molecular dynamic studies [18, 64]) could help explain the conductance discrepancies in large diameter DNA nanostructures.

Another advantage of our nanopore design is the horizontal routing approach that allows high design flexibility, which means making small adjustments to tailor the pore to a required function is not a labor-intensive process. For example, tailoring pore diameters for size-dependent analysis of folded proteins, or adjusting lid opening/closing for real-time analysis of protein folding interactions. Our protein transport studies in planar lipid membranes have shown that relatively high concentrations of trypsin (between 66 nM and 6.6 μM) are required for adequate analysis of translocation events (**Supplementary Figure 33**). Protein translocation under voltage is a rapid process, with the majority of proteins passing through the nanopore with dwell times ¡20 μs, too fast to detect with electrophysiological equipment. Therefore, protein translocation can only be detected in this case when trypsin translocation is slowed, such as via interaction with the negatively charged DNA of the pore lumen. This interaction has been noted previously with trypsin translocation through a DNA nanopore [12], and is in concordance with simulation data of trypsin translocation through a DNA nanopore [40]. Only trypsin that has adequate interaction with the DNA pore lumen will therefore be detected, accounting for the larger concentration of protein required in these translocation experiments. Future work could look at adding protein-specific tags inside the pore lumen to increase the specificity of protein interactions, whilst also increasing protein dwell times.

2.4 Discussion

Here we pioneered a large diameter DNA nanopore with a sequence-specific, fully reversible gating. By controlling the transport of various cargoes ranging from small-molecule dye to folded proteins, the DNA pores exceed the natural analog—ligand-gated ion channels which have much narrower pore dimension. The DNA nanopore is also innovative as it offers reversible and tunable pore gating to control transmembrane transport of protein cargo. The design freedom offered in the current work may enable the creation of pores to reversibly capture proteins and study their interaction with free-flowing ligands [51, 57]) or real-time protein folding and unfolding [50]. The reversibly controlled flow of cargo by a nanomechanical lid may also be exploited to transport bioactive cargo into cells, or to construct cell–cell communication [38] for artificial gap junctions and to enable integration of artificial tissues with living cells and tissues for tissue engineering [14]. In conclusion, by offering solutions to several challenges in nanopore sensing our study extends the versatility and scope of artificial nanopores beyond nature and thus opens various exciting applications.

2.5 Author Contributions

S.H. and H.Y. conceived the idea of the project. S.D. and F.Z. designed the nanopores and performed AFM experiments for the formation of the nanopore. S.D and L.A. designed and performed the FRET experiments for dynamic opening and closing of the nanopore. S.D and L.A. designed and performed experiments and data analysis for confocal microscopy images for the GUV influx assays. Y.X. and S.D. performed TEM imaging of the nanopore formation. Y.X. and S.D. performed TEM imaging of the nanopore interaction with SUVs. Y.X. carried out agarose gel experiments for studying the interaction of nanopores with SUVs. Y.X. prepared nanopore

samples for the electrophysiological measurements. A.D. carried out the electrophysiological characterization of the nanopore including analysis and interpretation. I.Z. helped S.D. and L.A. to optimize GUV formation protocol. S.D. wrote the manuscript with inputs from L.A., A.D., Y.X., and F.Z. under the supervision of S.H. and H.Y.

2.6 Materials and Methods

All DNA oligonucleotides were purchased from Integrated DNA Technologies Inc. with standard desalting unless mentioned otherwise. The strands used for dynamic reconfiguration were purified in house with denaturing PAGE gels. Lipids were purchased from Avanti Polar Lipids Inc. All other chemicals (e.g.Sucrose, Glucose, FITC-Dextran, alpha-hemolysin etc.) were purchased from Sigma Aldrich Inc.

2.6.1 Large Diameter Nanopore Design and Assembly

The nanostructures were designed de novo by Tiamat software. Information on the DNA oligonucleotide sequences, two-dimensional DNA maps are provided in Supplementary Data 1 and Supplementary Figure 2. Assembly of the structures were done by mixing a final concentration of the scaffold strand at 50 nM and staples at 5x excess concentration in 12.5 mM $MgCl_2$ in 1x TAE buffer (40mM Triacetate and 1mM EDTA, pH 8.3). The structures were folded in Life Technologies SimpliAmp thermal cycler by the following annealing protocol – 10 mins consecutively at 90°C, 80°C, 70°C and 60°C; 20mins consecutively at 50°C, 40°C, 30°C and 20°C. Following the annealing the structures were stored at 4 ^{o}C until further use.

2.6.2 Purification of DNA Nanopores

The folded DNA origami nanopores were purified either by filter centrifuge or by agarose gel purification (see the native agarose gel electrophoresis section below). For

a typical purification using Amicon centrifugal filter (100kDa MWCO), the filter was firstly washed with 1× TAE-Mg buffer (20 mM Tris base, 10 mM acetic acid, 0.5 mM EDTA, 12.5mM $Mg(OAc)_2$, (pH 8.3), then added the origami solution and spin at 1500 xg for 2 min, and followed with 5 additional spinning steps by filling 400 μL 1× TAE-Mg buffer before each step. The purified samples were stored at 4°C until further use.

2.6.3 Native Agarose Gel Electrophoresis

For characterizing the formation of the pore, a 1.5% agarose gel was casted 1× TAE-Mg buffer. The gel was run at 120V in ice-water bath for 1.5h. Sybr green stain was added with the sample which was used for the gel imaging. For gel purification, after the gel running was done, the gel was illuminated under a UV lamp (365 nm) and bands of interest were carefully cut out from the gel. The gel pieces were frozen at -20°C and the purified nanopores sample solutions can then be recovered by using Freeze 'N Squeeze spin columns. To make Mg^2+ free nanopore samples, the recovered solutions were further proceeded with a buffer exchange treatment using Amicon filter, The operations were same to the filter centrifuge purification method above except that the buffer used here was Mg2+ free: 50 mM HEPES (pH 7.6) supplemented with 500 mM NaCl. The purified pores, optionally incubated with SUVs, were analyzed using 1.5% agarose gel electrophoresis in 0.5 × TAE buffer (20 mM Tris base, 10 mM acetic acid, 0.5 mM EDTA, pH 8.3) and 0.5 × TAE-Mg buffer (20 mM Tris base, 10 mM acetic acid, 0.5 mM EDTA, 10 mM $MgCl_(2)$, pH 8.3) at 65 V in ice-water bath for 1.5 h. Uncropped and unprocessed scans of all the gels are provided in the source data.

2.6.4 Atomic Force Microscopy (AFM)

Sample were prepared for AFM imaging as described. A 3 μL annealed sample was deposited onto a freshly cleaved mica surface (Ted Pella) and samples 60 μl 1× TAE-Mg2+ buffer was added immediately to the sample. After about 30 sec, 3 μl NiCl2 (25 mM) was added. An extra 60 μl of the same buffer was deposited on the AFM tip. AFM imaging was performed in the 'ScanAsyst mode in fluid' on the Dimension FastScan, Bruker with the Scanasyst-Fluid+ tips from Bruker.

2.6.5 Transmission Electron Microscopy (TEM)

Samples for the TEM were prepared as described. 10 μL of each sample was added to a plasma treated TEM grids (Agar Scientific, AGG2050C) for 1 min or negative stain carbon B type grid for 10 mins and wicked off. The sample was first quickly and then for 10 sec stained with 2% uranyl formate or 1% uranyl acetate with 2mM NaOH. The stain buffer was then wicked off and the grid air dried for 20 mins. The grid was then imaged using a JEM-2100 electron microscope (equipped with an Orius SC200 camera) or Philips TM 12 TEM operated at 120 kV at 33000× to 80000× magnification.

2.6.6 Preparation of Small Unilamellar Vesicles (SUVs)

A lipid solution (DOPC/DOPE = 7:3, 10 mg/mL in chloroform) dispensed in a 2 mL-glass vial was blown dry with argon airflow. The dried lipid film was then suspended in 50 mM HEPES (pH 7.6) supplemented with 500 mM NaCl, and treated by sonication for 30 min. the solution was then put through 10 freeze thaw cycles in liquid nitrogen and 60°C water respectively.

2.6.7 Cholesterol Modification of Nanopore

Cholesterol modified strands were purchased from Integrated DNA Technologies Inc. with PAGE purification. The strand was dissolved in water to make 100 µM solution. Immediately the solution was made into 5, 10 and 20 µl aliquots and lyophilized. This was done in order to avoid aggregation of the cholesterol modified strands in water. The structures were then incubated with 2× excess concentration of cholesterol modified strands (64 cholesterol modified positions on the structure were accounted for) at 37°C for 12 hrs.

2.6.8 Preparation of Giant Unilamellar Vesicles (GUVs) for Confocal Measurements

The GUVs were prepared by inverted emulsion method 49. POPC (150 μL, 10 mM) in chloroform was added to a 1 mL glass vial, the solvent was removed under vacuum and rotation using a Buchi rotary evaporator set at high vacuum for at least 30minutes. The thin film generated was resuspended in mineral oil (150μL) by vortexing and sonicating for 10 minutes. 25μL of inner solution (IS, the solution that will be encapsulated inside GUVs) containing 435 mOsm/kg sucrose added to the mineral oil. A water-in-oil emulsion was created by suspending the IS into the mineral oil by pipetting up and down for 10 times followed by vortexing at highest speed for 30 seconds and sonicating for 10 minutes at room temperature. This emulsion was then carefully added to the top of 1mL external solution (ES, the solution to be kept outside the GUVs) containing 435mOsm/kg glucose in a plastic microcentrifuge tube. The osmolarities of the IS and ES were measured by an osmometer (Advanced Instruments Model 3320 Osmometer 2996) and balanced properly such that the osmolarity difference is less than 20 mOsm/kg. The GUVs

were generated by centrifuging at 21k × g at 4°C for 15 minutes. The mineral oil top layer and most of the sucrose layer (900μL) was carefully removed by pipettor, every time using a fresh tip. The remaining solution containing the pelleted vesicles was gently mixed with a pipettor, then transferred to a clean plastic vial leaving a small quantity to avoid contamination of remaining trace amount of mineral oil to the GUVs.

2.6.9 Confocal Dye/Protein Influx Assay

For the confocal assay, samples were prepared as following. 3μL of GUV solution was mixed with 20nM of cy3/cy5 labelled-nanopore and 2 μM of dye (Atto633) or protein (GFP). The total solution was made up to 30μL by maintaining the osmolality balance of the inside and outside of the GUVs using a buffer containing 1M HEPES and 100 mM NaCl. This solution was added to an ibidi μ-Slide 18 Well – flat slide. The slide was then centrifuged at 1000 ×g for 10 mins to make sure that the GUVs are settled at the bottom of the slide. Then GUVs were then imaged on Nikon C2 Laser Scanning Confocal microscope at 40× magnification, 1.3 numerical aperture (NA) using a humidity chamber maintained at 32°C (dye)/ 37°C (GFP). Images were taken over 3 hrs at multiple points.

2.6.10 Calculating Percentage Influx

The mean intensity inside each GUV in a frame was measured using ImageJ software. For each experiment, the intensity inside the GUVs at t = 0 min (I0) and at t =180 min (I180) was measured and normalized by average intensity of the background at the same time point as $I_{(t,norm)} = I_{(t,i)}/I_{(t,b)}$; where: It, norm = normalized GUV interior intensity at time t; It, i = GUV interior intensity at time t and It,b = average background intensity at time t. GUVs that satisfied the threshold

criteria $(I_{(180,norm)} - I_{(0,norm)}) > 0.5$ were considered to have shown influx over 3 hours and from this the percentage of GUVs showing influx was calculated.

2.6.11 Single-channel Current Recordings

For planar lipid bilayer electrophysiological current measurements, integrated chip-based, parallel bilayer recording setups (Orbit 16 and Orbit Mini; Nanion Technologies, Munich, Germany) with multielectrode- cavity-array (MECA) chips (IONERA, Freiburg, Germany) were used66. Bilayers were formed of DPhPC lipid dissolved in octane (10 mg/mL). The electrolyte solution was 1M KCl and 10 mM HEPES, pH 7.6. For pore insertion, a 2:1 DNA nanopore and 0.5% OPOE (n- octyloligooxyethylene, in 1M KCl, 10 mM HEPES, pH 7.6) was added to the cis chamber. Successful incorporation was observed by detecting current steps. Current traces were acquired at 10 kHz or 50 kHz where specified and subsequently Bessel-filtered, using Element Data Recorder software (Element s.r.l., Italy). Single-channel analysis was performed using Clampfit (Molecular Devices, Sunnyvale, CA, USA).

2.6.12 LGC Scheme Creation and Simulation

The LGC schemes were generated by converting the original Tiamat structures to .pdb structures using the TacoxDNA webserver85 and UCSF chimera molecular visualization tool. The simulations shown in Supplementary Figure 6b were generated using oxDNA simulations in oxDNA.org.

REFERENCES

[1] Andersen, E. S., M. Dong, M. M. Nielsen, K. Jahn, R. Subramani, W. Mamdouh, M. M. Golas, B. Sander, H. Stark, C. L. P. Oliveira, J. S. Pedersen, V. Birkedal, F. Besenbacher, K. V. Gothelf and J. Kjems, "Self-assembly of a nanoscale DNA box with a controllable lid", Nature **459**, 7243, 73–76, URL `http://www.nature.com/articles/nature07971` (2009).

[2] Armstrong, J. K., R. B. Wenby, H. J. Meiselman and T. C. Fisher, "The hydrodynamic radii of macromolecules and their effect on red blood cell aggregation", Biophysical Journal **87**, 6 (2004).

[3] Arulkumaran, N., C. Lanphere, C. Gaupp, J. R. Burns, M. Singer and S. Howorka, "DNA Nanodevices with Selective Immune Cell Interaction and Function", ACS Nano **15**, 3, 4394–4404, URL `https://doi.org/10.1021/acsnano.0c07915` (2021).

[4] Banghart, M., K. Borges, E. Isacoff, D. Trauner and R. H. Kramer, "Light-activated ion channels for remote control of neuronal firing", Nature Neuroscience **7**, 12 (2004).

[5] Bull, R. A., T. N. Adikari, J. M. Ferguson, J. M. Hammond, I. Stevanovski, A. G. Beukers, Z. Naing, M. Yeang, A. Verich, H. Gamaarachchi, K. W. Kim, F. Luciani, S. Stelzer-Braid, J. S. Eden, W. D. Rawlinson, S. J. van Hal and I. W. Deveson, "Analytical validity of nanopore sequencing for rapid SARS-CoV-2 genome analysis", Nature Communications **11**, 1 (2020).

[6] Burns, J. R., A. Seifert, N. Fertig and S. Howorka, "A biomimetic DNA-based channel for the ligand-controlled transport of charged molecular cargo across a biological membrane", Nature Nanotechnology **11**, 2 (2016).

[7] Burns, J. R., E. Stulz and S. Howorka, "Self-assembled DNA nanopores that span lipid bilayers", Nano Letters **13**, 6 (2013).

[8] Cao, C., Y. L. Ying, Z. L. Hu, D. F. Liao, H. Tian and Y. T. Long, "Discrimination of oligonucleotides of different lengths with a wild-type aerolysin nanopore", Nature Nanotechnology **11**, 8 (2016).

[9] Chen, Y. J., B. Groves, R. A. Muscat and G. Seelig, "DNA nanotechnology from the test tube to the cell", (2015).

[10] Cherf, G. M., K. R. Lieberman, H. Rashid, C. E. Lam, K. Karplus and M. Akeson, "Automated forward and reverse ratcheting of DNA in a nanopore at 5-Å precision", Nature Biotechnology **30**, 4 (2012).

[11] Dey, S., C. Fan, K. V. Gothelf, J. Li, C. Lin, L. Liu, N. Liu, M. A. D. Nijenhuis, B. Saccà, F. C. Simmel, H. Yan and P. Zhan, "DNA origami", Nature Reviews Methods Primers **1**, 1, 13, URL `https://doi.org/10.1038/s43586-020-00009-8` (2021).

[12] Diederichs, T., G. Pugh, A. Dorey, Y. Xing, J. R. Burns, Q. Hung Nguyen, M. Tornow, R. Tampé and S. Howorka, "Synthetic protein-conductive membrane nanopores built with DNA", Nature Communications **10**, 1 (2019).

[13] Dunn, K. E., F. Dannenberg, T. E. Ouldridge, M. Kwiatkowska, A. J. Turberfield and J. Bath, "Guiding the folding pathway of DNA origami", Nature **525**, 7567 (2015).

[14] Eroglu, A., M. J. Russo, R. Bieganski, A. Fowler, S. Cheley, H. Bayley and M. Toner, "Intracellular trehalose improves the survival of cryopreserved mammalian cells", Nature Biotechnology **18**, 2 (2000).

[15] Fragasso, A., N. De Franceschi, P. Stömmer, E. O. van der Sluis, H. Dietz and C. Dekker, "Reconstitution of Ultrawide DNA Origami Pores in Liposomes for Transmembrane Transport of Macromolecules", ACS Nano **15**, 8, 12768–12779, URL `https://doi.org/10.1021/acsnano.1c01669` (2021).

[16] Galenkamp, N. S., A. Biesemans and G. Maglia, "Directional conformer exchange in dihydrofolate reductase revealed by single-molecule nanopore recordings", Nature Chemistry **12**, 5 (2020).

[17] Goodchild, J., "Conjugates of Oligonucleotides and Modified Oligonucleotides: A Review of Their Synthesis and Properties", (1990).

[18] Göpfrich, K., C. Y. Li, I. Mames, S. P. Bhamidimarri, M. Ricci, J. Yoo, A. Mames, A. Ohmann, M. Winterhalter, E. Stulz, A. Aksimentiev and U. F. Keyser, "Ion channels made from a single membrane-spanning DNA duplex", Nano Letters **16**, 7 (2016).

[19] Göpfrich, K., C.-Y. Li, M. Ricci, S. P. Bhamidimarri, J. Yoo, B. Gyenes, A. Ohmann, M. Winterhalter, A. Aksimentiev and U. F. Keyser, "Large-Conductance Transmembrane Porin Made from DNA Origami", ACS Nano **10**, 9, 8207–8214, URL `https://doi.org/10.1021/acsnano.6b03759` (2016).

[20] Gtari, W., H. Bey, A. Aschi, L. Bitri and T. Othman, "Impact of macromolecular crowding on structure and properties of pepsin and trypsin", Materials Science and Engineering C **72** (2017).

[21] Guo, Y., B. Wei, S. Xiao, D. Yao, H. Li, H. Xu, T. Song, X. Li and H. Liang, "Recent advances in molecular machines based on toehold-mediated strand displacement reaction", (2017).

[22] Han, C., R. Hao, Y. Fan, M. A. Edwards, H. Gao and B. Zhang, "Observing Transient Bipolar Electrochemical Coupling on Single Nanoparticles Translocating through a Nanopore", Langmuir **35**, 22 (2019).

[23] Hernández-Ainsa, S., N. A. Bell, V. V. Thacker, K. Göpfrich, K. Misiunas, M. E. Fuentes-Perez, F. Moreno-Herrero and U. F. Keyser, "DNA origami nanopores for controlling DNA translocation", ACS Nano **7**, 7 (2013).

[24] Iwabuchi, S., I. Kawamata, S. Murata and S. I. M. Nomura, "A large, square-shaped, DNA origami nanopore with sealing function on a giant vesicle membrane", Chemical Communications **57**, 24 (2021).

[25] Jain, M., S. Koren, K. H. Miga, J. Quick, A. C. Rand, T. A. Sasani, J. R. Tyson, A. D. Beggs, A. T. Dilthey, I. T. Fiddes, S. Malla, H. Marriott, T. Nieto, J. O'Grady, H. E. Olsen, B. S. Pedersen, A. Rhie, H. Richardson, A. R. Quinlan, T. P. Snutch, L. Tee, B. Paten, A. M. Phillippy, J. T. Simpson, N. J. Loman and M. Loose, "Nanopore sequencing and assembly of a human genome with ultra-long reads", Nature Biotechnology **36**, 4 (2018).

[26] Ke, Y., L. L. Ong, W. M. Shih and P. Yin, "Three-dimensional structures self-assembled from DNA bricks", Science **338**, 6111 (2012).

[27] Krishnan, S., D. Ziegler, V. Arnaut, T. G. Martin, K. Kapsner, K. Henneberg, A. R. Bausch, H. Dietz and F. C. Simmel, "Molecular transport through large-diameter DNA nanopores", Nature Communications **7** (2016).

[28] Kuzyk, A., R. Schreiber, H. Zhang, A. O. Govorov, T. Liedl and N. Liu, "Reconfigurable 3D plasmonic metamolecules", Nature Materials **13**, 9 (2014).

[29] Langecker, M., V. Arnaut, T. G. Martin, J. List, S. Renner, M. Mayer, H. Dietz and F. C. Simmel, "Synthetic lipid membrane channels formed by designed DNA nanostructures", Science **338**, 6109 (2012).

[30] Lanphere, C., P. M. Arnott, S. F. Jones, K. Korlova and S. Howorka, "A Biomimetic DNA-Based Membrane Gate for Protein-Controlled Transport of Cytotoxic Drugs", Angewandte Chemie - International Edition (2020).

[31] List, J., M. Weber and F. C. Simmel, "Hydrophobic actuation of a DNA origami bilayer structure", Angewandte Chemie - International Edition **53**, 16 (2014).

[32] Liu, M., J. Fu, C. Hejesen, Y. Yang, N. W. Woodbury, K. Gothelf, Y. Liu and H. Yan, "A DNA tweezer-actuated enzyme nanoreactor", Nature Communications **4**, 1, 2127, URL https://www.nature.com/articles/ncomms3127 (2013).

[33] Liu, M., S. Jiang, O. Loza, N. E. Fahmi, P. Šulc and N. Stephanopoulos, "Rapid Photoactuation of a DNA Nanostructure using an Internal Photocaged Trigger Strand", Angewandte Chemie International Edition **57**, 30, 9341–9345, URL https://doi.org/10.1002/anie.201804264 (2018).

[34] Liu, W. W. and R. I. Wilson, "Transient and specific inactivation of drosophila neurons in vivo using a native ligand-gated ion channel", Current Biology **23**, 13 (2013).

[35] Lv, C., X. Gu, H. Li, Y. Zhao, D. Yang, W. Yu, D. Han, J. Li and W. Tan, "Molecular transport through a biomimetic DNA channel on live cell membranes", ACS Nano **14**, 11 (2020).

[36] Lyubchenko, Y. L., L. S. Shlyakhtenko and T. Ando, "Imaging of nucleic acids with atomic force microscopy", (2011).

[37] Mahendran, K. R., A. Niitsu, L. Kong, A. R. Thomson, R. B. Sessions, D. N. Woolfson and H. Bayley, "A monodisperse transmembrane α-helical peptide barrel", Nature Chemistry **9**, 5 (2017).

[38] Mantri, S., K. Tanuj Sapra, S. Cheley, T. H. Sharp and H. Bayley, "An engineered dimeric protein pore that spans adjacent lipid bilayers", Nature Communications **4** (2013).

[39] Miles, B. N., A. P. Ivanov, K. A. Wilson, F. Dogan, D. Japrung and J. B. Edel, "Single molecule sensing with solid-state nanopores: Novel materials, methods, and applications", Chemical Society Reviews **42**, 1 (2013).

[40] Mitscha-Baude, G., B. Stadlbauer, S. Howorka and C. Heitzinger, "Protein Transport through Nanopores Illuminated by Long-Time-Scale Simulations", ACS Nano **15**, 6, 9900–9912, URL https://doi.org/10.1021/acsnano.1c01078 (2021).

[41] Muraoka, T., D. Noguchi, R. S. Kasai, K. Sato, R. Sasaki, K. V. Tabata, T. Ekimoto, M. Ikeguchi, K. Kamagata, N. Hoshino, H. Noji, T. Akutagawa, K. Ichimura and K. Kinbara, "A synthetic ion channel with anisotropic ligand response", Nature Communications **11**, 1 (2020).

[42] Ouldali, H., K. Sarthak, T. Ensslen, F. Piguet, P. Manivet, J. Pelta, J. C. Behrends, A. Aksimentiev and A. Oukhaled, "Electrical recognition of the twenty proteinogenic amino acids using an aerolysin nanopore", (2020).

[43] Pal, S., Z. Deng, B. Ding, H. Yan and Y. Liu, "DNA-origami-directed self-assembly of discrete silver-nanoparticle architectures", Angewandte Chemie - International Edition **49**, 15 (2010).

[44] Pei, H., N. Lu, Y. Wen, S. Song, Y. Liu, H. Yan and C. Fan, "A DNA nanostructure-based biomolecular probe carrier platform for electrochemical biosensing", Advanced Materials **22**, 42 (2010).

[45] Pinheiro, V. B., A. I. Taylor, C. Cozens, M. Abramov, M. Renders, S. Zhang, J. C. Chaput, J. Wengel, S. Y. Peak-Chew, S. H. McLaughlin, P. Herdewijn and P. Holliger, "Synthetic genetic polymers capable of heredity and evolution", Science **336**, 6079 (2012).

[46] Qing, Y., H. Tamagaki-Asahina, S. A. Ionescu, M. D. Liu and H. Bayley, "Catalytic site-selective substrate processing within a tubular nanoreactor", Nature Nanotechnology **14**, 12 (2019).

[47] Ramakrishnan, S., H. Ijäs, V. Linko and A. Keller, "Structural stability of DNA origami nanostructures under application-specific conditions", (2018).

[48] Rothemund, P. W. K., "Folding DNA to create nanoscale shapes and patterns", Nature **440**, 7082, 297–302, URL http://www.nature.com/articles/nature04586 (2006).

[49] Shoji, K., R. Kawano and R. J. White, "Correction to: Spatially Resolved Chemical Detection with a Nanoneedle-Probe-Supported Biological Nanopore (ACS Nano (2019) 13:2 (2606?2614) DOI: 10.1021/acsnano.8b09667)", (2019).

[50] Si, W. and A. Aksimentiev, "Nanopore Sensing of Protein Folding", ACS Nano **11**, 7, 7091–7100, URL https://doi.org/10.1021/acsnano.7b02718 (2017).

[51] Soskine, M., A. Biesemans and G. Maglia, "Single-molecule analyte recognition with ClyA nanopores equipped with internal protein adaptors", Journal of the American Chemical Society **137**, 17 (2015).

[52] Tan, S. J., M. J. Campolongo, D. Luo and W. Cheng, "Building plasmonic nanostructures with DNA", (2011).

[53] Terry, B. R., E. K. Matthews and J. Haseloff, "Molecular Characterization of Recombinant Green Fluorescent Protein by Fluorescence Correlation Microscopy", Biochemical and Biophysical Research Communications **217**, 1 (1995).

[54] Thacker, V. V., L. O. Herrmann, D. O. Sigle, T. Zhang, T. Liedl, J. J. Baumberg and U. F. Keyser, "DNA origami based assembly of gold nanoparticle dimers for surface-enhanced Raman scattering", Nature Communications **5** (2014).

[55] Thomsen, R. P., M. G. Malle, A. H. Okholm, S. Krishnan, S. S. Bohr, R. S. Sørensen, O. Ries, S. Vogel, F. C. Simmel, N. S. Hatzakis and J. Kjems, "A large size-selective DNA nanopore with sensing applications", Nature Communications **10**, 1 (2019).

[56] Van der Verren, S. E., N. Van Gerven, W. Jonckheere, R. Hambley, P. Singh, J. Kilgour, M. Jordan, E. J. Wallace, L. Jayasinghe and H. Remaut, "A dual-constriction biological nanopore resolves homonucleotide sequences with high fidelity", Nature Biotechnology **38**, 12 (2020).

[57] Van Meervelt, V., M. Soskine, S. Singh, G. K. Schuurman-Wolters, H. J. Wijma, B. Poolman and G. Maglia, "Real-Time Conformational Changes and Controlled Orientation of Native Proteins Inside a Protein Nanoreactor", Journal of the American Chemical Society **139**, 51 (2017).

[58] Walter, H. K., J. Bauer, J. Steinmeyer, A. Kuzuya, C. M. Niemeyer and H. A. Wagenknecht, "DNA Origami Traffic Lights with a Split Aptamer Sensor for a Bicolor Fluorescence Readout", Nano Letters **17**, 4 (2017).

[59] Wang, J., J. Ma, Z. Ni, L. Zhang and G. Hu, "Effects of access resistance on the resistive-pulse caused by translocating of a nanoparticle through a nanopore", RSC Advances **4**, 15 (2014).

[60] Wang, Y., D. Zheng, Q. Tan, M. X. Wang and L. Q. Gu, "Nanopore-based detection of circulating microRNAs in lung cancer patients", Nature Nanotechnology **6**, 10 (2011).

[61] Wei, R., T. G. Martin, U. Rant and H. Dietz, "DNA origami gatekeepers for solid-state nanopores", Angewandte Chemie - International Edition **51**, 20 (2012).

[62] Xu, C., P. Lu, T. M. Gamal El-Din, X. Y. Pei, M. C. Johnson, A. Uyeda, M. J. Bick, Q. Xu, D. Jiang, H. Bai, G. Reggiano, Y. Hsia, T. J. Brunette, J. Dou, D. Ma, E. M. Lynch, S. E. Boyken, P. S. Huang, L. Stewart, F. DiMaio, J. M. Kollman, B. F. Luisi, T. Matsuura, W. A. Catterall and D. Baker, "Computational design of transmembrane pores", Nature **585**, 7823 (2020).

[63] Yang, Y. R., Y. Liu and H. Yan, "DNA Nanostructures as Programmable Biomolecular Scaffolds", (2015).

[64] Yoo, J. and A. Aksimentiev, "Molecular Dynamics of Membrane-Spanning DNA Channels: Conductance Mechanism, Electro-Osmotic Transport, and Mechanical Gating", Journal of Physical Chemistry Letters **6**, 23 (2015).

[65] Yurke, B., A. J. Turberfield, A. P. Mills, F. C. Simmel and J. L. Neumann, "A DNA-fuelled molecular machine made of DNA", Nature **406**, 6796 (2000).

[66] Zhan, C., B. Li, L. Hu, X. Wei, L. Feng, W. Fu and W. Lu, "Micelle-based brain-targeted drug delivery enabled by a nicotine acetylcholine receptor ligand", Angewandte Chemie - International Edition **50**, 24 (2011).

[67] Zhang, Z., X. Y. Kong, K. Xiao, G. Xie, Q. Liu, Y. Tian, H. Zhang, J. Ma, L. Wen and L. Jiang, "A Bioinspired Multifunctional Heterogeneous Membrane with Ultrahigh Ionic Rectification and Highly Efficient Selective Ionic Gating", Advanced Materials **28**, 1 (2016).

[68] Zhou, C., Z. Yang and D. Liu, "Reversible regulation of protein binding affinity by a DNA machine", Journal of the American Chemical Society **134**, 3 (2012).

Chapter 3

NANOPORE SENSOR FOR DETECTING OLIGONUCLEOTIDES ACROSS LIPID MEMBRANES

3.1 Abstract

Transmembrane signal transduction via membrane proteins like ion channels and GPCRs are important for cellular interaction with the environment. Multiple bio inspired ion channels have been reported but signal transduction systems like GPCRs are lacking. Such systems would be employable as sensors of biomarkers like micro RNAs present within membrane bound structures like cells or extracellular vesicles. DNA nanotechnology is a great tool that can be used to build biomimetic nanostructures. In previous chapter, we demonstrated a DNA nanopore that can insert into a lipid layer and interact with the internal contents of the membrane. In this work we use this property of the nanopore to design and build a sensor that can detect targets inside a membrane enclosed space and transmit this to the outside keeping the membrane intact. The sensor is then employed to detect cancer marker miRNA-21 enclosed within a giant unilamellar vesicle. The sensor does not require any amplification step and therefore has the ability to provide faster diagnosis.

3.2 Introduction

Communication is essential for all living things, and cells are no exception. As cells do not live in isolation, communication between other cells, with the environment and internally within itself is nuanced and intricate. It is also important in detecting changes in temperature or pH, nutrient availability or variations in light levels to carry out essential activities. Since cells are mostly compartmentalized by membranes from the environment and within itself, signal transduction through the membrane is a

major focus of cell communication studies. Three important protein types responsible for the cellular communication across membranes are ion channels, G-protein coupled receptors (GPCRs) and Receptor tyrosine kinases (RTK) [6]. Ion channels open or close in response to mechanical or chemical stimuli and this enables the selective passage of ions through the pores. The passage of these ions converts the information into electric signals that can then trigger reactions [12]. GPCRs are also membrane receptors, that transverse the membrane multiple times. These creates loops of amino acid outside the membrane to which specific targets can bind to. On binding of targets, a structural reconfiguration of the protein prompts the relay of the signal to the inside of the cell, thus helping the cell communicate with the environment.

Many attempts to mimic these proteins have been reported. Ion channels made of macromolecules, peptides and DNA have shown transport of ions and even proteins [9]. Transmembrane signaling through RTK mimics have also been made of macromolecules that bind to external chemicals and lead to internal reaction [1]. Several structures using DNA as the building materials, that imitate these membrane proteins have also been build. As described in the previous chapter, DNA nanopores have been successfully designed and used for controlled transport of small molecules to larger proteins into membrane bound vesicles.

While DNA provides structure to these protein mimics, other molecules have to be added to functionalize the system. Molecular beacons using fluorophores and quenchers have been used widely in designing sensors to detect various targets. Fluorescein (FAM) and blackhole quencher (BAM) are an example of a fluorophore-quencher pair that are used in sensors that lead to changes in spatially arrangement of the molecules on binding to the target. Due to this change in arrangement, fluorescence intensity of the fluorophore also changes and this can be detected using fluorescence measurements. Due to the ease of chemical modifications on DNA, flu-

orophores and quenchers have be easily attached to DNA devices [14].

As these DNA nanopores are capable of inserting into membranes while keeping them intact, they are ideal candidates to use as sensing devices of biomarkers that are bound within lipid bi layers. MicroRNAs (miRNAs) fall into the category of biomarkers that are found in membrane enclosed spaces. These are small non coding RNAs of 18 to 25 nucleotides that potentially regulate upto 30% of cellular protein synthesis. They bind to the untranslated region of their target messenger RNAs (mRNAs) to inhibit their expression [16]. They control many important biological processes like cell division, cell differentiation and apoptosis and as a result are over expressed in many cancer cells. This makes them excellent markers for cancer diagnosis. The technology to detect them in their native state will be an excellent tool in cancer detection and treatment.

As shown in the previous chapter, DNA nanopore modified with cholesterol can insert into a lipid membrane to form membrane spanning structures. This can be done by just adding the nanopore exogenously in solution with the lipid membrane bound vesicle. The signal transduction is carried out by extensions from the pore that can bind to target oligonucleotides. The binding of the target leads a structural reconfiguration, mimicking GPCRs and conveys the message through change in fluorescence intensity of the fluorophore dye pairs that are chemically modified on to the DNA extension. The device can be modified for the specific targets it was built to sense while maintaining the same design principles for membrane insertion and signal transduction. We demonstrate the identification of several different targets to optimize the sensing capability of the the nanopore based sensor. Finally we also design and build a sensor to detect microRNA 21 (miR21) which is a cancer bio marker.

3.3 Results

3.3.1 Design and Characterization of Nanopore Based Sensor

We designed a nanopore based sensor (NpS) that can insert into a lipid bi-layer and dynamically reconfigure to relay information from the membrane enclosed space to the outside through fluorescence signalling. In order to improve the signal we have incorporated 5 to 20 sensor units on each nanopore. The lidless nanopore design (LGC) described in chapter 2 was adapted for inserting the sensor into the lipid bi-layer. The 60 cholesterol modifications on the underside of the plate of the nanopore ensured the insertion [13]. In order to modify the nanopore with sensors, extensions of DNA strand were added to the inside of the pore with relatively equal distribution across the area of the inside of the nanopore. The sensor consisted of a stem-loop with the fluorophore FAM and quencher BHQ placed as shown in **Figure 3.1.A**. The sensor also has extensions complementary to the strand extensions on the pore. Two different sensor design were tried out as shown in **Supplementary Figure 38**. Upon binding to the target DNA or RNA strand the sensor opens up to form a double strand. The FAM dye spatially separated from the quencher and as a result its fluorescence intensity increases [14], which can be detected by fluorimeter measurements or confocal imaging.

OxDNA simulations [11] were first performed on the modified nanopore design to ensure that the modifications do not overlap each other,

crowding the pore or cause any structural deformation to the nanopore **Figure 3.1.A**. Agarose gel electrophoresis and AFM imaging showed the formation of the nanopore with sensor modifications. AFM confirmed that the sensor modification of the nanopore does not cause any structural defect. Sensors were added on to the nanopore after the initial annealing and purification of the nanopore with amicon

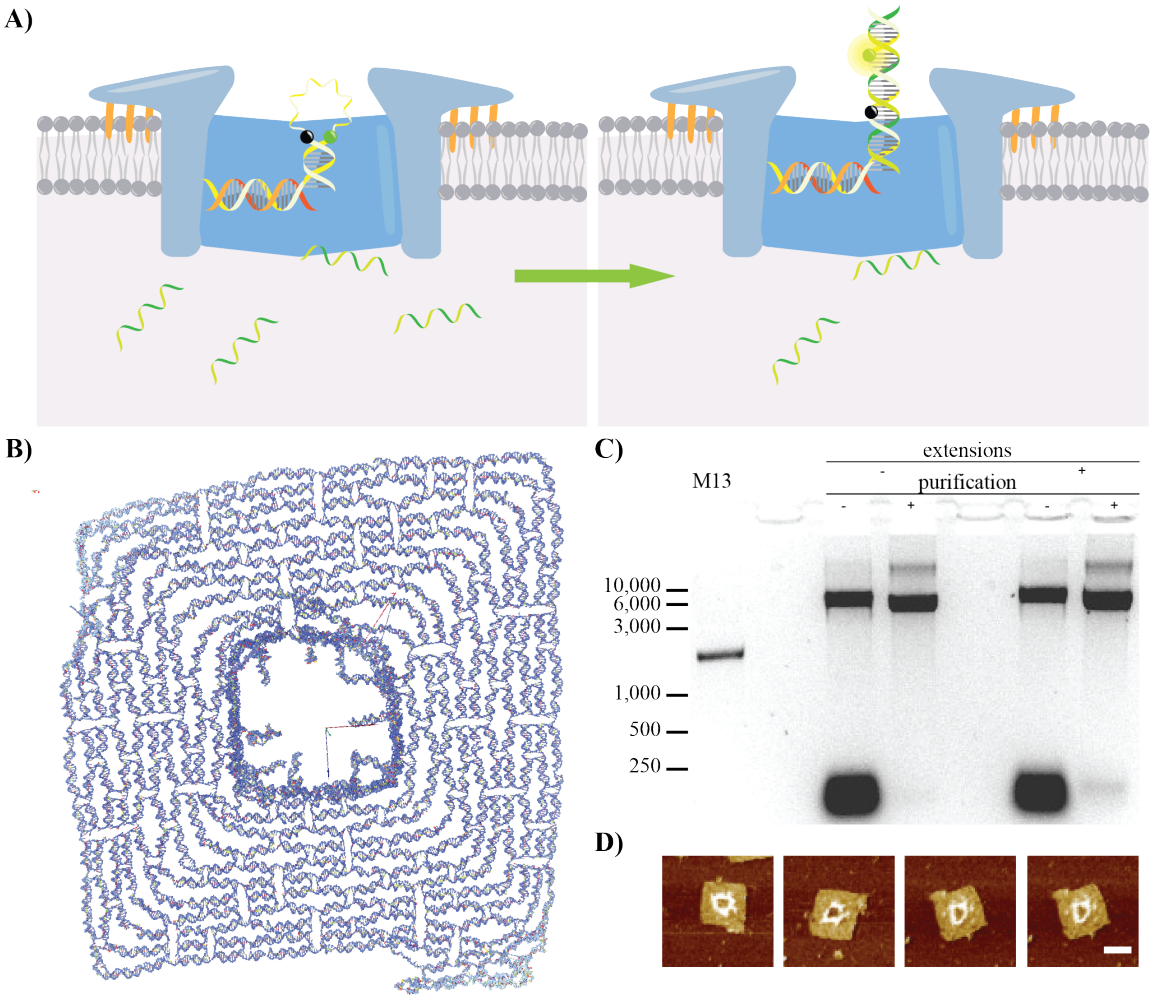

Figure 3.1: (A) Schematic of a rationally designed trans membrane sensor (NpS) for membrane enclosed oligonucleotide detection. (B) OxDNA simulation of NpS with extensions for sensor modification. (C) 1% agarose gel that shows the formation of nanopore with sesnor modifications. (D) Representative AFM images of NpS. Scale bar - 50 nm.

filtration in order to avoid the sensor binding to staple strands.

3.3.2 Optimizing Sensor Design

In order to build a sensor with high efficiency, several parameters were optimized. Since the sensor modifications are on the membrane inserting part of the pore, we tested out nanopores modified with 5, 10, 15 and 20 sensor extensions to ascertain the maximum number of sensors that could be added without hampering the insertion efficiency. The nanopore was modified with cy3 dye to monitor the insertion on confocal microscopy. Nanopores with 5, 10 and 15 sensor extensions show insertion to the membrane as evidenced by the increased fluorescence intensity around the periphery of the GUVs. Nanopore with 20 extensions do not show any significant increase in the fluorescence intensity around the periphery as compared to the background showing that more than 20 or more extensions on the pore might be hampering the insertion efficiency of the nanopore.

3.3.3 Sensitivity and Specificity of the Sensor

The sensitivity of the NpS was tested by incubating the sensor with different concentrations of target sequence in solution. By measuring the fluorescence intensity change we were able to detect target at concentrations as low as 5nM in solution with NpS **(Supplementary Figure 39)**. A library of sequences that have consecutive 4 or 5 nucleotides same as the sensor was build to analyse the specificity of the NpS. These sequences were incubated with the sensor strands at 5 times the concentration of the sensor and using a plate reader the fluorescence intensity of the sensor was measured. For 5 consecutive nucleotides in this assay, it was observed that if sequences

complementary to the stem of the sensor motif was present, there was a higher chance of the sensor binding to that sequence and giving false positives. But se-

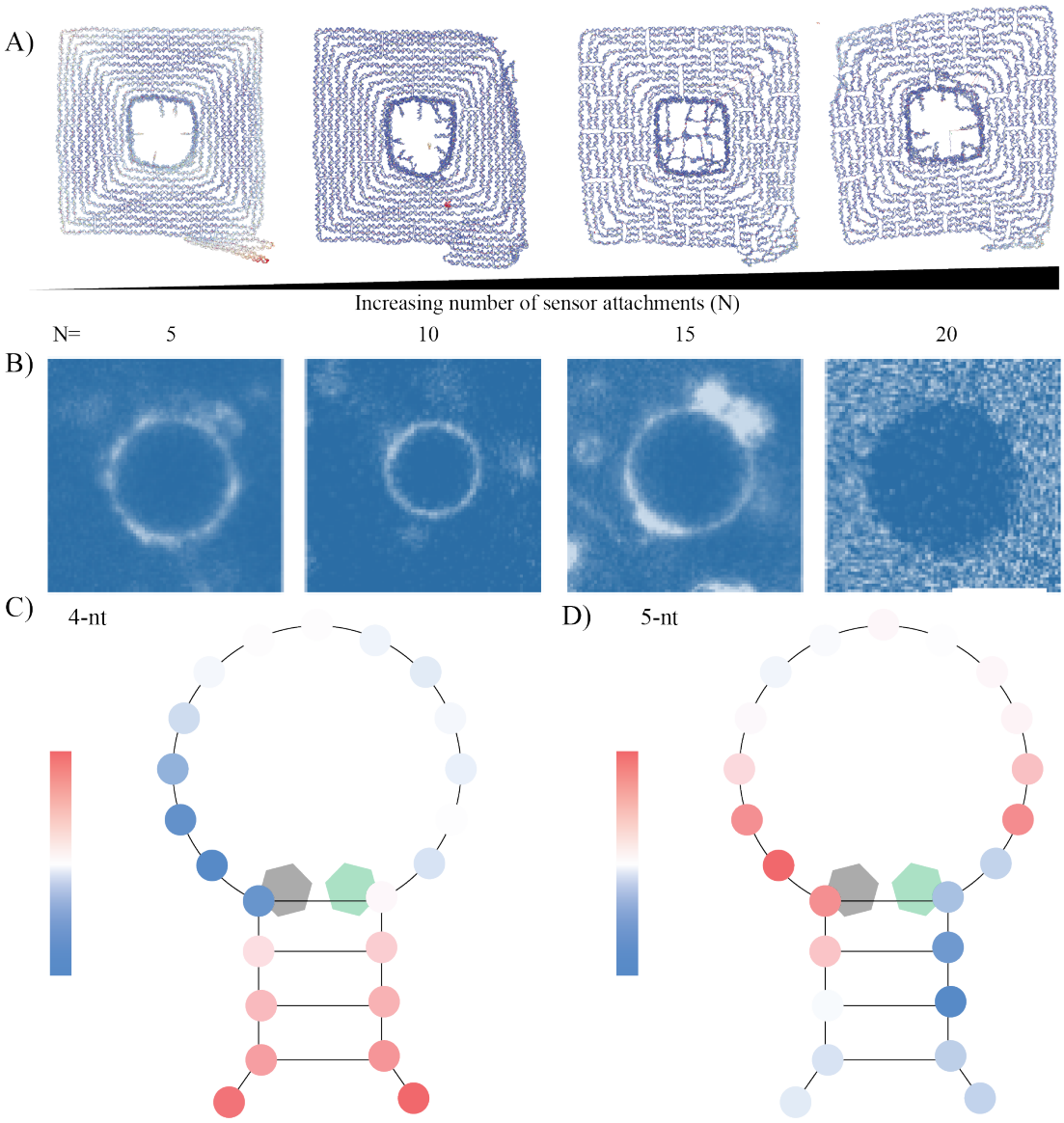

Figure 3.2: (A) OxDNA simulation of NpS with different number of sensors (n= 5, 10, 15, 20). (B) Representative images of GUVs showing insertion of NpS with different number of sensors. Scale bar - 5 μm. (C) and (D) Representation of how the sequence affects the sensitivity of detection based on its position for 4-nt (C) and 5-nt (D).

quences complementary to the loop region are less likely to bind to the sensor. For 4 consecutive nucleotides assay the specificity was more affected by the complementary sequences in the stem part closer the nanopore extension sequence. The loop area is more resistant like in the case of 5 nucleotides. These factors have to be kept in mind while selecting the targets for a particular sensor. The sensor should also be designed to avoid false positives.

Since a no lid version of the nanopore was used we needed to make sure that the pore formed by the nanopore do not lead to the leakage of the contents of the membrane bound vesicle. To study this we used confocal microscopy assay where GUVs encapsulated with fluorophore labelled oligonucleotide sequences of various lengths were incubated with NpS. It was observed that a 20-mer poly A strand was not able to move out the nanopore with sensor modifications even after 3 hrs at 37°C. But shorter DNA strand, an 8-mer leaked out the NpS after 3 hrs at 37°C.

3.3.4 Sensing of Membrane Bound Oligonucleotides

As the NpS is modified with the sensor strands after purification of the annealed nanopore structure, different folds of sensor concentration was added to the nanopore to identify the optimum concentration. To test out the NpS' ability to sense the target steady state fluorescence measurements with the target in solution were performed. The steady state fluorescence spectra shows an increase in fluorescence intensity when both the cholesterol modified and unmodified NpS interacts with the target due to the spatial separation of the fluorophore from the quencher **(Figure 3.B.)** as desired. The increase in fluorescence intensity is greater in the cholesterol modified NpS which could be due to hydrophobic interaction between the fluorophore and the cholesterol molecule [8]. The trend is same in the three different concentration of sensors incubated with NpS.

To test the insertion of the NpS into the lipid membrane and detection of the enclosed oligonucleotides, we used a model membrane system. Giant unilamellar vesicles are excellent model systems for studying pore interactions with membranes [**?**].

The target DNA (key) was encapsulated within the GUVs and this was mixed with cholesterol modified NpS, maintaining the osmolarity of the solution. Since the GUVs can break due to changes in osmotic pressure, releasing the targets into solution, the complementary strand of the key strand was added in excess to prevent false positives. Fluorescence spectra of the sensor with the key shows an increase in intensity in comparison to scramble DNA sequence which indicates that the cholesterol modified NpS is able to successfully insert into the membrane and bind to the key **(Figure 3.3.C)**. Negative control experiments where NpS without cholesterol modification and NpS with cholesterol modification incubated with scramble sequence enclosed in GUV showed less increase in fluorescence intensity. This ascertains that only NpS with cholesterol modification can insert into a membrane and specifically indicate the presence of the key sequence through change in fluorescence intensity. To further validate this claim we also performed confocal microscopy assays. When cholesterol modified NpS is incubated with key filled GUVs the membrane becomes brighter than the surrounding **(Figure3.3.D)**, indicating that the NpS was able to insert into the membrane and bind to the key sequence. Negative control experiments with Nps without cholesterol incubated with scramble and key and Nps with cholesterol modification incubated with scramble did not lead to increased fluorescence intensity around the membrane **(Figure 3.3.D)**, confirming that the NpS sensor is specific for target sequences enclosed in a membrane.

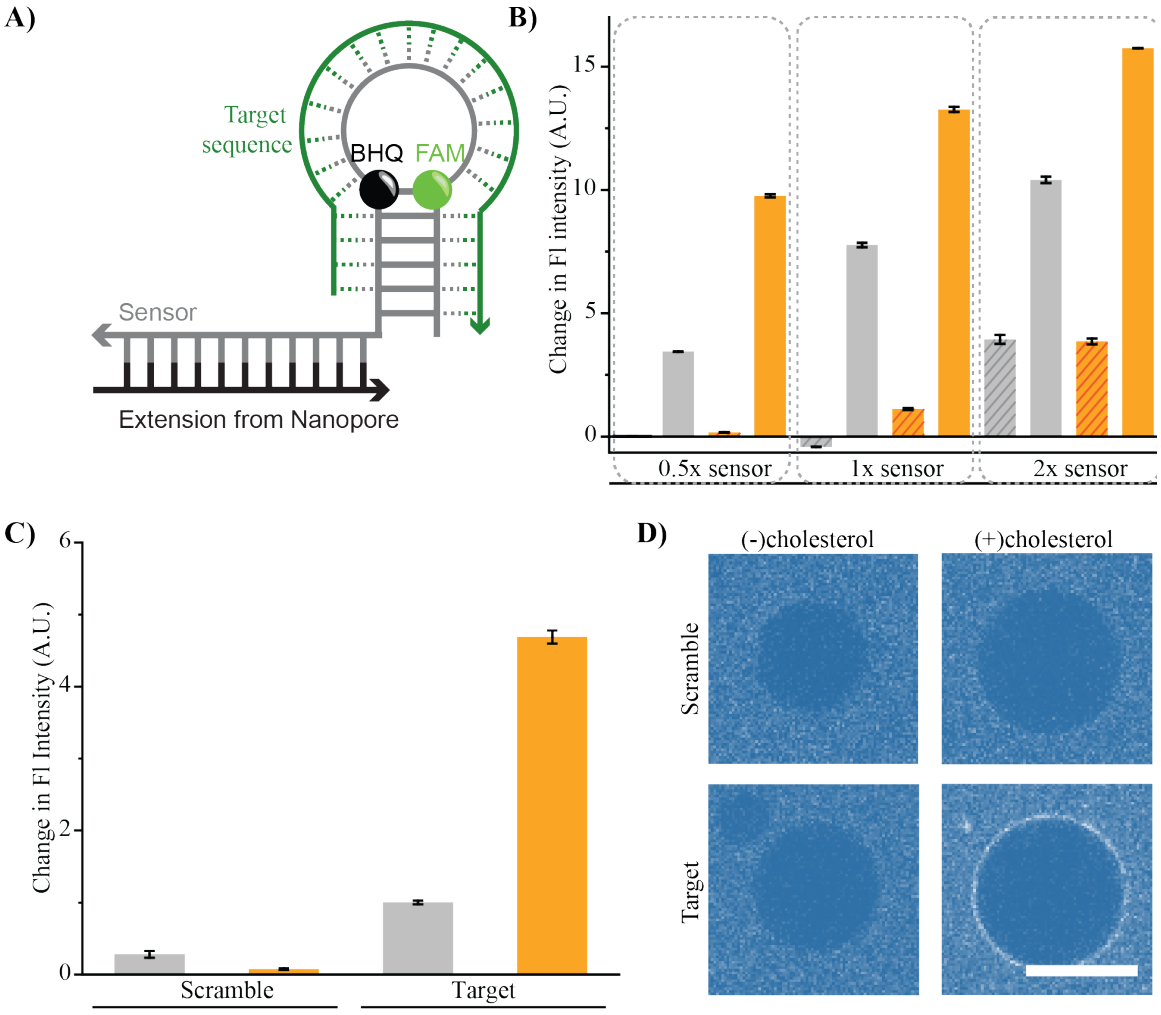

Figure 3.3: (A) Schematic of the design of the sensor that the target binds to. (B) Bar plot showing the change in fluorescence intensity of NpS when incubated with different oligonucleotide sequences in solution. Orange bars correspond to cholesterol modified NpS and grey bars correspond to non cholesterol modified NpS. The lined bars correspond to scrambled sequence and non lined bars correspond to target sequence. (C) Bar plot showing the change in fluorescence intensity of the NpS when incubated with GUVs containing different oligonucleotide sequences. Orange bar corresponds to cholesterol modified NpS and grey bars correspond to non cholesterol modified NpS. (D) Representative images of GUVs incubated with NpS with and without cholesterol. Scale bar- 10μm

3.3.5 Sensing Cancer Specific MicroRNA

Cancer specific micro RNAs (miRNAs) are fast becoming leading biomarkers. Recent research has shown that many of these have been identified in extracellular vesiciles like exosomes, microvesicles or apoptotic bodies. Since these structures are made of lipid based membranes, our NpS is an ideal candidate to sense their contents. In this study we used miRNA-21 as a target miRNA as it has been found to be biomarker for non-small lung cancer (NSCLC) [15]. Kinetic fluorescence measurements show that the NpS specific to the miRNA-21 is able to detect the RNA and DNA analog in solution within 10 mins **(Figure 3.4.2.)**. The rate constant for the sensor binding to the DNA and RNA were calculated by fitting the following equation to the kinetics graph.

$$I_t = I_\infty - (I_\infty - I_o).\frac{(n-1)}{n.exp[ln(n) + kt(n-1)[T]_o] - 1}$$

Where, I_t, I_o and I_∞ are normalized fluorescence intensities at time t, 0 and ∞ respectively, n is fold of excess target strand added, k is the rate of the reaction and $[T]_o$ is the starting sensor concentration.

DNA molecules bind to the sensor faster (k_{on} = 14402.06 $M^{-1}sec^{-1}$) than RNA (k_{on} = 8308.89 $M^{-1}sec^{-1}$). This could be due to lesser unpaired nucleotide in the RNA due to wobble base pairing. Steady state fluorescence measurements showed that when the cholesterol modified NpS (for miRNA-21) was incubated with the target miRNA-21, there is more than 2x increase in fluorescence than in case of unmodified NpS **(Figure 3.4.C.)**. Negative control experiments with NpS with and without cholesterol incubated with GUV enclosing scramble sequence also show minimal increase in fluorescence measurements.

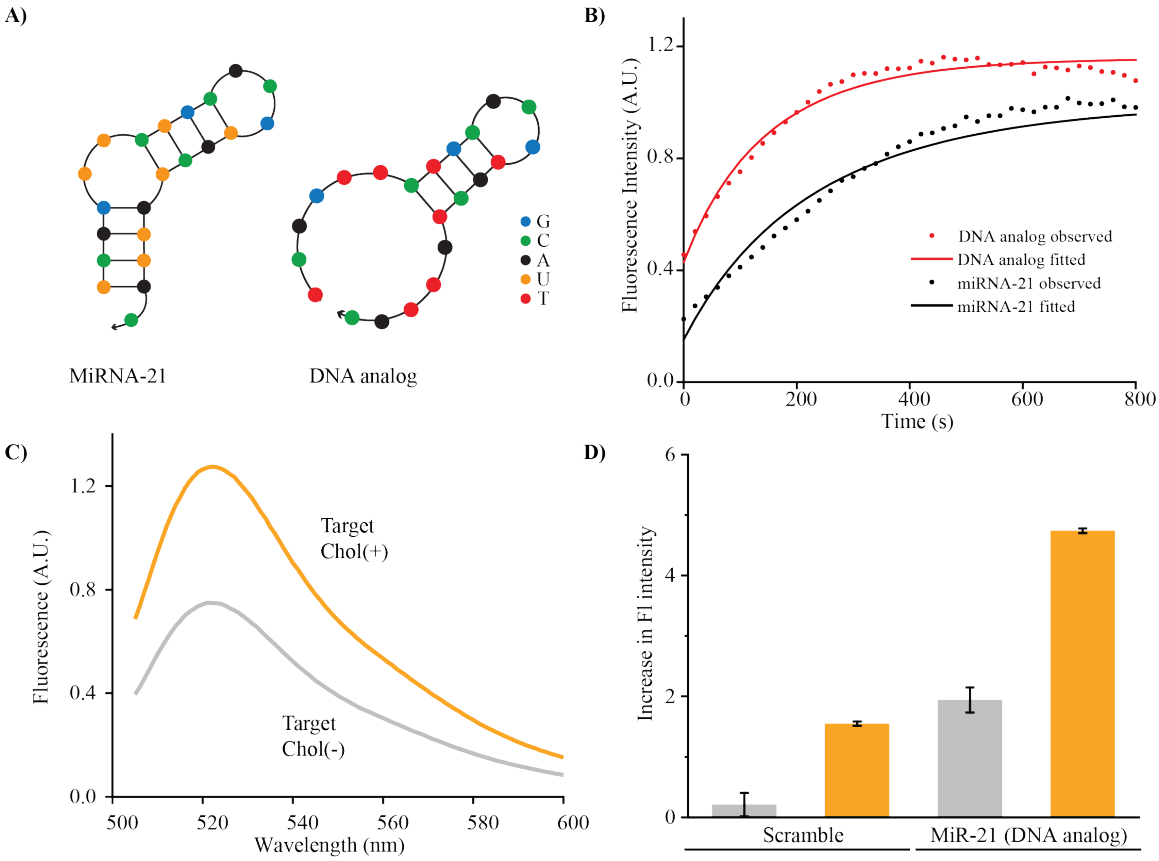

Figure 3.4: (A) Secondary structures of the target miRNA-21 and its DNA analog. (B) Kinetic fluorescence measurements of NpS incubated with miRNA-21 aand its DNA analog. (C) Steady state fluorescence measurements of NpS with and without cholesterol incubated with miRNA-21. (D) Bar plot showing the change in fluorescence intesity of the NpS when incubated with GUVs contianing different oligonucleotide sequences. Orange bar corresponds to cholesterol modified NpS and grey bars correspond to non cholesterol modified NpS.

3.4 Discussion

We have successfully developed a nanomechanical device with DNA that was inspired by nature. We mimicked trans membrane proteins like GPCR that can transduce signal from the inside of the cell to the outside. Many different bio-mimetic machines have been build to date with DNA nanotechnology like ion channels, scramblers, motors, etc. [2, 3] but a DNA based system that can detect oligonucleotides in its native environment have not been reported. The well established design principles

and addresability of DNA nanostructures has enabled the development of a nanosensor that can insert into the membrane. The ease of design and synthesis of the NpS will also facilitate its use by professionals not specialised in DNA nanotechnology as well. Although we have not shown any real time application of the system, the transition from model systems like GUVs to cells is possible as DNA nanostructures that can insert into a cell membrane has already been reported [7]. However there are a few challenges that needs to be addressed before the NpS can be widely adopted. DNA can be damaged in physiological conditions due to the presence of DNAses, though this can be solved by various techniques that can make DNA immune to enzyme activity like UV cross linking [5], PEGylation [4], oligolysine coating [10], etc.

We envision that the device has the potential to be a diagnostic tool in early detection of cancer and other diseases that have oligonucleotide based biomarkers. Since a nanopore also provides a channel to transport molecule or proteins into a membrane bound vesicle we predict that the structure can act as a platform to combine therapeutic intervention in addition to its diagnostic capacity. Again, due to the ease of functionalization of DNA structures, we imagine that a combination of sensors can be easily added to the nanopore to simultaneously detect various targets for multiplexed detection to enhance the precision and efficiency of diagnosis. In conclusion, we have developed a promising new technology that brings together DNA nanotechnology, disease diagnosis and therapeutics.

3.5 Materials and Methods

3.5.1 Sensor Design and Assembly

The nanopore with sensor attached to it was designed using the Tiamat software de novo. Target specificity and binding of the sensors were ensured using the NUPACK

software package. The nanopore was assembled as mentioned in section 2.1. After the structure was purified and quantified, the sensor strand was attached by incubating the structure with 10x folds of sensor at 37°C for 12 hrs.

3.5.2 Measuring Change in Fluorescence on Target Binding

To detect the change in fluorescence intensity of the sensor on identifying the target, 10nM sensor was incubated with the target oligonucleotide enclosed in lipid membrane (GUVs) at 37°C for 3 hrs. The fluorescence was measured using a Nanolog fluorometer (Horiba Jobin Yvon) with a 1 cm path length quartz cell (Hellma). The fluorescence intensity at 520nm was used to calculate the change in fluorescence intensity.

3.5.3 Assessment of the Orthogonality of the Sensor to the Target Sequence

A library of sequences were created that contained consecutive 4 or 5 nucleotides same as the target. The sensor strand was then incubated with all the sequences in the library and the change in the fluorescence intensity was measured using the SynergyNeo2 Biotek microplate reader at 487 nm excitation and 528 nm emission from the bottom of the plate for 3 hours. The change in intensities for each nucleotide was averaged for all the sequences that contained that particular nucleotide and the value was normalized with the fluorescence intensity of the target sequence. A color gradient was applied to the values from blue to red, blue being the least change in intensity and red being the highest.

3.5.4 Confocal Imaging

For the confocal assay, samples were prepared as following. 3μL of GUV (enclosing target) solution was mixed with 20nM nanopore. The total solution was made up to

30μL by maintaining the osmolality balance of the inside and outside of the GUVs using a buffer containing 1M HEPES and 100 mM NaCl. This solution was added to an ibidi μ-Slide 18 Well – flat slide. The slide was then centrifuged at 1000 $\times$g for 10 mins to make sure that the GUVs are settled at the bottom of the slide. Then GUVs were then imaged on Nikon C2 Laser Scanning Confocal microscope at 40$\times$ magnification, 1.3 numerical aperture (NA).

3.5.5 Kinetic Measurement of Sensor Binding to Mirna-21 and Its Dna Analog

100 nM of the sensor strand was incubated with 5x concentration of the target in 96 well plate. The fluorescence intensity was measured using the SynergyNeo2 Biotek microplate reader at 487 nm excitation and 528 nm emission from the bottom of the plate for 20 mins.

REFERENCES

[1] Barton, P., C. A. Hunter, T. J. Potter, S. J. Webb and N. H. Williams, "Transmembrane signalling", Angewandte Chemie - International Edition **41**, 20 (2002).

[2] Burns, J. R., A. Seifert, N. Fertig and S. Howorka, "A biomimetic DNA-based channel for the ligand-controlled transport of charged molecular cargo across a biological membrane", Nature Nanotechnology **11**, 2 (2016).

[3] Burns, J. R., E. Stulz and S. Howorka, "Self-assembled DNA nanopores that span lipid bilayers", Nano Letters **13**, 6 (2013).

[4] Chandrasekaran, A. R., "Nuclease resistance of DNA nanostructures", (2021).

[5] Gerling, T., M. Kube, B. Kick and H. Dietz, "Sequence-programmable covalent bonding of designed DNA assemblies", Science Advances **4**, 8 (2018).

[6] Kholodenko, B. N., "Cell-signalling dynamics in time and space", (2006).

[7] Li, X., T. Wang, Y. Sun, C. Li, T. Peng and L. Qiu, "DNA-Based Molecular Engineering of the Cell Membrane", (2022).

[8] Maxfield, F. R. and D. Wüstner, "Analysis of Cholesterol Trafficking with Fluorescent Probes", Methods in Cell Biology **108**, 367–393 (2012).

[9] Muraoka, T., D. Noguchi, R. S. Kasai, K. Sato, R. Sasaki, K. V. Tabata, T. Ekimoto, M. Ikeguchi, K. Kamagata, N. Hoshino, H. Noji, T. Akutagawa, K. Ichimura and K. Kinbara, "A synthetic ion channel with anisotropic ligand response", Nature Communications **11**, 1 (2020).

[10] Ponnuswamy, N., M. M. Bastings, B. Nathwani, J. H. Ryu, L. Y. Chou, M. Vinther, W. A. Li, F. M. Anastassacos, D. J. Mooney and W. M. Shih, "Oligolysine-based coating protects DNA nanostructures from low-salt denaturation and nuclease degradation", Nature Communications **8** (2017).

[11] Poppleton, E., R. Romero, A. Mallya, L. Rovigatti and P. Šulc, "OxDNA.org: A public webserver for coarse-grained simulations of DNA and RNA nanostructures", Nucleic Acids Research **49**, W1 (2021).

[12] Shi, N., S. Ye, A. Alam, L. Chen and Y. Jiang, "Atomic structure of a Na+- and K+-conducting channel", Nature **440**, 7083 (2006).

[13] Thomsen, R. P., M. G. Malle, A. H. Okholm, S. Krishnan, S. S. Bohr, R. S. Sørensen, O. Ries, S. Vogel, F. C. Simmel, N. S. Hatzakis and J. Kjems, "A large size-selective DNA nanopore with sensing applications", Nature Communications **10**, 1 (2019).

[14] Tyagi, S. and F. R. Kramer, "Molecular Beacons: Probes that Fluoresce Upon Hybridization", Nature Biotechnology **14**, 3 (1996).

[15] Zheng, W., J. J. Zhao, Y. Tao, M. Guo, Z. Ya, C. Chen, N. Qin, J. Zheng, J. Luo and L. Xu, "MicroRNA-21: A promising biomarker for the prognosis and diagnosis of non-small cell lung cancer", (2018).

[16] Zhu, W. and B. Xu, "MicroRNA-21 identified as predictor of cancer outcome: A meta-analysis", PLoS ONE **9**, 8 (2014).

Chapter 4

DNA TETRABODY MEDIATED RECRUITMENT OF NK CELLS TO TUMOR MICRO ENVIRONMENT

4.1 Abstract

NK cells, the effector cells of the innate immune system, can target and eliminate the cancer cells that down regulate MHC class I proteins, filling in the gaps in the immunosurveillance of T cells. But due to mutations, tumors find a way to escape NK cell recognition. Using different methods like introducing chimeric antigen receptors, antibodies and other engineered proteins, researchers have armed NK cells to target and eliminate these cancer cells. Although these interventions are effective, they require time taking genetic engineering. This creates a bottleneck in designing higher valent structures that improves the NK cell binding to target cells. In this chapter, we have designed a DNA based tetrabody modified with cholesterol and tumor targeting affibody that recruit NK cells to tumor sites. Various analyses validate that the presence of the DNA tetrabody accelerates the NK cell attack on the target cancer cell by several folds in vitro. With this study we hypothesise that the DNA tetrabody develops a contact zone between the NK cells and the tumor cells lines thus enabling the NK cells to recognize and eliminate the tumor.

4.2 Introduction

NK cells constitute an essential part in the immunosurveillance for aberrant cells like cancer cells. Unlike T cells, they have the ability to recognise and act against tumor cells without prior sensitization [8]. NK cells recognise these transformed cells by the lack of MHC class I receptors on cell surfaces that help them evade T cell surveillance [7]. They also produce immune stimulants like chemokines and cytokines

for modulating adaptive immune response. On activation they release cytotoxic granules containing perforin and granzyme that activate the apoptosis pathways in target cells. By killing circulating tumor cells, NK cells are also prevalent in preventing tumor metastasis [10]. Inspite of being classified under the innate immune system, NK cells have also shown to have adoptive-like long lived nature with respect to infections [3].

Reports from various in vivo and mouse models strongly demonstrate the anti-tumor activity of the NK cells [17]. As a result they are actively being explored as anti-cancer living drugs [14]. Genetic manipulation of the NK cells has been explored to enhance its efficacy in tumor infiltration and elimination. Modifying the NK cells for overexpression of activating ligands like NKGD2 has proven to induce substantially higher cytotoxic effect against several types of tumor cell lines in vitro and in xenograft models [4].

NK cells have also been modified with chimeric antigen receptors (CAR) that helps them to target certain tumor markers like CD-19 on acute lymphoblastic leukemia cells [6]. But genetically modified NK cells need to be irradiated with UV in order to prevent in vivo expansion to prevent tumor formation thus reduings the number of circulating CAR-NK cells as time progresses.

Another strategy that involves NK cell therapy is antibody dependent cell mediated cytotoxicity (ADCC). In this therapy, specific antibodies bind to the effector cells to target cancer cell, which leads to its lysis [9]. There are also engineered antibody like systems like bispecific killer engagers (BiKEs) and trispecific killer engagers (TriKEs) that augment the activity and specificity of NK cells [12]. These systems have been used in clinical trials, but due to side effects like cytokine release syndrome and nonspecific immune activation further progression remains stalled [1]. Further, the design and synthesis of these products are time consuming and developing en-

gagers specific to certain cancers might not be feasible.

As NK cells already have the mechanism to differentiate between normal and cancer cells, bringing them in close contact can activate the NK cell against the cancer. This requires a system that can bind to both the NK cells and the target cells. DNA nanotechnology provides an easy solution to this. DNA can be used to build various structures and can also be easily modified with other molecules like proteins or peptides to functionalize the system. DNA nanostructures also provide the possibility to increase the valency of the system with ease as the design principles are well established and time effective. In literature, tumor targeting moieties like antibodies [11], affibodies [5], aptamers [13] and peptides are abundantly available and these molecules can easily be conjugated to DNA using simple chemistry.

Specific recruitment of NK cells to Her2 expressing cancer cell by simultaneous binding of a nanostructure to NK cell surface and cancer cell marker can induce effects similar to ADCC. High specificity of Her2 affibody to Her2 can inhibit off target NK cell recruitment as well. Here we demonstrate the use of DNA nanostructure that was modified with cholesterol and Her2 affibody (DNA tetrabody) to recruit NK cells to tumor cells. The presence of the tetrabody accelerates the NK cell attack on the Her2 positive cell lines in vitro.

4.3 Results

4.3.1 Design and Characterisation of DNA Tetrabody

We designed a 4 arm junction DNA nanostructure, DNA tetrabody (D-TB-F) to act as mediator between immune cells (NK cells) and cancer cells **(Figre 4.1 A)**. The four arm DNA tile (D-TB) was designed using the Tiamat software keeping the design rules of DNA tiles. Using OxDNA simulation, the mean structure of the D-TB was

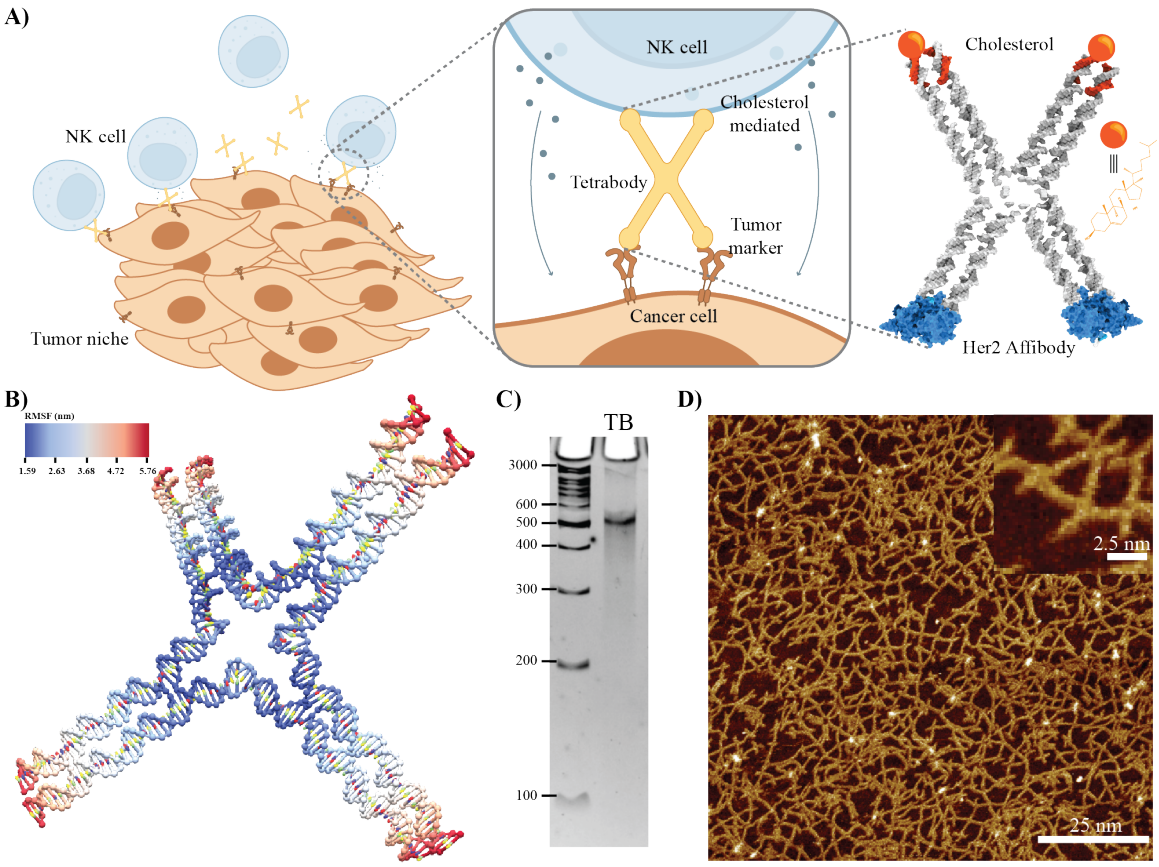

Figure 4.1: (A) Schematic of DNA tetrabody that can recruit NK cell to cancer cells. (B) RMSF of OxDNA simulation of the DNA tetrabody.(C) 5% Native PAGE gel that shows the formation of DNA tetrabody. (D) AFM image of the DNA tetrabody.

observed to take up the desired configuration **()Figure 4.1 B**. Effective formation of the D-TB was first characterized by gel electrophoresis as shown in **Figure 4.1 C**. Imaging the D-TB using atomic force microscopy (AFM) further confirm the formation of the structure. In the AFM it was also observed that due to non specific interaction the D-TB tend to form higher order structures instead of individual four arm tiles **(Figure 4.1 D)**.

For immunotherapeutics NK cells are purified out of blood plasma and expanded in vivo. Due to this the NK cell surface can be decorated with DNA structure in vivo. This takes away the requirement for specificity. NK-92 cell line taken from a

patient with non-Hodgkin lymphoma was reported to have similar cytotoxicity like primary NK cells [15]. As a result we chose this cell line as the model for NK cells. For NK cells to interact with the D-TB, it was modified with cholesterol **(Figure 4.2. A)**. Cholesterol being hydrophobic in nature is able to insert into the lipid membrane of cells. In order to do that, a cholesterol modified strand was annealed with the D-TB. The formation of the D-TB with the cholesterol was confirmed by gel electrophoresis **(Figure 4.2. B)**. The structure was aggregated due to the cholesterol forming aggregates in water.

This was further established by AFM which shows the D-TB-cholesterol structure formed but aggregated as shown in **Figure 4.2. C**. The aggregation does not hamper the D-TB-cholesterol insertion into the lipid membrane of the NK cells as seen in later experiments. The D-TB-cholesterol can modify the cell membrane which was confirmed by confocal microscopy. D-TB-cholesterol was modified with Atto 647 fluorophore and incubated with NK-92 cells for 20 min at 37°C. The NK-92 cell membrane showed strong Atto 647 signal when it was incubated with D-TB-cholesterol. When incubated with D-TB without cholesterol there was no increased fluorescence around the membrane showing that the cholesterol is necessary for the D-TB to interact with the cell membrane. These results are depicted in **Figure 4.2. C**.

4.3.2 Expression of Her2 Affibody and Conjugation to DNA

To demonstrate the ability of D-TB-F to recruit immune cells to cancer lines we chose SKBR3 as the model cancer system. SKBR3 is a Her2 positive cell line. In order for the D-TB to interact with SKBR3 we chose Her2 affibody a small protein that binds to Her2 **Figure 4.3. C**. An additional cysteine was added to the Her2 affibody to conjugate it DNA. Through a bifunctional linker, sulfosuccinimidyl-4-(N-maleimidomethyl)cyclohexane-1-carboxylate (Sulfo-SMCC), the Her2 affibody was

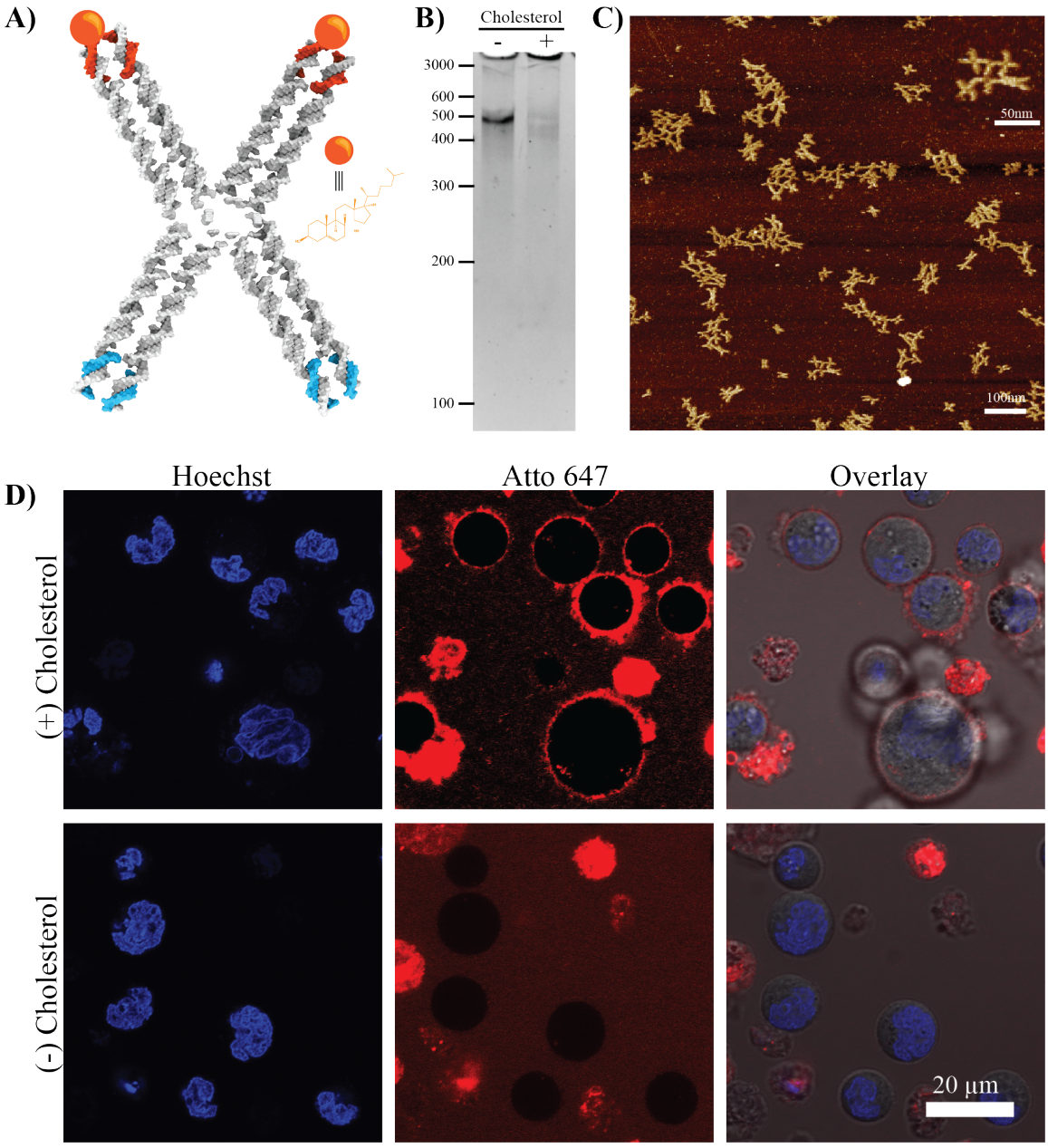

Figure 4.2: (A) Schematic of DNA tetrabody modified with a cholesterol molecule. (B) 5% Native PAGe gel showing the DNA tetrabody in the first lane and the cholesterol modified DNA tetrabody in the second lane (C) AFM image of DNA tetrabody with cholesterol molecules attached to it. The inset shows a magnified view of the same. (D) Confocal laser scanning fluorescence microscopy (CLSM) images of NK cells incubated with DNA tetrabody with and without cholesterol modification. Red shows DNA tetrabody and blue is the Hoechst stain for the nuclei.

conjugated to an amine modified DNA as depicted in **Figure 4.3. A**. This was confirmed using an SDS PAGE gel which shows a slower migrating band corresponding to DNA modified Her2 affibody than the Her2 affibody band **(Figure 4.3. B)**. On annealing with the D-TB, the Her2 affibody DNA conjugate breaks up some of the non specific higher order structure formed by the D-TB which can be seen in the faster migrating band in gel electrophoresis **(Figure 4.3. D)** and broken up higher order structures in AFM **(Figure 4.3. E)**.

To confirm that D-TB with Her2 affibody selectively binds to Her2 positive cells, SKBR3 cells were incubated with D-TB modified with Her2 affibody and fluorophore (Atto 647) and D-TB with just the fluorophore. The cells incubated with D-TB-Her2 affibody showed intense fluorescence around the membrane of the cells and the cells incubated with just D-TB does not, confirming that the Her2 affibody helps D-TB to selectively bind to Her2 positive cells **(Figure 4.3. F)**.

4.3.3 DNA-TB for Recruiting Nk Cell to Cancer Cells

To determine the effect of D-TB-F on the NK cell activation in presence of cancer cells, several assays were performed. D-TB with both cholesterol and Her2 affibody (D-TB-F) was used for this. The experiments were carried out as described in the methods section. Firstly CLSm images were taken to visualize the effect of D-TB-F decorated NK cells on target cells. The NK cells armed with D-TB-F was incubated with SKBR3 cells for different time periods (15 mins, 30 mins and 60 mins). To differentiate between the two cells, the NK cells were marked with green cell tracker dyes. In all three cases NK cells with D-TB-F showed higher interaction with the SKBR3 cells when compared to cells with no D-TB-F as seen in **Figure 4.4**. In 15 mins there was a higher density of NK cells on the SKBR3 cells when modified with D-TB-F and in 60 mins these samples show greater morphological changes to

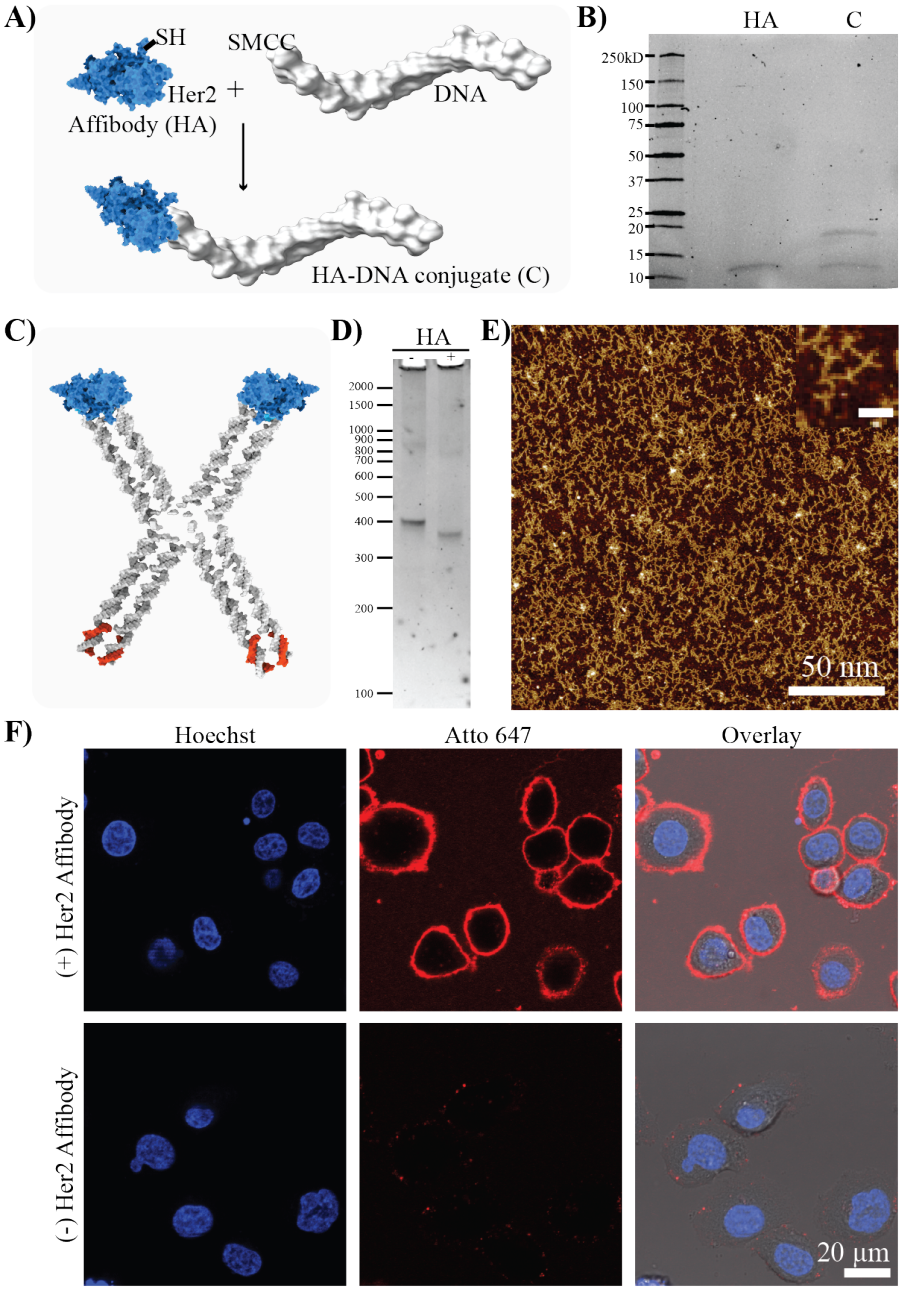

Figure 4.3: (A) Schematic of conjugation of Her2 affibody to DNA strand through SMCC linker. (B) SDS PAGE gel showing the change in migration distance of DNA conjugated Her2 affibody protein,C when compared to native Her2affibody, HA. (C) Schematic of D-TB modified with Her2 affibody protein. (D) 5% Native PAGE gel showing the change in migration of D-TB modified with Her2 affibody when compared to D-TB. (E) AFM image of DNA tetrabody with Her2 affibody attached to it. The inset shows a magnified view of the same. (F) CLSM images of D-TB with Her2 affibody incubated with SKBR3 (Her2 (+) cell line) and MCF7 (Her2(-) cell line). Red shows DNA tertabody and blue is the Hoechst stain for the nuclei.

the SKBR3 cells showing cell death. At 60 min the NK cells also show morphological changes indicating exhaustion of the immune cells. As seen in the **Figure 4.5. A**., there is a 66.3%, 124.2% and 158.3% increase in the amount of NK cells around cancer cells at 15 min, 30 min and 60 min respectively in case of NK cells armed with D-TB-F when compared to NK cells without D-TB-F.

To perform RT-qPCR and flow cytometric evaluation, NK cells modified with D-Tb-F were collected after 1 hour incubation with SKBR3 cells. After RNA extraction and cDNA preparation, RT-qPCR was performed on the samples to identify the relative expression of activation marker, tumor necrosis factor (TNFRSF92) and NK cell affector proteins peforin and granzyme B in the NK cells. As a positive control, known NK cell activators, PMA and Ionomycin were used to ctivate teh NK cells. TNFRSF9 or CD137 is a transmembrane receptor expressed on immune cell surface on activation and it is involved in immune regulation [16]. Perforin and grazyme B are the effector molecule of NK cell cytotoxicity. These are secreted by NK cells on activation against target cells [2]. These three proteins are therefore a good indicator of NK cell activation. On analysis it was found the TNFRSF9 expression in NK cells with D-TB-F increases around 6 folds in the presence of SKBR3 cells when compared to the NK cells without D-TB-F. There is also an increase in the expression levels of the effectors perforin and grazyme B, the increase being 22 and 6.7 times that of the negative control respectively **(Figure 4.5. B)**.

Flowcytometric evaluations to assess the cell death caused by NK cells were also performed. SKBR3 cells were collected to determine the number of cells undergoing apoptosis. Annexin V dye was used to mark cells undergoing apoptosis and propidium iodide was used to stain dead cells. Results show increase in the number of cells showing early apoptosis in the case of cells incubated with NK cells modified with D-TB-F. The percentage of cells undergoing apoptosis was 12.3, 19.9 and 19.2 for

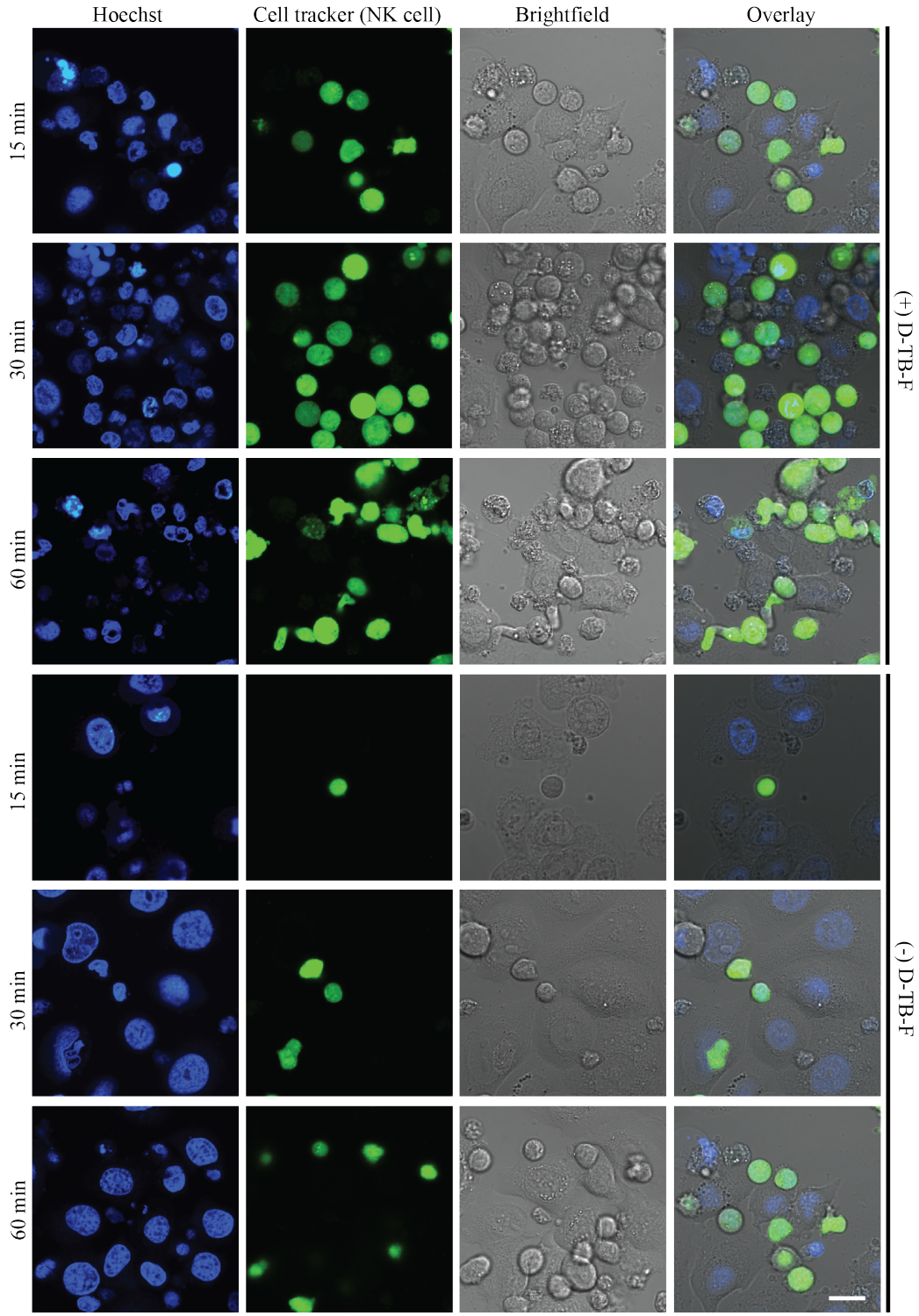

Figure 4.4: CLSM analysis of D-TB-F mediated NK cell recruitment to cancer cells. Blue color shows Hoechst stain staining the nuclei and the green shows the NK cells. Scale bar - 20 μm.

samples without D-TB-F, with D-TB-F and those incubated with PMA/Ionomycin respectively **(Figure 4.5. C)**. As the percentage of cancer cells undergoing apoptosis in the sample with

NK cells with D-TB-F are comparable to that of the positive control, we can conclude that the D-TB-F are aiding the NK cells in activation against the cancer cells. Negative controls with D-TB (without cholesterol and Her2 affibody) showed lower percentage of cells undergoing apoptosis showing that the NK cell activation is not due to just the presence of DNA **(Supplementary Figure 40)**. We also incubated the NK cells with D-TB-F with SKBR3 for different time periods. As the time of incubation increases, the effect also increase, resulting in a bigger fraction of cancer cells undergoing apoptosis **(Figure 4.5. D)**. After 2 and 3 hours of incubation the percentage of cells undergoing early apoptosis went up to 19.5 and 23.7 respectively from 16.2. This indicates that the NK cells are able to maintain the activated state for longer periods of time.

4.4 Discussion

By using a DNA tetrabody conjugated to cholesterol and Her2 targeting affibody we were able to accelerate NK cell targeting of cancer cells. Using different analysis techniques, we showed increased tumor targeting by the NK cell through D-TB-F influenced proximity development. The density of NK cells surrounding target cells increased by about 4 folds in the presence of D-TB-F. There was also several fold increase in gene expression relating to activation in NK cells and increased percentage of cancer cells undergoing apoptosis when the NK cells were armed with D-TB-F.

Unlike the usual protein based systems, no time consuming genetic engineering techniques were required to build a target specific system. With DNA nanotechnology multivalent structures can also be easily designed and build. In the future, DNA

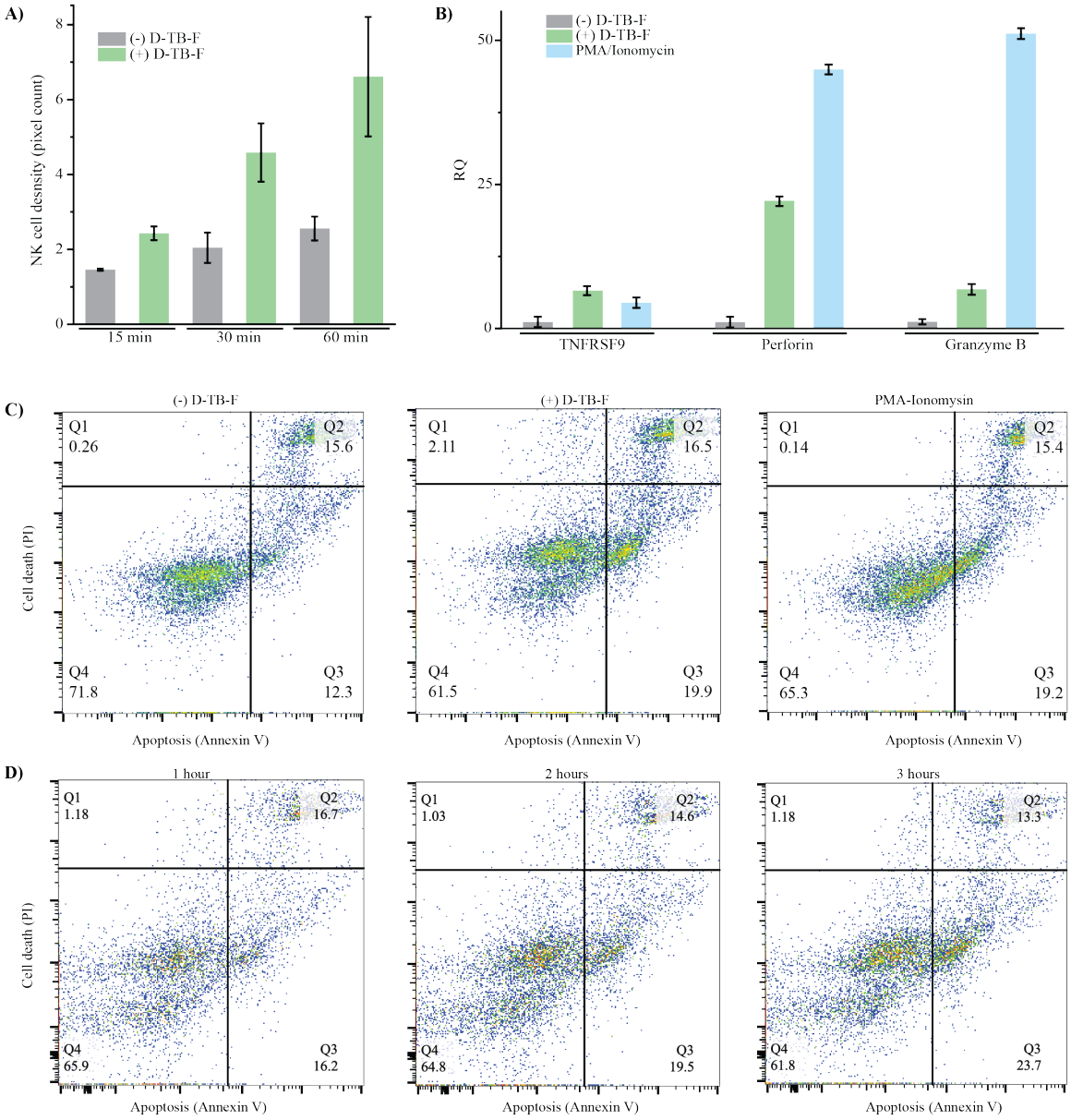

Figure 4.5: (A) Bar plot showing the intensity of cell tracker dye staining the NK cells attached SKBR3 cells after washing away the unattached NK cells. (B) Bar plot showing the gene expression of different NK cell activation markers. (C) Flow cytometry analysis of SKBR3 incubated NK cells with and without D-TB-F. (D) Flow cytometry analysis of SKBR3 cells incubated with NK cells with D-TB-F at different time points of incubation.

structures that can have multiple targets on the same structure can be developed. This will help to modulate the tumor microenvironment by bringing together different types of immune cells at the location. The increased multi valency can also lead to stronger interaction and therefore greater cell death.

4.5 Materials and Methods

4.5.1 Cell Lines and Cell Culture

All cell lines used in this project was obtained from ATCC. The natural killer cell line is NK-92; Her2 positive cell line is SKBR3; Her2 negative cell lines were HEK293T and MCF-7. NK-92 cells were cultured in MyeloCult H5100 (StemCell Technologies cat # 05150) supplemented with 10μg IL-2 (Miltenyi cat # 130-097-744), 63 mL Horse Serum and 1% Penicillin-Streptomycin (Pen-Strep). SKBR3 cells were cultured in Mcoy's Eagle media supplemented with 10% FBS and 1% Pen-Strep.

4.5.2 Her2 Affibody Protein Expression and Purification

Plasmid for the expression of the Her2 affibody (with a cysteine at terminus) was bought from Synbio technologies. DE3* *E.coli* with the plasmid were grown to 0.6 OD and induced with 0.1 mM IPTG. After 3 hours the cells were collected and centrifuged to remove the media and frozen at -80°C overnight. For purification the cell pellet was dissolved in lysis buffer (25mM Tris, 300mM NaCl (pH 8)) and sonicated. It was then centrifuged and the supernatant was collected. The protein was purified by Nickel column (HisTrap HP, cytvia) on AKTA Pure FPLC.

4.5.3 Her2 Affibody Conjugation to DNA(TB4)

DNA with amine modification on teh 3' end was conjugated to sulpho SMCC according to the manufacturer's protocol. The SMCC modified DNA was ethanol precipitated and dried to remove excess sulpho SMCC. The cysteines on the Her2 affibody was reduced using TCEP and excess TCEP was removed by using NAP10 column. The reduced Her2 affibody was then mixed with DNA SMCC and incubated at room temperature overnight. The DNA-protein conjugate was purified using anion exchange chromatography followed by affinity chromatography. The fractions collected were dialysed in PBS to removed excess imidazole and lyophilized overnight.

4.5.4 ULBP6(Az) Protein Expression

Plasmid for the expression of the ULBP6 with azide was bought from Synbio technologies. The P4 on the ULBP6 protein was mutated to the amber stop codon (TAG) for the incorporation of the unnatural amino acid 4-azidophenylalanine. Rossetta stain was co tranformed with the plasmid encoding ULBP6(Az) and the plasmid encoding for expression of aminoacyl-tRNA synthetase. After anhour of growing 1L of the Rossetta *E.coli*, L-arabinose (final concentration 0.2%(w/w)) and 5mL 4-azido phenyalanine (50nM) was added to the culture. At 0.6 OD the culture was induced with 0.1 mM IPTG. The culture was placed at 18°C and after 20 hours the cells were collected and centrifuged to remove the media and frozen at -80°C overnight. For purification the cell pellet was dissolved in lysis buffer (25mM Tris, 300mM NaCl (pH 8)) and sonicated. It was then centrifuged and the supernatant was collected. The protein was purified by Nickel column (HisTrap HP, cytvia) on AKTA Pure FPLC.

4.5.5 ULBP6 Conjugation to DNA

DNA with an amine modification on 3'end was modified with DBCO-sulpho-NHS ester according to manufacturer's protocol. The modified DNA was purified by reverse phase HPLC. The fractions containing the DBCO modified DNA was collected and pooled and lyophilized. MALDI was performed to ensure that the obtained strand is of expected molecular weight. To prepare ULBP6-DNA conjugate, freshly purified ULBP6 and DBCO modified DNA was mixed in the ratio 1:4 with 100mM $MgCl_2$. The reaction mixture was shaken at 4°C overnight.

4.5.6 DNA Tetrabody Design and Assembly

DNA tetrabody was designed on Tiamat software. DNA sequences for the structure are given in Table 4.1. To assemble structure, equimolar concentration of the component strands were mixed together in 1X TAE Mg^{2+} buffer. The structure was annealed in an Eppendorf thermocycler with heating the strands at 90°C for 5 mins and rapidly cooling it to 4°C. For adding the proteins to the structure, after the initial annealing, the protein-DNA conjuagate was incubated with the strands at 36°C for 12 hours. The structure was imaged using AFM as described in previous chapters.

4.5.7 Confocal Imaging of Cells Incubated with Fluorophore Modified D-Tb (Her2affibody/Cholesterol)

Cells were plated at a density of $5x10^4$ cells/ml in 18 well ibidi chambers. SKBR3 cells were plated atleast two days prior to imaging to make sure the all the cells had similar morphology. Before imaging the cells were incubated with D-TB for 15 mins along with Hoechst dye for staining the nuclei. After incubation the cells were washed with 1x DPBS for 3 times. Imaging of cells were performed on Nikon AX R Confocal

microscope at 40x magnification and numerical aperture (NA) 1.3.

4.5.8 Confocal Imaging of NK Cells Incubated With Cancer Cells for Analysing NK Cell Activation

SKBR3 cells were plated on 18 well ibidi chambers at a cell density of $5x10^4$ cells/ml two days prior to imaging. On the day of imaging about 4 times NK-92 cells were incubated with D-TB-F for 20 mins along with 5mM CelTtracker Green CMFDA dye (Invitrogen) to track the NK cells. After this washed NK cells were incubated with plated SKBR3 cells were various time periods. The unattached NK-92 cells were washed to make sure that only NK cells that are in close proximity with SKBR3 cells remains. The cells were incubated with Hoechst to stain the nuclei. Imaging of cells were performed on Nikon AX R Confocal microscope at 40x magnifiation and numerical aperture (NA) 1.3.

4.5.9 RT-qPCR Analysis of NK Cell Activation

Primers used for the RT-qPCR analysis given in the table were purchased from IDT. RNA from NK cells were extracted using the TRIzol reagent (Life corporations) following the instructions from the manufacturer. The RNA was then reverse transcribed to cDNA using the kit Superscript III first-strand synthesis superMix according to the manufacturer's protocol. The cDNA was then used for RT-qPCR analysis using the primers listed and the Sybr green master mix was used. RT-qPCR analysis was performed using ViiA7 Real Time PCR system. Relative expressions were determined by normalizing expression of each C_t value to β - actin C_t value and data were analyzed according to the $2^{-\Delta\Delta C_t}$ formula.

Target	Primer sequence
β -actin	Forward 5'-ACCACACCTTCTACAATGAGC-3' Reverse 5'-GGTCTCAAACATGATCTGGGTC-3'
Tumor necrosis factor (TNFRSF92)	Forward 5'-ACTGCGTTGCTCTTCCTG-3' Reverse 5'-CAGCCATCTTCCTCTTGAGTAG-3'
Perforin	Forward 5'-CAGGGCAGATGCAGACTTTTC-3' Reverse 5'-AAGATAAGCCATGTAGGGGCG-3'
Granzyme B	Forward 5'-GGCCACCTAAAATTCCGCTA-3' Reverse 5'-CAGAAGCATTTGGGGGACAT-3'

Table 4.1: Sequence of primers using in RT-qPCR

4.5.10 Flowcytometric Analysis

Flowcytometric analysis was performed to determine the percentage of cell death of SKBR3 cells on incubation with NK cells. After incubation of the two cell lines together for 1 hr, the NK cells were removed by removing the media and washing the cells two times with 1xDPBS. The SKBR3 cells adhered to the plate was then removed using trypsin. The cells were washed with 1X DPBS three times by centrifuging at 4°C. The cells were then stained with Annexin (apoptosis marker) and propidium iodide (dead cell marker) using the FITC Annexin V Apoptosis Detection Kit with PI from Biolegend. The manufacturer's protocol was followed. For positive control, cells were frozen at -80°C and thawed to ensure that all cells died. The flowcytometry analysis was performed using the Thermofischer Attune NxT cell analyser.

The analysis of the data was performed using the FlowJo software.

REFERENCES

[1] Allen, C., A. M. Zeidan and J. P. Bewersdorf, "Bites, darts, bikes and trikes—are antibody based therapies changing the future treatment of aml?", (2021).

[2] Ambrose, A. R., K. S. Hazime, J. D. Worboys, O. Niembro-Vivanco and D. M. Davis, "Synaptic secretion from human natural killer cells is diverse and includes supramolecular attack particles", Proceedings of the National Academy of Sciences **117**, 38, 23717–23720, URL `https://www.pnas.org/doi/abs/10.1073/pnas.2010274117` (2020).

[3] Cerwenka, A. and L. L. Lanier, "Natural killer cell memory in infection, inflammation and cancer", (2016).

[4] Chang, Y. H., J. Connolly, N. Shimasaki, K. Mimura, K. Kono and D. Campana, "A chimeric receptor with NKG2D specificity enhances natural killer cell activation and killing of tumor cells", Cancer Research **73**, 6 (2013).

[5] Frejd, F. Y. and K. T. Kim, "Affibody molecules as engineered protein drugs", (2017).

[6] Imai, C., S. Iwamoto and D. Campana, "Genetic modification of primary natural killer cells overcomes inhibitory signals and induces specific killing of leukemic cells", Blood **106**, 1 (2005).

[7] Lanier, L. L., "Up on the tightrope: Natural killer cell activation and inhibition", (2008).

[8] Liu, S., V. Galat, Y. Galat4, Y. K. A. Lee, D. Wainwright and J. Wu, "NK cell-based cancer immunotherapy: from basic biology to clinical development", (2021).

[9] Lo Nigro, C., M. Macagno, D. Sangiolo, L. Bertolaccini, M. Aglietta and M. C. Merlano, "NK-mediated antibody-dependent cell-mediated cytotoxicity in solid tumors: biological evidence and clinical perspectives", Annals of Translational Medicine **7**, 5 (2019).

[10] López-Soto, A., S. Gonzalez, M. J. Smyth and L. Galluzzi, "Control of Metastasis by NK Cells", (2017).

[11] Scott, A. M., J. P. Allison and J. D. Wolchok, "Monoclonal antibodies in cancer therapy", Cancer Immunity **12**, 1, 14, URL `https://doi.org/10.1158/1424-9634.DCL-14.12.1` (2012).

[12] Shevtsov, M. and G. Multhoff, "Immunological and translational aspects of NK cell-based antitumor immunotherapies", (2016).

[13] Shigdar, S., B. Schrand, P. H. Giangrande and V. de Franciscis, "Aptamers: Cutting edge of cancer therapies", (2021).

[14] Shimasaki, N., A. Jain and D. Campana, "NK cells for cancer immunotherapy", (2020).

[15] Tam, Y. K., J. A. Martinson, K. Doligosa and H. G. Klingemann, "Ex vivo expansion of the highly cytotoxic human natural killer cell line NK-92 under current good manufacturing practice conditions for clinical adoptive cellular immunotherapy", Cytotherapy **5**, 3 (2003).

[16] Thum, E., S. Zhe and H. Schwarz, "CD137, implications in immunity and potential for therapy", Frontiers in Bioscience **14**, 11 (2009).

[17] Yang, Q., S. R. Goding, M. E. Hokland and P. H. Basse, "Antitumor activity of NK cells", Immunologic Research **36**, 1, 13–25, URL `https://doi.org/10.1385/IR:36:1:13` (2006).

Chapter 5

CONCLUSION

Borrowing ideas from nature to create simple and efficient systems is a story with rich history. Molecular biomimetics has added another chapter to this. With the help of recent developments in science and technology arraying into micro and nanoscale biomimetics has been made possible. Harnessing unique properties of materials like that of DNA we are now able to create programmable nanodevices that help us to go beyond the nature's remit. Although large strides have been made in the field, there is still a rich source to draw inspiration from. In this dissertation I have described novel and varied ways through which we can utilize DNA nanostructures to manipulate the cell membrane with ideas borrowed from the nature.

To start with, we show a large diameter DNA nanopore that can be reversibly gated through a nanomechanical lid that is an homage to protein channels. The nanopore creates a channel of 20.4 nm x20.4 nm wide and shows controllable substrate transport when inserted into a lipid bilayer. The lid on the nanopore is locked by complementary overhangs which can be opened through toehold mediated strand displacement, making the opening specific to a DNA sequence. Through confocal microscopy and current recordings we have demonstrated small molecule and protein transport across the membrane through the gated DNA nanopore. To our knowledge this is the first time a fully reversible gated pore has been demonstrated. We envision that the nanopore used for specific delivery of therapeutic drugs, membrane based diagnostic tools and even for DNA or protein sequencing.

The membrane inserting capability of the DNA nanopore was subsequently used to design a sensor to detect oligonucleotide targets inside a membrane bound vesicle. In the third chapter I have described the Np-S that can insert into a GUV and detect

specific oligonucleotide sequences. Through fluorophore quencher pair, the signal of sequence binding can be detected by fluorescence measurements through fluorimeter reading or confocal fluorescence microscopy. The Np-S can be easily modified to target any oligonucleotide based disease marker. This was demonstrated by designing an Np-S sensor that can detect miRNA21, a cancer marker for non small cell lung cancer (NSCLC). This device does not require any processing of samples and can therefore be used for non destructive diagnosis of different diseases. Yet to employ the device for detecting biomarkers in real patient samples several challenges remain. Actual cell membranes are far more complex than the lipid bilayer of a GUV as a result the insertion mechanism can also vary [**?**]. Another important roadblock is that the formation of excessive number of pores on the cell membrane could lead to its death. These obstacles needs to be addressed and resolved to utilize the NpS for cellular sensing.

In the fourth chapter, I deviate from nanopores and move towards DNA nanodevices for immunotherapeutics. In this chapter I have described a DNA nanodevice that can recruit NK cells, the killer cells of the innate immune system to tumor microenvironment. The DNA device, DNA tetrabody, has cholesterol modifications on two of its four arms and this inserts into the lipid bilayer of the NK cells. On the other two hands the DNA tetrabody is modified with Her2 affibody which can strongly bind to Her2 protein expressed on certain breast cancer cell lines. We have demonstrated through various analysis methods like confocal microscopy, RT-qPCR and flowcytometry that the presence of the DNA tetrabody enables the NK cells to identify the target cells and eliminate them quicker than in the absence of the tetrabody. We believe the tetrabody can also be used in conjugation to standard NK cell therapy to boost NK cell activity in vivo. The next step in this project is to study the efficacy of the tetrabody modified NK cells in mouse model. Since DNA can be easily

degraded inside in the body due to the presence of DNAses, the tetrabody needs to be protected against it before being employed in therapeutic interventions.

5.1 Future Outlook

5.1.1 Light Gated DNA Nanopore

There are several naturally occurring protein pores that are reversibly gated. But it is not easy or straightforward to modify them to respond to novel stimuli like different wavelengths of light. Such systems will have multitude of application in optogentics, artificial light harvesting systems, and site specific drug release. In chapter 2 we described a reversibly opened and closed nanomechanical lid on the DNA nanopore using DNA based locking system. Due to easy chemical modification a variety of functionalities can be easily added to a DNA based nanopore. A DNA lock with azobenzene modification can be controlled by exposing the system to different wavelengths of light. The azobenzene on exposure to UV light can reconfigure which causes the lock strands to open. It will reconfigure back to its initial configuration once exposed to visible light thus closing the lock. As a result light controlled nanopores are a possible next step in this field of research.

5.1.2 Artificial Gap Junction

Cells have the capability to form gap junctions between them with the help of protein clusters of connexins and innexins. These are responsible for different functions like homeostasis, passive ion exchange, regeneration and development ([**?**]). Due to the complex arrangement of cell clusters, it is difficult to study the ion transport through these channels in cell systems. In this scenario, designing a simplified system using DNA nanotechnology will be advantageous in understanding the interaction be-

tween cells through gap junctions and also for creating artificial cellular components to the aim of building artificial cells. DNA nanopore inserted into lipid bilayers could be connected to a nanopore on different vesicles through complementary overhangs. These connections can be made specific and can be reversibly gated through the same design principles like the DNA nanopore described in this dissertation thus paving way to artificial gap junctions.

5.1.3 Detector for Sensing Oligonucleotides Inside Cells

In chapter 4, the Np-S described was employed to detect specific oligonucleotide sequence bound within a lipid membrane vesicle. This provides a prototype of sensor that can be redesigned for creating diagnostic tools for different disease markers that are oligonucleotides like miRNA. Cells and extracellular vesicles have valuable information in terms of oligonucleotides bound within its membrane. The Np-S can be designed to identify these specific markers. On identification these cells are marked with increase fluorescence signals which can be used to sort the cells expressing these markers through FACS. This will help to concentrate the target cells for further analysis.

5.1.4 Multi-valent DNA Nanostructure for Cancer Therapeutics

Through DNA nanotechnology we have demonstrated the ability of a four armed DNA structure to improve the NK cell targeting ability. This opens up a door to several other immunotherapy capabilities of different DNA nanostructures. Multi-valent DNA nanostructures have been explored as a promising platform for immunotherapeutics due to their ability to present multiple copies of antigens or immunostimulatory molecules in a controlled and precise manner. DNA nanostructures can be used as a scaffold to present multiple copies of antigens or epitopes in a highly ordered

and repetitive manner, which can enhance the immunogenicity and efficacy of vaccines. Increasing the number of stimulatory molecules or targeting moeities on the DNA nanostructure can possibly enhance the efficiency of attack on the cancer cells due to improved avidity. Overall, multi-valent DNA nanostructures offer a versatile and customizable platform for immunotherapy with potential applications in vaccine design, immunomodulatory therapy and targeted drug delivery.

REFERENCES

[1] Allen, C., A. M. Zeidan and J. P. Bewersdorf, "Bites, darts, bikes and trikes—are antibody based therapies changing the future treatment of aml?", (2021).

[2] Ambrose, A. R., K. S. Hazime, J. D. Worboys, O. Niembro-Vivanco and D. M. Davis, "Synaptic secretion from human natural killer cells is diverse and includes supramolecular attack particles", Proceedings of the National Academy of Sciences **117**, 38, 23717–23720, URL `https://www.pnas.org/doi/abs/10.1073/pnas.2010274117` (2020).

[3] Andersen, E. S., M. Dong, M. M. Nielsen, K. Jahn, R. Subramani, W. Mamdouh, M. M. Golas, B. Sander, H. Stark, C. L. P. Oliveira, J. S. Pedersen, V. Birkedal, F. Besenbacher, K. V. Gothelf and J. Kjems, "Self-assembly of a nanoscale DNA box with a controllable lid", Nature **459**, 7243, 73–76, URL `http://www.nature.com/articles/nature07971` (2009).

[4] Armstrong, J. K., R. B. Wenby, H. J. Meiselman and T. C. Fisher, "The hydrodynamic radii of macromolecules and their effect on red blood cell aggregation", Biophysical Journal **87**, 6 (2004).

[5] Arulkumaran, N., C. Lanphere, C. Gaupp, J. R. Burns, M. Singer and S. Howorka, "DNA Nanodevices with Selective Immune Cell Interaction and Function", ACS Nano **15**, 3, 4394–4404, URL `https://doi.org/10.1021/acsnano.0c07915` (2021).

[6] Banghart, M., K. Borges, E. Isacoff, D. Trauner and R. H. Kramer, "Light-activated ion channels for remote control of neuronal firing", Nature Neuroscience **7**, 12 (2004).

[7] Barton, P., C. A. Hunter, T. J. Potter, S. J. Webb and N. H. Williams, "Transmembrane signalling", Angewandte Chemie - International Edition **41**, 20 (2002).

[8] Blamires, S. J., P. T. Spicer and P. J. Flanagan, "Spider Silk Biomimetics Programs to Inform the Development of New Wearable Technologies", (2020).

[9] Bull, R. A., T. N. Adikari, J. M. Ferguson, J. M. Hammond, I. Stevanovski, A. G. Beukers, Z. Naing, M. Yeang, A. Verich, H. Gamaarachchi, K. W. Kim, F. Luciani, S. Stelzer-Braid, J. S. Eden, W. D. Rawlinson, S. J. van Hal and I. W. Deveson, "Analytical validity of nanopore sequencing for rapid SARS-CoV-2 genome analysis", Nature Communications **11**, 1 (2020).

[10] Burns, J. R., A. Seifert, N. Fertig and S. Howorka, "A biomimetic DNA-based channel for the ligand-controlled transport of charged molecular cargo across a biological membrane", Nature Nanotechnology **11**, 2 (2016).

[11] Burns, J. R., E. Stulz and S. Howorka, "Self-assembled DNA nanopores that span lipid bilayers", Nano Letters **13**, 6 (2013).

[12] Cao, C., Y. L. Ying, Z. L. Hu, D. F. Liao, H. Tian and Y. T. Long, "Discrimination of oligonucleotides of different lengths with a wild-type aerolysin nanopore", Nature Nanotechnology **11**, 8 (2016).

[13] Cerwenka, A. and L. L. Lanier, "Natural killer cell memory in infection, inflammation and cancer", (2016).

[14] Chandrasekaran, A. R., "Nuclease resistance of DNA nanostructures", (2021).

[15] Chang, Y. H., J. Connolly, N. Shimasaki, K. Mimura, K. Kono and D. Campana, "A chimeric receptor with NKG2D specificity enhances natural killer cell activation and killing of tumor cells", Cancer Research **73**, 6 (2013).

[16] Chen, D., Y. Liu, H. Chen and D. Zhang, "Bio[U+2010]inspired drag reduction surface from sharkskin", Biosurface and Biotribology **4**, 2, 39–45, URL https://onlinelibrary.wiley.com/doi/10.1049/bsbt.2018.0006 (2018).

[17] Chen, Y. J., B. Groves, R. A. Muscat and G. Seelig, "DNA nanotechnology from the test tube to the cell", (2015).

[18] Cherf, G. M., K. R. Lieberman, H. Rashid, C. E. Lam, K. Karplus and M. Akeson, "Automated forward and reverse ratcheting of DNA in a nanopore at 5-Å precision", Nature Biotechnology **30**, 4 (2012).

[19] Chung, K., S. Yu, C. J. Heo, J. W. Shim, S. M. Yang, M. G. Han, H. S. Lee, Y. Jin, S. Y. Lee, N. Park and J. H. Shin, "Flexible, angle-independent, structural color reflectors inspired by morpho butterfly wings", Advanced Materials **24**, 18 (2012).

[20] Da vinci, "Da vinci's flying machine", (????).

[21] Dey, S., C. Fan, K. V. Gothelf, J. Li, C. Lin, L. Liu, N. Liu, M. A. D. Nijenhuis, B. Saccà, F. C. Simmel, H. Yan and P. Zhan, "DNA origami", Nature Reviews Methods Primers **1**, 1, 13, URL https://doi.org/10.1038/s43586-020-00009-8 (2021).

[22] Diederichs, T., G. Pugh, A. Dorey, Y. Xing, J. R. Burns, Q. Hung Nguyen, M. Tornow, R. Tampé and S. Howorka, "Synthetic protein-conductive membrane nanopores built with DNA", Nature Communications **10**, 1 (2019).

[23] Du, Y., Y. Lyu, J. Lin, C. Ma, Q. Zhang, Y. Zhang, L. Qiu and W. Tan, "Membrane-anchored DNA nanojunctions enable closer antigen-presenting cell–T-cell contact in elevated T-cell receptor triggering", Nature Nanotechnology URL https://doi.org/10.1038/s41565-023-01333-2 (2023).

[24] Dunn, K. E., F. Dannenberg, T. E. Ouldridge, M. Kwiatkowska, A. J. Turberfield and J. Bath, "Guiding the folding pathway of DNA origami", Nature **525**, 7567 (2015).

[25] Eroglu, A., M. J. Russo, R. Bieganski, A. Fowler, S. Cheley, H. Bayley and M. Toner, "Intracellular trehalose improves the survival of cryopreserved mammalian cells", Nature Biotechnology **18**, 2 (2000).

[26] Fragasso, A., N. De Franceschi, P. Stömmer, E. O. van der Sluis, H. Dietz and C. Dekker, "Reconstitution of Ultrawide DNA Origami Pores in Liposomes for Transmembrane Transport of Macromolecules", ACS Nano **15**, 8, 12768–12779, URL https://doi.org/10.1021/acsnano.1c01669 (2021).

[27] Frejd, F. Y. and K. T. Kim, "Affibody molecules as engineered protein drugs", (2017).

[28] Fu, T. J. and N. C. Seeman, "DNA double-crossover molecules", Biochemistry **32**, 13, 3211–3220, URL https://doi.org/10.1021/bi00064a003 (1993).

[29] Gajewski, T. F., H. Schreiber and Y. X. Fu, "Innate and adaptive immune cells in the tumor microenvironment", (2013).

[30] Galenkamp, N. S., A. Biesemans and G. Maglia, "Directional conformer exchange in dihydrofolate reductase revealed by single-molecule nanopore recordings", Nature Chemistry **12**, 5 (2020).

[31] Ge, Z., J. Liu, L. Guo, G. Yao, Q. Li, L. Wang, J. Li and C. Fan, "Programming Cell-Cell Communications with Engineered Cell Origami Clusters", Journal of the American Chemical Society **142**, 19 (2020).

[32] Gerling, T., M. Kube, B. Kick and H. Dietz, "Sequence-programmable covalent bonding of designed DNA assemblies", Science Advances **4**, 8 (2018).

[33] Goodchild, J., "Conjugates of Oligonucleotides and Modified Oligonucleotides: A Review of Their Synthesis and Properties", (1990).

[34] Goodenough, D. A. and D. L. Paul, "Gap junctions.", (2009).

[35] Göpfrich, K., C. Y. Li, I. Mames, S. P. Bhamidimarri, M. Ricci, J. Yoo, A. Mames, A. Ohmann, M. Winterhalter, E. Stulz, A. Aksimentiev and U. F. Keyser, "Ion channels made from a single membrane-spanning DNA duplex", Nano Letters **16**, 7 (2016).

[36] Göpfrich, K., C.-Y. Li, M. Ricci, S. P. Bhamidimarri, J. Yoo, B. Gyenes, A. Ohmann, M. Winterhalter, A. Aksimentiev and U. F. Keyser, "Large-Conductance Transmembrane Porin Made from DNA Origami", ACS Nano **10**, 9, 8207–8214, URL `https://doi.org/10.1021/acsnano.6b03759` (2016).

[37] Gtari, W., H. Bey, A. Aschi, L. Bitri and T. Othman, "Impact of macromolecular crowding on structure and properties of pepsin and trypsin", Materials Science and Engineering C **72** (2017).

[38] Guo, Y., B. Wei, S. Xiao, D. Yao, H. Li, H. Xu, T. Song, X. Li and H. Liang, "Recent advances in molecular machines based on toehold-mediated strand displacement reaction", (2017).

[39] Han, C., R. Hao, Y. Fan, M. A. Edwards, H. Gao and B. Zhang, "Observing Transient Bipolar Electrochemical Coupling on Single Nanoparticles Translocating through a Nanopore", Langmuir **35**, 22 (2019).

[40] Harayama, T. and H. Riezman, "Understanding the diversity of membrane lipid composition", (2018).

[41] Hellmeier, J., R. Platzer, A. S. Eklund, T. Schlichthaerle, A. Karner, V. Motsch, M. C. Schneider, E. Kurz, V. Bamieh, M. Brameshuber, J. Preiner, R. Jungmann, H. Stockinger, G. J. Schütz, J. B. Huppa and E. Sevcsik, "DNA origami demonstrate the unique stimulatory power of single pMHCs as T cell antigens", Proceedings of the National Academy of Sciences **118**, 4, URL `https://pnas.org/doi/full/10.1073/pnas.2016857118` (2021).

[42] Hernández-Ainsa, S., N. A. Bell, V. V. Thacker, K. Göpfrich, K. Misiunas, M. E. Fuentes-Perez, F. Moreno-Herrero and U. F. Keyser, "DNA origami nanopores for controlling DNA translocation", ACS Nano **7**, 7 (2013).

[43] Imai, C., S. Iwamoto and D. Campana, "Genetic modification of primary natural killer cells overcomes inhibitory signals and induces specific killing of leukemic cells", Blood **106**, 1 (2005).

[44] Iwabuchi, S., I. Kawamata, S. Murata and S. I. M. Nomura, "A large, square-shaped, DNA origami nanopore with sealing function on a giant vesicle membrane", Chemical Communications **57**, 24 (2021).

[45] Jain, M., S. Koren, K. H. Miga, J. Quick, A. C. Rand, T. A. Sasani, J. R. Tyson, A. D. Beggs, A. T. Dilthey, I. T. Fiddes, S. Malla, H. Marriott, T. Nieto, J. O'Grady, H. E. Olsen, B. S. Pedersen, A. Rhie, H. Richardson, A. R. Quinlan, T. P. Snutch, L. Tee, B. Paten, A. M. Phillippy, J. T. Simpson, N. J. Loman and M. Loose, "Nanopore sequencing and assembly of a human genome with ultra-long reads", Nature Biotechnology **36**, 4 (2018).

[46] Japanese, "Japanese bullet train", (????).

[47] Ke, Y., L. L. Ong, W. M. Shih and P. Yin, "Three-dimensional structures self-assembled from DNA bricks", Science **338**, 6111 (2012).

[48] Kholodenko, B. N., "Cell-signalling dynamics in time and space", (2006).

[49] Kinoshita, S., S. Yoshioka and J. Miyazaki, "Physics of structural colors", Reports on Progress in Physics **71**, 7 (2008).

[50] Krishnan, S., D. Ziegler, V. Arnaut, T. G. Martin, K. Kapsner, K. Henneberg, A. R. Bausch, H. Dietz and F. C. Simmel, "Molecular transport through large-diameter DNA nanopores", Nature Communications **7** (2016).

[51] Kuzyk, A., R. Schreiber, H. Zhang, A. O. Govorov, T. Liedl and N. Liu, "Reconfigurable 3D plasmonic metamolecules", Nature Materials **13**, 9 (2014).

[52] Langecker, M., V. Arnaut, T. G. Martin, J. List, S. Renner, M. Mayer, H. Dietz and F. C. Simmel, "Synthetic lipid membrane channels formed by designed DNA nanostructures", Science **338**, 6109 (2012).

[53] Lanier, L. L., "Up on the tightrope: Natural killer cell activation and inhibition", (2008).

[54] Lanphere, C., P. M. Arnott, S. F. Jones, K. Korlova and S. Howorka, "A Biomimetic DNA-Based Membrane Gate for Protein-Controlled Transport of Cytotoxic Drugs", Angewandte Chemie - International Edition (2020).

[55] Li, S., Q. Jiang, S. Liu, Y. Zhang, Y. Tian, C. Song, J. Wang, Y. Zou, G. J. Anderson, J.-Y. Han, Y. Chang, Y. Liu, C. Zhang, L. Chen, G. Zhou, G. Nie, H. Yan, B. Ding and Y. Zhao, "A DNA nanorobot functions as a cancer therapeutic in response to a molecular trigger in vivo", Nature Biotechnology **36**, 3, 258–264, URL `http://www.nature.com/articles/nbt.4071` (2018).

[56] Li, X., T. Wang, Y. Sun, C. Li, T. Peng and L. Qiu, "DNA-Based Molecular Engineering of the Cell Membrane", (2022).

[57] Lin, C., Y. Ke, Z. Li, J. H. Wang, Y. Liu and H. Yan, "Mirror image DNA nanostructures for chiral supramolecular assemblies", Nano Letters **9**, 1 (2009).

[58] List, J., M. Weber and F. C. Simmel, "Hydrophobic actuation of a DNA origami bilayer structure", Angewandte Chemie - International Edition **53**, 16 (2014).

[59] Liu, M., J. Fu, C. Hejesen, Y. Yang, N. W. Woodbury, K. Gothelf, Y. Liu and H. Yan, "A DNA tweezer-actuated enzyme nanoreactor", Nature Communications **4**, 1, 2127, URL `https://www.nature.com/articles/ncomms3127` (2013).

[60] Liu, M., S. Jiang, O. Loza, N. E. Fahmi, P. Šulc and N. Stephanopoulos, "Rapid Photoactuation of a DNA Nanostructure using an Internal Photocaged Trigger Strand", Angewandte Chemie International Edition **57**, 30, 9341–9345, URL `https://doi.org/10.1002/anie.201804264` (2018).

[61] Liu, S., V. Galat, Y. Galat4, Y. K. A. Lee, D. Wainwright and J. Wu, "NK cell-based cancer immunotherapy: from basic biology to clinical development", (2021).

[62] Liu, W. W. and R. I. Wilson, "Transient and specific inactivation of drosophila neurons in vivo using a native ligand-gated ion channel", Current Biology **23**, 13 (2013).

[63] Lo Nigro, C., M. Macagno, D. Sangiolo, L. Bertolaccini, M. Aglietta and M. C. Merlano, "NK-mediated antibody-dependent cell-mediated cytotoxicity in solid tumors: biological evidence and clinical perspectives", Annals of Translational Medicine **7**, 5 (2019).

[64] López-Soto, A., S. Gonzalez, M. J. Smyth and L. Galluzzi, "Control of Metastasis by NK Cells", (2017).

[65] Lv, C., X. Gu, H. Li, Y. Zhao, D. Yang, W. Yu, D. Han, J. Li and W. Tan, "Molecular transport through a biomimetic DNA channel on live cell membranes", ACS Nano **14**, 11 (2020).

[66] Lyubchenko, Y. L., L. S. Shlyakhtenko and T. Ando, "Imaging of nucleic acids with atomic force microscopy", (2011).

[67] Mahendran, K. R., A. Niitsu, L. Kong, A. R. Thomson, R. B. Sessions, D. N. Woolfson and H. Bayley, "A monodisperse transmembrane α-helical peptide barrel", Nature Chemistry **9**, 5 (2017).

[68] Mantri, S., K. Tanuj Sapra, S. Cheley, T. H. Sharp and H. Bayley, "An engineered dimeric protein pore that spans adjacent lipid bilayers", Nature Communications **4** (2013).

[69] Mao, C., W. Sun and N. C. Seeman, "Designed Two-Dimensional DNA Holliday Junction Arrays Visualized by Atomic Force Microscopy", Journal of the American Chemical Society **121**, 23, 5437–5443, URL `https://pubs.acs.org/doi/10.1021/ja9900398` (1999).

[70] Maxfield, F. R. and D. Wüstner, "Analysis of Cholesterol Trafficking with Fluorescent Probes", Methods in Cell Biology **108**, 367–393 (2012).

[71] Miles, B. N., A. P. Ivanov, K. A. Wilson, F. Dogan, D. Japrung and J. B. Edel, "Single molecule sensing with solid-state nanopores: Novel materials, methods, and applications", Chemical Society Reviews **42**, 1 (2013).

[72] Mitscha-Baude, G., B. Stadlbauer, S. Howorka and C. Heitzinger, "Protein Transport through Nanopores Illuminated by Long-Time-Scale Simulations", ACS Nano **15**, 6, 9900–9912, URL `https://doi.org/10.1021/acsnano.1c01078` (2021).

[73] Muraoka, T., D. Noguchi, R. S. Kasai, K. Sato, R. Sasaki, K. V. Tabata, T. Ekimoto, M. Ikeguchi, K. Kamagata, N. Hoshino, H. Noji, T. Akutagawa, K. Ichimura and K. Kinbara, "A synthetic ion channel with anisotropic ligand response", Nature Communications **11**, 1 (2020).

[74] Ouldali, H., K. Sarthak, T. Ensslen, F. Piguet, P. Manivet, J. Pelta, J. C. Behrends, A. Aksimentiev and A. Oukhaled, "Electrical recognition of the twenty proteinogenic amino acids using an aerolysin nanopore", (2020).

[75] Pal, S., Z. Deng, B. Ding, H. Yan and Y. Liu, "DNA-origami-directed self-assembly of discrete silver-nanoparticle architectures", Angewandte Chemie - International Edition **49**, 15 (2010).

[76] Pei, H., N. Lu, Y. Wen, S. Song, Y. Liu, H. Yan and C. Fan, "A DNA nanostructure-based biomolecular probe carrier platform for electrochemical biosensing", Advanced Materials **22**, 42 (2010).

[77] Pinheiro, V. B., A. I. Taylor, C. Cozens, M. Abramov, M. Renders, S. Zhang, J. C. Chaput, J. Wengel, S. Y. Peak-Chew, S. H. McLaughlin, P. Herdewijn and P. Holliger, "Synthetic genetic polymers capable of heredity and evolution", Science **336**, 6079 (2012).

[78] Ponnuswamy, N., M. M. Bastings, B. Nathwani, J. H. Ryu, L. Y. Chou, M. Vinther, W. A. Li, F. M. Anastassacos, D. J. Mooney and W. M. Shih, "Oligolysine-based coating protects DNA nanostructures from low-salt denaturation and nuclease degradation", Nature Communications **8** (2017).

[79] Poppleton, E., R. Romero, A. Mallya, L. Rovigatti and P. Šulc, "OxDNA.org: A public webserver for coarse-grained simulations of DNA and RNA nanostructures", Nucleic Acids Research **49**, W1 (2021).

[80] Qing, Y., H. Tamagaki-Asahina, S. A. Ionescu, M. D. Liu and H. Bayley, "Catalytic site-selective substrate processing within a tubular nanoreactor", Nature Nanotechnology **14**, 12 (2019).

[81] Ramakrishnan, S., H. Ijäs, V. Linko and A. Keller, "Structural stability of DNA origami nanostructures under application-specific conditions", (2018).

[82] Römer, L. and T. Scheibel, "The elaborate structure of spider silk", Prion **2**, 4 (2008).

[83] Rothemund, P. W. K., "Folding DNA to create nanoscale shapes and patterns", Nature **440**, 7082, 297–302, URL `http://www.nature.com/articles/nature04586` (2006).

[84] Schoenit, A., E. A. Cavalcanti-Adam and K. Göpfrich, "Functionalization of Cellular Membranes with DNA Nanotechnology", Trends in Biotechnology **39**, 11, 1208–1220, URL `https://linkinghub.elsevier.com/retrieve/pii/S0167779921000342` (2021).

[85] Scott, A. M., J. P. Allison and J. D. Wolchok, "Monoclonal antibodies in cancer therapy", Cancer Immunity **12**, 1, 14, URL `https://doi.org/10.1158/1424-9634.DCL-14.12.1` (2012).

[86] Seeman, N. C., "Nucleic acid junctions and lattices", Journal of Theoretical Biology **99**, 2 (1982).

[87] Shevtsov, M. and G. Multhoff, "Immunological and translational aspects of NK cell-based antitumor immunotherapies", (2016).

[88] Shi, N., S. Ye, A. Alam, L. Chen and Y. Jiang, "Atomic structure of a Na+- and K+-conducting channel", Nature **440**, 7083 (2006).

[89] Shi, P., N. Zhao, J. Lai, J. Coyne, E. R. Gaddes and Y. Wang, "Polyvalent Display of Biomolecules on Live Cells", Angewandte Chemie **130**, 23, 6916–6920, URL `https://onlinelibrary.wiley.com/doi/10.1002/ange.201712596` (2018).

[90] Shigdar, S., B. Schrand, P. H. Giangrande and V. de Franciscis, "Aptamers: Cutting edge of cancer therapies", (2021).

[91] Shih, W. M., J. D. Quispe and G. F. Joyce, "A 1.7-kilobase single-stranded DNA that folds into a nanoscale octahedron", Nature **427**, 6975, 618–621, URL `https://doi.org/10.1038/nature02307` (2004).

[92] Shimasaki, N., A. Jain and D. Campana, "NK cells for cancer immunotherapy", (2020).

[93] Shin, J. S. and N. A. Pierce, "A synthetic DNA walker for molecular transport", Journal of the American Chemical Society **126**, 35 (2004).

[94] Shoji, K., R. Kawano and R. J. White, "Correction to: Spatially Resolved Chemical Detection with a Nanoneedle-Probe-Supported Biological Nanopore (ACS Nano (2019) 13:2 (2606?2614) DOI: 10.1021/acsnano.8b09667)", (2019).

[95] Si, W. and A. Aksimentiev, "Nanopore Sensing of Protein Folding", ACS Nano **11**, 7, 7091–7100, URL `https://doi.org/10.1021/acsnano.7b02718` (2017).

[96] Song, J., Z. Li, P. Wang, T. Meyer, C. Mao and Y. Ke, "Reconfiguration of DNA molecular arrays driven by information relay", Science **357**, 6349, URL `https://www.science.org/doi/10.1126/science.aan3377` (2017).

[97] Soskine, M., A. Biesemans and G. Maglia, "Single-molecule analyte recognition with ClyA nanopores equipped with internal protein adaptors", Journal of the American Chemical Society **137**, 17 (2015).

[98] Sun, L., Y. Su, J. G. Wang, F. Xia, Y. Xu and D. Li, "DNA nanotweezers for stabilizing and dynamically lighting up a lipid raft on living cell membranes and the activation of T cells", Chemical Science **11**, 6 (2020).

[99] Tam, Y. K., J. A. Martinson, K. Doligosa and H. G. Klingemann, "Ex vivo expansion of the highly cytotoxic human natural killer cell line NK-92 under current good manufacturing practice conditions for clinical adoptive cellular immunotherapy", Cytotherapy **5**, 3 (2003).

[100] Tan, S. J., M. J. Campolongo, D. Luo and W. Cheng, "Building plasmonic nanostructures with DNA", (2011).

[101] Terry, B. R., E. K. Matthews and J. Haseloff, "Molecular Characterization of Recombinant Green Fluorescent Protein by Fluorescence Correlation Microscopy", Biochemical and Biophysical Research Communications **217**, 1 (1995).

[102] Thacker, V. V., L. O. Herrmann, D. O. Sigle, T. Zhang, T. Liedl, J. J. Baumberg and U. F. Keyser, "DNA origami based assembly of gold nanoparticle dimers for surface-enhanced Raman scattering", Nature Communications **5** (2014).

[103] Thomsen, R. P., M. G. Malle, A. H. Okholm, S. Krishnan, S. S. Bohr, R. S. Sørensen, O. Ries, S. Vogel, F. C. Simmel, N. S. Hatzakis and J. Kjems, "A large size-selective DNA nanopore with sensing applications", Nature Communications **10**, 1 (2019).

[104] Thum, E., S. Zhe and H. Schwarz, "CD137, implications in immunity and potential for therapy", Frontiers in Bioscience **14**, 11 (2009).

[105] Tseng, C. Y., W. X. Wang, T. R. Douglas and L. Y. Chou, "Engineering DNA Nanostructures to Manipulate Immune Receptor Signaling and Immune Cell Fates", (2022).

[106] Tyagi, S. and F. R. Kramer, "Molecular Beacons: Probes that Fluoresce Upon Hybridization", Nature Biotechnology **14**, 3 (1996).

[107] Van der Verren, S. E., N. Van Gerven, W. Jonckheere, R. Hambley, P. Singh, J. Kilgour, M. Jordan, E. J. Wallace, L. Jayasinghe and H. Remaut, "A dual-constriction biological nanopore resolves homonucleotide sequences with high fidelity", Nature Biotechnology **38**, 12 (2020).

[108] Van Meervelt, V., M. Soskine, S. Singh, G. K. Schuurman-Wolters, H. J. Wijma, B. Poolman and G. Maglia, "Real-Time Conformational Changes and Controlled Orientation of Native Proteins Inside a Protein Nanoreactor", Journal of the American Chemical Society **139**, 51 (2017).

[109] Walter, H. K., J. Bauer, J. Steinmeyer, A. Kuzuya, C. M. Niemeyer and H. A. Wagenknecht, "DNA Origami Traffic Lights with a Split Aptamer Sensor for a Bicolor Fluorescence Readout", Nano Letters **17**, 4 (2017).

[110] Wang, J., J. Ma, Z. Ni, L. Zhang and G. Hu, "Effects of access resistance on the resistive-pulse caused by translocating of a nanoparticle through a nanopore", RSC Advances **4**, 15 (2014).

[111] Wang, W., B. Chopra, V. Walawalkar, Z. Liang, R. Adams, M. Deserno, X. Ren and R. E. Taylor, "Membrane and glycocalyx tethering of DNA nanostructures for enhanced uptake", bioRxiv URL `https://www.biorxiv.org/content/early/2023/03/10/2023.03.09.529286` (2023).

[112] Wang, W., P. Hayes, X. Ren and R. Taylor, "Synthetic cell armor made of DNA origami", URL https://doi.org/10.1101/2023.02.20.529284 (2023).

[113] Wang, Y., D. Zheng, Q. Tan, M. X. Wang and L. Q. Gu, "Nanopore-based detection of circulating microRNAs in lung cancer patients", Nature Nanotechnology **6**, 10 (2011).

[114] Watson, J. D. and F. H. Crick, "Molecular structure of nucleic acids: A structure for deoxyribose nucleic acid", Nature **171**, 4356 (1953).

[115] Wei, R., T. G. Martin, U. Rant and H. Dietz, "DNA origami gatekeepers for solid-state nanopores", Angewandte Chemie - International Edition **51**, 20 (2012).

[116] Winfree, E., F. Liu, L. A. Wenzler and N. C. Seeman, "Design and self-assembly of two-dimensional DNA crystals", Nature **394**, 6693, 539–544, URL http://www.nature.com/articles/28998 (1998).

[117] Xing, Y., A. Dorey and S. Howorka, "Multi-Stimuli Responsive and Mechano-Actuated Biomimetic Membrane Nanopores Self-Assembled from DNA", Advanced Materials **n/a**, n/a, 2300589, URL https://doi.org/10.1002/adma.202300589 (2023).

[118] Xu, C., P. Lu, T. M. Gamal El-Din, X. Y. Pei, M. C. Johnson, A. Uyeda, M. J. Bick, Q. Xu, D. Jiang, H. Bai, G. Reggiano, Y. Hsia, T. J. Brunette, J. Dou, D. Ma, E. M. Lynch, S. E. Boyken, P. S. Huang, L. Stewart, F. DiMaio, J. M. Kollman, B. F. Luisi, T. Matsuura, W. A. Catterall and D. Baker, "Computational design of transmembrane pores", Nature **585**, 7823 (2020).

[119] Yang, Q., S. R. Goding, M. E. Hokland and P. H. Basse, "Antitumor activity of NK cells", Immunologic Research **36**, 1, 13–25, URL https://doi.org/10.1385/IR:36:1:13 (2006).

[120] Yang, Y. R., Y. Liu and H. Yan, "DNA Nanostructures as Programmable Biomolecular Scaffolds", (2015).

[121] Yin, P., H. M. Choi, C. R. Calvert and N. A. Pierce, "Programming biomolecular self-assembly pathways", Nature **451**, 7176 (2008).

[122] Yoo, J. and A. Aksimentiev, "Molecular Dynamics of Membrane-Spanning DNA Channels: Conductance Mechanism, Electro-Osmotic Transport, and Mechanical Gating", Journal of Physical Chemistry Letters **6**, 23 (2015).

[123] You, M., Y. Lyu, D. Han, L. Qiu, Q. Liu, T. Chen, C. Sam Wu, L. Peng, L. Zhang, G. Bao and W. Tan, "DNA probes for monitoring dynamic and transient molecular encounters on live cell membranes", Nature Nanotechnology **12**, 5, 453–459, URL http://www.nature.com/articles/nnano.2017.23 (2017).

[124] Yurke, B., A. J. Turberfield, A. P. Mills, F. C. Simmel and J. L. Neumann, "A DNA-fuelled molecular machine made of DNA", Nature **406**, 6796 (2000).

[125] Zhan, C., B. Li, L. Hu, X. Wei, L. Feng, W. Fu and W. Lu, "Micelle-based brain-targeted drug delivery enabled by a nicotine acetylcholine receptor ligand", Angewandte Chemie - International Edition **50**, 24 (2011).

[126] Zhang, F., J. Nangreave, Y. Liu and H. Yan, "Reconfigurable DNA Origami to Generate Quasifractal Patterns", Nano Letters **12**, 6, 3290–3295, URL https://pubs.acs.org/doi/10.1021/nl301399z (2012).

[127] Zhang, Z., X. Y. Kong, K. Xiao, G. Xie, Q. Liu, Y. Tian, H. Zhang, J. Ma, L. Wen and L. Jiang, "A Bioinspired Multifunctional Heterogeneous Membrane with Ultrahigh Ionic Rectification and Highly Efficient Selective Ionic Gating", Advanced Materials **28**, 1 (2016).

[128] Zheng, W., J. J. Zhao, Y. Tao, M. Guo, Z. Ya, C. Chen, N. Qin, J. Zheng, J. Luo and L. Xu, "MicroRNA-21: A promising biomarker for the prognosis and diagnosis of non-small cell lung cancer", (2018).

[129] Zhou, C., Z. Yang and D. Liu, "Reversible regulation of protein binding affinity by a DNA machine", Journal of the American Chemical Society **134**, 3 (2012).

[130] Zhu, W. and B. Xu, "MicroRNA-21 identified as predictor of cancer outcome: A meta-analysis", PLoS ONE **9**, 8 (2014).

APPENDIX A

SUPPLEMENTARY DATA

Supplementary Note 1: Agarose gel electrophoresis analysis of the interaction of LGC-N pore with SUVs under different conditions

Here, two types of purified LGC-N pore samples: LGC-N +Mg (dissolved in 0.5 × TAE buffer containing 10 mM $MgCl_2$ and LGC-N -Mg (dissolved in 50 mM HEPES (pH 7.6) supplemented with 500 mM NaCl), and two cholesterol-modified variants and their incubations with SUVs, were run on 1.5% agarose gel with running buffer 0.5 × TAE buffer containing 10 mM $MgCl_2$ (Supplementary Figure 8a,b) or 1.5% agarose gel with running buffer 0.5 × TAE buffer without 10 mM $MgCl_2$ (Supplementary Figure 8c,d). From the gel images, we can see that all the LGC-N +Mg pores incubated with SUVs showed upshift bands in the gel pockets, suggesting a strong binding of pores with SUVs, no matter with or without cholesterol modifications, so there were non-specific adsorption interactions between the pores without cholesterol modifications and SUVs; while for LGC-N -Mg pores, only the sample run in $MgCl_2$ containing gel (Supplementary Figure 8b) showed non-specific binding and the one in $MgCl_2$ free gel (Supplementary Figure 8d) showed a clear band shift similar to the pore alone, meaning no binding of the pore with the SUVs. We assume the non-specific binding is caused by $MgCl_2$, either it originating from the LGC-N +Mg pore solution, or from the gel/running buffer, or both, and the divalent cation $MgCl_2$ can mediate the adsorption of negatively changed LGC-N pore and the phospholipid membrane. Therefore, it's essential to keep a $MgCl_2$ free condition to avoid non-specific interactions between the pores and lipid membrane.

Supplementary note 2: Kinetics of dye influx

The kinetics of dye influx inside the GUVs was estimated using the Fick's law following calculation by [**?**]. As per the calculation shown there, the rate of Atto633 dye diffusion into the GUV interior through LGC is given by

$$n_i(t) = n_o(1 - e^{-k_o t})(1)$$

Where, $n_i(t)$= dye concentration inside the GUVs at time t; $n_o(t)$= dye concentration outside the GUVs k_o= first order dye diffusion rate constant= DA/LV; Where, D = diffusion coefficient of the dye, A = Cross-sectional area of the nanopore, L = Length of the nanopore and V = internal volume of the GUVs. The value of diffusion coefficient of atto dyes 4,5 has been found close to D = 426 $\mu m^2/sec$. Now putting the values A = 416 nm^2, L = 10nm from the nanopore design and V = 117.1 μm^3, derived from the average diameter of GUVs in the confocal measurements as 6.07 μm. This yields $k_o = 0.015s^{-1}$. Now the time required for dye influx through a single nanopore (2)

$$\tau_{single} = 1/k_o = 1/(0.015sec^{-1}) = 6.6sec$$

In our actual observation (Supplementary Fig. 13) we see much slower diffusion rates. This is contrasting to the previous reports, where the observed for dye diffusion was always faster compared to the theoretically predicted value. The observed rate of dye diffusion through DNA nanopore is a combination of several inter-dependent phenomena, i.e.- i) nanopore binding to the membrane, ii) reorientation of its stem in the bilayer to form a channel and finally iii) the diffusion of the dye through the pore. The nanopore binding to membrane is strongly governed by the number of cholesterol molecules, ionic concentration, temperature etc. While the reorientation step is supposedly the slowest and rate determining step, that depends on the flexibility of

the cholesterol bearing segments of the nanopore. The final step of dye diffusion is a function of the size of dye molecule, medium viscosity, temperature, concentration gradient and pore dimensions. We attribute the faster flux in case of our LGC pore compared to the previous pores due to the placement of large number of cholesterol anchors to help the step (i). The cholesterol-bearing one layer origami plate being flexible enough for rapid re-orientation of the pores, probably led to faster insertion kinetics compared to the previous origami pores that always placed the cholesterol molecules in a rigid framework, thereby slowing the reorientation step. Interestingly, the dye diffusion rate in LGC pore was 5 times slower compared to the theoretically calculated time required for diffusion (Supplementary Fig. 13). This might have resulted as contribution of the wider pore dimension of LGC toward the diffusion rate was overcome by the reorientation step that governs the overall observed rate of dye influx. Further detailed investigation is required to decouple the absolute contributions of the three steps in the insertion of hydrophobically modified DNA nanostructures into lipid bilayer.

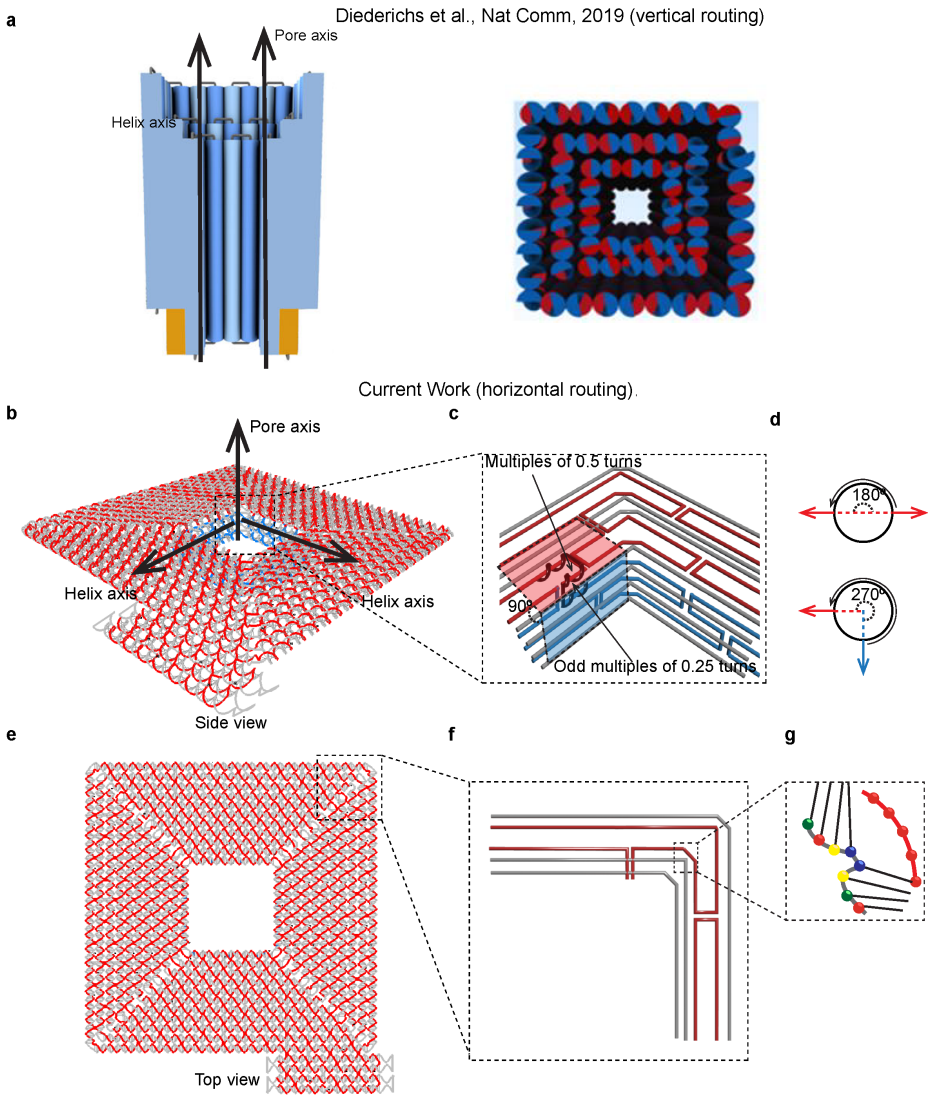

Figure A.1: (a) Side view (left) and top view (right) of the nanopore of Diederichs et al, Nat Comm, 2019,1 exemplifying routing of helices in previously published DNA nanopores. The helical axis of the component helices ran vertically in these DNA nanopores, i.e. – parallel to the vertical axis of the nanopore. (b-i) Side view of LGC. Grey, red and blue strands represent, respectively - M13 scaffold, plate forming staples and pore forming staples. The pore forming helices run horizontally, i.e. – perpendicular to the pore axis. This horizontal routing ensures fine tuning of the pore diameter as well as having a large surface area of the plate, available for cholesterol placement. (b-ii) Zoomed-in image of the pore region showing layered crossover design to form the plate and the pore of LGC, routed in mutually normal planes (red plane – plate forming helices, blue plane – pore forming helices). The distance between two interhelical crossovers determines their relative spatial alignment. Hence, we create interhelical crossovers spaced apart in a multiple of 0.5 turns, i.e. - 1 $\times$ 0.5 turns = 6nt; 2 $\times$ 0.5 turns = 10.5nt; 3 $\times$ 0.5 turns = 16nt etc. for the helices on the same plane (i.e – among plate forming helices in the red plane and among pore forming helices in the blue plane). Whereas the gap between a crossover in the red 'plate plane' and a crossover in the blue 'pore plane' is kept as an odd multiple of 0.25 turns, except 1 $\times$ 0.25 turns i.e. – 3 $\times$ 0.25 turns = 8nt; 5 $\times$ 0.25 turns = 13nt; 7 $\times$ 0.25 turns = 18nt etc. This ensures

Figure A.1: the red 'plate plane' and the blue 'pore plane' to be perpendicular to each other. (b-iii) The direction of the helices at crossover points. Circle represents top view of a helix and arrows represent tangent drawn to a helix at a given point to show its direction, red arrow – helices in plate plane and blue arrows – helices in pore plane. Top panel – relative angle between the helical direction at two crossover points in the plate plane. Bottom panel – relative angle between the direction of a helix at a crossover in the plate plane and a crossover in the pore plane. (c-i) Top view of the pore. (c-ii) Zoomed-in view of the corners where a 4 base loops in only one of the two strands in each helix imposes a 90^{o} curvature in the same plane. (c-iii) Zoom in view of a corner crossover showing the 4 base loop insertion strategy.

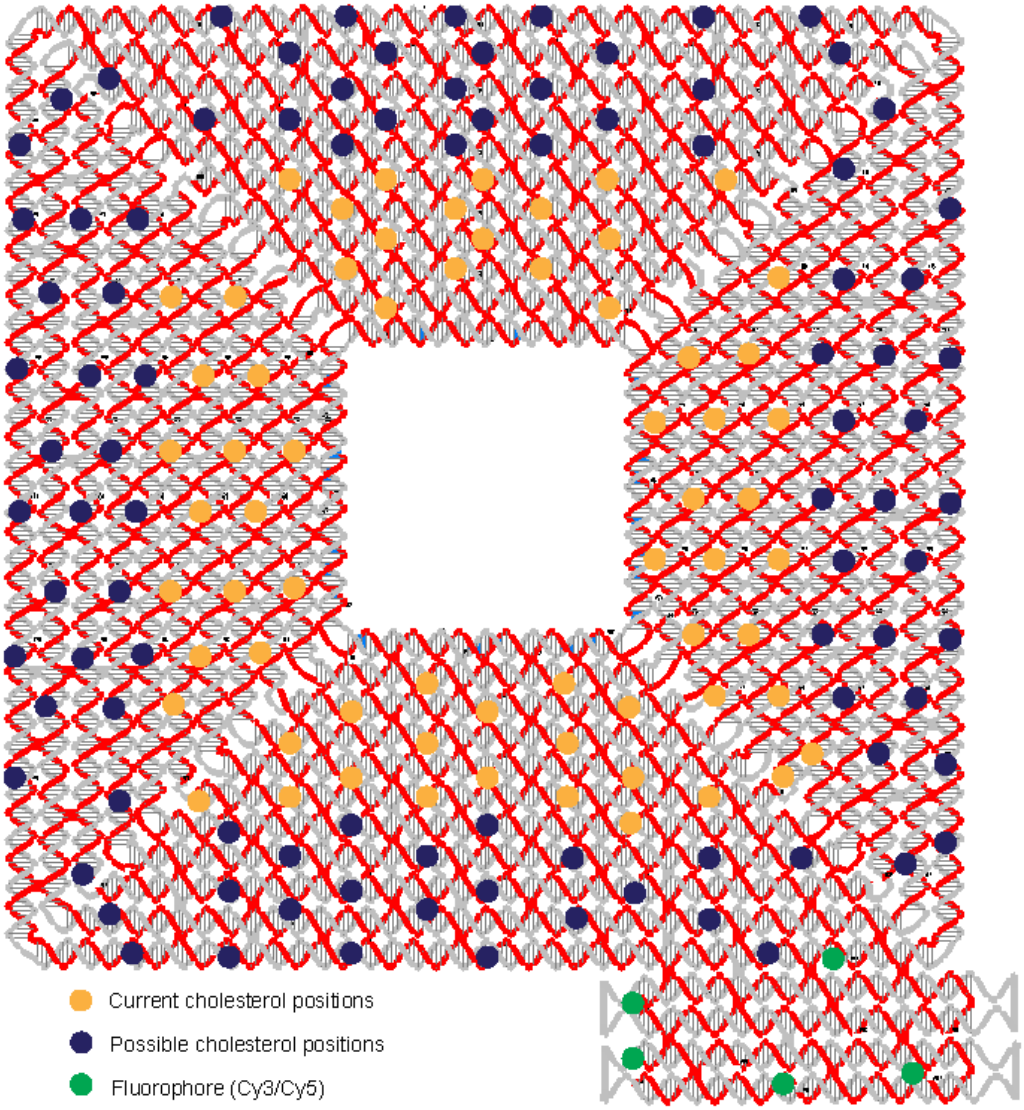

Figure A.2: [Position of hydrophobic cholesterol anchors (orange spheres) and optional fluorophore modification (green spheres) in the large diameter nanopore]. According to Thompson et al, Nat Comm, 2019's continuum model and MD simulation predictions (Supplementary Fig. 2, Thompson et al, Nat Comm 2019) a pore of 20nm width would require greater than 60 cholesterol probes. Thus, we used 64 cholesterol probes.

Figure A.2: ensuring the downward orientation of the helices at the location. When cholesterol bearing anti-handle strand is added, their binding at the handle strand bearing locations tag the nanopore with 64 cholesterol molecules that help its insertion into the lipid bilayer. Although, this work only uses the denoted locations, the horizontally routed flat design offers more place that can accommodate at least 96 more cholesterol molecules (blue spheres) for future design of larger pore. The fluorophores are placed in the index region to ensure sufficient distance from the functional regions of the nanopore to avoid any undesired non-specific interactions.

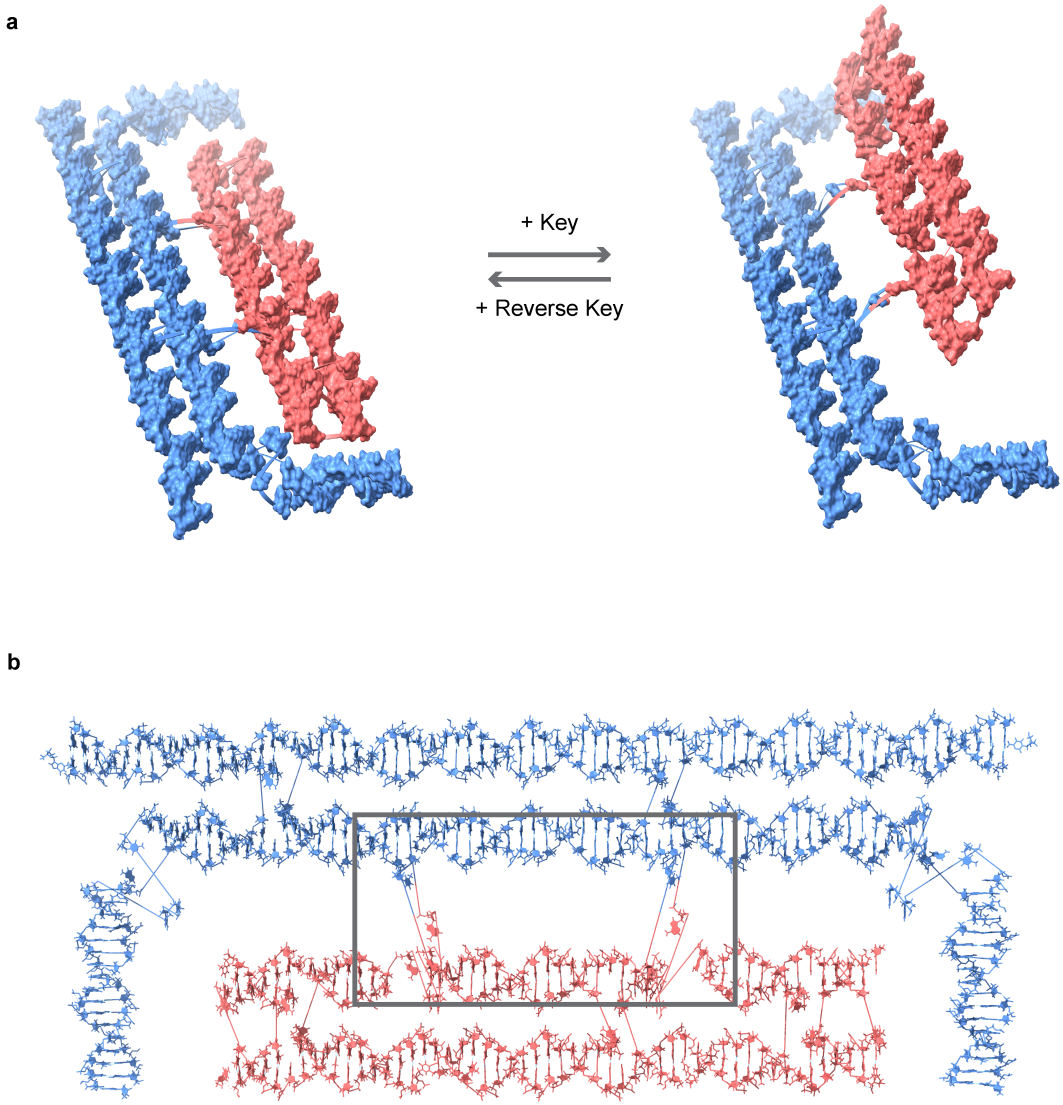

Figure A.3: (a) Side view and (b) top view of the optimally designed flexible hinge of the LGC lid formed by a 4-nucleotide single stranded region in each hinge. Several designs with rigid hinge (data not shown) did not lead to successful closure of the lid, perhaps because of strain in the hinge region.

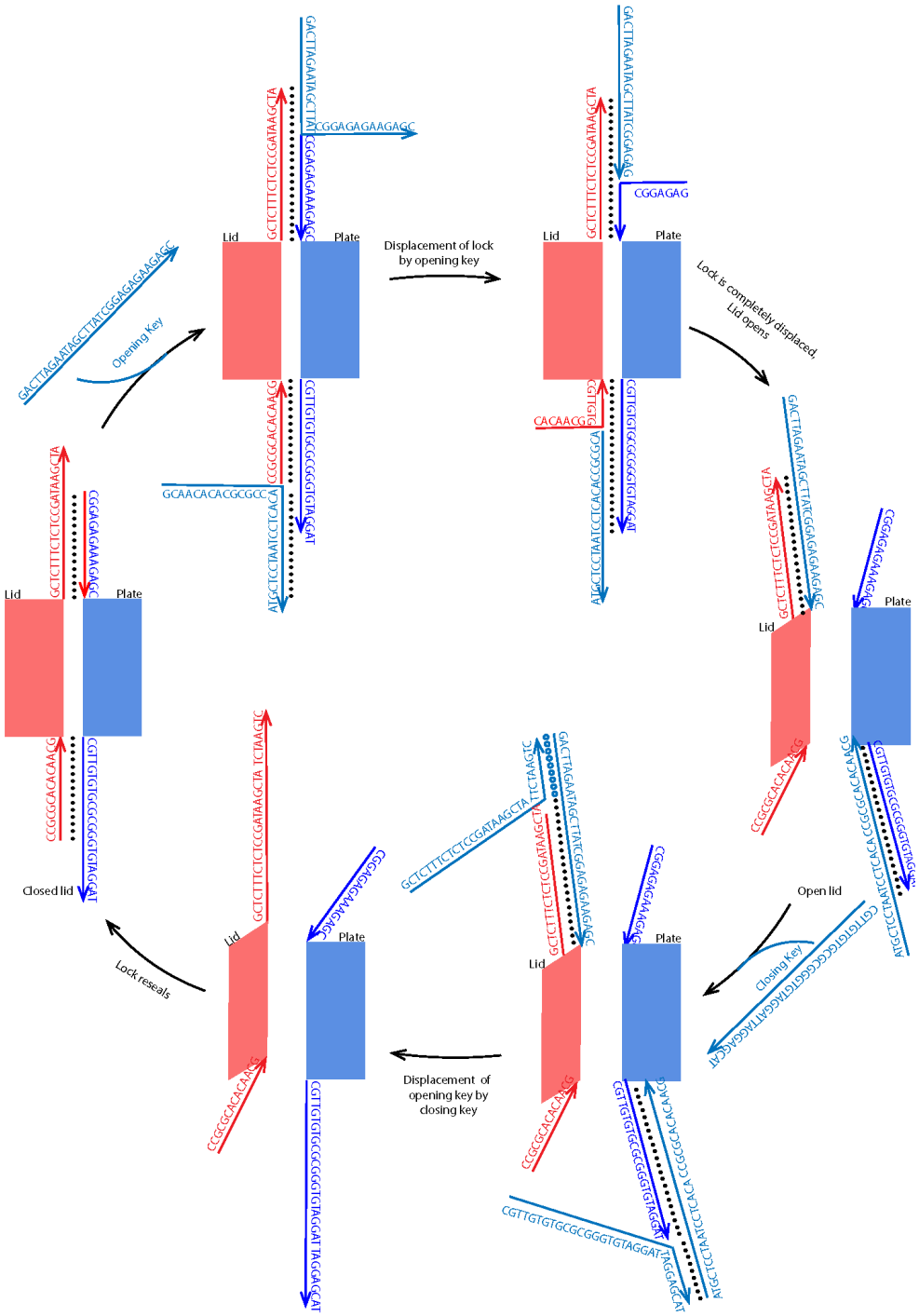

Figure A.4: Lid (pink) and plate (blue) are locked in two positions, each lock containing a strand with a toehold. Opening key (light blue) opens the lock by toehold mediated strand displacement (TMSD), leading to open lid. The opening key also contains a toehold which then initiates a second TMSD when closing keys (light blue) are added. As a result, the opening key dissociates from the lock strands and lock strands reseal to form the closed lid.

[H]

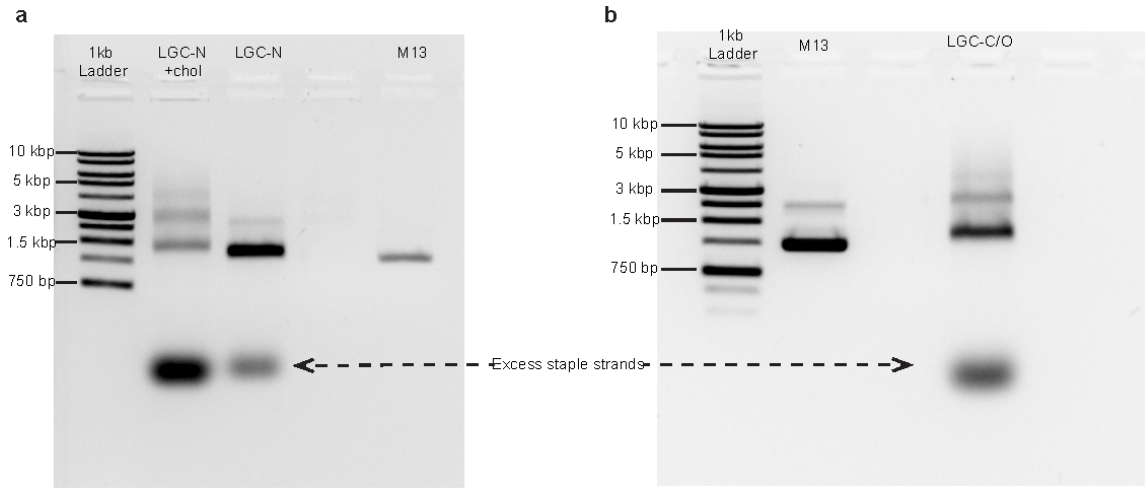

Figure A.5: (a) No lid-LGC with cholesterol (LGC-N +chol) and without cholesterol (LGC-N). Slight upshift of the LGC-N with respect to the scaffold M13 shows its correct formation with a predominant monomer band a slight dimer band. The successful cholesterol modification is shown by upshift of monomer as well as dimer bands of LGC-N +Chol compared to the LGC-N band and increased smearing due to aggregation in case of LGC-N +Chol. (b) Formation of non-cholesterol LGC with lid (LGC-C/O) in 1.5% agarose gel. The predominant band of LGC-C/O with lid upshifts compared to that for LGC-N which indicates successful formation of the lid.

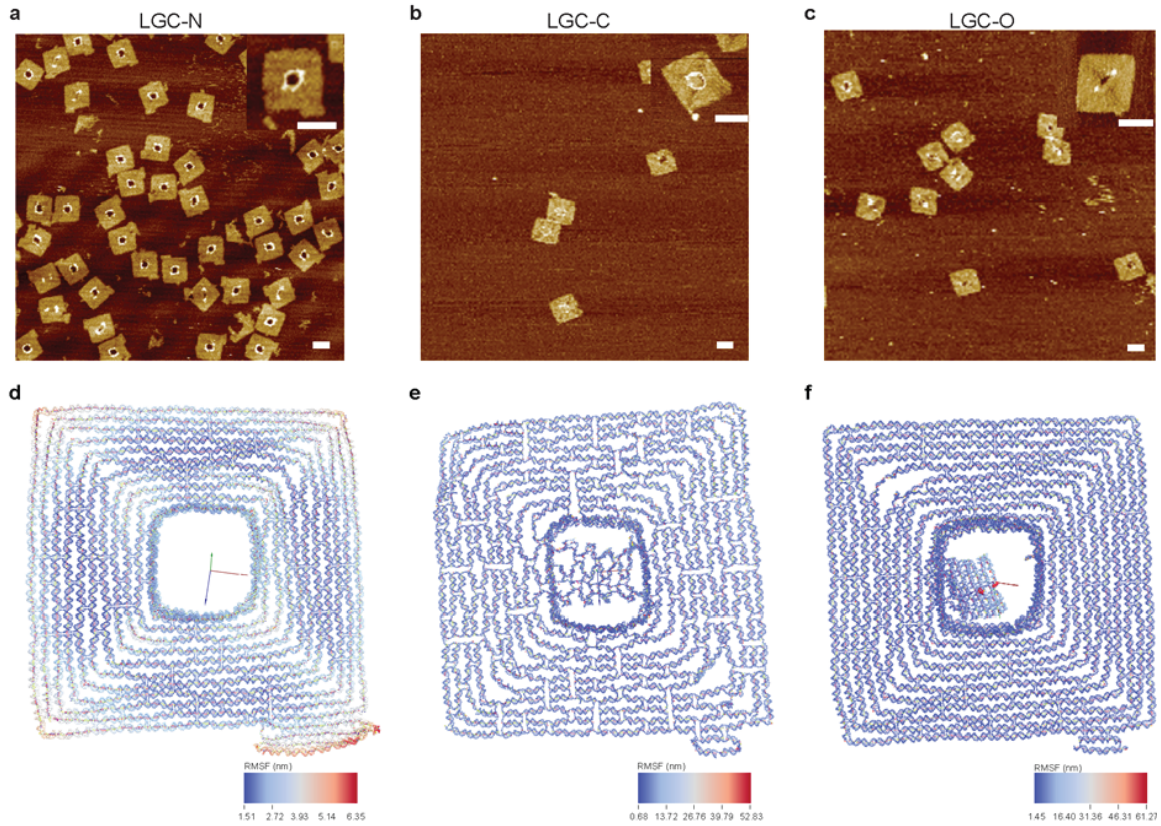

Figure A.6: (a) AFM images and (b) mean structure and root mean squared fluctuations (RMSF) obtained from oxDNA simulations for non-cholesterol versions of – (i) LGC without lid (LGC-N) (ii) LGC with closed lid (LGC-C) and (iii) LGC with open lid (LGC-O). AFM scale bars: 50 nm.

[H]

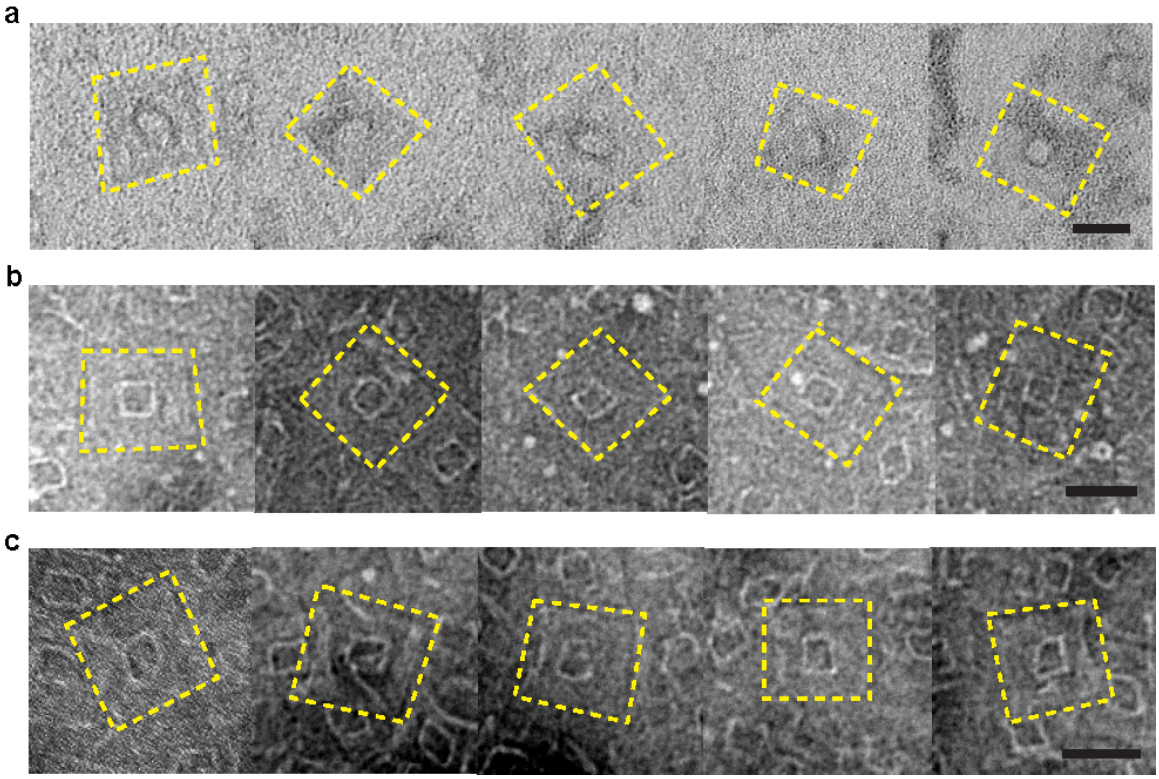

Figure A.7: (a) Without lid. (b) With closed lid and (c) With open lid. The edge of the nanopore is annotated with dashed line for ease of understanding. The pore in the middle of the square is visible in all cases. The pore is empty in case of LGC without lid (a). A lid is clearly visible in the middle of the pore in case of LGC with closed lid (b) and open lid (c). In case of LGC with closed lid in (b), the lid looks flat on the pore covering it whereas in case of LGC with open lid in (c), the lid looks slightly tilted owing to its open form. Scale bar: 50 nm.

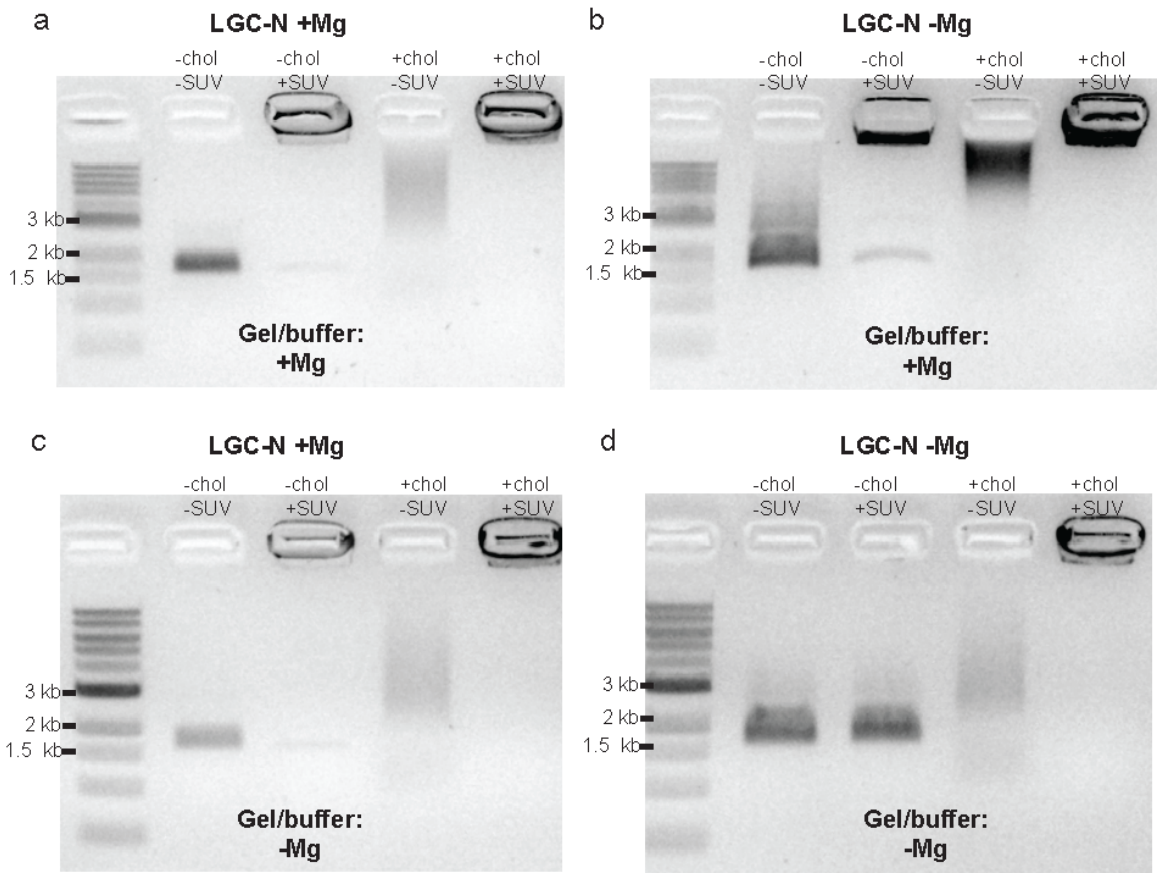

Figure A.8: The purified LGC-N pores (a) LGC-N +Mg dissolved in 0.5 × TAE buffer containing 10 mM MgCl2 and (b) LGC-N -Mg dissolved in 50 mM HEPES (pH 7.6) supplemented with 500 mM NaCl were run on 1.5% agarose gel with running buffer 0.5 × TAE buffer containing 10 mM MgCl2; (c) LGC-N +Mg and (d) LGC-N -Mg were run on 1.5% agarose gel with running buffer 0.5 × TAE buffer without 10 mM MgCl2. The left lanes on each gel were 1 kb DNA ladder, the next four lanes from left to right are the unmodified pore only, unmodified pore incubated with SUVs, cholesterol-modified pore, and cholesterol-modified pore incubated with SUVs. Both the SUVs solution and incubation buffer (50 mM HEPES (pH 7.6) supplemented with 500 mM NaCl) had no added Mg2+. All experiments are repeated at least three times.

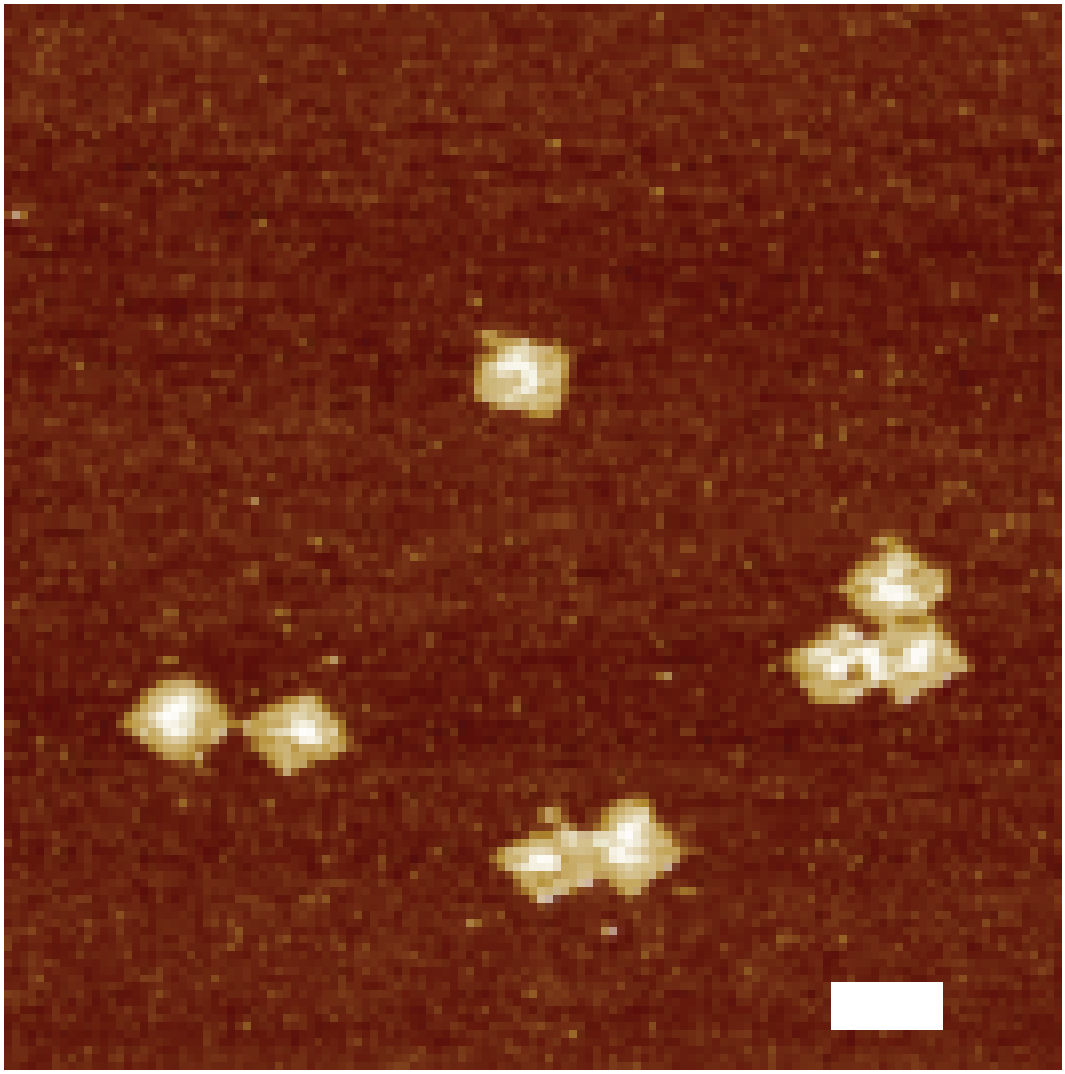

Figure A.9: (a) Scheme and (b) Transmitted light (grey) and Cy3 channel (magenta) merged images of GUV influx assay, showing that the GUVs remained on focus across the imaging. Top: no lid LGC with cholesterol (LGC-N +Chol), bottom: no lid LGC without cholesterol (LGC-N -chol). Scale bar: 10 μm

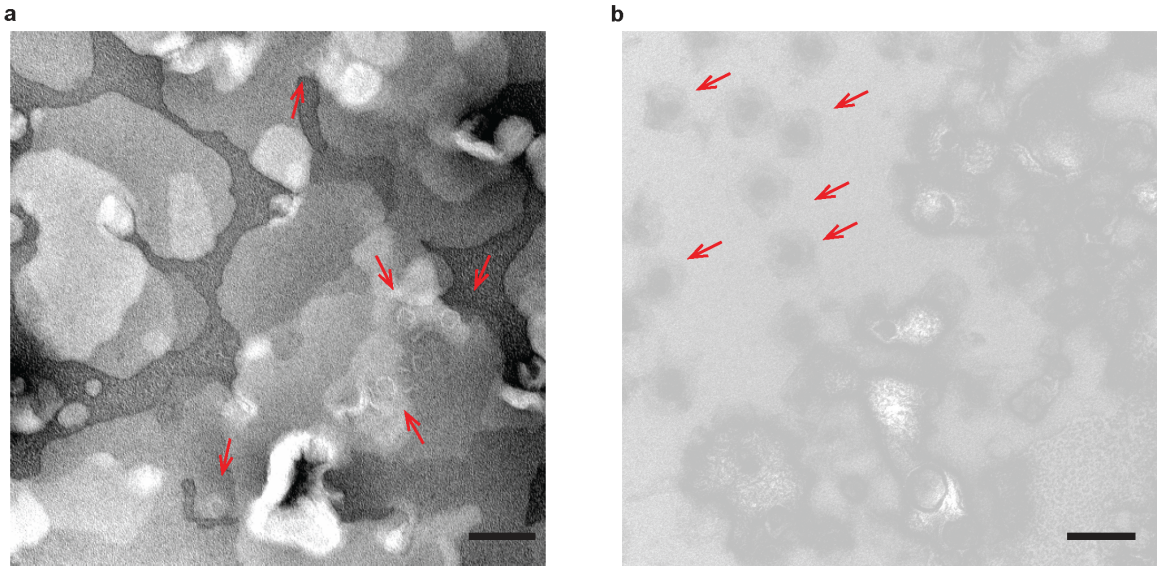

Figure A.10: (LGC-N structures are marked with red arrows. Scale bars: 100 nm. (a) POPC-SUVs + LGC-N with cholesterol TEM images show most LGC-N structures on top of the lipid membranes as they strongly interact with the lipid membrane. (b) POPC-SUVs + LGC-N without cholesterol TEM images show most LGC structures away from the SUVs due to lack of interaction between unmodified LGC-N structures and lipid membrane. The data is representative of n=2 independent experiments

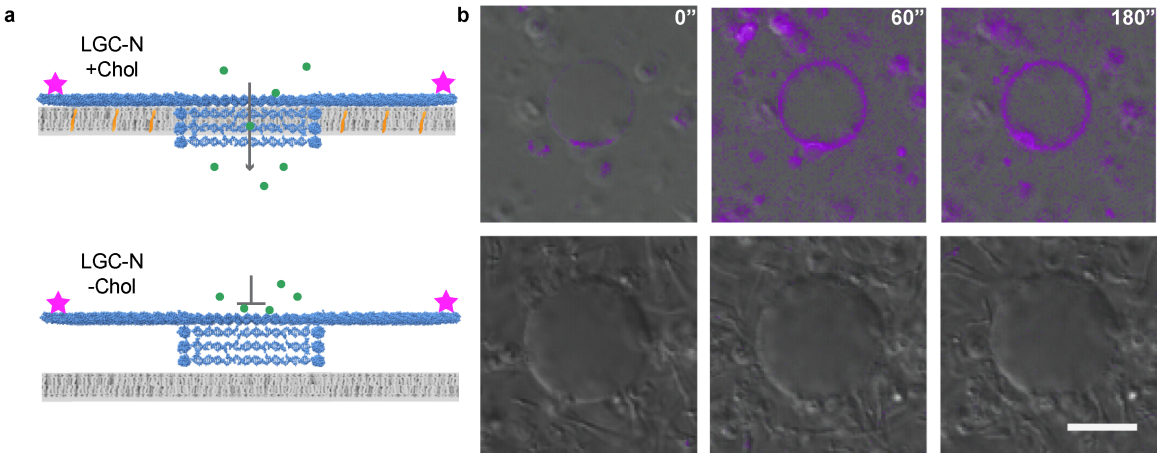

Figure A.11: (a) Scheme and (b) Transmitted light (grey) and Cy3 channel (magenta) merged images of GUV influx assay in Fig. 2c-ii in main text, showing that the GUVs remained on focus across the imaging. Top: no lid LGC with cholesterol (LGC-N +Chol), bottom: no lid LGC without cholesterol (LGC-N -chol). Scale bar: 10 µm. The data is representative of n=3 independent experiments.

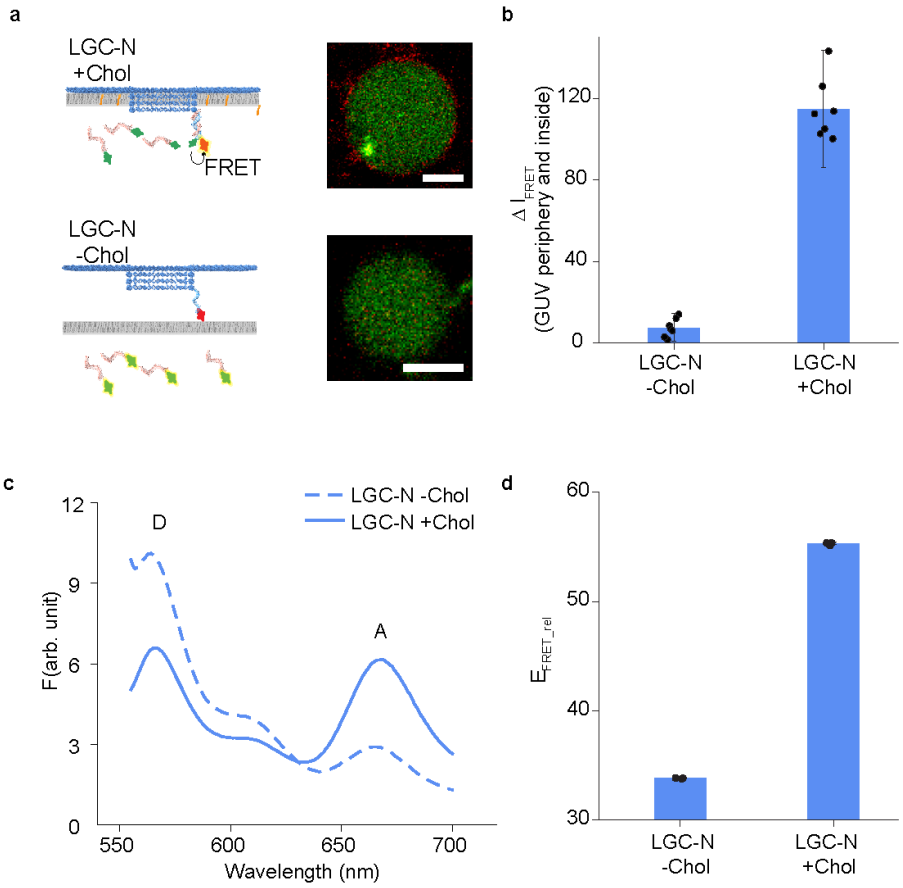

Figure A.12: FRET measurements for insertion of the nanopore into the lipid bilayer. a, Scheme (left panels) and corresponding FRET confocal micrographs (right panels) of no lid pore (LGC-N) bearing a Cy5 labelled probe strand is added to GUVs filled with Cy3 labelled strand complementary to the Cy5 labelled probe. Cholesterol labelled pores span the bilayer, causing hybridization of the Cy5 labelled probe strand of LGC-N with the Cy3 labelled strands inside the GUV (a, top row). This results in FRET signal observed as a red perimeter around the GUVs showing that the LGC (+Chol) has inserted into the lipid bilayer and the pore is formed without collapsing. Similar red FRET perimeter is not observed in case of non-cholesterol LGC which cannot insert into the lipid bilayer (a, bottom row). FRET confocal micrographs obtained by overlaying the Cy3 donor emission at donor excitation (green) and the Cy5 acceptor emission at donor excitation (red). The data is representative of 3 independent experiments. (Scale bar: 5 µm). b, Difference of FRET intensity (Cy5 acceptor emission at Cy3 donor excitation, red) between the perimeter and the inside of the GUV was used to quantify the FRET from 10-13 GUVs across 3 technical replicates observed when the nanopore inserts into the lipid bilayer and error bar shows the standard deviation of mean of the difference in the FRET intensity between the perimeter and inside of the GUV. Cholesterol modified LGC-N shows much higher FRET compared to that of non-cholesterol LGC-N. c, Representative ensemble FRET spectra and d, corresponding relative FRET efficiency obtained when no lid pore (LGC-N) bearing a Cy5 labelled probe strand is added to GUVs filled with Cy3 labelled strand complementary to the Cy5 labelled probe. (D and A on graph represent fluorescence maxima for donor and acceptor respectively). Cholesterol modified LGC-N shows lower donor fluorescence, higher acceptor fluorescence (c, solid line) and high FRET efficiency (d, LGC-N+Chol). Non-cholesterol LGC-N shows higher donor fluorescence, lower acceptor fluorescence (c, dashed line) and lower FRET efficiency (d, Open, LGC-N-chol). The FRET efficiency bars and error bars in d represents mean relative FRET efficiency and standard deviation of the mean respectively, obtained from three technical replicates. Both the FRET confocal micrographs and the spectral data demonstrate that the LGC is able to successfully insert into the bilayer and maintain the structure without collapsing.

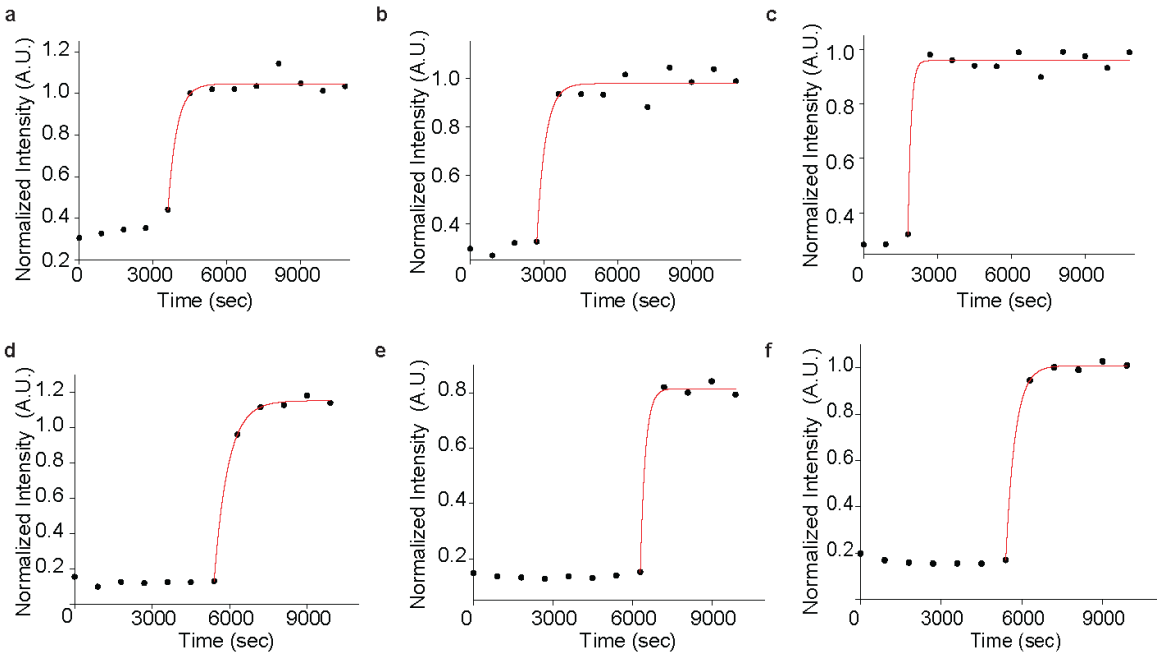

Figure A.13: Single traces demonstrating the increase of fluorescence inside the vesicles due to the influx of (a-c) Atto 633 and (d-f) GFP protein through no lid pore LGC-N. The traces are fit using mono-exponential model.

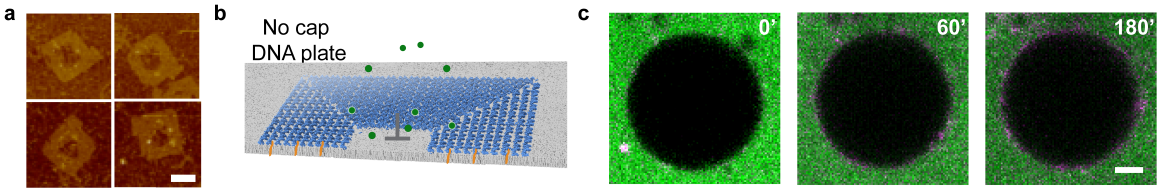

Figure A.14: (a) AFM images of the no cap DNA plate. Compared to the AFM images of the original LGC, the region around the hole in the middle of this structure has the same height as the rest of the structure showing the absence of the pore forming stem region in this structure. (Scale bar: 50 nm). The data is representative of n=3 technical repeats. (b) Schematic of the no cap DNA plate structure inserted into the lipid bilayer of a GUV. Due to the absence of the pore, dye influx should not happen. (c) The cy3 labelled no cap DNA plate is able to insert into the GUV as seen by the magenta around the GUVs. But due to the lack of pore formation, no dye influx is observed even after 3 hrs. This shows that the cholesterol insertion itself is not causing the dye influx but the ability of the structure itself to form a pore in the membrane is leading to transport of dye across the membrane. (Scale bar: 5µm). The data is representative of n=2 independent experiments.

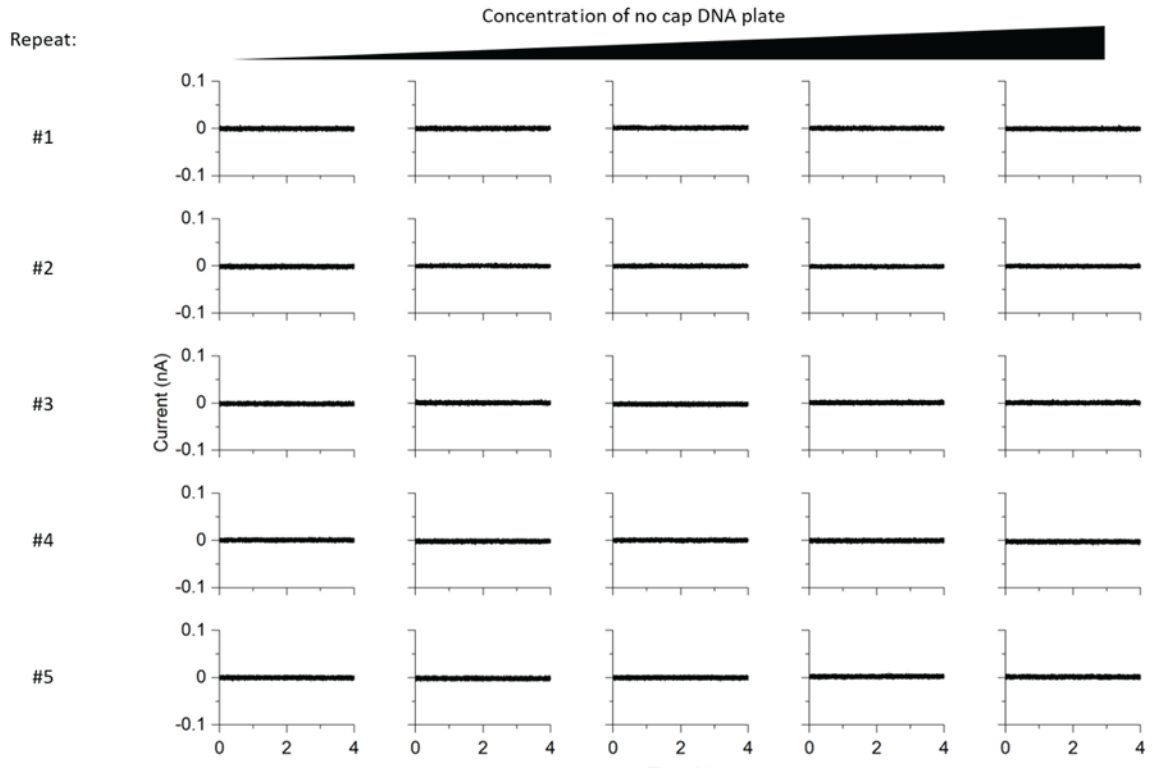

Figure A.15: A no cap DNA plate does not cause pore forming currents. Single-channel current recordings of DPhPC membranes after the addition of increasing concentrations of LGC-N without the pore forming cap region. Even after high concentrations of the DNA plate have been added, no pore forming currents were recorded.

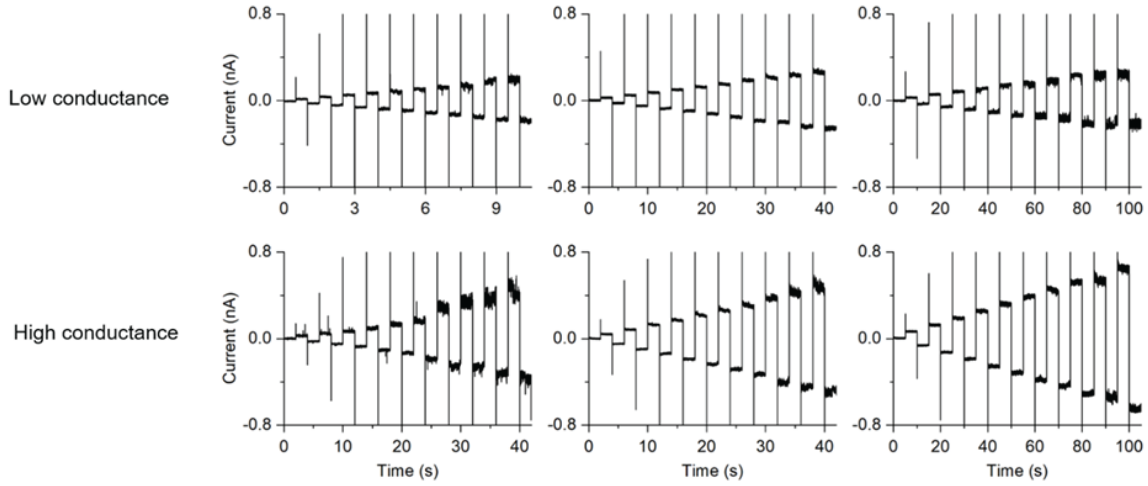

Figure A.16: LGC-N has high and low conductance states. Example electrophysiological traces showing six individual pore insertions of LGC-N, three low conductance pores (¡5 nS) and three high conductance pores (¿5 nS). Example traces measured by alternating voltage in +/- 10 mV steps starting at 0 mV and ending at -100 mV.

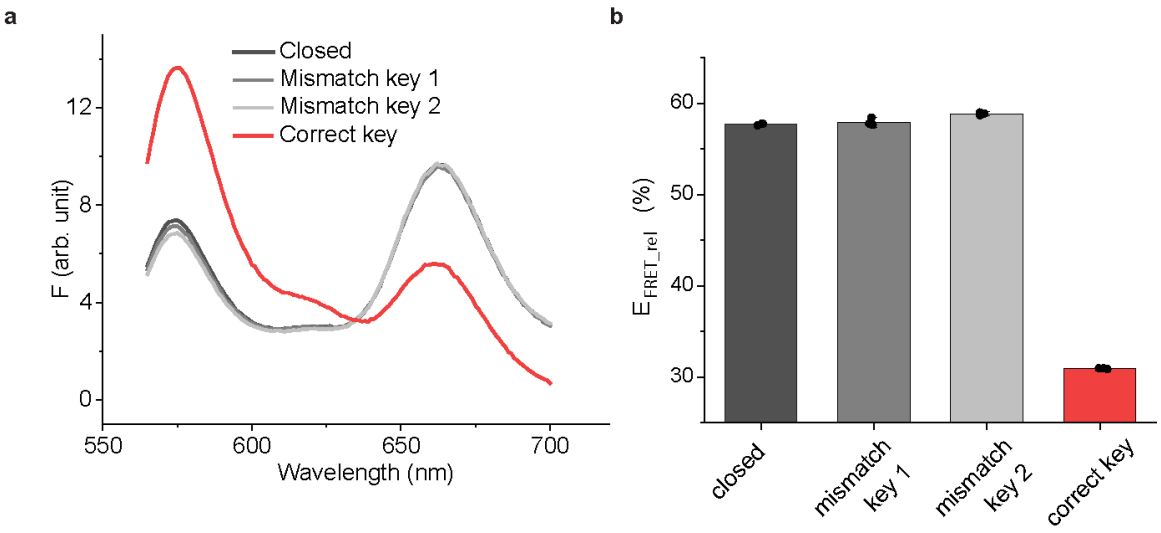

Figure A.17: (a) FRET spectra and (b) corresponding FRET efficiencies - for opening of LGC with closed lid by mismatch key and correct key. FRET spectra and FRET efficiencies of the LGC with closed lid with two different sets of mismatch keys behave similar to closed lid structure only, i.e. – low donor fluorescence at $\lambda_{max}Cy3$=564nm and higher acceptor fluorescence at$\lambda_{max}Cy5$=670nm (a-i; black, light grey and dark grey curves) and higher FRET efficiency, a-ii; black, dark grey and light grey bars). Whereas the same with the correct opening key (Fig.1 - red) leads to opening of the lid and hence shows higher donor fluorescence at $\lambda_{max}Cy3$=564nm and lower acceptor fluorescence at $\lambda_{max}Cy5$=670nm (a, solid red curve) and higher FRET efficiency (b, red bar). The FRET efficiency bars and error bars represents mean relative FRET efficiency and standard deviation of the mean respectively, obtained from three technical replicates.

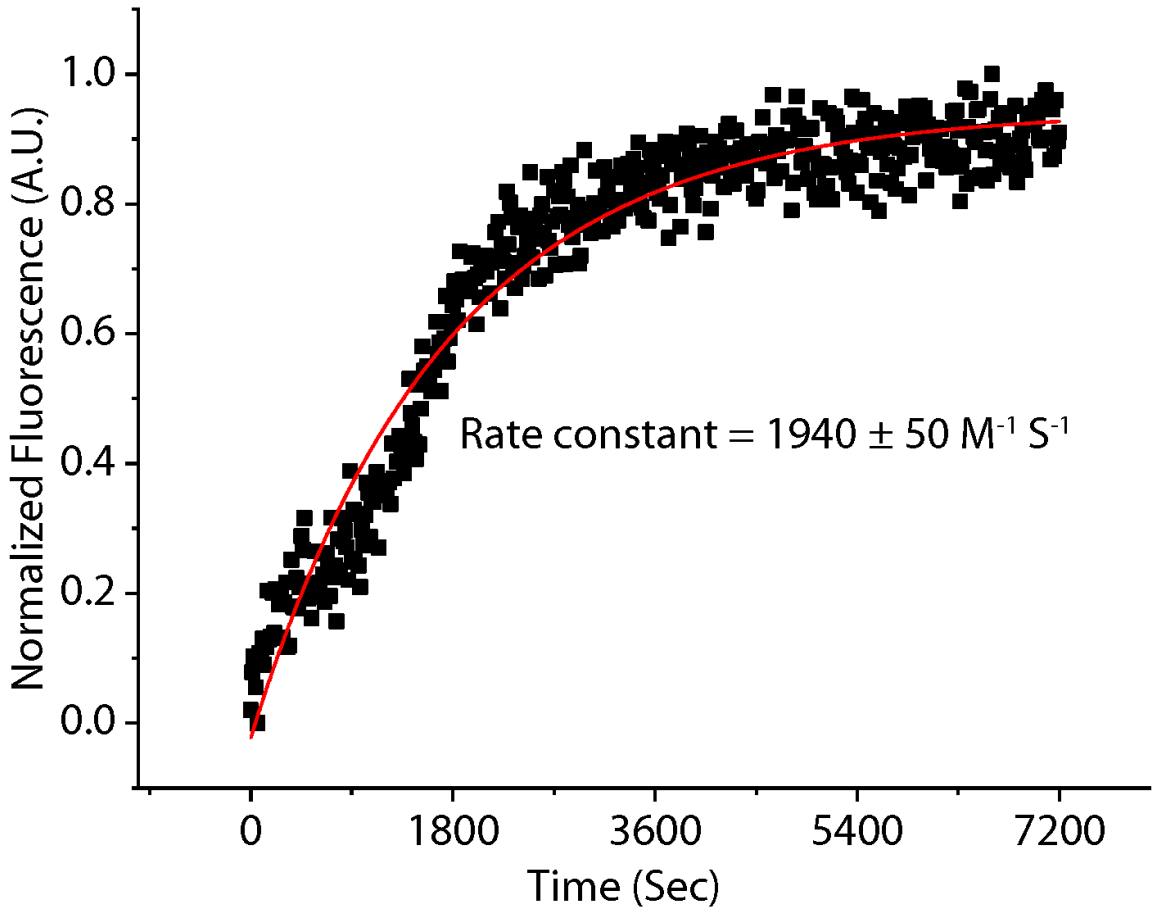

Figure A.18: Kinetics of lid opening. Data is fitted with second order kinetic rate equation ($R^2 = 0.94995$)$toobtain Rate constant = 1940 \pm 50 M^{-1} S^{-1}$.

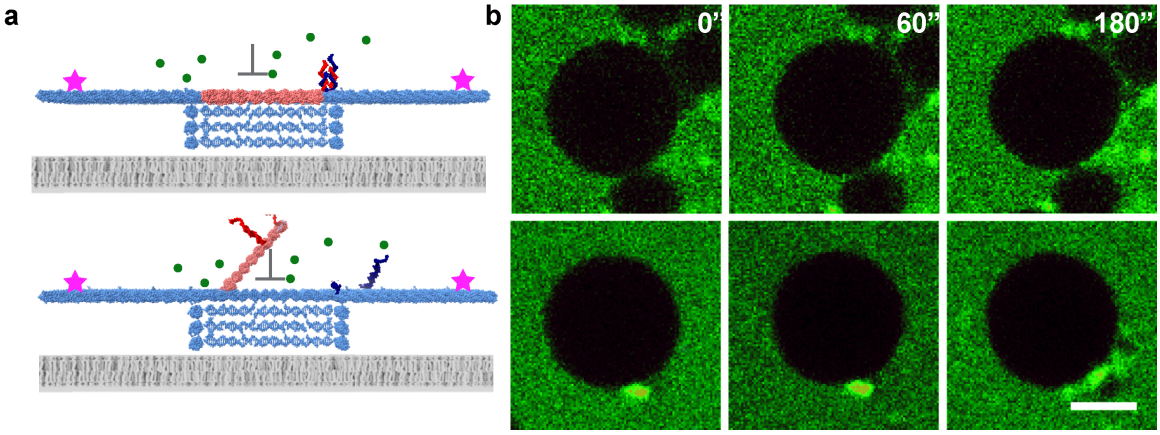

Figure A.19: Negative control experiments for Fig. 3b-ii in the main text. (a) Cy3 labelled LGC structures (magenta) without cholesterol modification don't bind to the GUV membrane. (b) Unmodified LGC with closed lid (top panels) or with opened lid (bottom panels) does not show any influx of atto-633 dye (green) into GUVs. Scale bar- 10 µm. The data is representative of n=3 independent experiments.

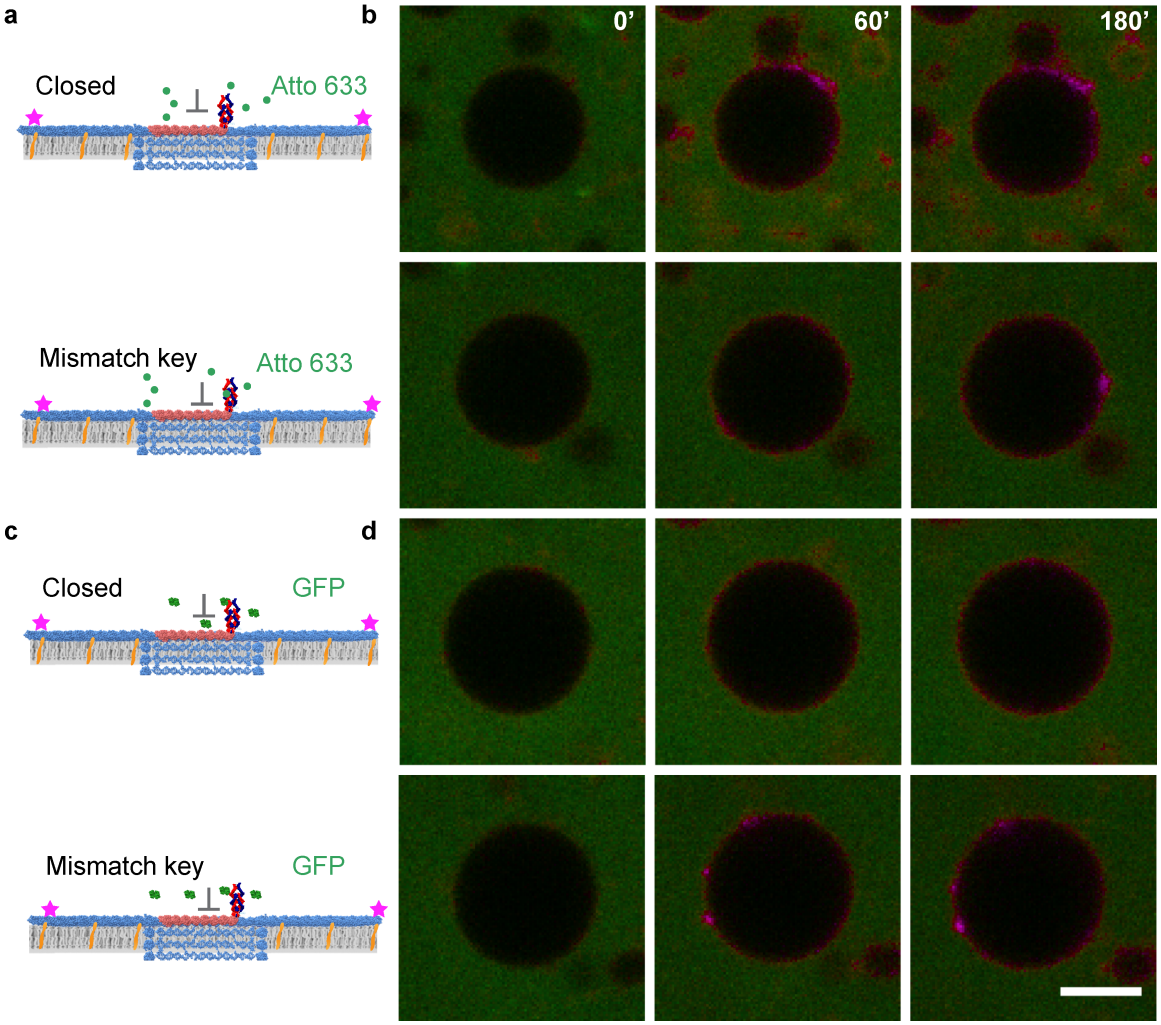

Figure A.20: (a) Scheme and (b) confocal images of Atto 633 influx in GUVs showing – top: Cy3 (magenta) and cholesterol labelled LGC with closed lid inserts in GUV but prevents Atto 633 influx. Bottom – addition of mismatch key does not open the LGC lid and thus no Atto-633 influx is observed unlike that in the case of correct opening key in Fig. 3e in the main text. The data is representative of n=3 independent experiments. (c) Scheme and (d) confocal images of GFP influx in GUVs showing – top: Cy5 (magenta) and cholesterol labelled LGC with closed lid inserts in GUV but prevents GFP influx. Bottom – addition of mismatch key does not open the LGC lid and thus no GFP influx is observed unlike that in the case of correct opening key in Fig. 4b in the main text. The data is representative of n=3 independent experiments. Scale bar: 10 μm.

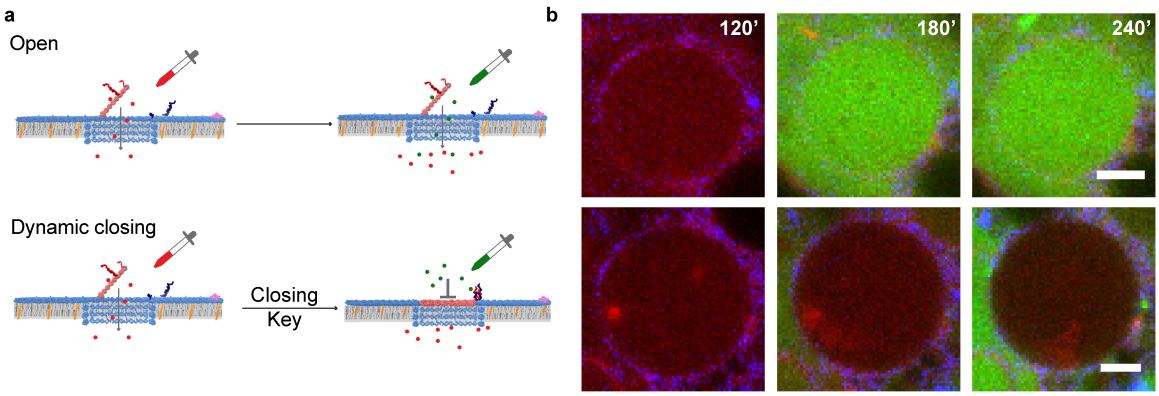

Figure A.21: (a) Scheme and (b) Fluorescence microscopy images to show dynamic closing using two dyes. First a red dye (Atto 633) is added to the LGC-O. Due to the open pore the dye is able to influx into the vesicle. Later the reverseclosing key is added only to the bottom panel. In the top panel the pore remains open while in the bottom panel the reverseclosing key renders the pore closed. A green dye (Atto 488) was then added to both samples. The dye only influxes into the vesicle where the pore is open. The data is representative of n=2 independent experiments. (Scale bar: 5 mum)

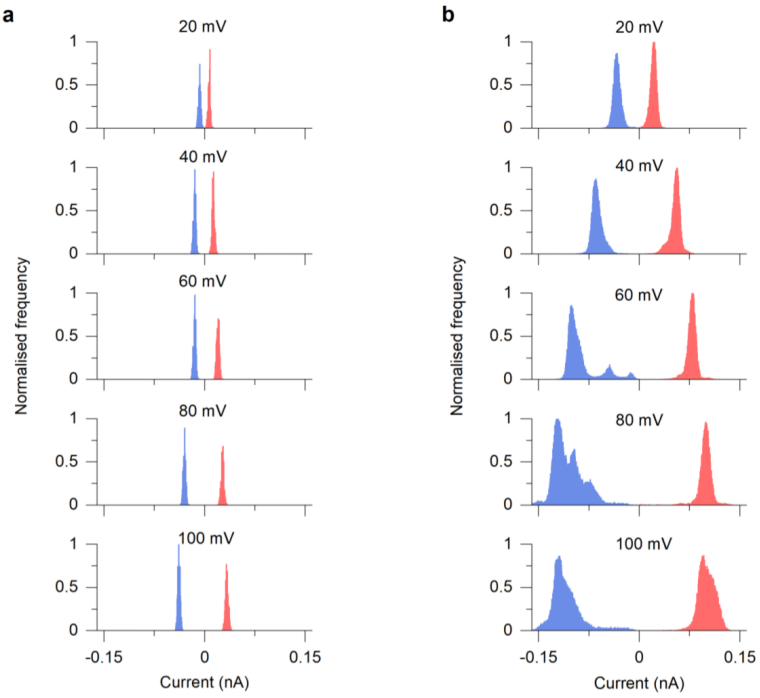

Figure A.22: All point histogram analysis of (a) LGC-closed and (b) LGC-open at positive (red) and negative (blue) 20, 40, 60, 80 and 100 mV.

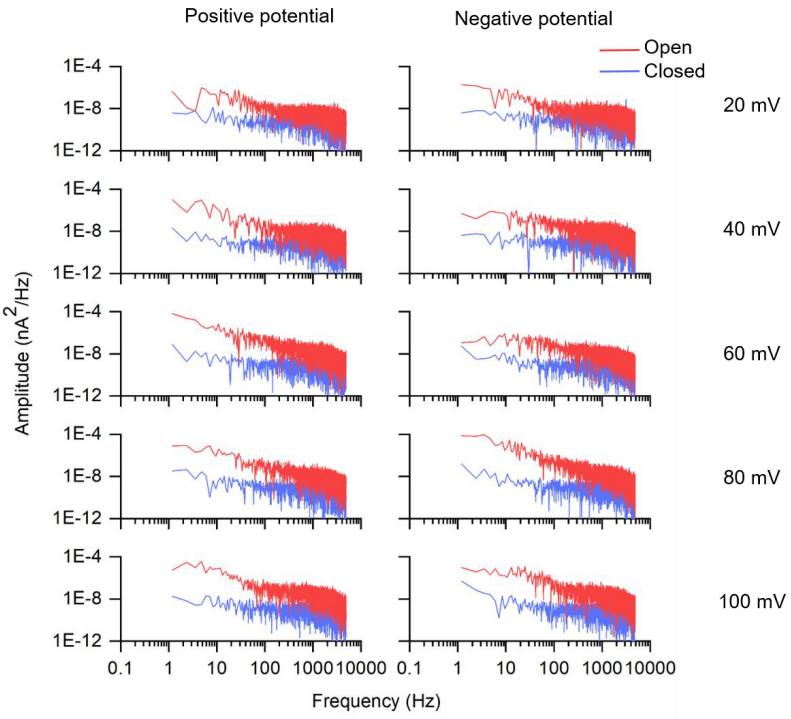

Figure A.23: LGC-O has a greater noise profile in comparison to LGC-C. Power spectrum analysis of LGC-C (blue, closed) and LGC-O (red, open) at positive and negative potentials ranging from 20 mV to 100 mV at 20 mV intervals.

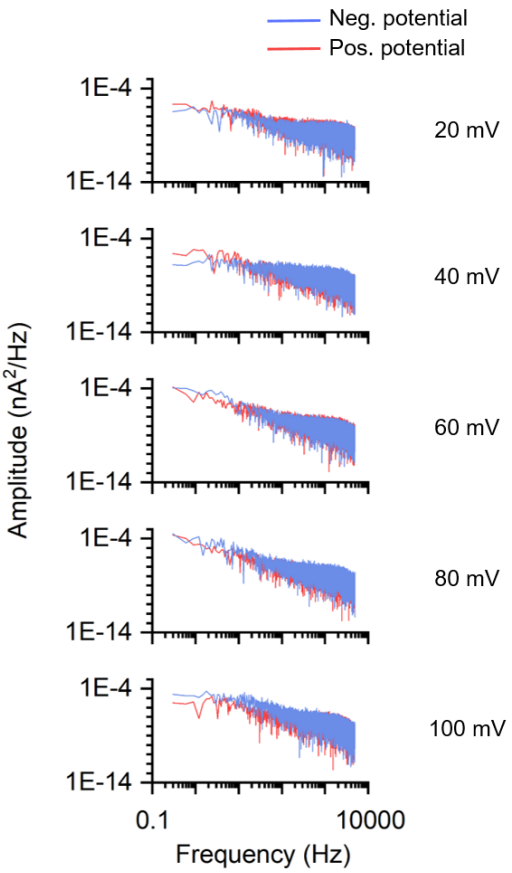

Figure A.24: LGC-O has more noise at negative potential. Power spectrum analysis of LGC-O at negative (blue) and positive (red) potentials, ranging from 20 mV to 100 mV at 20 mV intervals.

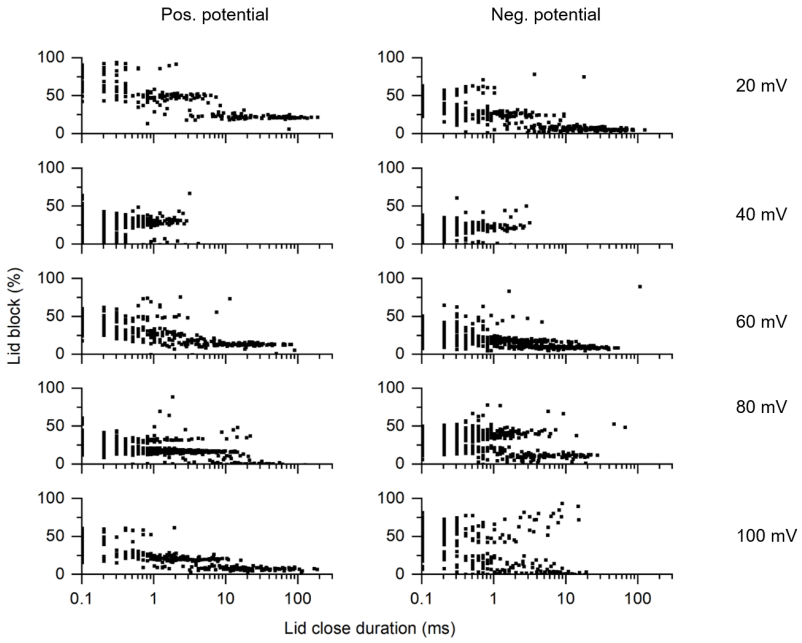

Figure A.25: LGC-O has a higher frequency of gating effects at negative potentials. Scatter plots of lid closure time compared to the percentage block in current of closure events at positive and negative membrane potentials ranging from 20 mV to 100 mV in 20 mV steps.

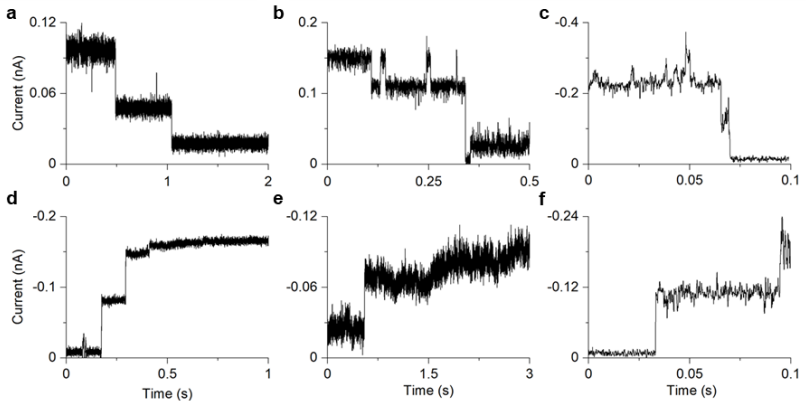

Figure A.26: (a-c) Dynamic closing of open DNA pores at 10 mV (a), 50 mV (b) and -50 mV (c). ClosingReverse key DNA strands added at a concentration of 15 nM to the buffer solution at 37°C. (d-f) Dynamic opening of closed DNA pores at -10 mV (d), -20 mV (e) and -50 mV (f). Opening DNA strands added at a concentration of 15 nM to the buffer solution at 37°C.

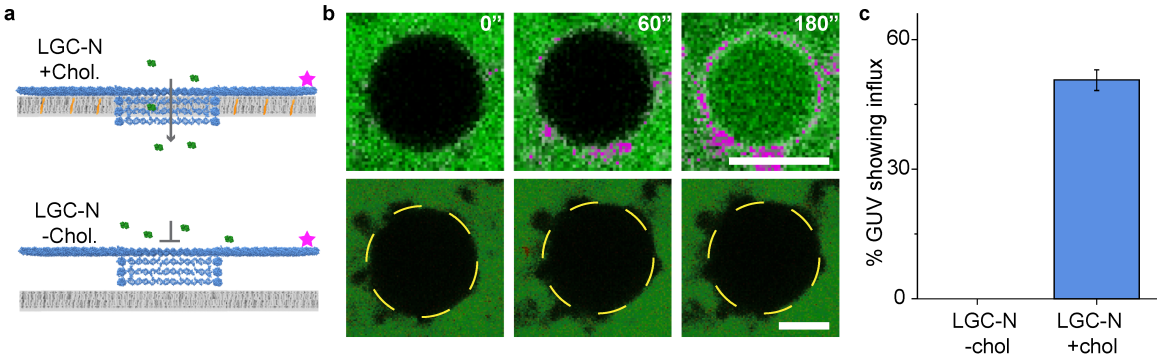

Figure A.27: (a) GUV dye-influx assay scheme and (b) their respective time series confocal images at the given intervals with Cy5-labelled LGC-N (magenta) and GFP (green). Top: Cholesterol modified LGC-N (LGC-N +Chol) readily interacts with bilayer (magenta circle around GUVs) and their insertion leads to influx of the atto-633 dye inside the GUV interior. Bottom: LGC without cholesterol modification (LGC-N -chol) does not interact with bilayer (no magenta circle around GUV) or insert into the GUV, showing no dye influx over the course of 3 hours. The data is representative of n=3 independent experiments. Scale bar: 10 µm. (c) Bar plot showing percentage of GUVs showing a filled interior after 3 hours. Data shows average percentage of influx and error bars show standard deviation of mean percentage influx counted from 3 independent experiments across n = 52 GUVs in case of LGC-N + Chol and n = 124 for LGC-N-Chol.

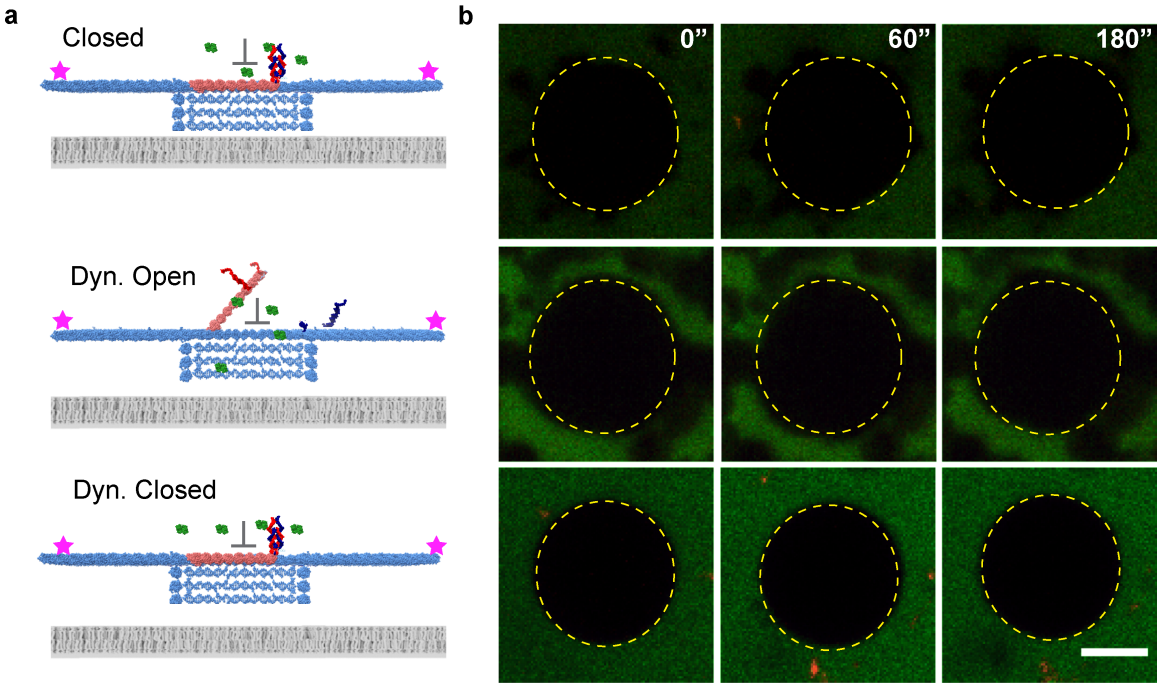

Figure A.28: Negative control experiments for main text Fig. 4a-ii. (a) Cy5 labelled LGC structures without cholesterol modification don't bind to the GUV membrane. (b) GUV influx assay with non-cholesterol LGC, no lid (top row), with closed lid (middle row) or with opened lid (bottom row) does not show any influx of GFP into GUVs. The data is representative of n=3 independent experiments. Scale bar: 10 mum

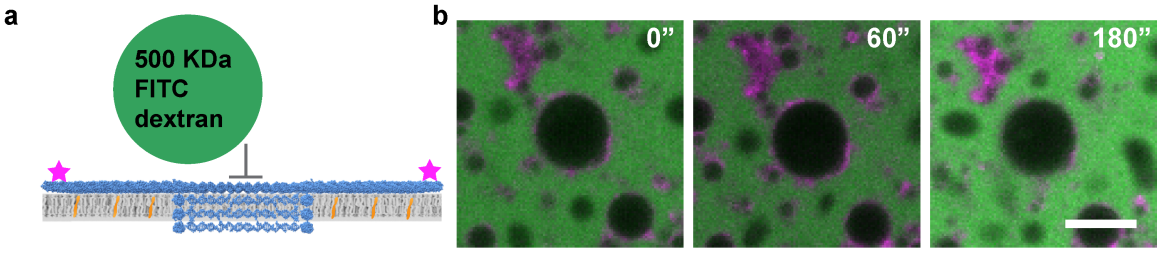

Figure A.29: Size-selective transport through nanopore. Cy3 (magenta) and cholesterol labelled nanopore without lid inserts through the bilayer but a large molecule such as 500 kDa FITC-Dextran (green) cannot pass through the nanopore. The data is representative of n=3 independent experiment. Scale bar: 10 mum

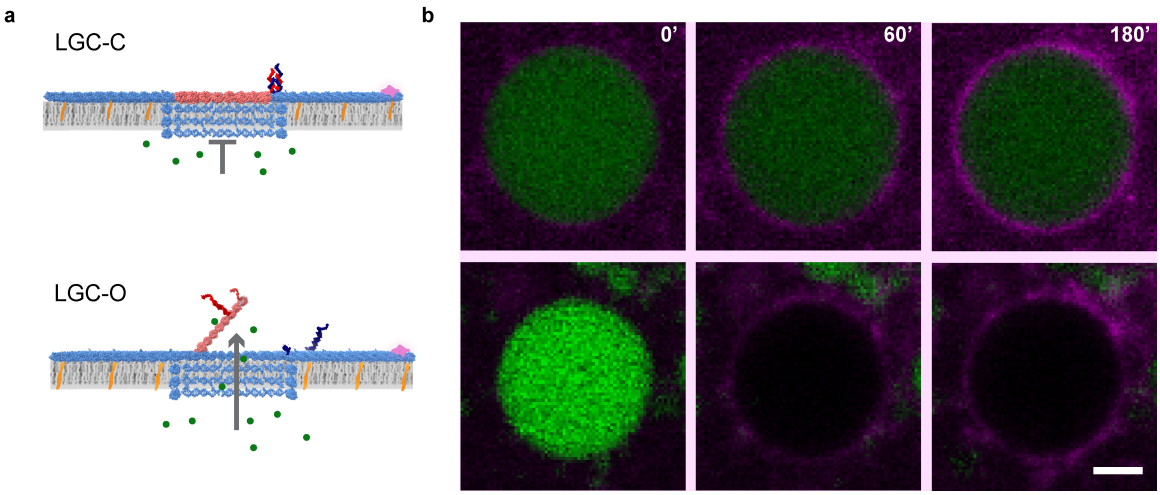

Figure A.30: (a) Schematic of LGC inserted into the lipid membrane of a GUV loaded with cy3 labelled DNA strand (8 nucleotide long). On insertion of LGC-C, the cargo inside the GUV cannot be released outside as the channel is blocked (top) but in the open state the cargo can be released to the outside (bottom). (b) The cy3 labelled LGC-N (magenta) has inserted around the GUV and the cargo inside of the GUV (green), stays inside when the LGC is in closed state. But after the LGC is opened using the key, the cargo is able to leave through the pore. This shows that the structure can potentially be used in drug delivery. The data is representative of n=2 independent experiments. Scale: 5mum

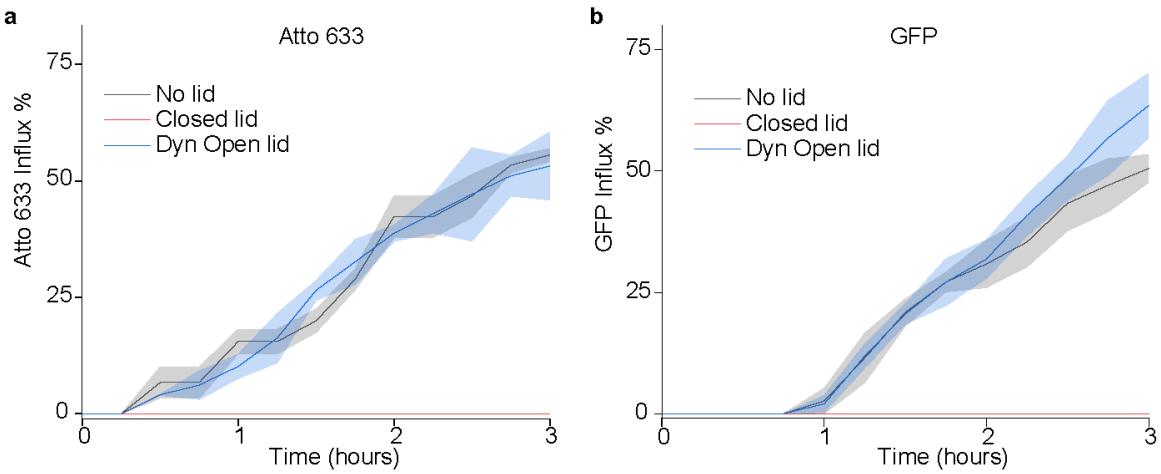

Figure A.31: Rate of influx % for (a) Atto-633 dye and (b) GFP protein. Although atto-633 and GFP differs in hydrodynamic diameter, both show similar rate of influx %, perhaps because the LGC pore being large enough compared to both Atto 633 as well as GFP. Moreover, the no lid and dynamically opened lid LGC pores show similar rate of influx % whereas the closed lid pore showing no influx % indicates that the open lid is equivalent to no lid in terms of passage of molecules through the LGC channel. Lines represent average fraction of GUVs (%) that had full influx of Atto-633 dye or GFP protein and grey or blue shades represent standard deviation of the mean obtained from n = 156 GUVs.

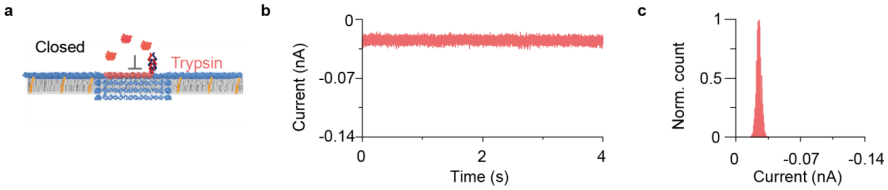

Figure A.32: (a) Trypsin does not translocate through LGC-C. Schematic illustration of LGC-C, with the lid impeding the translocation of trypsin. (b) Example trace after addition of 6.6 µM trypsin shows no translocation events. (c) Current histogram shows a single peak, indicative of a single current level.

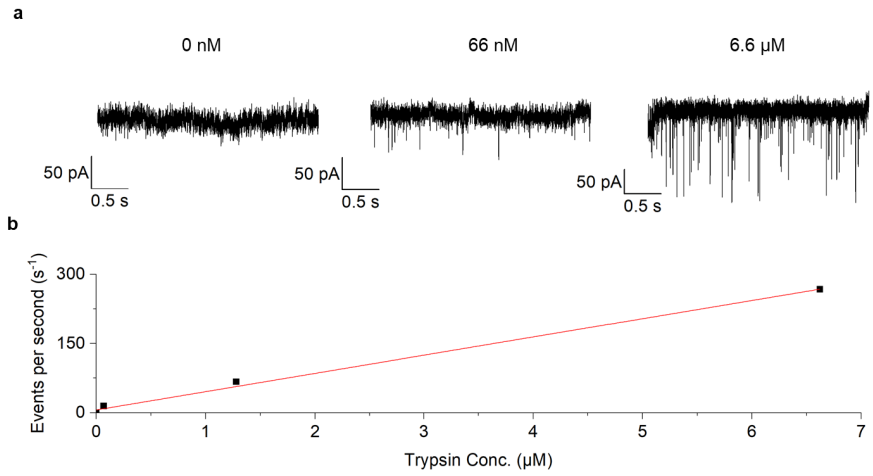

Figure A.33: Concentration-dependent trypsin translocation through LGC-N at 70 mV. (a) Example traces showing increasing concentrations of trypsin from 0 nM to 6.6 μM. (b) Graph showing the relationship between trypsin concentration and translocation events per second seen.

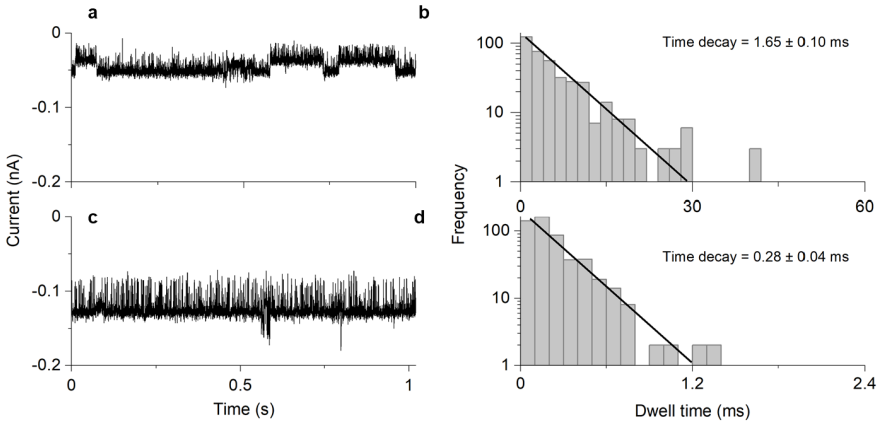

Figure A.34: Voltage-dependent trypsin translocation through LGC-N at (a-b) -20 mV and (c-d) -50 mV. (a+c) Example traces and (b+d) frequency histograms reveal that lower voltages result in a longer dwell time as shown by the time decay, calculated from the single-exponential fit to the dwell time frequency histograms. Data recorded using Orbit 16.

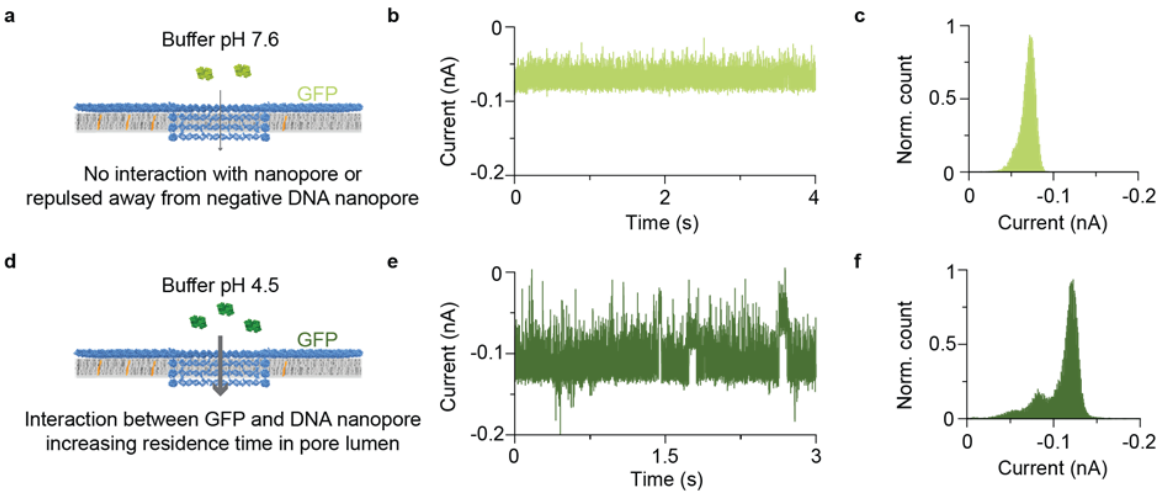

Figure A.35: (a) GFP translocation is not seen with normal electrophysiological buffers of pH 7.6 due to net negative charge of the GFP in these conditions. (b) LGC-N example trace after addition of GFP at pH 7.6. (c) Current frequency histogram showing a single peak after addition of GFP to LGC-N at pH 7.6. (d) At a buffer pH below the pI of GFP translocation events can now be resolved. (e) LGC-N example trace after addition of GFP at pH 4.5, showing an increase in translocation events. (f) Current frequency histogram showing multiple peaks, indicative of the different current levels caused by translocating GFP. Data recorded using the Orbit 16.

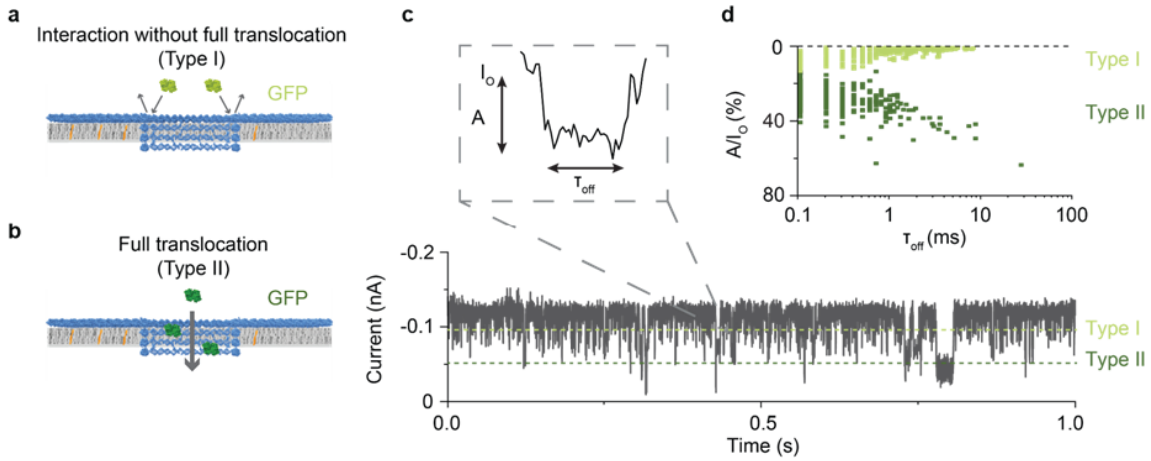

Figure A.36: (a) GFP translocation clusters into type I and type II events. Type I events are predicted to be GFP interaction with the nanopore lumen, without full translocation. (b) Type II events are predicted to be fully translocating GFP. (c) Example trace showing translocation events after addition of GFP at pH 4.5. Inset shows a single isolated translocation event with respect to amplitude (A), open current (I_O) and dwell time (τ_{off}). (d) Scatter plot representing off and A, each point in the diagram represents an individual encounter event of protein with the DNA nanopore. Points cluster into type I (light green) and type II (dark green) events. Data recorded using the Orbit 16.

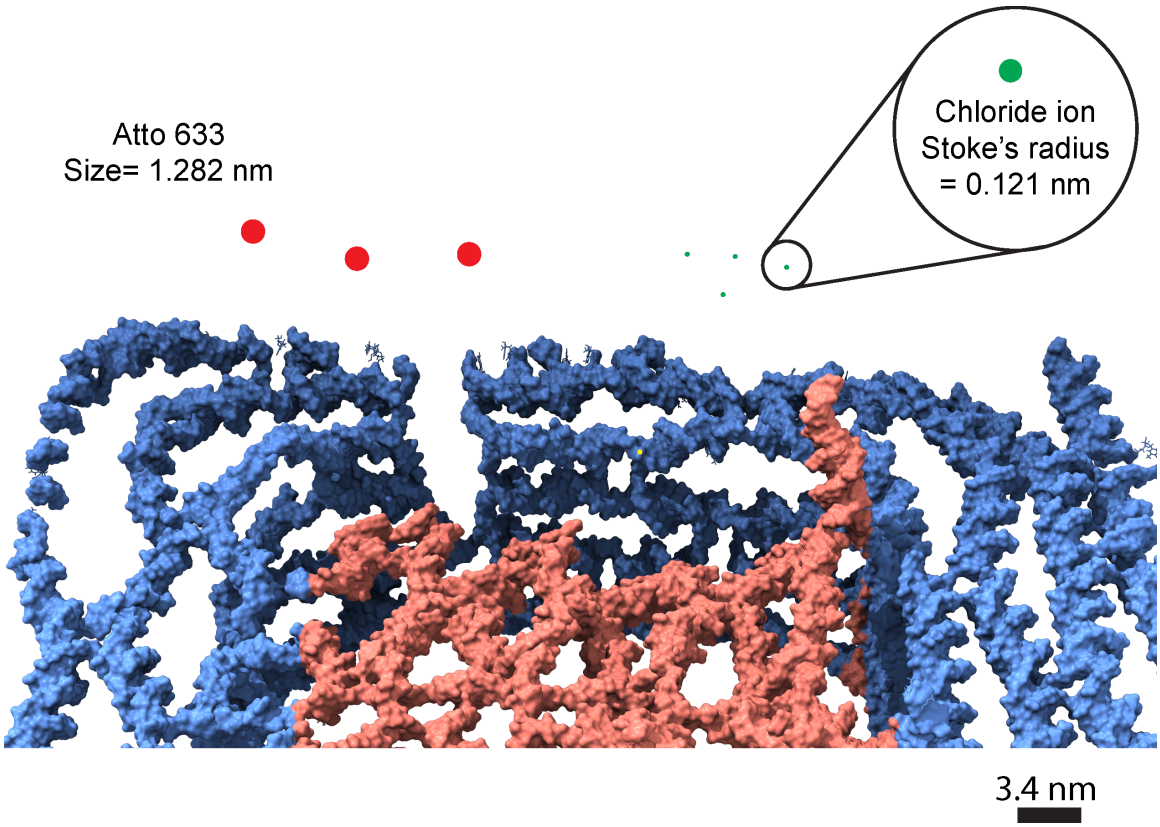

Figure A.37: Comparing the sizes of Chloride ion (green) and Atto 633 dye (red) used in electrophysiological measurements and dye influx confocal assay respectively to the close up of LGC-C (plate-blue, lid-pink). The scale bar is 3.4 nm or the length of one turn of B-form duplex DNA. Dye transport studies (Figure 3b) show that the closed lid nanopore is not permeable to the larger dyes (Atto 633 diameter = 1.3 nm), suggesting the leak of ions only (chloride ion Stoke's radius = 0.1 nm).

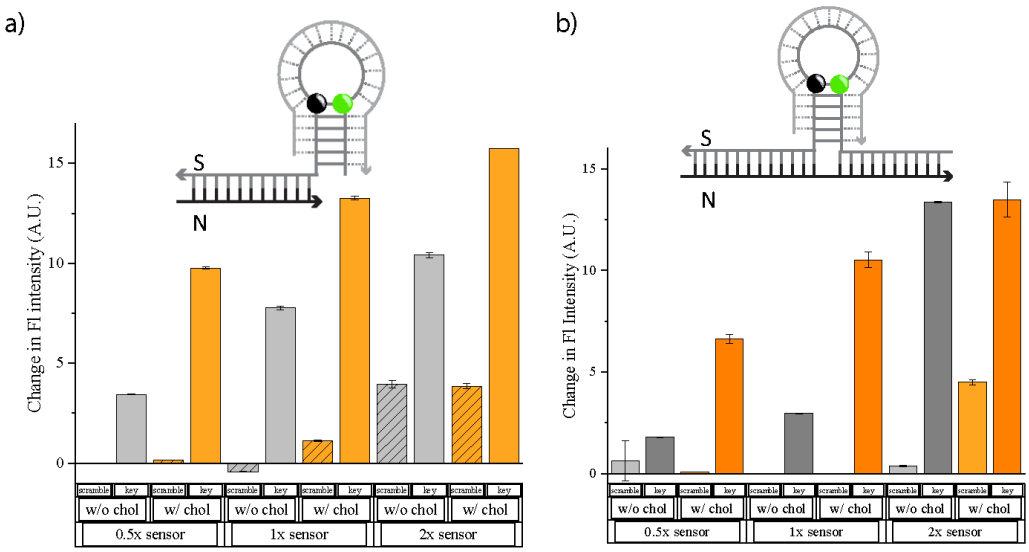

Figure A.38: (a) Bar plot showing the change in fluorescence intensity of NpS (sensor 1) when incubated with different oligonucleotide sequences in solution. Orange bars correspond to cholesterol modified NpS and grey bars correspond to non cholesterol modified NpS (sensor-1). The lined bars correspond to scrambled sequence and non lined bars correspond to target sequence.

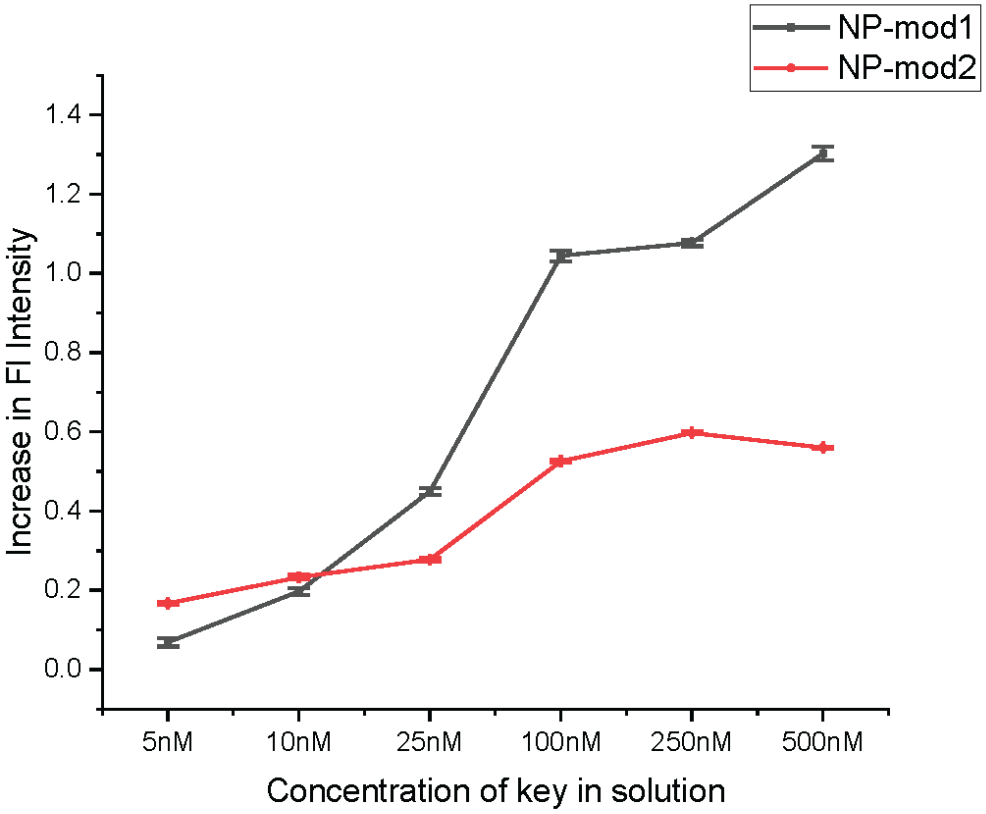

Figure A.39: Fluorescence intensity changes when NpS was incubated with different concentrations of target sequence

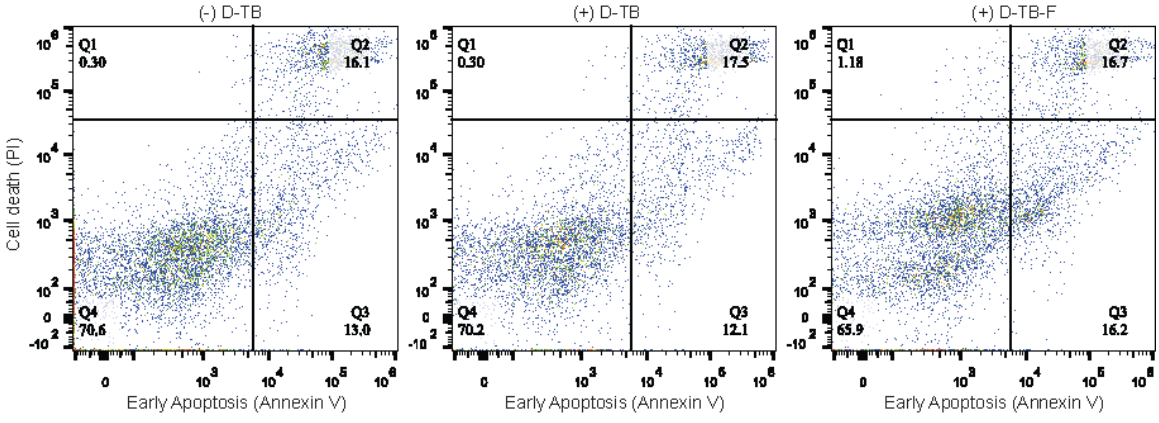

Figure A.40: Flowcytometric analysis of SKBR3 cells incubated with NK cells (left), NK cells with D-TB (middle) and NK cells with D-TB-F (right)

Name	Sequence
NL-core-1	GTAGCATTCCACAGTTTTGTCGTCTTTCCGGAATTGCGAATAATACGCGAAAC
NL-core-2	ACGTTGAAAGCGTAACGATCTAAAGACAGCCC
NL-core-3	TCATAGTTGAACCGCCACCCTCAGGAGACTCC
NL-core-4	ACCCTCATCTTACCGAAGCCCTAAATAGCA
NL-core-5	AGAGAGATAGAGCAAGAAACAATGTTTTAAGA
NL-core-6	AAAGTAAGGTACTCAGGAGGTTTAGGGGTTTT
NL-core-7	GTATCACCCAGATAGCCGAACAAAGTTAAGCC
NL-core-8	ATCCCAACAAAATAAACAGCCAGTTACCAG
NL-core-9	AAGGAAATATAAGTATAGCCCGCGTCGAGA
NL-core-10	AGTAAGCAGGATTAGGATTAGCGTACCGCC
NL-core-11	TAAGAGGCTAACCGCCACCCTCAGAttttGCCACCACCCTCA
NL-core-12	TGAGCCATCCAGGCGGATAAGTGCGAATAGGT
NL-core-13	TCAAGAGAGTCATACATGGCTTTTGAACAGGAGCTGAAACATGAAAG
NL-core-14	ATTGGCCTATTCACAAACAAATAAATCCTCATTAACCGTTCC
NL-core-15	AGCCCCCTTTGGGAATTAGAGCCACACCGACT
NL-core-16	AATCAAAATCATTACCAGAGCCACCACCGG
NL-core-17	GGGTAACGGACGGCCAGTGCCGCGAAGAGAGTTG
NL-core-18	GCCTGAGTTTGATTAGTAATAACACGACGTCGATGTTTTTACCCTAAA
NL-core-19	CTCGTCAAAGGAAGCTTGCttttATG
NL-core-20	AACCGCCTCAGGAGGTTGAGGCAGTTTAACGG
NL-core-21	TTTTCAGGAACACTGAGTTTCGTCGAACCGAA
NL-core-22	GAATTACCAGTCAGGACGTTGGGACGGAACAA
NL-core-23	CATTATTACAACACTATCATAACCTCAGAAAA
NL-core-24	AGTAAGAGCAGGTAGAAAGATTCAACTGGCTC
NL-core-25	TTCATCACCAGGCGCATAGGCTTCAGTTGA
NL-core-26	GATTTAGCGCCAAAAGGAATTACCCGTATA
NL-core-27	ATACATAAGAATACCACATTCAACATGAACGG
NL-core-28	TATTCATTCTTTGAAAGAGGACAGGGAACCCA
NL-core-29	TGTACCGTGATAGCAAGCCCAATATTCGGAAC
NL-core-30	GGTCAGTGAATGCCCCCTGCCTATTAATGCAG
NL-core-31	ACCGCCACGAACCACCACCAGAGCAAGCAAAT
NL-core-32	ATTTAAATAACAGGAAGATTGTATCGAGGCAT
NL-core-33	GTGGTTCCGGCGCCAGGGTGGTTTTTCTTATCCTAGTTTGGAACAAGAGATCCCCGG
NL-core-34	TACGCCATCGACTCTAGAGGTCCACTGCCCCAGCAGGCGAAATTCACCAGTG
NL-core-35	GGAAGGGCCGAATTCGTAATCGGTTGAGTGTTGTTCCGTTTGATG
NL-core-36	AAGAATCGAGATAGATGGTCATttttAGCTGTTTCCTGCAAAGCGCC
NL-core-37	AAGAACGGGTATTAAACCATATCAACAATAGttttATAAGTCCTG
NL-core-38	AACAAGAAAAATACCAATCAATAATCGGCATCATTACCGCGCCCACGGTATTC
NL-core-39	CAAATCAGTACGAGCATGTAGAAAATATCCCA
NL-core-40	TCCTAATTGCCAGTAATAAGAGAACATACATA
NL-core-41	TTTTCGAAACACCGGAATCATACGTTAAAT
NL-core-42	GACAAAAAACATATAAAAGAAACAGAGGCA
NL-core-43	TAGAAAATATATAAAGTACCGACAAttttAAGGTAAAGTAAT
NL-core-44	AAGGTGGCGGGCGACATTCAACCGATGGAGGGACAGTATGTTAGCAA
NL-core-45	GAAACGTCATGAAACCATCGATAGCAGCACCGTAGCGCCAAA
NL-core-46	ACTTTGCTTTGACCGTTGTttttAGC
NL-core-47	CGTGAACCCAGGGCGCGTAATACTTCTAGAAGAACT
NL-core-48	GTAGCGCGGCACCATTACCATTAGAAATTATT
NL-core-49	TCTGTCCAGCAGAACGCGCCTGTTTCTTACCA
NL-core-50	ATACCCAACCGAGGAAACGCAATACCTAATTT
NL-core-51	TTAACGTCGAGCGTCTTTCCAGAGAACATGTT
NL-core-52	CAGCTAATGACGACGACAATAAACAAGACTCC
NL-core-53	CATTAAAGAAGAACTGGCATGATTATAACGGA
NL-core-54	AAACCAGGTGTGAAATTGTTCCGGAAGCATAAAATCAA
NL-core-55	AGAACAATATCACGCAAATTAACGAGCACCCGCC
NL-core-56	AGGGAAGAAAGCGAGCGGGTTAGGAGTAAAAG
NL-core-57	AAAAACGCAGTGAGGCCACCAATCAG
NL-core-58	TCACACGACCATTAAAAGGGACATTCTGGC
NL-core-59	AAATGGATTACGCCAGAATCCGGATTTTAGACAGGAAAGTGAGCGTGCC
NL-core-60	GATTGACCTGGGATAGGTCACGTTGGTGTAGATGTTGTTAAA
NL-core-61	GACAGTATGATTCTCCGTGGGAACCATCAAAA
NL-core-62	ATTCGCATACCCCGGTTGATAACTCGTTTA
NL-core-63	ATCATATGTTAAATTTTTGTTAAATCCATTTTTATCGATGAACGGTA
NL-core-64	GTAAAACTATAGCGAGAGGCTTTTGttttCAAAAGAAGTTTT
NL-core-65	GCCAGAGGTCCAATACTGCGGAATAAGTACGG
NL-core-66	TTCATCTTCGTGTGATAAATAAGGATTACTAG
NL-core-67	AAAAAGCCCAACATGTAATTTAGGCGCAAAGA
NL-core-68	AACAACGCTGTTTAGTATCATATGGGTTTGAA
NL-core-69	GAGTCAAAGCTTAGATTAAGACCGTTATAC
NL-core-70	AAATTCTCTTAATTGAGAATCGTCAACAGT
NL-core-71	CAGTAGGGTACCAGTATAAAGCCATTGAAAAC
NL-core-72	TCTGAGAGTTTTCCCTTAGAATCCTTGTTTGG
NL-core-73	ATTATACTATCAATATAATCCTGACTAAAATA
NL-core-74	GGCAATTCTCTGAATAATGGAAGGCGTCGCTA
NL-core-75	GATTAGAGCTATCATCATATTCCTGttttATTATCAGATGAT
NL-core-76	TTTTACATCGGGAGAAACAGTTAGAACCTACttttCATATCAAAA
NL-core-77	TTATTTGCACGTAGGTTTAACGTCAGATGGGCGAATTATTCATTTAACATCAA
NL-core-78	TGAGCAAAATTGCGTAGATTTTCAAAACAGAA
NL-core-79	ATAAAGAACCAGAAGGAGCGGAATCGTCAATA
NL-core-80	GAAACCACAAATCACCATCAATAAGGCCGG

Table A.1: Core sequences of no lid pore (LGC-N)

Name	Sequence
NL-core-81	TATATTTTATTCAAAAGGGTGAGAATGATATT
NL-core-82	CAACCGTTAACATTATCATTTTGCAGTATTAG
NL-core-83	GTTTGAGTCTAGCTGATAAATTAATAATGTGT
NL-core-84	TGACCATTCTGCGAACGAGTAGTGCCGGAG
NL-core-85	AGGGTAGCCCGAACGTTATTAAGTATTAAA
NL-core-86	CTATCAGGCTATTTTTGAGAGATCACAGTTGA
NL-core-87	TAACCTGTAGTTTCATTCCATATATTTAGACT
NL-core-88	GGATAGCGGGGTAATAGTAAAATGTGGAGCAA
NL-core-89	CCAGACGAATAAAACGAACTAAAGAAAAAT
NL-core-90	TTCAGAAAACGATAAAAACCAAAAGCATGTCA
NL-core-91	GGAAGCAAACGAGAATGACCATAATTAAACAG
NL-core-92	CCCCTCAAATGCTATCAAAAATCAGGTCTTCGAGCTTCAAAGCGAATTAGAGA
NL-core-93	CAGAAGCAAAGCGGATTGCCGTCATAAATATttttTCATTGAATC
NL-core-94	ATAATTCGTCATTGCCTGAGAGTCTACAAAGG
NL-core-95	TTTCATCAAACAATTCGACAACTCTTTTAAAA
NL-core-96	CAGCAGCATTTGAGGATTTAGAGGAACAAA
NL-core-97	TCAATATCAATTGAGGAAGGTTATACGCTCAA
NL-core-98	ATAGAAAAAATAAGTTTATTTTGTCCATATTT
NL-core-99	GATAATACAAATGAAAAATCTAAAGCCCTTGCTAGCACTAACAACTA
NL-core-100	AGCCAGCTACATTAAATGTGAGCGTAGCCAGC
NL-core-101	ACGAACCACAGAAGATAAAACAGAGGTGAGGCGGCTGAGAGC
NL-core-102	CAACAGAGAAACATCGCCATTAAAACCCTCAA
NL-core-103	CGTAAGAATTAGTCTTTAATGCGCCACAATCA
NL-core-104	CAATAATAAACCCACAAGAATTGAGAAGCGCA
NL-core-105	ACGCTAACACAATTTTATCCTGAATATTTTGC
NL-core-106	GCCAGTTATCCAAATAAGAAACGAGCCTTTAC
NL-core-107	TTGTATCAGAAAGGAACAACTAAAAGACGTTAGTAAAT
NL-core-108	CTGACCAAACGGTCAATCATAAGGCCGGAACG
NL-core-109	TGTACAGAAGAGTAATCTTGACAACAAAGCTG
NL-core-110	ATTATACCTTATGCGATTTTAAGACCTGACGA
NL-core-111	GTACCTTTAATTGCTCCTTTTGATAATATCGCGTTTTAATTTACCCTGACTATT
NL-core-112	CTACGTTTTAATTTCAACTTTATGGGCTTG
NL-core-113	TTAATTAACCTTGCTTCTGTAAATATATGTGA
NL-core-114	ATAGCGATTAGTGAATTTATCAAACCGGCTTA
NL-core-115	TAAGAACGCGAGGCGTTTTAGCGATATTTTCATCGTAGGATGTCTTTCCTTATC
NL-core-116	AAGAATATTTTCAAATATATTTGAACGCGA
NL-core-117	ATACCGACCTGACCTAAATTTAATAAATGCTG
NL-core-118	GAAAACAAAATTAATTACATTTAATACAAAATCGCGCAGAAATATACAGTAACA
NL-core-119	TGTCTGGATTTAAATATGCAACTACTGTAGCT
NL-core-120	TTCCCAATTAGATACATTTCGCAATTGGGGCG
NL-core-121	AGGTAAAGAAATGCAATGCCTGAGTCTACTAA
NL-core-122	AGACAGTGATAAAAATTTTTAGTTATTTCA
NL-core-123	TTGCCCTCGCCTGGCCCTGA
NL-core-124	AAAGCACTAAATCGGAGGGGTCGA
NL-core-125	GGGAGCCCCCGATATCACCCAAATCAAGTGCCCACTA
NL-core-126	GCGCTttttTAATGCGCCGCTATTAGAGCTTGACGAAGCCG
NL-core-127	GAGGCGGCGTATTGGAAATCGGttttCAAAATCCCTTATGCGGGGA
NL-core-128	CAGCAttttAGCGGTCCACGCTAGCTGA
NL-core-129	AGCTGCATTAATGAACTGGGGTGCCTAATGCACACAA
NL-core-130	AAGTGTAAAGCTCGGCCAACGC
NL-core-131	CGGGCGCTACACTGCCCTCCAGTCGGGAAACCTGTCTAACTCACA
NL-core-132	AGCGGGAGCTGGGCGCTGGCAAGTGTAAAGGAG
NL-core-133	GCTTTCCTCTCACGCTGCGCGTAACAGAAAGGA
NL-core-134	GCGAACGTGGCGCACCACACGTATAACGT
NL-core-135	TTAATTGCttttGTTGCGCTAAACAGGAGATTAAAG
NL-core-136	GAAAACTATATAGAAGGCTTATCATAGCAAG
NL-core-137	ATGCAAATCCAATCGCAAGACAAATAGTTAAT
NL-core-138	GGTTGGGTTATATAACTATATGTGCTGAGAA
NL-core-139	GTGAATAAACTACCTTTTTAACCTATCATAGG
NL-core-140	TACATAAATCAATATAACGGATTCGCCTGAT
NL-core-141	TGCTTTGACAAGTCAATTTCATTTGACCTTTTTTAATGGAAACAG
NL-core-142	AACAAGCAGTTTTACCTCCCGACTTGAGGTTTTGAAGCCTTAAAT
NL-core-143	AGAGAGAATAACATAAAAACAGGTATTATTT
NL-core-144	CAAGATTAGTTGCAGTACCGCACTCATCGAG
NL-core-145	ACCCAGCTAAAAATGAAAATAGCATTTTTTGT
NL-core-146	CGAAGGGGCAAAAGAATACACTTGATAAAGTCGAAATCCGCGACCTGCT
NL-core-147	TCAGCGGAGAATATCGCCAAAACACTCATCTTTGAACGG
NL-core-148	TTAGACGGGAGAATTAACTGAACACTAATATC
NL-core-149	AGGAGCCTAATCTCCAAAAAAAAGATTTTTTC
NL-core-150	AAGCCCGACTTCAAAGAGGTCATTTGGATGGCTTAGAGCTTAATT
NL-core-151	GCTGAATATAATGATCAAAAAGATTAAGAGG
NL-core-152	CGAGCTGAAAAGGTGGCATCAATATTTAGTT
NL-core-153	CCATGTTACTTAGAAACAACTTTCAACAGTT
NL-core-154	CTCATTCAGTGAATAAGGCTTGCGGCTGACC
NL-core-155	AGGCGCAGACCCAAATCAACGTAAGAACCGGA
NL-core-156	AGATGGTACTCCAACAGGTCAGGACCAGACC
NL-core-157	GAAACACCAGAACGAGTAGTAAATATCATTGT
NL-core-158	CAACATGTTTAGCTATATTTTCATATGGTCAA
NL-core-159	TAGTAGTAGCATTGGGAGAAGCCTAACCCTCA
NL-core-160	ACGCAAGAGAAGATGATGAAACACAATTACC
NL-core-161	TATATTCGGTCGCTACAACAGAGGTGAATTTCTTAAGCTCCAAA
NL-core-162	CGCTTTTGTCATGAGGAACCGATAGTTGC
NL-core-163	GAAAGACAGCGGCTACAGAGGCTTTGAATGCCACTA
NL-core-164	TTCTGTATGGGATTTTGCTACCAGTACAAACttttTACAACGCCT

Table A.2: Core sequences of no lid pore (LGC-N)

Name	Sequence
NL-chol-1	GCTCAGTACGCAGTCTCTGAATTTAAGCCAGAtaacaggattagcagagcgagg
NL-chol-2	GGGTTGAGTGAATTATCACCGTGCAAAATCtaacaggattagcagagcgagg
NL-chol-3	ATGGAAAGTATTAGCGTTTGCCATATTAAGTTtaacaggattagcagagcgagg
NL-chol-4	ACCAGTATTTTCATCGGCATTTCATCACTTtaacaggattagcagagcgagg
NL-chol-5	AAGGGGGATGttttTGCTGCAAGGCGCTTTTCATtaacaggattagcagagcgagg
NL-chol-6	CTATTATTTGTACTGGTAATAAGTGTCAGACGtaacaggattagcagagcgagg
NL-chol-7	GCATTGACCCTCAGAGCCGCCATTCGCTATtaacaggattagcagagcgagg
NL-chol-8	AACAGTTCCTTGAGTAACAGTGCGCCGCCAtaacaggattagcagagcgagg
NL-chol-9	CGCCACCACCTCAGAGCCACCACCAACTGTTGtaacaggattagcagagcgagg
NL-chol-10	GCCCCAAATGTAAACGTTAATATTCTCAGAGCtaacaggattagcagagcgagg
NL-chol-11	GTACCGAGCTGATCGGTGCGGGCCTCCCCTCAGAtaacaggattagcagagcgagg
NL-chol-12	CAAACTATttttCGGCCTTGCTGGATCAGTAGtaacaggattagcagagcgagg
NL-chol-13	CGACAGAATCATTGCCTTTAGCGTCAGACTtaacaggattagcagagcgagg
NL-chol-14	TTATTACGAGGTAAATATTGACGGCAAGGCCGtaacaggattagcagagcgagg
NL-chol-15	ATTCGCCAttttTTCAGGCTGCGCGGCGCATCtaacaggattagcagagcgagg
NL-chol-16	GTAACCGTGCATTCAGTTTGAGGGGACGACtaacaggattagcagagcgagg
NL-chol-17	AGTCTGTCCATTACCGCCAGCCATTCCTGAAAGtaacaggattagcagagcgagg
NL-chol-18	TGAGAAGTttttGTTTTTATAATCTCATGGAtaacaggattagcagagcgagg
NL-chol-19	AATACCTACAttttTTTTGACGCTCATTCACCAGtaacaggattagcagagcgagg
NL-chol-20	CCCGTCGCGGCCTCAGGAAGATGGTGCCGGtaacaggattagcagagcgagg
NL-chol-21	ACAAGAGATAACCAATAGGAACGCAAACGGCGtaacaggattagcagagcgagg
NL-chol-22	CACCACGGTTCATATGGTTTACCATATTTTTGtaacaggattagcagagcgagg
NL-chol-23	TGAAAGGTGGTCAGTTGGCAAAGAACTGATtaacaggattagcagagcgagg
NL-chol-24	TCTTTAGGGAACCTCAAATATCAAAATACCGAtaacaggattagcagagcgagg
NL-chol-25	ACTTTACACTGCAACAGTGCCACGTCAGTATTtaacaggattagcagagcgagg
NL-chol-26	TCCTTTGCGTCTGGCCTTCCTGAGTAACAAtaacaggattagcagagcgagg
NL-chol-27	AATGGCTATACGTGGCACAGACAATAATATCCtaacaggattagcagagcgagg
NL-chol-28	AGCCCTAATAGAACCCTTCTGAGCAACAGGtaacaggattagcagagcgagg
NL-chol-29	AACACCGCTATTTACATTGGCAGAATCGTCTGtaacaggattagcagagcgagg
NL-chol-30	GGTGCCGTAAACCGTCTATCAGGGTGTAAAACCCAGGGTTTTCCCAGTTCGGTCATtaacaggattagcagagcgagg
NL-chol-31	AGACGGGCAACGGTTTATTAAAGAACGTGGACCTGCAGGGCTGGCGAtaacaggattagcagagcgagg
NL-chol-32	CATACGAGATCCGCTCACAATTCCGGTTCCGGCACCGCTTCTCGCACTCCtaacaggattagcagagcgagg
NL-chol-33	TCATAGTTGAACCGCCACCCTCAGGAGACTCCtaacaggattagcagagcgagg
NL-chol-34	AAAGTAAGGTACTCAGGAGGTTTAGGGGTTTTtaacaggattagcagagcgagg
NL-chol-35	AAGGAAATATAAGTATAGCCCGCGTCGAGAtaacaggattagcagagcgagg
NL-chol-36	AGCCCCCTTTGGGAATTAGAGCCACACCGACTtaacaggattagcagagcgagg
NL-chol-37	AACCGCCTCAGGAGGTTGAGGCAGTTTAACGGtaacaggattagcagagcgagg
NL-chol-38	CATTATTACAACACTATCATAACCTCAGAAAAtaacaggattagcagagcgagg
NL-chol-39	GATTTAGCGCCAAAAGGAATTACCCGTATAtaacaggattagcagagcgagg
NL-chol-40	TGTACCGTGATAGCAAGCCCAATATTCGGAACtaacaggattagcagagcgagg
NL-chol-41	ACCGCCACGAACCACCACCAGAGCAAGCAAATtaacaggattagcagagcgagg
NL-chol-42	TCCTAATTGCCAGTAATAAGAGAACATACATAtaacaggattagcagagcgagg
NL-chol-43	GTAGCGCGGCACCATTACCATTAGAAATTATTtaacaggattagcagagcgagg
NL-chol-44	CAGCTAATGACGACGACAATAAACAAGACTCCtaacaggattagcagagcgagg
NL-chol-45	GACAGTATGATTCTCCGTGGGAACCATCAAAAtaacaggattagcagagcgagg
NL-chol-46	AAAAAGCCCAACATGTAATTTAGGCGCAAAGAtaacaggattagcagagcgagg
NL-chol-47	AAATTCTCTTAATTGAGAATCGTCAACAGTtaacaggattagcagagcgagg
NL-chol-48	ATTATACTATCAATATAATCCTGACTAAAATAtaacaggattagcagagcgagg
NL-chol-49	GAAACCACAAATCACCATCAATAAGGCCGGtaacaggattagcagagcgagg
NL-chol-50	CAACCGTTAACATTATCATTTTGCAGTATTAGtaacaggattagcagagcgagg
NL-chol-51	AGGGTAGCCCGAACGTTATTAAGTATTAAAtaacaggattagcagagcgagg
NL-chol-52	GGATAGCGGGGTAATAGTAAAATGTGGAGCAAtaacaggattagcagagcgagg
NL-chol-53	TTCAGAAAACGATAAAAACCAAAAGCATGTCAtaacaggattagcagagcgagg
NL-chol-54	AGCCAGCTACATTAAATGTGAGCGTAGCCAGCtaacaggattagcagagcgagg
NL-chol-55	CAACAGAGAAACATCGCCATTAAAACCCTCAAtaacaggattagcagagcgagg
NL-chol-56	CGTAAGAATTAGTCTTTAATGCGCCACAATCAtaacaggattagcagagcgagg
NL-chol-57	TCAAGAGAGTCATACATGGCTTTTGAACAGGAGCTGAAACATGAAAGtaacaggattagcagagcgagg
NL-chol-58	ATTGGCCTATTCACAAACAAATAAATCCTCATTAACCGTTCCtaacaggattagcagagcgagg
NL-chol-59	AAGGTGGCGGGCGACATTCAACCGATGGAGGGACAGTATGTTAGCAAtaacaggattagcagagcgagg
NL-chol-60	GAAACGTCATGAAACCATCGATAGCAGCACCGTAGCGCCAAAtaacaggattagcagagcgagg
NL-chol-61	GATTGACCTGGGATAGGTCACGTTGGTGTAGATGTTGTTAAAtaacaggattagcagagcgagg
NL-chol-62	ATCATATGTTAAATTTTTGTTAAATCCATTTTTATCGATGAACGGTAtaacaggattagcagagcgagg
NL-chol-63	GATAATACAAATGAAAAATCTAAAGCCCTTGCTAGCACTAACAACTAtaacaggattagcagagcgagg
NL-chol-64	ACGAACCACAGAAGATAAAACAGAGGTGAGGCGGCTGAGAGCtaacaggattagcagagcgagg

Table A.3: Strands for cholesterol modification (64 sites)

Name	Sequence
NL-f-1	GCCGACAATGGAGGCTTGCAGGGAGTTAAAGGCttttttttttttttttttttt
NL-f-2	TGCTTTCACCATCGCttttttttttttttttttttt
NL-f-3	ATAGCTAGAGGGTAATTGAGCGCCCTGAACAAAGTCATTAATTGttttttttttttttttttttt
NL-f-4	AAAGTACACAGCGATTATACCAAGACAGCTTGATAGTTTCCATTAACCCCACGGAGATttttttttttttttttttttt
NL-f-5	GTAAAATACGTAGGACTAAAGACTTTTCGGGATCGTCACCCTCAGCAGCttttttttttttttttttttt

Table A.4: Strands for fluorophore modification (5 sites)

Name	Sequence
L-core-1	GCGTTTTGTCGCTGAGGCTTGCTAACCGAT
L-core-2	TAAACAGCAACCATCGCCCACGCAAGGGAGTT
L-core-3	ATTAAGAGCTTTTGCGGGATCGTCCGCCGACA
L-core-4	ACAACTTTTTTCTGTATGGGATACCCTCAG
L-core-5	TATCATACAGAAAACGAGAATGCAAATATC
L-core-6	TCCCCCTCACGAACCAGACCGGAAGTTTTCAAACTCCAACAG
L-core-7	GTCAATCACAGGTCTTTACCCTGATCAAAAAG
L-core-8	GCTTGAGATGGTTTTTCAACTTTAATCATT
L-core-9	TGCTGGTAAACAGG
L-core-10	ACAGTATTAAACTCATGGATTTTAAT
L-core-11	TTGAGAATCTACCGCCAATTTTCAAAGTTCCTGAT
L-core-12	AGAAGGAGTGCCCGAACGTTATTAGCC
L-core-13	AAAAACGTCCTTTATCAAAC
L-core-14	GTCAGGATGAGGTCATTTTTGCGGTTAGAACC
L-core-15	TAAAACTACAGAAAAGCCCCAAAATTGTAAAC
L-core-16	TTCCTGTATTTGTTAAAATTCGCATACCCCGG
L-core-17	GCCGGAGAAAGATTCAAAAGGGTTAAATTT
L-core-18	GAACGCCAATCAGCTCATTTTTTATGAGTAAT
L-core-19	TATTCAACTTTTAAATGCAATGCCTTGCTCCT
L-core-20	AAAGAAGTAGACTGGATAGCGTCCACCAATAG
L-core-21	TAATAACTTTGAC
L-core-22	GGCAGATAATAGATAATACATTTAATTGAGG
L-core-23	TAATAGGAGCCGTCTCACCAGTttttCACACGACCAGGTGAGGCCAC
L-core-24	CCGTCGAGAGGGTTGATATCGGAACCTATTATTTTTTCTGAAACA
L-core-25	TGAAAGTATTAAGTAGCGGGGTTTTGCTCCACCCTCAGAACCGCCCCTCATTT
L-core-26	AACCGCCAAGAGAAGGATTAGGATAGGCTGAG
L-core-27	TCATACACGCCACCAGAACCACCACCACCC
L-core-28	AAGTACAGAAGGCACCAACCTAAGTAAGCG
L-core-29	CGGGTAAAAAGGAGTGTACTGGTAATTTTTAAGTTTTAACGG
L-core-30	AGTTTTACATCGCCAACGCttttTCA
L-core-31	GAGTAACAATACAGTAACACAGTAGGGCCAACATGT
L-core-32	GGTCAGTGTGCCCCCTGCCTATTTGCGTAACG
L-core-33	AACGGCTAAGACAGCATCGGAACGGACGTTAG
L-core-34	TAGAAAGGTTTTGTCGTCTTTCCACCGTATAA
L-core-35	CATGTTACCAGAGGCTTTGAGGACAGGGTAGC
L-core-36	ATAATCATAATA
L-core-37	AAAGGGACACCTGAAAGCGTAACAAC
L-core-38	CCCTTCTGATTCTGGCCAAC
L-core-39	TAATAAGAATACCAGTATAAAGGGAGATTTTCAG
L-core-40	ATAATGGAAGGGTAAAACATTGCAAATCCAAT
L-core-41	AAAGTAAAAAACAAAATTGCTTTGAA
L-core-42	TAAGTCCTGAATTAAAATAATATCCCATCC
L-core-43	AAGAAGATTATTCATTTCAATTATTTGAAACCGAA
L-core-44	AATGCAGAGAGCAA
L-core-45	CTAAAGGTCTATCAGGGCGATGATTAAATG
L-core-46	TCCAACGTCTTCTCCGTGGGAACAATTTTACGGCGGATTGAC
L-core-47	CGTAATGGTAACCGTGCATCTGCCCCTGTGTG
L-core-48	ACCACCGGCCGCCACCCTCAGAGCCACCAGAG
L-core-49	CGCAGTCTAGCATTGACAGGAGGTGCCGCCAC
L-core-50	AATGAAATTAGCAAGGCCGGAATGAGGCAG
L-core-51	AATAAATCGATTGGCCTTGATATTAGTAGCAC
L-core-52	GTAGCGACAGCCAGCAAAATCACCGAAATAGC
L-core-53	CCAATAATTCTTACCGAAGCCCTTGCCATTTG
L-core-54	ATTATTTATAGAGATAACCCACAAGTTTTAATTGAGTTAAGC
L-core-55	TTATTACGCAGTATGTTAGTTTAAGAAAAGTTTTTAAGCAGATAG
L-core-56	CCGAACAAAGTTAGGAATACCCAAAAGAAAGACACCACGGAATAAATGGTTTA
L-core-57	TGTCACAAGAAACGCAATAATAACCCAGAAGG
L-core-58	GGGTAATCTGGTTTGCCCCAGCAGCAAGCG
L-core-59	CCAGTGAGGCCCTGAGAGAGTTGCAGGCGAAA
L-core-60	AGAATTAATGATGGTGGTTCCGAATGCCCTTC
L-core-61	GGGTGCCGGAAGCATAAAGTGTATCGGCAA
L-core-62	ATAGGGTTTATAAATCAAAAGAATACACAACA
L-core-63	ATTGCGTTATCCGCTCACAATTCCGTAGATGG
L-core-64	TGAGCGAAAGCAAATATTTAAAACAGGAAG
L-core-65	AAGTTGGGAGCTTTCCGGCACCGCAGATCGCA
L-core-66	ATCGGCCTCAGGATTCTGGTGCCGGAAACAGGGGGATGTGCTGCACCAGTCAC
L-core-67	CATTCAGGCTGCGCAACTGAGTTTGAGGGGATTTTCGACGACAGT
L-core-68	AAGGGAAGGAGTGTTGTTCCAGTTAGCCCGAG
L-core-69	GGCGCTGGATAGCAGCCTTTACAGTAGACGGG
L-core-70	GAACCTCAACGATTTTTTGTTTAAGTCAGA
L-core-71	CCCAGCTACGAGCGTCTTTCCAGACACAAACA
L-core-72	TGACCCCCAGAATACACTAAAACAATGGAAAG
L-core-73	ATGACAACTTGATACCGATAGTTGCCAAAAAA
L-core-74	ATCTAAAGACAGCCCTCATAGTTACTGTAGCA
L-core-75	TAAATGAATCAACAGTTTCAGCGGGCGAATAA
L-core-76	CTCATATAGCAAGGATAAAAATTTAAGCCTTT
L-core-77	GTGTAGGTACAGTCAAATCACCATTTAATGCC
L-core-78	TTGATAATGCATGTCAATCATATGGATCTACA
L-core-79	GACGTTGTAAAACGACGGCCAGTGTACGCCAGCTGGCGAACAGGCAAAGCGCCA
L-core-80	ATTGTATAGAGAATCGATGAACAGTCTGGA

Table A.5: Core sequences of Lidded pore (LGC-CO)

Name	Sequence
L-core-81	GGAATTAGACCGTCACCGACTTGATTAAAGGT
L-core-82	CATTACCACCATCGATAGCAGCACTTAGCGTC
L-core-83	TCAGGGATAGCAAGCCCAATAGGAGGAGGTTTAGTACCGCAGTACCAGGCGGAT
L-core-84	TCAGAGCTCAAAATCACCGGAAGCCATCTT
L-core-85	CCTCAGAAAACCGCCTCCCTCAGACATTTTCG
L-core-86	CCAGCGCCAAAGACAAAAGGGCGATATAAAAGAAACGCAACTGGCATGATTAAG
L-core-87	AAATTGTTATGGTCATAGCTGTTTGCTCGAAT
L-core-88	TACGAGCCTAATGAGTGAGCTAACTTCCAGTC
L-core-89	ACCGCCTGACGGGCAACAGCTGATATTAATGA
L-core-90	GTCCACGCGCCAGGGTGGTTTTGGTTTGCG
L-core-91	AGCATCAGCTGAACCTCAAA
L-core-92	CGGAATTATCATCATAAAACCACC
L-core-93	TATCAGATGATGGTTATCATTTTGCGGAAAAAAGTTT
L-core-94	GTTTAttttACGTCAGATGAATCAATTCATCAATACCTGAT
L-core-95	GCGGTCTTAACACCCTAAAATAttttTCTTTAGGAGCACAGGTGAG
L-core-96	AAGGTTATGCCTGCAACAGTGCCACGCTGAAAGGGAGGATT
L-core-97	CCTCAttttATCAATATCTGGTATCTAA
L-core-98	CGAACCACCAGCAGAGGCACAGACAATATTGATAGAA
L-core-99	TAAGAATACGTAGATAAAACAG
L-core-100	TACCATATCTGATAGCCAACATCGCCATTAAAAATTGGCTATTAG
L-core-101	TACCAAGTTAAAAATTATTTGCACGTTAGAACC
L-core-102	ATTCGCCTGAGAAATAAAGAAATTGACTTCTGA
L-core-103	TGTTTGGATTATCGTAGAAACAATAACGG
L-core-104	TCTTTAATttttGCGCGAACCAAAATCGGAGGCGAA
L-core-105	TTCATAACCCTCAGAGCCACCACACCCTCAG
L-core-106	GTCATAGCCCCCTTATTAGCGTTTCCAGAGCC
L-core-107	AGACTGTAGCGCGTTTTCATCGGACGTCACC
L-core-108	GAATTATCAGAATCAAGTTTGCCTCGTAATCA
L-core-109	CGGAAATTATTCACAAACGTAGAAAATACAT
L-core-110	ACATAAAGCAACACATTCAACCGATGGAGGGAAGGTAAATATTGA
L-core-111	GTGTATCAACTCAACCCATGTACCGACTGAGTTTCGTCACCAGTA
L-core-112	TAATTTTTTCACGTTGAAAATCTTTTGCTAA
L-core-113	CAAACTACAACGCAAGTATAGCCCGGAATAG
L-core-114	TTCCACAGAACAACTAAAGGAATTAGTGAGAA
L-core-115	ATTAGATATCGCAAAATC
L-core-116	AAGGCTCCAAAAGGAGCCTTTAATGAATTTCT
L-core-117	GCGGGCCTGCTATCCAAGCTTGCATGCAGGTCGACTCTAGAGGAT
L-core-118	CCCCGGGTACCGATTGGGAAGGGCGATCGGT
L-core-119	GGGAAACCTGTCGTGCCAGCTGCAAAGCCTG
L-core-120	ACTTTTGCGGGAGAGTAGATTTAGTTTGACC
L-core-121	GGAGAGGGTAGCTATTTTTGAGATGAGAAAG
L-core-122	ATTTCAACCGTTCTAGCTGATAAACAATATGA
L-core-123	GCAAACATAACGCCAGGGTTTTCAGGCGATT
L-core-124	AAGGCTATCAGGTCATTGCCTGAGGGTAATCG
L-core-125	TCGTAATCGCGCTCACTGCCCGCTTCACATTA
L-core-126	ATCGGCCAACGCGCGGGGAGAGGCTCTTTTCA
L-core-127	TATTGGGTCAATAGAAAATTCATGTTTATTT
L-core-128	ATTCCCAATTCTGCGAACGATGGCTTAGAGCttttTTAATTGCTG
L-core-129	ATGCGTTATCAT
L-core-130	CCTTAGATTTTC
L-core-131	ACGCTGAGCTATTAATTAAATCCT
L-core-132	CTTCTGACCTTG
L-core-133	AATCATAGTGAGTGAATATAAATCGTCGAAGAGTCA
L-core-134	TCTGACGTTTGAAATAAGTTAAGATTAAG
L-core-135	ATAGTGAAATTTTCCGACCGTGTGTTAAATAAGAATATTTTATCAA
L-core-136	TTAATGCTAAAT
L-core-137	TAAGGCGATAAA
L-core-138	GACTACCTTTTCAAATAAACACCACTAGAAAAAAACTTTTTTAACC
L-core-139	TCCGGCTTTTTAATGGAATCAATATATGGTCTGAGA
L-core-140	CATAAAACAGTA
L-core-141	CATTTGCAATTT
L-core-142	ATAATTGGAATC
L-core-143	TAACAACGCTTAA
L-core-144	AATATAATGCTGTACGGTGTCTGGAAGTTTTTAGCTATATTTTCAAATTAAGC
L-core-145	GCGAGCTGAATATGCAACTAAAGTAGCTCAAC
L-core-146	ATATTCGGCTTGCTTTCGAGGTTGTATCGGT
L-core-147	TTATCAAAAAGGTGGCATCAATTTTGGGGC
L-core-148	TTATATAAGAGAAGCCTGTTTAGTATACAAA
L-core-149	ACATTTAAAATTACCTTTAGGTTGGG
L-core-150	CGCCTATATGTAAATGC

Table A.6: Core sequences of Lidded pore (LGC-CO)

Name	Sequence
L-chol-1	TCAAAAATTACGAGGCATAGTAAGTAACGCCAtaacaggattagcagagcgagg
L-chol-2	GTCAGAATTAGCCGGAACGAGGACCAACTTtaacaggattagcagagcgagg
L-chol-3	AAAGGAATACACCAGAACGAGTAGATCGGCCTtaacaggattagcagagcgagg
L-chol-4	TGAAAGAATTCAGTGAATAAGGGCCATATTtaacaggattagcagagcgagg
L-chol-5	CCTGAGTAGATTTTAGAACTCAAACTTAAATTGGtaacaggattagcagagcgagg
L-chol-6	GGAATCGTCCAAAATAGCGAGAGGCATCAGTTtaacaggattagcagagcgagg
L-chol-7	ACATTATCCTTATGCGATTTTATTGATTAGtaacaggattagcagagcgagg
L-chol-8	AATGTTTTTTGCCAGAGGGGGTACGGAACAtaacaggattagcagagcgagg
L-chol-9	CTCATTATTTAATAAAACGAACTATTTTTGGGtaacaggattagcagagcgagg
L-chol-10	AATCTACGACCAGTCtaacaggattagcagagcgagg
L-chol-11	CGTGAACCGCCGTAAAGCACTAAAGGAAGAAAtaacaggattagcagagcgagg
L-chol-12	AATTTAGGTTTTCAGAGGCATTTTTGACAAGAtaacaggattagcagagcgagg
L-chol-13	ACCGGATATTCTTCCAAATCAACGTAACAAtaacaggattagcagagcgagg
L-chol-14	TTTTCATGTGTGTCGAAATCCGCGTACAGACCtaacaggattagcagagcgagg
L-chol-15	CGAGTAAATTTTAGAGTCTGTCCATATAACGTtaacaggattagcagagcgagg
L-chol-16	GCTTTCCTCGTTTTCAGAGCGGGAGCTAAAtaacaggattagcagagcgagg
L-chol-17	CGCAAGACAGAATATAAAGTACCGAAATCAATAtaacaggattagcagagcgagg
L-chol-18	TGATGAAAttttCAAACATCAAGTTCTGTCCtaacaggattagcagagcgagg
L-chol-19	AGACGACGACTTTTAATAAACAACATACAATAGAtaacaggattagcagagcgagg
L-chol-20	TAACCACCGATTAAAGGGATTTGTGTTTTTtaacaggattagcagagcgagg
L-chol-21	GAGGCAAAAGCGATTATACCAAGCCAAGAACGtaacaggattagcagagcgagg
L-chol-22	ACGCTAACAATTTTATCCTGAAATCGAGAAtaacaggattagcagagcgagg
L-chol-23	TGCCAGTTATCAAGATTAGTTGCTTCGTAGGAtaacaggattagcagagcgagg
L-chol-24	AAATGAAATCTAAGAACGCGAGGCAAGGCTTAtaacaggattagcagagcgagg
L-chol-25	ACATAAAAAAGCGAAAGGAGCGGCTGCGCGtaacaggattagcagagcgagg
L-chol-26	GGTATTAATCTTTCCTTATCATTCCGAGCCAGtaacaggattagcagagcgagg
L-chol-27	CAAGCAAGAGCATGTAGAAACCCAAAAGGTtaacaggattagcagagcgagg
L-chol-28	TCCGGTATACGCGCCTGTTTATCAGTTCAGCTtaacaggattagcagagcgagg
L-chol-29	AGACCTGCCAGAATCCTGAGAATAGACAGGtaacaggattagcagagcgagg
L-chol-30	ATTGCATATCCAGAACAATATCTTGCCCTtaacaggattagcagagcgagg
L-chol-31	GCAAATGAAAACAGTTTTTACAAACAATTCGACCTACATATCACTTGtaacaggattagcagagcgagg
L-chol-32	GAGTCCACAGCCGGCGAACGTGGCAATGCGCCtaacaggattagcagagcgagg
L-chol-33	ATGTTTTAAATTCGAGCTTCAAAGAATGCTTTtaacaggattagcagagcgagg
L-chol-34	AAAGGCCGGAAGCCCGAAAGACTTACCATAAAtaacaggattagcagagcgagg
L-chol-35	CAGCGAAGCAAAGCGGATTGCACTATTATAtaacaggattagcagagcgagg
L-chol-36	GACGAGAATAAGGGAACCGAACTGCGCAGACGtaacaggattagcagagcgagg
L-chol-37	GTGAATTATACAGGTAGAAAGATTCTTTTGCAtaacaggattagcagagcgagg
L-chol-38	GTTAATATGCCAGCTTTCATCAACGCCCACTAtaacaggattagcagagcgagg
L-chol-39	TTGTTAATCAAAAATAATTCGCAATAGTAAtaacaggattagcagagcgagg
L-chol-40	TTTGATAATAGAGAGTACCTTTAAAATACTGCtaacaggattagcagagcgagg
L-chol-41	ACTCCTCATGGCTTTTGATGATACTACGTAATtaacaggattagcagagcgagg
L-chol-42	AGCTGCTCGGACAGATGAACGGTGACCTGCTCtaacaggattagcagagcgagg
L-chol-43	ACAGTTAACCTTGAGTAACAGTGCTAAAGACTtaacaggattagcagagcgagg
L-chol-44	CAGGAGGCCACACCCGCCGCGCTTGAGAAAGGtaacaggattagcagagcgagg
L-chol-45	CCGCCGCCCTGAATTTACCGTTCCAAACGAAAtaacaggattagcagagcgagg
L-chol-46	GTCAGACCTCATTAAAGCCAGATCTTACCAtaacaggattagcagagcgagg
L-chol-47	AATAGCTAAAGAGCAAGAAACAATGCCTAATTtaacaggattagcagagcgagg
L-chol-48	AAACCGAGTGAGCGCTAATATCAGCCCAATCCtaacaggattagcagagcgagg
L-chol-49	ATCCTGTTCTGAACACCCTGAACAAACGTCAAtaacaggattagcagagcgagg
L-chol-50	AATCCCTAACAGGGAAGCGCATAGAGAATAtaacaggattagcagagcgagg
L-chol-51	GCGCATCGGATAGGTCACGTTGGTTGGAACAAtaacaggattagcagagcgagg
L-chol-52	CTCCAGCCGTAACAACCCGTCGGAAAAGGGCGtaacaggattagcagagcgagg
L-chol-53	AACGGTACCAAGTGTAGCGGTCACGGCGCTAGtaacaggattagcagagcgagg
L-chol-54	TAATTTACGCCGTTTTTATTTTCAATTTTGCAtaacaggattagcagagcgagg
L-chol-55	ATCGGCTGACCAAGTACCGCACTCCTCATCTTtaacaggattagcagagcgagg
L-chol-56	AAACAGTTACCCTCGTTTACCAGACGATAAAAACATAAATATTCATTtaacaggattagcagagcgagg
L-chol-57	GAGATTTATACCACATTCAACTAATGCAGATACAAGCAACACtaacaggattagcagagcgagg
L-chol-58	GCCACTACACGGAGATTTGTATCATCGATAAATAGGAAGTTTCCATTtaacaggattagcagagcgagg
L-chol-59	AGGCGCATTGGCTGACCTTCATCAAGAGTAATCTGCGAAACAtaacaggattagcagagcgagg
L-chol-60	GCTACAGGGTACTATGGTTGCTTTGACGAGCACGTCGGAACCtaacaggattagcagagcgagg
L-chol-61	AAAAACCGGAGCCCCCGATTTAGAGCCGGGGAATATTAAAGAACGTGtaacaggattagcagagcgagg
L-chol-62	AAATAAGACCGACTTGCGGGAGGTTTGCCTTAAACAAAATAAACAGCtaacaggattagcagagcgagg
L-chol-63	ATCATTACCCCAATAGCAAGCAAATCAGATATAGGTTTTAGCtaacaggattagcagagcgagg
L-chol-64	GTCGAGGTATCACCCAAATCAAGTGTCTGGCCtaacaggattagcagagcgagg

Table A.7: Strands for cholesterol modification (64 sites) (LGC-CO)

Name	Sequence
L-f-1	ttttttttttttttttttttttATAAAGCTAATGGTCAATAACCTGTCATTCCATATAAC
L-f-2	ttttttttttttttttttttttGGTTGTAAAACATTATGACCCTGTAAT
L-f-3	ttttttttttttttttttttttATACAGGCAACTCAGAGC
L-f-4	ttttttttttttttttttttttAATAAAGCGGCAAAGAATTAGCAATCTAC
L-f-5	ttttttttttttttttttttttAATTTTAATAGTAGTAGCATTAACATCCAATAAATCCTTTT

Table A.8: Strands for fluorophore modification (5 sites) LGC-CO

Name	Sequence
Plate lock strand - 1	CGGAGAGAAAGAGCGCTCAATTTAGACGGCAAATCAACAGTTGAGAGCCAGCA
Plate lock strand -2	AGGACGTTGTCACGCAAATTAACCGTACATTTTTTCGTTGTGTGCGCGGGTGTAGGAT
Lid lock strand	CCGCGCACACAACGTGAAAACATAGCGATAGCTTATTTCATCTTTTTGCTCTTTCTCTCCGATAAGCTA

Table A.9: Sequences of Lock strands

Name	Sequence
Key 1	atgctcctaATCCTACACCCGCGCACA
Key 2	gacttagaaTAGCTTATCGGAGAGAA
Reverse key 1	GCGCGGGTGTAGGATtaggagcat
Reverse key 2	CTCCGATAAGCTAttctaagtc

Table A.10: Sequences of Keys

Name	Sequence
Cholesterol modified strand	CCTCGCTCTGCTAATCCTGTTA/3CholTEG/
Cy3 modified strand (confocal)	AAAAAAAAAAAAAAAAAAAA/3Cy3Sp/
Cy5 modified strand (confocal)	AAAAAAAAAAAAAAAAAAAA/3Cy5Sp/
Cy3 FRET (dye strand)	TAGAAGTACGTCTGAAATGGAT/iCy3/TATTTTGTAGCAATACTTCTAGAACTGG
Cy5 FRET (dye strand) (Cy5FR)	CCGCGCACACAACGTGAAAACAT/iCy5/AGCGATAGCTTATTTCATCTTTTTGCT CTTTCTCTCCGATAAGCTA

Table A.11: Sequences of modification strands

Name	Sequence
Sensor extension	TCGATTGTGTGGTTGTATACTGCttGCGGT[T(BHQ1)]AAGACCCACAA[T(FAM)]TCCGCtt
NP attachment sequence	GCAGTATACAACCACACAATCGA
Key sequence	AGCGGATTGTGGGTCTTACCGCA
Scramble sequence	TGCGGTAAGACCCACAATCCGCT

Table A.12: Nanopore sensor sequences

Name	Sequence
Tb-1	CTCACCTCCACGAAAACGTGCGAAGGAACCGCGTTTGACCTGTTGACCTGTTATT CCGCGGAGGAGGCAGTTGCGTCAGATTGGT
Tb-2	TGCCAGAATGGAAGTCATCGCGTACGATGGAATGCTACCTATAACCACAATTGGC GCTCATAATTCATTAACAGGTCAGTCCGCAGGTCAAACCAGCG
Tb-3	CTCCGCGGAAATACATGCCAAACTGCGTCTGGCAACTGCCTC
Tb-4-Aorg	ACCAATCTGACCCGGAATAGTC
Tb-5	GACTATTCCGGCAGACGCAGTTTGGCATGTATATGAATTATGCCAATTGTGGTGA CATGGTCTCCTGGCGTCCGTCAGATTGGT
Tb-6	GACCATGTCATTGTGTTATTCGGCACACTTCGGACGCCAGGA
Tb-8	GACTATTCCGGGAAGTGTGCCGAATAACACAATTATAGGTAGTCATCGTACGCCC TCGGTGGTAGTATTGGCCTAATTCGCCGAC
Tb-9	CTCACCTCCACGAAAGCGTTATCCATGGCTAGGATGACTTCCTGGCACGCTGCTT TCGCATTCAACCGGCAAGAATTCGCCGAC
Tb-10-Ulorg	GTCGGCGAATTGTGGAGGTGAG
Tb-11	AATGCGAAAGGCGGTTCCTTCGCACGTTTTCCTTGCCGGTTG
Tb-13	ACCACCGAGGCTAGCCATGGATAACGCTTTCAGGCCAATACT
Tb-4-Aa	ACCAATCTGACCCGGAATAGTC-Amine
Tb-10-Ula	GTCGGCGAATTGTGGAGGTGAG-Amine
Tb-4-cy3	ACCAATCTGACCCGGAATAGTC-cy3
Tb-10-cy3	GTCGGCGAATTGTGGAGGTGAG-cy3

Table A.13: Sequences of DNA tetrabody strands

Supplementary videos can be found at https://rb.gy/j14ta

APPENDIX B

PERMISSIONS FOR USING PUBLISHED ARTICLE AS CHAPTER 2

I hereby state that I have received permission for all the listed authors in the paper to use it in my dissertation.

APPENDIX C

PERMISSIONS FOR ADAPTED FIGURES

SPRINGER NATURE LICENSE
TERMS AND CONDITIONS

Apr 25, 2023

This Agreement between Arizona State University -- Leeza Abraham ("You") and Springer Nature ("Springer Nature") consists of your license details and the terms and conditions provided by Springer Nature and Copyright Clearance Center.

License Number	5535750227325
License date	Apr 25, 2023
Licensed Content Publisher	Springer Nature
Licensed Content Publication	Nature
Licensed Content Title	A 1.7-kilobase single-stranded DNA that folds into a nanoscale octahedron
Licensed Content Author	William M. Shih et al
Licensed Content Date	Feb 12, 2004
Type of Use	Thesis/Dissertation
Requestor type	academic/university or research institute
Format	print and electronic

SPRINGER NATURE LICENSE
TERMS AND CONDITIONS

Apr 25, 2023

This Agreement between Arizona State University -- Leeza Abraham ("You") and Springer Nature ("Springer Nature") consists of your license details and the terms and conditions provided by Springer Nature and Copyright Clearance Center.

License Number	5535750467324
License date	Apr 25, 2023
Licensed Content Publisher	Springer Nature
Licensed Content Publication	Nature
Licensed Content Title	Folding DNA to create nanoscale shapes and patterns
Licensed Content Author	Paul W. K. Rothemund
Licensed Content Date	Mar 16, 2006
Type of Use	Thesis/Dissertation
Requestor type	academic/university or research institute
Format	print and electronic

SPRINGER NATURE LICENSE
TERMS AND CONDITIONS

Apr 25, 2023

This Agreement between Arizona State University -- Leeza Abraham ("You") and Springer Nature ("Springer Nature") consists of your license details and the terms and conditions provided by Springer Nature and Copyright Clearance Center.

License Number	5535750661994
License date	Apr 25, 2023
Licensed Content Publisher	Springer Nature
Licensed Content Publication	Nature Communications
Licensed Content Title	A DNA tweezer-actuated enzyme nanoreactor
Licensed Content Author	Minghui Liu et al
Licensed Content Date	Jul 3, 2013
Type of Use	Thesis/Dissertation
Requestor type	academic/university or research institute
Format	print and electronic

SPRINGER NATURE LICENSE
TERMS AND CONDITIONS

Apr 25, 2023

This Agreement between Arizona State University -- Leeza Abraham ("You") and Springer Nature ("Springer Nature") consists of your license details and the terms and conditions provided by Springer Nature and Copyright Clearance Center.

License Number	5535751044939
License date	Apr 25, 2023
Licensed Content Publisher	Springer Nature
Licensed Content Publication	Nature
Licensed Content Title	Self-assembly of a nanoscale DNA box with a controllable lid
Licensed Content Author	Ebbe S. Andersen et al
Licensed Content Date	May 7, 2009
Type of Use	Thesis/Dissertation
Requestor type	academic/university or research institute
Format	print and electronic

SPRINGER NATURE LICENSE
TERMS AND CONDITIONS

Apr 25, 2023

This Agreement between Arizona State University -- Leeza Abraham ("You") and Springer Nature ("Springer Nature") consists of your license details and the terms and conditions provided by Springer Nature and Copyright Clearance Center.

License Number	5535751494388
License date	Apr 25, 2023
Licensed Content Publisher	Springer Nature
Licensed Content Publication	Nature Biotechnology
Licensed Content Title	A DNA nanorobot functions as a cancer therapeutic in response to a molecular trigger in vivo
Licensed Content Author	Suping Li et al
Licensed Content Date	Feb 12, 2018
Type of Use	Thesis/Dissertation
Requestor type	academic/university or research institute

ELSEVIER LICENSE
TERMS AND CONDITIONS

Apr 25, 2023

This Agreement between Arizona State University -- Leeza Abraham ("You") and Elsevier ("Elsevier") consists of your license details and the terms and conditions provided by Elsevier and Copyright Clearance Center.

License Number	5535760504159
License date	Apr 25, 2023
Licensed Content Publisher	Elsevier
Licensed Content Publication	Trends in Biotechnology
Licensed Content Title	Functionalization of Cellular Membranes with DNA Nanotechnology
Licensed Content Author	Andreas Schoenit,Elisabetta Ada Cavalcanti-Adam,Kerstin Göpfrich
Licensed Content Date	Nov 1, 2021
Licensed Content Volume	39
Licensed Content Issue	11

SPRINGER NATURE LICENSE
TERMS AND CONDITIONS

Apr 25, 2023

This Agreement between Arizona State University -- Leeza Abraham ("You") and Springer Nature ("Springer Nature") consists of your license details and the terms and conditions provided by Springer Nature and Copyright Clearance Center.

License Number	5535760775690
License date	Apr 25, 2023
Licensed Content Publisher	Springer Nature
Licensed Content Publication	Nature Nanotechnology
Licensed Content Title	DNA probes for monitoring dynamic and transient molecular encounters on live cell membranes
Licensed Content Author	Mingxu You et al
Licensed Content Date	Mar 20, 2017
Type of Use	Thesis/Dissertation
Requestor type	academic/university or research institute

JOHN WILEY AND SONS LICENSE
TERMS AND CONDITIONS

Apr 25, 2023

This Agreement between Arizona State University -- Leeza Abraham ("You") and John Wiley and Sons ("John Wiley and Sons") consists of your license details and the terms and conditions provided by John Wiley and Sons and Copyright Clearance Center.

License Number	5535761134245
License date	Apr 25, 2023
Licensed Content Publisher	John Wiley and Sons
Licensed Content Publication	Angewandte Chemie International Edition
Licensed Content Title	Polyvalent Display of Biomolecules on Live Cells
Licensed Content Author	Yong Wang, Erin R. Gaddes, James Coyne, et al
Licensed Content Date	Feb 15, 2018
Licensed Content Volume	57
Licensed Content Issue	23
Licensed Content Pages	5

SPRINGER NATURE LICENSE
TERMS AND CONDITIONS

Apr 25, 2023

This Agreement between Arizona State University -- Leeza Abraham ("You") and Springer Nature ("Springer Nature") consists of your license details and the terms and conditions provided by Springer Nature and Copyright Clearance Center.

License Number	5535770076069
License date	Apr 25, 2023
Licensed Content Publisher	Springer Nature
Licensed Content Publication	Nature Nanotechnology
Licensed Content Title	Membrane-anchored DNA nanojunctions enable closer antigen-presenting cell–T-cell contact in elevated T-cell receptor triggering
Licensed Content Author	Yulin Du et al
Licensed Content Date	Mar 9, 2023
Type of Use	Thesis/Dissertation
Requestor type	academic/university or research institute

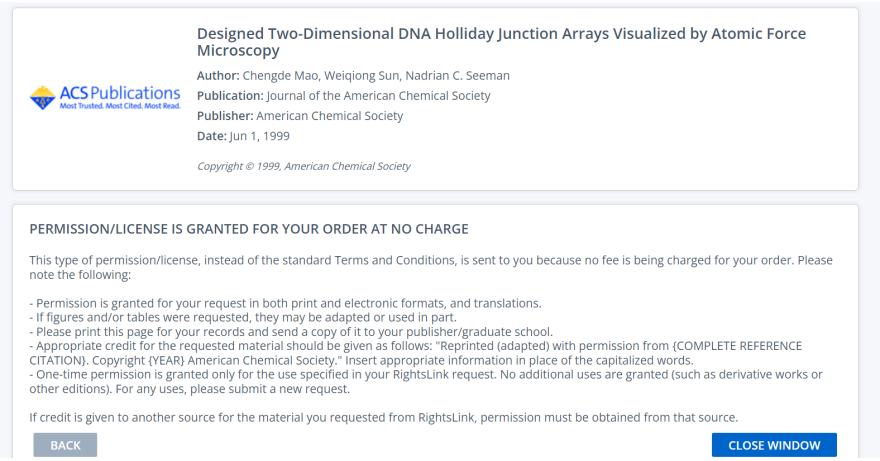

Designed Two-Dimensional DNA Holliday Junction Arrays Visualized by Atomic Force Microscopy

Author: Chengde Mao, Weiqiong Sun, Nadrian C. Seeman
Publication: Journal of the American Chemical Society
Publisher: American Chemical Society
Date: Jun 1, 1999

PERMISSION/LICENSE IS GRANTED FOR YOUR ORDER AT NO CHARGE

This type of permission/license, instead of the standard Terms and Conditions, is sent to you because no fee is being charged for your order. Please note the following:

- Permission is granted for your request in both print and electronic formats, and translations.
- If figures and/or tables were requested, they may be adapted or used in part.
- Please print this page for your records and send a copy of it to your publisher/graduate school.
- Appropriate credit for the requested material should be given as follows: "Reprinted (adapted) with permission from {COMPLETE REFERENCE CITATION}. Copyright {YEAR} American Chemical Society." Insert appropriate information in place of the capitalized words.
- One-time permission is granted only for the use specified in your RightsLink request. No additional uses are granted (such as derivative works or other editions). For any uses, please submit a new request.

If credit is given to another source for the material you requested from RightsLink, permission must be obtained from that source.

BACK CLOSE WINDOW

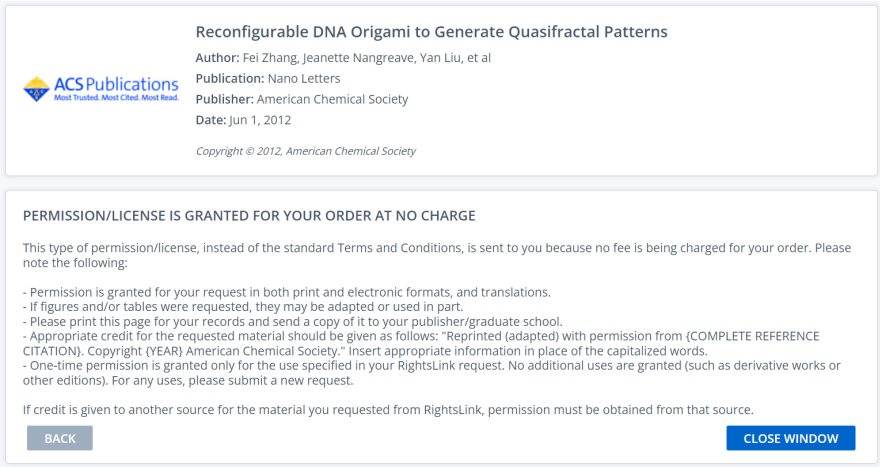

Reconfigurable DNA Origami to Generate Quasifractal Patterns

Author: Fei Zhang, Jeanette Nangreave, Yan Liu, et al
Publication: Nano Letters
Publisher: American Chemical Society
Date: Jun 1, 2012

PERMISSION/LICENSE IS GRANTED FOR YOUR ORDER AT NO CHARGE

This type of permission/license, instead of the standard Terms and Conditions, is sent to you because no fee is being charged for your order. Please note the following:

- Permission is granted for your request in both print and electronic formats, and translations.
- If figures and/or tables were requested, they may be adapted or used in part.
- Please print this page for your records and send a copy of it to your publisher/graduate school.
- Appropriate credit for the requested material should be given as follows: "Reprinted (adapted) with permission from {COMPLETE REFERENCE CITATION}. Copyright {YEAR} American Chemical Society." Insert appropriate information in place of the capitalized words.
- One-time permission is granted only for the use specified in your RightsLink request. No additional uses are granted (such as derivative works or other editions). For any uses, please submit a new request.

If credit is given to another source for the material you requested from RightsLink, permission must be obtained from that source.

BACK CLOSE WINDOW